Dynamics and statistical mechanics of point vortices in bounded domains

by

Thomas Lowday Ashbee

A thesis submitted in conformity with the requirements for the degree of Doctor of Philosophy.

Department of Mathematics
University College London

Supervisors: J. G. Esler & N. R. McDonald

October, 2013

I, Thomas Lowday Ashbee, confirm that the work presented in this thesis is my own. Where information has been derived from other sources, I confirm that this has been indicated in the thesis.

SIGNED

Abstract

A general treatment of the dynamics and statistical mechanics of point vortices in bounded domains is introduced in Chapter 1. Chapter 2 then considers high positive energy statistical mechanics of 2D Euler vortices. In this case, the most-probable equilibrium dynamics are given by solutions of the sinh-Poisson equation and a particular heart-shaped domain is found in which below a critical energy the solution has a dipolar structure and above it a monopolar structure. Sinh-Poisson predictions are compared to long-time averages of dynamical simulations of the N vortex system in the same domain.

Chapter 3 introduces a new algorithm (VOR-MFS) for the solution of generalised point vortex dynamics in an arbitrary domain. The algorithm only requires knowledge of the free-space Green's function and utilises the exponentially convergent method of fundamental solutions to obtain an approximation to the vortex Hamiltonian by solution of an appropriate boundary value problem. A number of test cases are presented, including quasi-geostrophic shallow water (QGSW) point vortex motion (governed by a Bessel function).

Chapter 4 concerns low energy (positive and negative) statistical mechanics of QGSW vortices in 'Neumann oval' domains. In this case, the 'vorticity fluctuation equation' – analogous to the sinh-Poisson equation – is derived and solved to give expressions for key thermodynamic quantities. These theoretical expressions are compared with results from direct sampling of the microcanonical ensemble, using VOR-MFS to calculate the energy of the QGSW system.

Chapter 5 considers the distribution of 2D Euler vortices in a Neumann oval. At high energies, vortices of one sign cluster in one lobe of the domain and vortices of the other sign cluster in the other lobe. For long-time simulations, these clusters are found to switch lobes. This behaviour is verified using results from the microcanonical ensemble.

Citations to previously published work

Chapter 3 forms the basis of the paper

> "Generalized Hamiltonian point vortex dynamics on arbitrary domains using the method of fundamental solutions", T. L. Ashbee, J. G. Esler, N. R. McDonald, *J. Comput. Phys.* 246: 289-303, 2013.

Chapter 4 is a generalisation and extension of the paper

> "Statistical mechanics of a neutral point-vortex gas at low energy", J. G. Esler, T. L. Ashbee, N. R. McDonald, *Phys. Rev. E* 88: 012109, 2013.

Disclaimer

The author benefited from an exchange of notes with J. G. Esler, regarding the material at the end of section 1.2.1, and in sections 1.3.5, 4.2, 4.3, 4.A and appendix B. These sections should be regarded as joint work.

Acknowledgments

First and foremost I would like to thank my supervisors Gavin Esler and Robb McDonald. Their passion for research has been a true inspiration. I would also like to thank my examiners Pierre-Henri Chavanis and David Dritschel for a very stimulating viva.

I would like to acknowledge the support the Department of Mathematics at UCL for providing funding for my PhD through a Postgraduate Teaching Assistant award. I would also like to thank the other members of the Department of Mathematics, particularly Bonita Carboo, Soheni Francis, Helen Higgins and Richard Hoyle for their assistance throughout my PhD.

My fellow PhD students have been a great support over the years. I would like to thank Ali Khalid, Huda Ramli, Olly Southwick and Ben Willcocks for numerous technical conversations that have been vital throughout my time at UCL. For less technical, but equally important conversations (and socialising) I would like to thank Pablo Soberón Bravo, Nyein Chan, Chris Daw, Rob Downes, Dan Ellam, Gin Grasso, Pete Kowalski, Rahul Nilawar, Edgardo Roldán Pensado, Jamie Rodney, Adam Townsend and of course Louise Jottrand.

I am also grateful to my A level mathematics teachers at Shrewsbury Sixth Form College Mike Braithwaite, Rob Kinnersley and Pip Lee who very much sowed the seed for my mathematical endeavours. Continuing the metaphor, this seed was cultivated at the University of Bristol by fellow students Conor Daly, Geriant Davies & Martin Hale and lecturers Richard Kerswell & Yevs Tourigny among many others.

And finally I would like to thank my family: my sister Ruth Ashbee & brother-in-law Tom Mosley, my dad Ken Ashbee, my uncles Peter & David Walter, my grandparents Gill & Braham Walter and most of all my mum Elizabeth Ashbee.

In memory of Elizabeth Ashbee (1957-2010).

Contents

Chapter 1

Introduction

1.1 Background and motivation

1.1.1 Historical perspective

The modern mathematical treatment of fluid dynamics dates back to 1757 when Euler [46] derived the dynamical equations of motion for an ideal fluid using Newtonian calculus. Since then fluid dynamics has become a key area of applied mathematics and continues to command a lively literature.

The focus of this thesis is on two dimensional (2D) flows involving points of vorticity in an otherwise irrotational fluid. The mathematical formulation of this 'point vortex' model was introduced in 1867 by Helmholtz [61]; by the 20^{th} century vortex dynamics was an established sub-field of fluid dynamics. A sample of modern vortex dynamics research is given in [2].

Following on from the work of Kirchhoff [69] and Routh [103], in 1942 Lin [76, 77] proved that the motion of N vortices in a bounded domain is a Hamiltonian system. This led, a few years later in 1949, to Onsager [93] applying the statistical mechanics theory, developed by Boltzmann [10] in the latter part of the 19^{th} century, to the vortex system with $N \gg 1$. Onsager thus postulated the remarkable concept of negative temperature for this system. The motivation behind Onsager's work was largely to explain the self-organisation of many turbulent 2D flows into isolated, large-scale, long-lived vortices. Due to the robustness of the self-organisation of these macro vortex structures it seems likely that their formation can be explained by

some fundamental physical principles such as those of thermodynamics and statistical mechanics. In the subsequent years, the point vortex statistical mechanics model has also been applied to a number of other physical systems, as detailed in section 1.1.2.

Further theoretical results [17, 43, 48, 52, 68] (among many others) have put point vortex statistical mechanics on a sound mathematical footing. Early numerical calculations [11, 64, 87, 95, 107, 121] of moderately large N ($O(10)$) vortex systems and partial differential equations derived from statistical assumptions allowed some verification of these ideas. Recent improvements in computing power have allowed simulations [13, 123] of larger N ($O(10^3 - 10^4)$) systems providing further validation. The historical review by Eyink and Sreenivasan [49] and chapter 6 of the book by Newton [91] offers an overview of the progress of point vortex statistical mechanics since 1949, as well as some open problems.

This thesis will present a number of new point vortex statistical mechanics results, with an emphasis on verification using numerical calculation. Before proceeding, some modern applications of point vortex statistical mechanics will be discussed.

1.1.2 Reasons for modern interest

Two geophysical examples of macro vortex structures in 2D turbulence, of the type that motivated Onsager to develop point vortex statistical mechanics as mentioned above, are ocean eddies and atmospheric vortices such as Jupiter's Great Red Spot. In strongly stratified, rapidly rotating flows, the motion is layer-wise, justifying the use of the 2D point vortex model. Eddies and vortices are intense localised structures in the ocean or atmosphere which rotate about a vertical axis. They can maintain a stable structure while traversing vast distances and, in the case of ocean eddies, can interact with topographic features such as islands and shorelines. They are often long-lived with oceanic eddies having been tracked for several years [99] and Jupiter's Great Red spot, having been first observed by Galileo Galilei in 1610 [49], persists to the present day. Oceanic eddies and atmospheric vortices play a key role in the climate system and because of this, modelling them is of vital importance.

A second application of point vortex statistical mechanics is to magnetised or 'guiding centre' plasmas [64, 110, 112], where the magnetic field induces 2D behaviour.

A plasma is a phase of matter in which the internal energy exceeds the atomic ionisation energy, and where the atoms have decomposed into negatively charged electrons and positively charged ions that interact with each others' electromagnetic fields. This can immediately be seen to be reminiscent of the 2D turbulence vortex model of interacting points of vorticity. In fact, aside from a scale factor, the equations of motion (which will be given in the next section) for the vortex and plasma models are identical. The modelling of plasmas is important in many physical systems with two examples being the ionosphere (the part of the Earth's upper atmosphere, at heights of $5 - 30 \times 10^4$ m, that is partially photonised by solar ultraviolet radiation) and the solar wind (the stream of charged particles released by the Sun into the Solar System).

A third application of point vortex statistical mechanics is the modelling of quantum vortices in superfluids [6, 39]. A superfluid is a phase of matter which behaves like a fluid with zero viscosity and quantised circulation and was first observed experimentally in Helium II: the low temperature phase of ^{4}He. A relevant parent model for this system is the Gross-Pitaevskii equation (nonlinear Schrödinger equation) which, when modified by a 'quantum pressure' term, is equivalent to the compressible Euler equation. When the distance between the vortices is large compared to the size of the vortices themselves, the quantum pressure term can be neglected and close parallels can be made with classical incompressible Euler hydrodynamics. A remarkable feature of this system is that the assumption that vorticity can be discretised is in fact genuinely true, as vorticity can exist only within vortex filaments of small core size. In Helium II this core size is very small (about 10^{-10} m) and the point vortex model is appropriate. The study of quantum vortices is a fundamental problem in physics with applications to the liquid cooling of superconducting magnets in high-energy particle accelerators, fusion experiments and infrared astronomy.

A final application of point vortex statistical mechanics is to self-gravitating systems in astrophysics [19, 23] e.g. stars in a galaxy interacting via gravity and planetary formation from protoplanetary nebula. The details of this system differ significantly from those of the point vortex/plasma/superfluid systems described above, most notably the stellar systems being 3D as opposed to 2D. In spite of this, the details of Onsager's vortex statistical mechanics and self-gravitating particle statis-

tical mechanics are remarkably similar. Further, in terms of the physical model, the tendency of individual point vortices to self-organise into large structures (like ocean eddies) is closely reminiscent of the self-organisation of stars in galaxies – no such phenomena is observed in plasmas and superfluids [23]. It should be noted the mechanism for self organisation of vortices is different to that of self-gravitating systems.

1.2 Point vortex dynamics

1.2.1 The Hamiltonian model

For the motion of N vortices in a simply connected and bounded domain $\mathcal{D} \subset \mathbb{R}^2$, each with circulation Γ_i $(i = 1, \ldots, N)$ the equations of motion are Hamilton's equations [91, 104],

$$\Gamma_i \dot{x}_i = -\frac{\partial H}{\partial y_i}, \quad \Gamma_i \dot{y}_i = \frac{\partial H}{\partial x_i}, \qquad i = 1, ..., N. \tag{1.1}$$

The system (1.1) is unusual only in that the scaled vortex coordinates $|\Gamma_i|^{1/2}\boldsymbol{x}_i$, where $\boldsymbol{x}_i = (x_i y_i)^T$, take the role of canonical phase space coordinates.

A scale transformation of (1.1), such as in [110], and a change of terminology makes the system equivalent to that of a guiding centre plasma as mentioned in section 1.1.2. Specifically, the charged filaments (vortices) move in a uniform magnetic field B with charge (circulation) e_i. Hence the 2D plasmic form of (1.1) is

$$e_i \dot{x}_i = -\frac{1}{B}\frac{\partial H}{\partial y_i}, \quad e_i \dot{y}_i = \frac{1}{B}\frac{\partial H}{\partial x_i}, \qquad i = 1, ..., N.$$

Throughout this thesis the point vortex dynamics terminology will be used.

In the most general formulation of point vortex dynamics (e.g. [76]), the vortex Hamiltonian can be written as

$$H(\boldsymbol{x}_1, \ldots, \boldsymbol{x}_N) = -\sum_{i=1}^{N}\sum_{j=i+1}^{N} \Gamma_i \Gamma_j G(\boldsymbol{x}_i, \boldsymbol{x}_j) - \frac{1}{2}\sum_{i=1}^{N} \Gamma_i^2 g(\boldsymbol{x}_i, \boldsymbol{x}_i), \tag{1.2}$$

and is a conserved quantity (see section 1.2.2 for further details). The function

$G(\boldsymbol{x}, \boldsymbol{x}')$ is the Green's function of the first kind for the domain $\mathcal{D}$, defined by

$$\mathcal{L}G(\boldsymbol{x}, \boldsymbol{x}') = \delta(\boldsymbol{x} - \boldsymbol{x}') \qquad \boldsymbol{x}, \boldsymbol{x}' \in \mathcal{D}, \tag{1.3a}$$

$$G(\boldsymbol{x}, \boldsymbol{x}') = 0. \qquad \boldsymbol{x} \in \partial\mathcal{D}. \tag{1.3b}$$

The linear, elliptic and self-adjoint operator $\mathcal{L}$, which acts on the $\boldsymbol{x}$ variable only, is in most formulations the Laplacian ($\mathcal{L} \equiv \nabla^2$), and the result is the point vortex dynamical system of the 2D Euler equations or, equivalently, the Coulomb interaction of 2D plasma. Other choices of $\mathcal{L}$ result in alternative dynamics with relevance to various problems in geophysical fluid dynamics and 2D plasmas; some examples of which are given below. The self-adjointness of $\mathcal{L}$ guarantees the symmetry $G(\boldsymbol{x}, \boldsymbol{x}') = G(\boldsymbol{x}', \boldsymbol{x})$; see [37].

The remaining function $g(\boldsymbol{x}, \boldsymbol{x}')$ appearing in (1.2), which we shall term the residual Green's function, is defined by

$$g(\boldsymbol{x}, \boldsymbol{x}') = G(\boldsymbol{x}, \boldsymbol{x}') - G_0(\boldsymbol{x}, \boldsymbol{x}') \tag{1.4}$$

where G_0 is the corresponding free-space ($\mathbb{R}^2$) Green's function satisfying

$$\mathcal{L}G_0(\boldsymbol{x}, \boldsymbol{x}') = \delta(\boldsymbol{x} - \boldsymbol{x}') \qquad \boldsymbol{x}, \boldsymbol{x}' \in \mathbb{R}^2, \tag{1.5a}$$

$$|\nabla G_0(\boldsymbol{x}, \boldsymbol{x}')| \to 0 \qquad |\boldsymbol{x} - \boldsymbol{x}'| \to \infty. \tag{1.5b}$$

As mentioned above, numerical solution of the system (1.1) has understandably focused on the 2D Euler system, for which

$$\mathcal{L} \equiv \nabla^2, \quad G_0(\boldsymbol{x}, \boldsymbol{x}') = \frac{1}{2\pi} \log(|\boldsymbol{x} - \boldsymbol{x}'|), \tag{1.6}$$

and interaction of the vortices is called 'long-ranged' due to the slow decay of the logarithmic function. Although most early calculations (e.g. [95]) have focussed on circular or doubly periodic[1] domains for which explicit expressions for G (and thus

[1]The 2D Euler system in doubly periodic domains requires a different approach from that of a bounded domain. In this situation each vortex has infinitely many images as, due to periodicity, each image vortex also requires its own image and so on. Thus, the velocity of a vortex is given by two doubly infinite summations which can be evaluated using the so-called 'Ewald summation' [47,58]. Such domains will not be considered in this thesis.

g) are available via the method of images, it has been long known [77] that the 2D Euler point vortex system can be solved in any simply connected domain $\mathcal{D}$ using the conformal map to the unit circle. The method exploits the so-called Routh rule to make suitable modifications to the Hamiltonian H. These techniques will be used throughout this thesis and details are given in appendix A. The conformal mapping of the vortex Hamiltonian has recently [35] been extended to multiply connected domains using the Riemann mapping function of that domain onto a topologically equivalent domain with all boundaries being circles.

For systems governed by operators $\mathcal{L}$ other than the Laplacian, the method of images is typically restricted to polygonal domains since there is no equivalent of the Routh rule. An important example of such a system with applications to geophysical fluid dynamics [94] and 2D plasmas [20,59,110] is governed by the modified Helmholtz operator

$$\mathcal{L} \equiv \nabla^2 - \lambda^2, \qquad G_0(\boldsymbol{x}, \boldsymbol{x}') = -\frac{1}{2\pi} K_0(\lambda|\boldsymbol{x} - \boldsymbol{x}'|), \tag{1.7}$$

where $K_0(\cdot)$ is the modified Bessel function of the second kind of zeroth order. The parameter λ^{-1} has the dimension of length and controls the range of the interaction. This system differs from that governed by (1.6) in that the dynamical influence of vortices/plasma decays rapidly on lengthscales $\sim \lambda^{-1}$, localising the dynamics (i.e. a short-ranged interaction).

In the context of geophysical fluid dynamics, (1.7) is known as the '*quasi-geostrophic shallow water*' (QGSW[2]) model and the parameter λ^{-1} is the 'Rossby deformation radius'. For dynamics of ocean vortices, typically λ^{-1} is of the order of $1 - 5 \times 10^4$ m.

In the context of 2D plasmas, (1.7) can be used in two separate models. In the first case [110], (1.7) is known as the '*Deybe screened interaction*' model and λ^{-1} is the 'Debye length' which is of the order of 10^{-3} m for the dynamics of plasma in the ionosphere and 10 m for the solar wind. In the second case [20, 59], (1.7) is known

[2]Note that in the terminology of low N point vortex dynamics (e.g. [92]) this system is usually referred to simply as a 'quasi-geostrophic' (QG) vortex, whereas in the statistical mechanics literature (e.g. [63]), a 'quasi-geostrophic' system refers to a two layer model governed by $\mathcal{L} \equiv \nabla^2$, $G_0(\boldsymbol{x}, \boldsymbol{x}') = \frac{1}{4\pi}|\boldsymbol{x} - \boldsymbol{x}'|^{-1}$ for $\boldsymbol{x} \in \mathbb{R}^3$. Due to the focus of this thesis, the 2D statistical mechanics term QGSW will be used.

as the '*Charney-Hasegawa-Mima*' equation with λ^{-1} the 'gyroradius' which is of the order of 2 m for the ionosphere and 10^4 m for the solar wind [34].

A second example of a vortex system not governed by the Laplacian operator is the 'surface quasi-geostrophic' (SQG) system [60], for which

$$\mathcal{L} \equiv -(-\nabla^2)^{1/2}, \quad G_0(\boldsymbol{x}, \boldsymbol{x}') = -\frac{1}{2\pi}(|\boldsymbol{x} - \boldsymbol{x}'|)^{-1}.$$

The SQG system describes the motion induced by surface concentrated potential vorticity anomalies in the ocean or atmosphere, or equivalently, surface potential buoyancy anomalies (ocean) or potential temperature anomalies (atmosphere) at the planetary surface or tropopause [65]. The singularity associated with an SQG vortex is a simple pole rather than a logarthmic singularity, and the result is dynamics that is much more active on small scales [60]. The turbulent cascade in the SQG model is also thought relevant to three-dimensional turbulence in the Euler equations [33].

At this juncture, an important point is made with regards to the formulation of the different point vortex models in an arbitrary bounded domain $\mathcal{D}$. First, consider the streamfunction $\psi(\boldsymbol{x})$, which may be defined in terms of Green's function of the first kind, as

$$\psi(\boldsymbol{x}) = \sum_{i=1}^{N} \Gamma_i G(\boldsymbol{x}, \boldsymbol{x}_i), \quad \boldsymbol{x} \in \mathcal{D}. \tag{1.8}$$

It is required that the flow satisfies the impenetrability constraint i.e. no flow across the boundary $\partial\mathcal{D}$. This means that (1.8) is *constant* along the boundary. In the 2D Euler case the constant is arbitrary, so can simply taken to be zero i.e.

$$\psi(\boldsymbol{x}) = 0, \quad \boldsymbol{x} \in \partial\mathcal{D}. \tag{1.9}$$

However, as noted in [118], for the QGSW system mentioned above (and the SQG system as well), the constant cannot, in general, be set to zero. Instead

$$\psi(\boldsymbol{x}) = \text{constant} \neq 0, \quad \boldsymbol{x} \in \partial\mathcal{D}, \tag{1.10}$$

is the most physically relevant boundary condition, with the constant being deter-

mined from the mass conservation constraint $\int_{\mathcal{D}} \psi \, d\boldsymbol{x} = 0$.

The QGSW calculations presented in chapters 3 and 4 were performed using the less physically relevant condition (1.9). New calculations with the boundary condition (1.10) are underway, with early indictions that very minimal difference is observed compared to the results obtained using (1.9).

The final part of this subsection will offer a brief outline of the relationship between the point vortex model described above and the continuous 2D Euler equations. In an incompressible 2D fluid the vorticity of the flow is given by

$$\boldsymbol{\omega}(\boldsymbol{x}, t) = \nabla \times \boldsymbol{u}(\boldsymbol{x}, t) = \omega(\boldsymbol{x}, t)\boldsymbol{z}, \tag{1.11}$$

where $\boldsymbol{u} = \dot{\boldsymbol{x}} = (u, v)$ is the velocity field of the fluid and $\boldsymbol{z}$ is the unit normal perpendicular to the plane of the velocity of the fluid. The 2D Euler equations may be defined in terms of the transport of vorticity by the velocity field as

$$\frac{\partial \omega}{\partial t} + (\boldsymbol{u} \cdot \nabla)\omega = 0, \tag{1.12}$$

$$\omega = \nabla^2 \psi \tag{1.13}$$

$$\boldsymbol{u} = \boldsymbol{z} \times \nabla \psi, \tag{1.14}$$

where $\psi(\boldsymbol{x}, t)$ is the streamfunction.

The vorticity of the point vortex system as considered in this thesis is given by the singular distribution

$$\omega(\boldsymbol{x}, t) = \sum_{i=1}^{N} \Gamma_i \delta(\boldsymbol{x} - \boldsymbol{x}_i(t)). \tag{1.15}$$

The connections between the two definitions of vorticity (1.11) and (1.15) were considered in a rigorous mathematical work by Marchioro & Pulverenti [80]. Two theorems in [80] are of particular relevance here. Firstly, in their theorem 4.2.2 they consider whether the discrete system of point vortices is a limit of a smooth solution of the 2D Euler equations. To do this they take the approach of 'smearing' the point vortices into patches of vorticity and then compared the evolution of the point vortices under their Hamiltonian dynamics to the evolution of the vortex patches as

solutions of the 2D Euler equations. They prove that when the distance between patches is much greater than the size of the patches themselves, and over a sufficiently short time interval, that the positions of the centroids of the vortex patches converge to the positions of the point vortices as the smearing decreases to zero. Thus they conclude that the motion of point vortices is close to exact Euler flows in the sense of vorticity.

On the other hand, in theorem 5.3.1 of [80], the authors address the question as to whether a similar result holds in the opposite direction i.e. does a discretisation of the flow by finitely many vortices converge to a smooth solution of the 2D Euler equations as the number of vortices goes to infinity? First it is noted that the convergence of point vortices is difficult to prove analytically due to their inherent singularities. Instead, smoothed versions of such systems were considered and it was proved that as the smoothing goes to zero and number of vortices tends to infinity in an appropriate way, the vorticity (1.15) does converge to the vorticity field that is a solution of the 2D Euler equations.

Some further results on the relationship between energy in the 2D Euler equations and the point vortex model are also of interest. The total energy of the fluid described by the 2D Euler equations is purely kinetic and is given by

$$E = \frac{1}{2}\int_{\mathcal{D}} |\boldsymbol{u}|^2 \, d\boldsymbol{x}. \tag{1.16}$$

Using (1.14) and integration by parts, (1.16) can also be expressed as

$$\begin{aligned} E &= \frac{1}{2}\int_{\mathcal{D}} |\nabla\psi|^2 \, d\boldsymbol{x} \\ &= \frac{1}{2}\oint_{\partial\mathcal{D}} \psi\nabla\psi\cdot\boldsymbol{n}\, dS - \frac{1}{2}\int_{\mathcal{D}} \psi\nabla^2\psi \, d\boldsymbol{x}. \end{aligned} \tag{1.17}$$

Assuming[3] $\psi(\boldsymbol{x}) = 0$ for $\boldsymbol{x} \in \partial\mathcal{D}$, the first term in (1.17) is zero, leading to

$$\begin{aligned} E &= -\frac{1}{2}\int_{\mathcal{D}} \psi\nabla^2\psi \, d\boldsymbol{x} \\ &= -\frac{1}{2}\int_{\mathcal{D}} \omega(\boldsymbol{x})\psi(\boldsymbol{x}) \, d\boldsymbol{x} \\ &= -\frac{1}{2}\int_{\mathcal{D}^2} \omega(\boldsymbol{x})G(\boldsymbol{x},\boldsymbol{x}')\omega(\boldsymbol{x}') \, d\boldsymbol{x} \, d\boldsymbol{x}', \end{aligned} \tag{1.18}$$

where the vorticity and streamfunction relation

$$\psi(\boldsymbol{x}) = \int_{\mathcal{D}} G(\boldsymbol{x},\boldsymbol{x}')\omega(\boldsymbol{x}') \, d\boldsymbol{x}',$$

has been used in the final line.

As will be shown below, the energy expression (1.18), and hence (1.16), are equivalent to the point vortex Hamiltonian H (i.e. (1.2)). In doing so we will have to reconcile apparent contradiction that the 2D Euler energy (1.16) is always positive, while the Hamiltonian vortex energy (1.2) can have positive *and* negative values.

A sensible first step in demonstrating the equivalence of (1.18) and (1.2) would be to substitute the singular point vortex vorticity distribution (1.15) i.e. $\omega(\boldsymbol{x}) = \omega_0(\boldsymbol{x}) = \sum_{i=1}^{N} \Gamma_i \delta(\boldsymbol{x} - \boldsymbol{x}_i)$ into (1.18). However, this results in an undefined integral, suggesting a more subtle approach is required.

In particular, we must relax the assumption that vorticity is singular and instead consider a solution to the 2D Euler equations in which the vorticity is uniformly distributed over a finite area or 'patch'. There are various types of vortex patch [91], with the one considered here being the Rankine vortex, which is defined by solid body rotation inside a patch of radius a, centred on the point vortex location $\boldsymbol{x}_i$. The Rankine vortex may be defined by the indicator function

$$I_a(r) = \frac{1}{\pi a^2}\begin{cases} 1, & r \leq a \\ 0, & r > a, \end{cases} \tag{1.19}$$

[3]Note that as mentioned above, the assumption $\psi(\boldsymbol{x}) = 0, \ \boldsymbol{x} \in \partial\mathcal{D}$ is not always valid, particularly when considering other types of vortices.

from which the (bounded) vorticity field is given by

$$\omega_a(\boldsymbol{x}) = \sum_{i=1}^{N} \Gamma_i I_a(|\boldsymbol{x} - \boldsymbol{x}_i|). \tag{1.20}$$

Note that it is assumed that a is sufficiently small, and that $\mathcal{D}$ sufficiently large, so that no patches overlap. Clearly, in the limit $a \to 0$, the point vortex vorticity ω_0 is recovered from (1.20).

Substituting (1.20) into (1.18) gives the energy of N Rankine vortices to be

$$E_a = -\frac{1}{2} \int_{\mathcal{D}^2} \omega_a(\boldsymbol{x}) G(\boldsymbol{x}, \boldsymbol{x}') \omega_a(\boldsymbol{x}') \, d\boldsymbol{x} \, d\boldsymbol{x}'. \tag{1.21}$$

The key question now concerns the relationship between $\lim_{a\to 0} E_a$ and H. Using (1.4), we evaluate (1.21) in the limit $a \to 0$ to give

$$\begin{aligned} \lim_{a\to 0} E_a \;=\; & \lim_{a\to 0} -\frac{1}{2} \sum_{i=1}^{N} \sum_{j\neq i}^{N} \Gamma_i \Gamma_j \int_{\mathcal{D}^2} I_a(|\boldsymbol{x} - \boldsymbol{x}_i|) G(\boldsymbol{x}, \boldsymbol{x}') I_a(|\boldsymbol{x}' - \boldsymbol{x}_j|) \, d\boldsymbol{x} \, d\boldsymbol{x}' \\ & + \lim_{a\to 0} -\frac{1}{2} \sum_{i=1}^{N} \Gamma_i^2 \int_{\mathcal{D}^2} I_a(|\boldsymbol{x} - \boldsymbol{x}_i|) g(\boldsymbol{x}, \boldsymbol{x}') I_a(|\boldsymbol{x}' - \boldsymbol{x}_i|) \, d\boldsymbol{x} \, d\boldsymbol{x}' \\ & + \lim_{a\to 0} -\frac{1}{2} \sum_{i=1}^{N} \Gamma_i^2 \int_{\mathcal{D}^2} I_a(|\boldsymbol{x} - \boldsymbol{x}_i|) G_0(\boldsymbol{x}, \boldsymbol{x}') I_a(|\boldsymbol{x}' - \boldsymbol{x}_i|) \, d\boldsymbol{x} \, d\boldsymbol{x}'. \end{aligned} \tag{1.22}$$

The limit $a \to 0$ in the first and second lines of (1.22) may be taken by simply substituting $\delta(\boldsymbol{x} - \boldsymbol{x}_i)$ for $I(|\boldsymbol{x} - \boldsymbol{x}_i|)$ and $\delta(\boldsymbol{x}' - \boldsymbol{x}_j)$ for $I(|\boldsymbol{x}' - \boldsymbol{x}_j|)$. Then the straightforward evaluation of the double integrals yields the first and second terms of the Hamiltonian (1.2). Consequently, if we can ignore the third line of (1.22), we would have exact equivalence between (1.22) and the vortex Hamiltonian (1.2), as required. To justify ignoring the third line of (1.22), we take a different approach than for the first two lines: evaluate the double integral first, *then* take the limit

$a \to 0$. First, let

$$\begin{aligned}\mathcal{I} &= \int_{\mathcal{D}^2} I_a(|\boldsymbol{x}-\boldsymbol{x}_i|)G_0(\boldsymbol{x},\boldsymbol{x}')I_a(|\boldsymbol{x}'-\boldsymbol{x}_i|)\,d\boldsymbol{x}\,d\boldsymbol{x}' \\ &= \frac{1}{2\pi}\int_{\mathcal{D}^2} I_a(|\boldsymbol{x}-\boldsymbol{x}_i|)\log(|\boldsymbol{x}-\boldsymbol{x}'|)I_a(|\boldsymbol{x}'-\boldsymbol{x}_i|)\,d\boldsymbol{x}\,d\boldsymbol{x}' \end{aligned} \tag{1.23}$$

Now define $R = |\boldsymbol{x}-\boldsymbol{x}_i|$ and $R' = |\boldsymbol{x}-\boldsymbol{x}_i|$, with Θ and Θ' the corresponding azimuthal arguments. We now can use the planar multipole expansion [1] to write

$$\begin{aligned}\log(|\boldsymbol{x}-\boldsymbol{x}'|) &= \log(|(\boldsymbol{x}-\boldsymbol{x}_i)-(\boldsymbol{x}'-\boldsymbol{x}_i)|) \\ &= \log\left(R^2+R'^2-2RR'\cos\mu\right)^{1/2} \\ &= \begin{cases} \log R - \displaystyle\sum_{k=1}^{\infty}\left(\frac{R'}{R}\right)^k \frac{\cos k\mu}{k} & (R>R') \\ \log R' - \displaystyle\sum_{k=1}^{\infty}\left(\frac{R}{R'}\right)^k \frac{\cos k\mu}{k} & (R<R'), \end{cases}\end{aligned} \tag{1.24}$$

where $\mu = \Theta - \Theta'$. Using (1.24), the integral over $\boldsymbol{x}'$ appearing in (1.23) can be evaluated as

$$\begin{aligned}&\int_{\mathcal{D}} \log(|\boldsymbol{x}-\boldsymbol{x}'|)\, I_a\left(|\boldsymbol{x}'-\boldsymbol{x}_i|\right) d\boldsymbol{x}' \\ &\qquad = \frac{1}{\pi a^2}\int_0^{2\pi}\int_0^a \log\left(R^2+R'^2-2RR'\cos\mu\right)^{1/2}\, R'\,dR'\,d\Theta' \\ &\qquad = \frac{2}{a^2}\left(\int_0^R R'\,\log R\,dR' + \int_R^a R'\log R'\,dR'\right) \\ &\qquad = \frac{2}{a^2}\left(\frac{(R^2-a^2)}{4}+\frac{a^2\log a}{2}\right).\end{aligned} \tag{1.25}$$

Inserting (1.25) into (1.23), the integral over $\boldsymbol{x}$ can be evaluated (using the indicator function to restrict it to the patch $R<a$) as

$$\begin{aligned}\mathcal{I} &= \frac{1}{2\pi}\frac{2}{\pi a^4}\int_0^{2\pi}\int_0^a\left(\frac{(R^2-a^2)}{4}+\frac{a^2\log a}{2}\right)R\,dR\,d\Theta \\ &= \frac{2}{\pi a^4}\left(-\frac{a^4}{16}+\frac{a^4\log a}{4}\right) \\ &= \frac{1}{2\pi}\left(\log a - \tfrac{1}{4}\right).\end{aligned}$$

Clearly $\lim_{a\to 0}\mathcal{I}$ does not exist.

From the above we can see that as $a \to 0$ the fluid energy

$$E_a \to E_s(a) + H \quad \text{where} \quad E_s(a) = \frac{1}{4\pi}\left(\sum_{i=1}^{N} \Gamma_i^2\right)\left(\frac{1}{4} - \log a\right).$$

For fixed vortex radius a, E_s is a constant, positive (since $a \ll 1$) reference energy, which we refer to here as the 'self-energy of the vortices'. Because it doesn't depend on the vortex positions it has no bearing on the dynamics. Because E_s is singular in the limit $\epsilon \to 0$ it must be subtracted off in the point vortex formulation. This is sometimes referred to as the 'core energy method' [51].

For a system with finite but small vortices to which the point vortex model applies, the correct interpretation of the point vortex energy H, then, is as a small correction to the large and positive 'self-energy' term $E_s(\epsilon)$.

The important point to note is that in the continuous 2D Euler system the energy of the fluid (1.16) is the *kinetic energy* (which is strictly positive), whereas in the case of point vortices, the Hamiltonian energy (1.2) represents the *potential energy* of the interaction between vortices (which can take both positive and negative values).

1.2.2 Conservation properties and integrability

The conserved quantities (or 'invariants') of the Hamiltonian (1.2) can be determined using Noether's theorem, which states that to every local symmetry of a physical system there corresponds a conservation law. For an unbounded system they are

- Energy H (due to invariance with respect to time)
- Angular momentum L (due to invariance with respect to coordinate rotation)
- Linear momentum in the x and y directions P and Q (due to invariance with respect to coordinate translation).

Energy is conserved for systems in any fixed geometry, but when a boundary is added the angular and linear momentum invariants may be lost as symmetry is broken.

The four conserved quantities H, L, P & Q allow conclusions to be made about the integrability of the system for certain N (see [91] and references therein). The

vital tool in this analysis is the Poisson bracket, which for two arbitrary functions $h_1(\boldsymbol{x}_i)$ and $h_2(\boldsymbol{x}_i)$ is defined by

$$\{h_1, h_2\} = \sum_{i=1}^{N} \frac{1}{\Gamma_i} \left(\frac{\partial h_1}{\partial x_i} \frac{\partial h_2}{\partial y_i} - \frac{\partial h_1}{\partial y_i} \frac{\partial h_2}{\partial x_i} \right).$$

In order for the system to be integrable all conserved quantities must have zero Poisson brackets with each other, a property known as 'mutual involution'.

For the unbounded $N = 3$ system, for all values of Γ_i, the three conserved quantities H, L & $P^2 + Q^2$ are mutually involutive, meaning the system is integrable for $N \leq 3$. For an unbounded neutral system i.e. $\sum_i \Gamma_i = 0$, then the four conserved quantities H, L, P & Q are mutually involutive, meaning the system is integrable for $N \leq 4$. The reason for this is that, in the neutral case, the origin can be shifted so that $P = Q = 0$.

In a similar manner, conclusions about the integrability of bounded systems can be made. In a bounded, rotationally symmetric system (i.e. a circle) there are two conserved quantities H & L meaning the system is only integrable for $N \leq 2$. For a system in the upper half plane the only conserved quantities are H, P so again the system is only integrable for $N \leq 2$. In a bounded system with no rotational or translational symmetry the only conserved quantity is H and so the system is only integrable when $N = 1$.

When any of the three types of system described above are not integrable, the behaviour of the vortices is chaotic and numerical integration, as described in the next section, is required. However, within the many-vortex system the qualitative behaviour of isolated pairs of vortices can be predicted. When a pair of the same-sign come close they will orbit each other, while a pair of equal and opposite circulations will propagate along a straight line to infinity. These isolated pairs will exhibit this behaviour until they are disrupted by another vortex or a boundary.

1.2.3 Direct numerical simulation of the N vortex system

Throughout this thesis direct numerical simulations (DNS) of the dynamical system (1.1) will be performed using the algorithm described in section 2.1 of [4].

Several different numerical algorithms have been employed to solve the point vortex equations (1.1) with 2D Euler dynamics. Two major limitations of such algorithms, that we do not try to resolve in this thesis, are: first that $O(N^2)$ evaluations of the partial derivatives of G and g are required at each time-step; and second, that variable time-stepping is necessary in order to resolve trajectories on the intermittent occasions when vortices pass close together.

It is difficult to avoid the $O(N^2)$ costs without resorting to approximate methods (e.g. [30]), and efforts at calculations for large N ($N \approx 7000$ at the time of writing) have instead been focussed on supercomputing efforts using specialised hardware [123].

One important feature that must be respected by any such algorithm is the invariance of the Hamiltonian H. Symplectic methods [96, 125] have been shown to have greatly improved conservation properties at fixed time-step. However this technique also scales $O(N^2)$, and can have poor stability properties when used with a variable time-step (which is necessary for large N simulations), though an alternative adaptive scheme is suggested in [83]. Two aspects of the symplectic method that have yet to be explored are its effectiveness in bounded domains and for large N simulations. Extensive transformations of the Hamiltonian are required in this case in order for it to be used with a symplectic integrator. Therefore, to keep the presentation simple, we use as our starting point a basic (but adaptive) algorithm in the spirit of that suggested by Bühler [13], the details of which are described below.

The algorithm proceeds by targeting solutions of (1.1) over intervals of length Δt. To advance the solution from the current time $t = t_n$ ($t_n = n\,\Delta t$), the equations of motion are solved repeatedly over the time interval $[t_n, t_n + \Delta t]$, by subdividing the interval into 2^m substeps ($m = 1, 2, 3, \ldots$), and integrating over the substeps using an explicit fourth-order Runge-Kutta method. If the solution at $t_n + \Delta t$ obtained using 2^m substeps is denoted $\{\boldsymbol{x}_1^{(m)}, ..., \boldsymbol{x}_N^{(m)}\}$, then the stopping criterion for the interval

is defined to be

$$\frac{1}{N}\sum_{i=1}^{N}\left|\boldsymbol{x}_i^{(m)}-\boldsymbol{x}_i^{(m-1)}\right|<\delta, \tag{1.26}$$

i.e. the mean absolute vortex positions must converge to be less than δ. The numerical parameter δ controls the accuracy of the algorithm and is referred to as the *tolerance parameter*.

The stopping criterion will be first met for some $m = m_*$, and the algorithm then moves onto the next time interval $[t_{n+1}, t_{n+1} + \Delta t]$. In practice, when many vortices are present, the number of substeps required (i.e 2^{m_*}), varies quite considerably. This is due to intermittent episodes during which vortices pass close together resulting in large propagation speeds, and it is the resolution of these episodes which accounts for the need for adaptivity.

1.3 Point vortex statistical mechanics

1.3.1 Background

In his seminal paper of 1949 Onsager [93] made use of the Hamiltonian structure outlined above to discuss a statistical mechanics model with point vortices acting as the 'particles' of the system. His motivation was a desire to explain the presence of isolated, large-scale, long-lived vortices that occur in a wide range of turbulent flows. In terms of the point vortex model this phenomenon would be modelled by large clusters of like-signed point vortices that persists over long time scales. A number of direct quotes from [93], Onsager's personal correspondences with C. C. Lin and also unpublished notes will be included in this section as well as others. Much of this historical material comes from the review [49], which is dedicated to Onsager's contributions to this problem as well as to the wider field of hydrodynamic turbulence.

From a general perspective [14] the principle aim of statistical mechanics is to model the statistical behaviour of a system subject to imperfectly known initial conditions; for example the average motion of particles in a bounded ideal gas, knowing

only their total energy and not their precise initial conditions.

Two important concepts in statistical mechanics are '*macrostates*' and '*microstates*'. The macrostate of a system is described by a macroscopic quantity such as total energy, average particle density etc. On the other hand the microstate is a specific state of the system that is governed by mechanical laws (i.e. the dynamical system) such as the position or velocity of individual particles. The crucial connection between macrostates and microstates is made using the concept of entropy, for which the fact that a given macrostate usually corresponds to a large number of equivalent microstates is key; see section 1.4.1.

One approach to determine a macrostate would be to integrate the dynamical system and take time averages using a range of initial conditions. This is a valid method but wasteful as detailed trajectories must be found, only to take the time average to obtain a few statistical quantities. Statistical mechanics uses a different approach in which deterministic equations are replaced by much simpler statistical quantities that are based on assumptions for the statistical behaviour of the system. In the case of point vortices, the power of modern computers has allowed the (wasteful) integrations described above to be used for the validation of statistical mechanics predictions.

The starting point for the classical statistical mechanical approach of an ideal gas consisting of N particles, indexed $i = 1, \ldots, N$, is the introduction of a probability density function $p(\boldsymbol{x}_i, \boldsymbol{v}_i)$ for the i^{th} particle at position $\boldsymbol{x}_i$ with velocity $\boldsymbol{v}_i$ as determined by the dynamical system of interest. The quantity $p(\boldsymbol{x}_i, \boldsymbol{v}_i)$ defines the microstate of the i^{th} particle and $p(\boldsymbol{x}_i, \boldsymbol{v}_i)d\boldsymbol{x}_i d\boldsymbol{v}_i$ defines the probability that the particle is in the neighbourhood $d\boldsymbol{x}_i$ of $\boldsymbol{x}_i$, with velocity in the neighbourhood $d\boldsymbol{v}_i$ of $\boldsymbol{v}_i$. The phase space of the system is $(\boldsymbol{x}_i, \boldsymbol{v}_i)$ $i = 1, \ldots, N$, and in most physical systems is unbounded even if the system itself is bounded e.g. a classical monatomic ideal gas in a bounded container which has an unbounded $6N$ dimensional phase space, since the microstate of each particle is given by position and velocity vectors in 3D space. However, for the point vortex system, phase space is the same as position space (scaled by the vortex circulation), and consequently the vortex system in a bounded domain[4] has a finite phase space volume of dimension $2N$.

[4]A system of like-signed vortices in an unbounded domain also has finite phase space volume

For a vortex system in a bounded domain with no symmetries, the vortices move on a fixed energy surface in phase space. If there are additional conserved quantities (see section 1.2.2), the vortices move on the surface made up of the intersecting hyper-surfaces due to each conserved quantity.

The work of this thesis concerns 'equilibrium' statistical mechanics. When a system is in equilibrium, the statistics of macroscopic quantities are stationary in time. Non-equilibrium statistical mechanics has also been successfully applied to the vortex model e.g. [25, 81].

1.3.2 The negative temperature state

Onsager's statistical hydrodynamics theory is now reviewed. Consider the same vortex system as described in section 1.2.1, consisting of N vortices with circulations Γ_i and positions $\boldsymbol{x}_i$, $i = 1, \ldots, N$ in a domain $\mathcal{D}$, with area $|\mathcal{D}|$. We denote the volume element of phase space (the Lebesgue measure on $\mathbb{R}^{2N}$) as

$$d\boldsymbol{x}_1 \cdots d\boldsymbol{x}_N,$$

and the total, finite phase space volume as

$$\Omega(\infty) = \int_{\mathcal{D}^N} d\boldsymbol{x}_1 \cdots d\boldsymbol{x}_N = |\mathcal{D}|^N.$$

We then consider the phase space volume only of energies less than E, i.e.,

$$\Omega(E) = \int_{\mathcal{D}^N} \mathcal{H}(E - H(\boldsymbol{x}_1, \ldots, \boldsymbol{x}_N))\, d\boldsymbol{x}_1 \cdots d\boldsymbol{x}_N, \tag{1.27}$$

where $\mathcal{H}$ is the Heaviside step function: $\mathcal{H}(x > 0) = 1$ (i.e. $H < E$) and $\mathcal{H}(x < 0) = 0$ (i.e. $H > E$). By construction $\Omega(E)$ is a monotonically increasing function of E, with constant limits $\Omega(-\infty) = 0$ and $\Omega(\infty) = |\mathcal{D}|^N$. Taking the derivative of (1.27) with respect to E gives

$$W(E) = \Omega'(E) = \int_{\mathcal{D}^N} \delta(E - H(\boldsymbol{x}_1, \ldots, \boldsymbol{x}_N))\, d\boldsymbol{x}_1 \cdots d\boldsymbol{x}_N, \tag{1.28}$$

due to the conservation of angular momentum.

which is a non-negative function called the 'density of states', with $W(\pm\infty) = 0$. The density of states must achieve a maximum at some finite E_{max} when $W'(E_{max}) = 0$.

The Boltzmann entropy, $S(E)$, is a measure of the number of microstates of a system in equilibrium corresponding to an energy surface and is defined to be

$$S = \log W(E), \tag{1.29}$$

(where the Boltzmann constant k_B that typically appears in (1.29) has been scaled to unity), and the temperature $\tilde{T}(E)$ and inverse temperature $\beta(E)$ are defined from $S(E)$ to be[5]

$$\frac{1}{\tilde{T}} \equiv \beta = \frac{1}{N}\frac{dS}{dE} = \frac{1}{N}\frac{W'(E)}{W(E)}. \tag{1.30}$$

Note that the function $\beta(E)$ is often refered to as the 'thermodynamic curve'.

Onsager's argument is as follows. When $E < E_{max}$, $\tilde{T} > 0$. In this 'positive temperature' state the vortices will tend to accumulate at the boundary (near to their opposite signed images) or equivalently vortices of opposite sign will pair up. However, when $E > E_{max}$, $\tilde{T} < 0$ and there is a '*negative temperature*' state which is a temperature 'greater' than $\tilde{T} = \infty$ where vortices of the same sign will tend to cluster, providing an explanation for the self-organisation of the flow into large vortex structures as mentioned in section 1.1.1. In this case adding more energy *decreases* the entropy i.e. the system becomes more ordered as bigger like-signed clusters form. This is the opposite to the usual statistical mechanics situation (e.g. an ideal gas) where adding more energy increases the entropy i.e. the system becomes less ordered as the particles of the ideal gas move faster.

The negative temperature state was the crucial insight Onsager gave to statistical hydrodynamics and its existence is only possible when the density of states, and hence the entropy, achieve a maximum, which requires a finite phase space volume. Negative temperature states are not unique to the point vortex system, and Purcell and Pound [97] proved their existence for nuclear spin systems in 1951, just two years after Onsager published the vortex argument given above.

[5]Note that in this thesis the inverse temperature β has been divided by N in order to have $\beta = O(1)$ in the limit $N \to \infty$. This is not the standard definition.

A final point in this section concerns the choice of ensemble for statistical mechanics of the vortex system [23]. This is an example of a key assumption of the statistical behaviour of the system of the type mentioned in section 1.3.1. In classical statistical mechanics there are three standard ensembles: the microcanonical ensemble, the canonical ensemble and the grand canonical ensemble. Each will be dealt with in turn next.

The probability density function (PDF) of the microcanonical ensemble is defined for a classical isolated system with fixed number of particles (vortices) by

$$p(\boldsymbol{x}_1, ..., \boldsymbol{x}_N) = \frac{\delta(E - H(\boldsymbol{x}_1, ..., \boldsymbol{x}_N))}{W(E)}, \tag{1.31}$$

which has the simple interpretation that all states with the same energy are equally probable; see section 1.4.1 for further details. Since the vortex system is isolated (see section 1.2) and has fixed N, (1.31) evidently represents a physically appropriate tool for its study.

The PDF of the canonical ensemble is defined for a classical system at fixed temperature $1/\beta$, that is in contact with a 'reservoir' (a system that is coupled to, and much larger than, the system under consideration), by

$$p(\boldsymbol{x}_1, ..., \boldsymbol{x}_N) = \frac{e^{-\beta H}}{\displaystyle\int_{\mathcal{D}^N} e^{-\beta H}\, d\boldsymbol{x}_1 \cdots d\boldsymbol{x}_N}.$$

In the canonical ensemble, energy flows between the system and the reservoir so that the temperature remains constant (the number of particles is constant as well). In classical statistical mechanics the microcanonical ensemble and canonical ensemble are said to be equivalent since the former can be recovered from the latter.

The grand canonical ensemble (which can be regarded as an extension of the canonical ensemble) describes a classical system in which the energy and the particles themselves can be exchanged with the reservoir. The PDF of the grand canonical distribution is given by

$$p(\boldsymbol{x}_1, ..., \boldsymbol{x}_N) = \frac{e^{-\beta(H-\mu N)}}{\displaystyle\int_{\mathcal{D}^N} e^{-\beta(H-\mu)}\, d\boldsymbol{x}_1 \cdots d\boldsymbol{x}_N},$$

where μ is the 'chemical potential', a parameter controlling the number of particles.

While the definitions of the canonical and grand canonical ensembles given above are formally correct, neither has a physical meaning for the point vortex system. Clearly fluctuations of the energy in both ensembles, and number of vortices in the grand canonical ensemble, are at odds with the fixed energy, fixed N point vortex system[6]. The reason for this incompatibility is that it is unknown how to impose the concept of a reservoir for negative temperatures of the point vortex system.

Another important property of ensembles in classical statistical mechanics is that if both the microcanonical ensemble and the canonical ensemble are physically valid for the given system, it should be possible to derive the latter from the former [57]. This derivation is only possible when the system in question is 'extensive'. Extensivity can be simply explained by first considering two subsystems A and B. If the total system is extensive then the energies of the two subsystems can be combined to give the total energy of the system as

$$H(\boldsymbol{x}_A, \boldsymbol{x}_B) = H_A(\boldsymbol{x}_A) + H_B(\boldsymbol{x}_B). \tag{1.32}$$

However the vortex energy (1.2) does not satisfy (1.32), as the two subsystems interact with each other giving rise to an 'interfacial energy' term H_I [13], meaning

$$H(\boldsymbol{x}_A, \boldsymbol{x}_B) = H_A(\boldsymbol{x}_A) + H_B(\boldsymbol{x}_B) + H_I(\boldsymbol{x}_A, \boldsymbol{x}_B). \tag{1.33}$$

Equation (1.33) shows that the vortex system in not extensive, meaning the microcanoncial ensemble cannot be derived from the canonical ensemble, and hence, in general, invalidating the canonical ensemble for use in point vortex statistical mechanics.

As a consequence of the factors outlined above, throughout this thesis, as well as in other most point vortex statistical mechanics studies, the microcanonical ensemble is used. Details of how it is used are given in section 1.3.3.

[6]Though for vortex systems governed by stochastic equations e.g. dissipative Brownian vortices [24], the canonical ensemble is appropriate.

1.3.3 Statistical sampling of the microcanonical ensemble

As stated in the previous section, the microcanonical ensemble is the most physically appropriate statistical mechanics tool with which to study the point vortex system. The most fundamental quantity to compute is the density of states (1.28) i.e. $W(E)$. This can be accomplished as follows. A large number of samples (Q) of N uniformly random vortex configurations are generated in $\mathcal{D}$ and for each sample the energy E_k, $k = 1, \ldots, Q$ is calculated. Then the integral in (1.28) is replaced by a sum over the total number of samples and the delta function is approximated by normalised kernel function $K(\cdot/\sigma)$ (e.g. Gaussian, top hat function [i.e. bin] etc), where σ is a smoothing parameter called the *bandwidth*. Details on this choice of σ are given in section 4.4.4.

From the above, the normalised density of states is given by the average over all members of the ensemble i.e.

$$p_0(E) = W(E) = \frac{1}{\sigma Q} \sum_{k=1}^{Q} K\left(\frac{E - E_k}{\sigma}\right).$$

From this, other statistical quantities can be calculated such as the inverse temperature (1.30).

The above procedure has been followed by [13, 18] among others. Campbell and O'Neil [18] showed that for N as low as 20 the density of states can be seen to converge for a particular $\mathcal{D}$ (namely a regular parallelogram). Further details of this are given in chapter 4.

The same technique can be extended to calculate joint probability density functions relating two macroscopic quantities. For example, for energy E and an arbitrary macroscopic variable f, the joint PDF is given by

$$p_0(E, f) = \frac{1}{\sigma_1 \sigma_2 Q} \sum_{k=1}^{Q} K\left(\frac{E - E_k}{\sigma_1}\right) K\left(\frac{f - f_k}{\sigma_2}\right).$$

Note that in general $\sigma_1 \neq \sigma_2$ as E and f will usually be on different length scales. Joint PDFs of the energy and angular momentum were used in [13] to investigate

the statistics of vortices in a circular domain. This technique will be used in chapter 5.

The generation of N uniformly random vortex configurations at relatively low E in a general domain $\mathcal{D}$ can be accomplished in the following manner, often referred to as the 'Monte Carlo' method[7]. Suppose the domain of interest $\mathcal{D}$ in the complex z-plane is defined via a conformal map $z = F(Z)$ from a unit circle $\mathcal{C}$ in the complex Z-plane (see appendix A and figure A.1). A rectangle of uniformly random points $\{z_i\}$ is generated in the z-plane that completely covers the domain of interest $\mathcal{D}$. To determine which of the points $\{z_i\}$ in the rectangle are inside $\mathcal{D}$, all the points are mapped to points Z_i in the Z-plane with the map $Z = f(z)$. If $|Z_i| < 1$, the point is in the $\mathcal{C}$ and hence, when mapped back to the Z-plane by $z = F(Z)$, is also in $\mathcal{D}$. This procedure is demonstrated for a 'Neumann oval' domain in figure 1.1.

The Monte Carlo procedure described above is not able to sample configurations at very high energies, as will be required in chapter 2. Instead the 'multi-canonical Markov chain Monte Carlo' (MCMCMC) sampling technique [8, 40] could be used. The MCMCMC method uses an ergodic Markov chain to sample states that are 'near' states with high (or low) energy and by keeping track of how improbable the steps in the Markov chain are it accepts or rejects the steps in order to sample the desired phase space efficiently. The MCMCMC algorithm has been implemented for high energy sampling by J. G. Esler[8] in a manner closely following the MATLAB implementation for the random walk PDF given in Fig. 4 of [40].

1.3.4 The two scaling limits

One issue not addressed by Onsager in [93] was the asymptotic limit for the theory i.e. the behaviour of the model as $N \to \infty$. In the standard thermodynamic limit that is often presented in textbooks (e.g. [57, 73]), the domain area $|\mathcal{D}|$ and N are simultaneously increased while keeping $N/|\mathcal{D}|$ constant, which would likely lead to a domain-independent system. In a rigorous mathematical work by Fröhlich and Ruelle [52] and a statistical investigation by Campbell and O'Neil [18], it was

[7] This technique can also be used to generate initial conditions for direct numerical simulations, as is done in chapter 5.

[8] The author's primary supervisor.

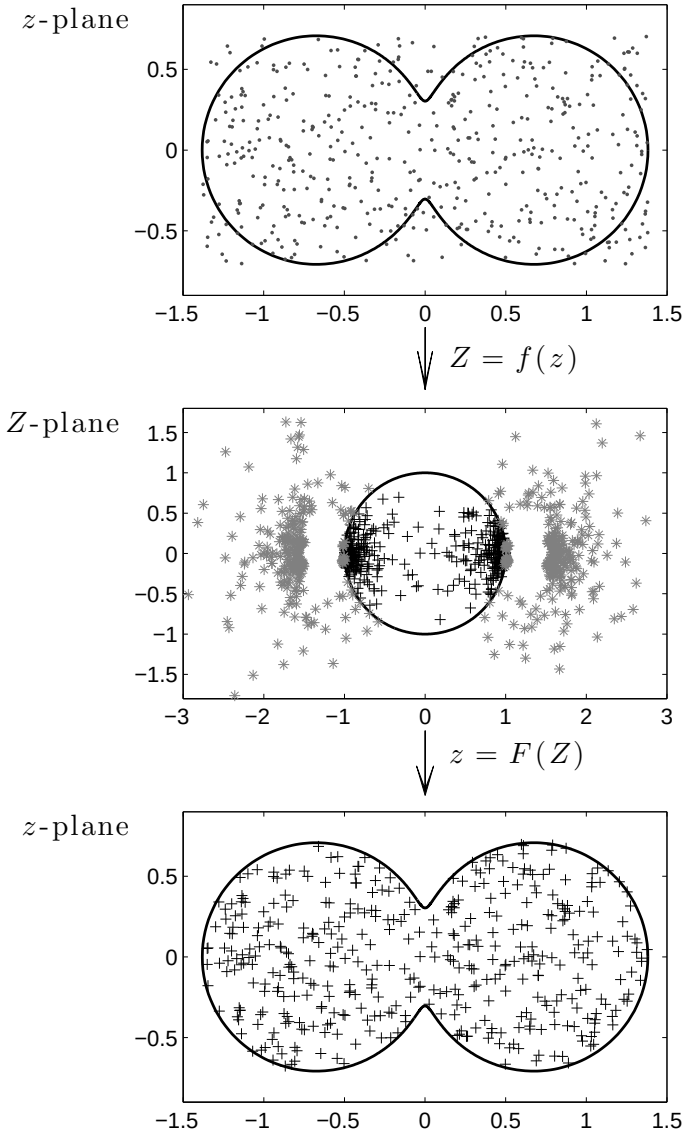

Figure 1.1: Procedure for obtaining a uniformly random distribution of N vortex positions inside a Neumann oval.

shown that in this textbook limit only positive temperature states are possible– contrary to Onsager's predicted negative temperature states. In fact since the system (1.1) is invariant under domain re-scalings (the energy is simply shifted by a factor proportional to the scaling), no additional information about the system is uncovered by taking $|\mathcal{D}| \to \infty$ in the textbook limit; in fact features of the system could even be obscured by doing so. In most cases, the vortex system is genuinely long-ranged and as such the influence of the domain is an inescapable feature as $N \to \infty$. In the case of QGSW vortices this system can become very short ranged.

Evidently the textbook thermodynamic limit is not particularly useful when considering the vortex system. Consequently, alternative limits must be considered.

For the system considered in this thesis with a fixed domain $\mathcal{D}$ and circulations $\Gamma_i = 1/N$, $i = 1, \ldots, N/2$ and $\Gamma_i = -1/N$, $i = N/2 + 1, \ldots, N$, two limits will be considered:

- **The hydrodynamic limit**: $N \to \infty$, $E =$ constant (energy scaled per number of vortices *squared*). This limit was considered mathematically for the vortex system in the canonical ensemble in [16] and the microcanonical ensemble in [17, 48, 68]. In this limit $\beta = \beta_h(E) \to$ constant < 0, i.e. only negative temperature states are accessed. The resulting states are dominated by the 'mean flow' (streamfunction $\psi_1(\boldsymbol{x})$), with 'fluctuations' about this mean flow taking a secondary role. Note that the arbitrary choice of $\Gamma = \pm 1/N$ makes expressions in the hydrodynamic limit simpler.

- **The thermodynamic limit**: $N \to \infty$, $\tilde{E} = NE \to$ constant (energy scaled per vortex). This limit has been studied in [45, 95]. In this limit $\beta = \beta_t(\tilde{E}) \to$ constant, and both positive and negative temperature states are possible. Fluctuations and mean flows can either be dominant or of equal importance. The transition between low positive or negative energy symmetric states dominated by fluctuations, and high positive energy asymmetric states dominated by the mean flow occurs at a constant value of $\tilde{E}$ in the thermodynamic limit: this is explored in [44].

With the hierarchy introduced in the next subsection, both the hydrodynamic and thermodynamic regimes can be explored separately; the hydrodynamic limit is

considered in chapter 2 and the thermodynamic limit in chapter 4. Note that there is also a possibility of an 'intermediate' scaling limit, that asymptotically matches the hydrodynamic and thermodynamic limits. As yet this remains unexplored.

1.3.5 The cumulant expansion method

The cumulant expansion method of Pointin & Lundgren [95] (PL76 hereafter) will form the basis of the statistical mechanics investigations in chapters 2 and 4. In this method a hierarchy of cumulant equations is derived that yields a number of theoretical descriptions for the equilibrium distribution of the point vortex system described above in *both* the hydrodynamic and thermodynamic limits.

In this subsection the cumulant expansion method is reformulated in a new setting allowing clearer interpretation and greater flexibility than PL76's original formulation (additional results are given in appendix B). Further, instead of focusing solely on the 2D Euler system as in PL76[9] and Esler, Ashbee & McDonald [45] (EAM13 here after), the hierarchy will be presented for a generalised vortex system i.e. for a vortex defined by any appropriate linear, elliptic and self-adjoint operator $\mathcal{L}$, such as those described in section 1.2.1.

For the system introduced in the previous sections, we consider the statistics of a certain energy shell ($H = E$) which are given by the microcanonical ensemble (1.31). PL76 then obtain a hierarchy of cumulant equations satisfied by the marginal densities (or reduced probability density functions) of (1.31),

$$\begin{aligned} p_+(\boldsymbol{x}_1) &= \int_{\mathcal{D}^{N-1}} p(\boldsymbol{x}_1, ..., \boldsymbol{x}_N)\, d\boldsymbol{x}_2 \cdots d\boldsymbol{x}_N \\ p_-(\boldsymbol{x}_N) &= \int_{\mathcal{D}^{N-1}} p(\boldsymbol{x}_1, ..., \boldsymbol{x}_N)\, d\boldsymbol{x}_1 \cdots d\boldsymbol{x}_{N-1} \\ p_{++}(\boldsymbol{x}_1, \boldsymbol{x}_2) &= \int_{\mathcal{D}^{N-2}} p(\boldsymbol{x}_1, ..., \boldsymbol{x}_N)\, d\boldsymbol{x}_3 \cdots d\boldsymbol{x}_N \\ &\vdots \end{aligned} \tag{1.34}$$

where the $\pm$ subscripts refer to vortices with positive (first $N/2$) and negative (remaining $N/2$) circulations respectively. These functions are the spatial equilibrium

[9]The 2D Euler system $\mathcal{L} = \nabla^2$ will, however, frequently be used in demonstrating the equivalence of the new hierarchy with PL76 and in the more general context of Eulerian fluid dynamics.

distribution of the vortices. It is assumed that vortices of the same sign are interchangeable, so the functions do not depend on the order in which the vortex arguments are taken i.e.

$$p_{++}(\boldsymbol{x}_1, \boldsymbol{x}_2) = p_{++}(\boldsymbol{x}_2, \boldsymbol{x}_1), \quad p_{+-}(\boldsymbol{x}_1, \boldsymbol{x}_2) = p_{-+}(\boldsymbol{x}_2, \boldsymbol{x}_1), \quad \text{etc.}$$

The Gibbs entropy of the two species system can be defined as

$$S = -\frac{1}{2}\int_{\mathcal{D}} \left[p_+(\boldsymbol{x}) \log\left(\frac{p_+(\boldsymbol{x})}{\rho_0}\right) + p_-(\boldsymbol{x}) \log\left(\frac{p_-(\boldsymbol{x})}{\rho_0}\right)\right] d\boldsymbol{x}, \tag{1.35}$$

where $\rho_0 = 1/|\mathcal{D}|$; the inverse of the domain area. Equation (1.35) can be shown to be equivalent to the Boltzmann entropy (1.29) in the hydrodynamic limit (see section 2.2.2).

Along with the singular vorticity distribution (1.15) (namely $\omega = \sum_i \Gamma_i \delta(\boldsymbol{x} - \boldsymbol{x}_i)$) as introduced in section 1.2.1, the vortex density is defined by

$$\rho(\boldsymbol{x}) = \frac{1}{N}\sum_{i=1}^{N} \delta(\boldsymbol{x} - \boldsymbol{x}_i), \tag{1.36}$$

(recall $\Gamma_i = \pm 1/N$). The ensemble average of an arbitrary function $f(\boldsymbol{x}_1, ..., \boldsymbol{x}_N)$ is given by

$$\langle f \rangle = \int_{\mathcal{D}^N} f(\boldsymbol{x}_1, ..., \boldsymbol{x}_N) p(\boldsymbol{x}_1, ..., \boldsymbol{x}_N)\, d\boldsymbol{x}_1 ... \, d\boldsymbol{x}_N, \tag{1.37}$$

and so vorticity (1.15) and vortex density (1.36) can be defined in terms of the ensemble means

$$\omega_1(\boldsymbol{x}) = \langle \omega(\boldsymbol{x}) \rangle = \tfrac{1}{2}\big(p_+(\boldsymbol{x}) - p_-(\boldsymbol{x})\big) \tag{1.38}$$

$$\rho_1(\boldsymbol{x}) = \langle \rho(\boldsymbol{x}) \rangle = \tfrac{1}{2}\big(p_+(\boldsymbol{x}) + p_-(\boldsymbol{x})\big), \tag{1.39}$$

with the *de-singularized* second-order cumulants, describing fluctuations about the

mean, defined by

$$\omega_2(\boldsymbol{x},\boldsymbol{x}') = \langle(\omega(\boldsymbol{x})-\omega_1(\boldsymbol{x}))(\omega(\boldsymbol{x}')-\omega_1(\boldsymbol{x}'))\rangle - (1/N)\rho_1(\boldsymbol{x})\delta(\boldsymbol{x}-\boldsymbol{x}') \quad (1.40)$$

$$c_2(\boldsymbol{x},\boldsymbol{x}') = \langle(\rho(\boldsymbol{x})-\rho_1(\boldsymbol{x}))(\omega(\boldsymbol{x}')-\omega_1(\boldsymbol{x}'))\rangle - (1/N)\omega_1(\boldsymbol{x})\delta(\boldsymbol{x}-\boldsymbol{x}') \quad (1.41)$$

$$\rho_2(\boldsymbol{x},\boldsymbol{x}') = \langle(\rho(\boldsymbol{x})-\rho_1(\boldsymbol{x}))(\rho(\boldsymbol{x}')-\rho_1(\boldsymbol{x}'))\rangle - (1/N)\rho_1(\boldsymbol{x})\delta(\boldsymbol{x}-\boldsymbol{x}'). \quad (1.42)$$

The unorthodox delta-function terms in (1.40-1.42) are 'natural' in the sense that they remove all singular terms, and permit ω_2, c_2 and ρ_2 to be expressed in terms of p_{++}, p_{+-} etc. It is straightforward to define higher cumulants by analogy. Some relevant expressions are given in appendix B.1.

The advantages of recasting PL76's cumulant expansion in this fashion are twofold. First, it simplifies some of PL76's expressions, notably the energy equation (equation (1.46) below). Second, it emphasises that vorticity and vortex density scale differently in the hydrodynamic and thermodynamic limits introduced in section 1.3.4, with the more fundamental terms, in the sense that they eventually determine the thermodynamic curve $\beta(E)$, being those related to vorticity and its fluctuations, ω_1 and ω_2 respectively.

It is useful at this point to reintroduce[10] a generalised streamfunction ψ_1 for the mean flow arising from the mean vorticity distribution ω_1, satisfying

$$\begin{aligned} \psi_1(\boldsymbol{x}) &= \int_{\mathcal{D}} G(\boldsymbol{x},\boldsymbol{x}')\omega_1(\boldsymbol{x}')\,d\boldsymbol{x}' \\ \text{or} \quad \mathcal{L}\psi_1 &= \omega_1, \quad \psi_1 = 0 \text{ on } \partial\mathcal{D}, \end{aligned} \quad (1.43)$$

where $\mathcal{L}$ is the linear, elliptic and self-adjoint operator introduced in section 1.2.1. Here, and throughout the rest of this thesis unless otherwise indicated, $\mathcal{L}$ and the gradient operator ∇ act on the variable $\boldsymbol{x}$. In a similar manner, higher order streamfunctions can also be defined e.g.

$$\begin{aligned} \psi_2(\boldsymbol{x},\boldsymbol{x}') &= \int_{\mathcal{D}} G(\boldsymbol{x},\boldsymbol{x}'')\omega_2(\boldsymbol{x}'',\boldsymbol{x}')\,d\boldsymbol{x}'' \\ &= \langle(\psi(\boldsymbol{x})-\psi_1(\boldsymbol{x}))\,(\omega(\boldsymbol{x}')-\omega_1(\boldsymbol{x}'))\rangle - \frac{1}{N}\rho_1(\boldsymbol{x}')G(\boldsymbol{x},\boldsymbol{x}'). \end{aligned} \quad (1.44)$$

[10]The relationship between the vorticity and the streamfunciton was first introduced for the continuous 2D Euler system with (1.13) in section 1.2.1.

In order to express the energy in terms of the cumulants defined above, it suffices to take the ensemble average of H,

$$\langle H \rangle = \int_{\mathcal{D}^N} H(\boldsymbol{x}_1, ..., \boldsymbol{x}_N) p(\boldsymbol{x}_1, ..., \boldsymbol{x}_N)\, d\boldsymbol{x}_1 \cdots d\boldsymbol{x}_N = E. \tag{1.45}$$

Substituting for H from its definition (1.2) and using the cumulants defined above, gives

$$E = -\frac{1}{2} \int_{\mathcal{D}^2} G(\boldsymbol{x}, \boldsymbol{x}') \left(\omega_1(\boldsymbol{x})\omega_1(\boldsymbol{x}') + \omega_2(\boldsymbol{x}, \boldsymbol{x}')\right)\, d\boldsymbol{x}\; d\boldsymbol{x}' - \frac{1}{2N} \int_{\mathcal{D}} g(\boldsymbol{x}, \boldsymbol{x}) \rho_1(\boldsymbol{x})\, d\boldsymbol{x}. \tag{1.46}$$

Equation (1.46), which is exact, simplifies PL76's equivalent expression (their eqn. 12), and more importantly admits simple interpretation. The first term involving ω_1 is the energy of the (ensemble) mean flow, and for $\mathcal{L} = \nabla^2$ is exactly the same as (1.17) i.e. the energy of continuous 2D Eulerian fluid. The second term involving ω_2 gives the energy associated with fluctuations or eddies about this mean flow, and the final density correction term corrects for the de-singularising term in the definition (1.41) of ω_2.

PL76's cumulant equations follow from applying the gradient operator to the marginal densities. For example, using ∇_1 to denote the gradient operation with respect to variable $\boldsymbol{x}_1$,

$$\begin{aligned}
\nabla_1 p_+(\boldsymbol{x}_1) &= \frac{1}{W(E)} \int_{\mathcal{D}^{N-1}} \nabla_1 \delta(H - E)\, d\boldsymbol{x}_2 \cdots d\boldsymbol{x}_N \\
&= -\frac{1}{W(E)} \int_{\mathcal{D}^{N-1}} \nabla_1 H \partial_E\, \delta(H - E)\;\, d\boldsymbol{x}_2 \cdots d\boldsymbol{x}_N \\
&= -N\left(\partial_{\tilde{E}} + \beta\right) \int_{\mathcal{D}^{N-1}} \nabla_1 H(\boldsymbol{x}_1, \ldots, \boldsymbol{x}_N) p(\boldsymbol{x}_1, \ldots, \boldsymbol{x}_N)\;\, d\boldsymbol{x}_2 \cdots d\boldsymbol{x}_N,
\end{aligned}$$

where $\tilde{E} = NE$ has been substituted, and use has been made of the identity

$$\partial_E p = W^{-1} \partial_E \delta(E - H) - \beta N p, \tag{1.47}$$

obtained from differentiating (1.31). Expanding H in terms of its definition (1.2), and then substituting $\boldsymbol{x}$ for $\boldsymbol{x}_1$ and $\boldsymbol{x}'$ for the variable of integration which cannot

be evaluated in each term in the sum leads to

$$\nabla p_+(\boldsymbol{x}) = \left(\partial_{\tilde{E}} + \beta\right)\left(\int_{\mathcal{D}} \nabla G(\boldsymbol{x},\boldsymbol{x}')\ \left(n_+ p_{++}(\boldsymbol{x},\boldsymbol{x}') - n_- p_{+-}(\boldsymbol{x},\boldsymbol{x}')\right) d\boldsymbol{x}' \right.$$
$$\left. - \frac{1}{N}\int_{\mathcal{D}} \nabla G(\boldsymbol{x},\boldsymbol{x}') p_{++}(\boldsymbol{x},\boldsymbol{x}')\ d\boldsymbol{x}' + \frac{1}{2N}\nabla g(\boldsymbol{x},\boldsymbol{x}) p_+(\boldsymbol{x})\right), \quad (1.48)$$

and similarly

$$\nabla p_-(\boldsymbol{x}) = \left(\partial_{\tilde{E}} + \beta\right)\left(\int_{\mathcal{D}} \nabla G(\boldsymbol{x},\boldsymbol{x}')\ \left(n_- p_{--}(\boldsymbol{x},\boldsymbol{x}') - n_+ p_{-+}(\boldsymbol{x},\boldsymbol{x}')\right) d\boldsymbol{x}' \right.$$
$$\left. - \frac{1}{N}\int_{\mathcal{D}} \nabla G(\boldsymbol{x},\boldsymbol{x}') p_{--}(\boldsymbol{x},\boldsymbol{x}')\ d\boldsymbol{x}' + \frac{1}{2N}\nabla g(\boldsymbol{x},\boldsymbol{x}) p_-(\boldsymbol{x})\right). \quad (1.49)$$

Combining (1.48) and (1.49), analogous expressions for $\nabla\omega_1$ and $\nabla\rho_1$ are found to be

$$\nabla\omega_1(\boldsymbol{x}) = \left(\partial_{\tilde{E}} + \beta\right)\left(\rho_1(\boldsymbol{x})\nabla\psi_1(\boldsymbol{x}) + \int_{\mathcal{D}} \nabla G(\boldsymbol{x},\boldsymbol{x}') c_2(\boldsymbol{x},\boldsymbol{x}')\, d\boldsymbol{x}' \right.$$
$$\left. + \frac{1}{2N}\omega_1(\boldsymbol{x})\nabla g(\boldsymbol{x},\boldsymbol{x})\right) \quad (1.50)$$

$$\nabla\rho_1(\boldsymbol{x}) = \left(\partial_{\tilde{E}} + \beta\right)\left(\omega_1(\boldsymbol{x})\nabla\psi_1(\boldsymbol{x}) + \int_{\mathcal{D}} \nabla G(\boldsymbol{x},\boldsymbol{x}')\omega_2(\boldsymbol{x},\boldsymbol{x}')\, d\boldsymbol{x}' \right.$$
$$\left. + \frac{1}{2N}\rho_1(\boldsymbol{x})\nabla g(\boldsymbol{x},\boldsymbol{x})\right). \quad (1.51)$$

Equivalent equations for second-order and higher-order cumulants are obtained following the same procedure. Details are given in appendix B.1. The resulting second-order cumulant equations are

$$\begin{aligned}\nabla\omega_2(\boldsymbol{x},\boldsymbol{x}') = \Big(\partial_{\tilde{E}}+\beta\Big)\Big(&\rho_1(\boldsymbol{x})\nabla\psi_2(\boldsymbol{x},\boldsymbol{x}')+c_2(\boldsymbol{x},\boldsymbol{x}')\nabla\psi_1(\boldsymbol{x})\\ &+\int_{\mathcal{D}}\nabla G(\boldsymbol{x},\boldsymbol{x}'')c_3(\boldsymbol{x},\boldsymbol{x}',\boldsymbol{x}'')\,d\boldsymbol{x}''\\ &+\frac{1}{N}\nabla G(\boldsymbol{x},\boldsymbol{x}')\left(\rho_2(\boldsymbol{x},\boldsymbol{x}')+\rho_1(\boldsymbol{x})\rho_1(\boldsymbol{x}')\right)\\ &+\frac{1}{2N}\omega_2(\boldsymbol{x},\boldsymbol{x}')\nabla g(\boldsymbol{x},\boldsymbol{x})\Big)\\ +\Big(\partial_{\tilde{E}}\omega_1(\boldsymbol{x}')\Big)\Big(&\rho_1(\boldsymbol{x})\nabla\psi_1(\boldsymbol{x})+\int_{\mathcal{D}}\nabla G(\boldsymbol{x},\boldsymbol{x}')c_2(\boldsymbol{x},\boldsymbol{x}')\,d\boldsymbol{x}'\\ &+\frac{1}{2N}\omega_1(\boldsymbol{x})\nabla g(\boldsymbol{x},\boldsymbol{x})\Big)\end{aligned}\tag{1.52}$$

$$\begin{aligned}\nabla c_2(\boldsymbol{x},\boldsymbol{x}') = \Big(\partial_{\tilde{E}}+\beta\Big)\Big(&\omega_1(\boldsymbol{x})\nabla\psi_2(\boldsymbol{x},\boldsymbol{x}')+\omega_2(\boldsymbol{x},\boldsymbol{x}')\nabla\psi_1(\boldsymbol{x})\\ &+\int_{\mathcal{D}}\nabla G(\boldsymbol{x},\boldsymbol{x}'')\omega_3(\boldsymbol{x},\boldsymbol{x}',\boldsymbol{x}'')\,d\boldsymbol{x}''\\ &+\frac{1}{N}\nabla G(\boldsymbol{x},\boldsymbol{x}')\left(c_2(\boldsymbol{x}',\boldsymbol{x})+\omega_1(\boldsymbol{x})\rho_1(\boldsymbol{x}')\right)\\ &+\frac{1}{2N}c_2(\boldsymbol{x},\boldsymbol{x}')\nabla g(\boldsymbol{x},\boldsymbol{x})\Big)\\ +\Big(\partial_{\tilde{E}}\omega_1(\boldsymbol{x}')\Big)\Big(&\omega_1(\boldsymbol{x})\nabla\psi_1(\boldsymbol{x})+\int_{\mathcal{D}}\nabla G(\boldsymbol{x},\boldsymbol{x}')\omega_2(\boldsymbol{x},\boldsymbol{x}')\,d\boldsymbol{x}'\\ &+\frac{1}{2N}\rho_1(\boldsymbol{x})\nabla g(\boldsymbol{x},\boldsymbol{x})\Big)\end{aligned}\tag{1.53}$$

$$\begin{aligned}\nabla\rho_2(\boldsymbol{x},\boldsymbol{x}') = \Big(\partial_{\tilde{E}}+\beta\Big)\Big(&\omega_1(\boldsymbol{x})\nabla\phi_2(\boldsymbol{x}',\boldsymbol{x})+c_2(\boldsymbol{x},\boldsymbol{x}')\nabla\psi_1(\boldsymbol{x})\\ &+\int_{\mathcal{D}}\nabla G(\boldsymbol{x},\boldsymbol{x}'')c_3(\boldsymbol{x}',\boldsymbol{x},\boldsymbol{x}'')\,d\boldsymbol{x}''\\ &+\frac{1}{N}\nabla G(\boldsymbol{x},\boldsymbol{x}')\big(\omega_2(\boldsymbol{x},\boldsymbol{x}')+\omega_1(\boldsymbol{x})\omega_1(\boldsymbol{x}')\big)\\ &+\frac{1}{2N}\rho_2(\boldsymbol{x},\boldsymbol{x}')\nabla g(\boldsymbol{x},\boldsymbol{x})\Big)\\ +\Big(\partial_{\tilde{E}}\omega_1(\boldsymbol{x}')\Big)\Big(&\omega_1(\boldsymbol{x})\nabla\psi_1(\boldsymbol{x})+\int_{\mathcal{D}}\nabla G(\boldsymbol{x},\boldsymbol{x}')\omega_2(\boldsymbol{x},\boldsymbol{x}')\,d\boldsymbol{x}'\\ &+\frac{1}{2N}\rho_1(\boldsymbol{x})\nabla g(\boldsymbol{x},\boldsymbol{x})\Big).\end{aligned}\tag{1.54}$$

The second-order cumulant expression ϕ_2 and the de-singularised third-order cumulants ω_3 and c_3 are defined in appendix B.1,

Taken together, the energy equation (1.46), the ensemble mean equations (1.50-1.51), the fluctuation equations (1.52-1.54), and the analogous equations for higher-order cumulants (c.f. PL76's eqn. 17) form an infinite hierarchy that, in principle, exactly describe the statistics of the point vortex system for an arbitrary number of vortices N. Progress can evidently be made by considering limits $N \to \infty$ as described in section 1.3.4. This hierarchy will form the parent model for the hydrodynamic limit investigation in chapter 2 and the thermodynamic limit investigation in section 4.

Before proceeding with using the PL76 hierarchy to study the vortex system, the assumptions of the model will be analysed. The whole of the theory of section 1.3 rests on two key assumptions: the ergodic hypothesis and the point vortex approximation itself. The former will be dealt with in section 1.4.1, while the latter will be considered in section 1.4.2.

1.4 Model assumptions

1.4.1 Ergodic theory

A standard assumption in justifying statistical mechanics theories is that the evolution of the relevant dynamical system is ergodic in phase space over the surface of constant energy, so that the microcanonical ensemble is valid at long times. In other words, spatial averages over all ensemble members are equivalent to the long-time average of a single member of the ensemble. The formal validity of this assumption for the finite N vortex system is currently an open question. The basis of ergodic theory will now be examined, and the key assumption of statistical mechanics stated. Further details for a general system are found in [14] and for the vortex system in [91].

Consider again the arbitrary macroscopic function $f(\boldsymbol{x}_1, \ldots, \boldsymbol{x}_N)$, for which the spatial (ensemble) average is given by (1.37) i.e.

$$\langle f \rangle = \int_{\mathcal{D}^N} f(\boldsymbol{x}_1, \ldots, \boldsymbol{x}_N) p(\boldsymbol{x}_1, \cdots, \boldsymbol{x}_N)\, d\boldsymbol{x}_1 \cdots d\boldsymbol{x}_N,$$

and the time average of the same function, integrated from $t = 0$ to $t = T$, is given by

$$\bar{f} = \lim_{T\to\infty} \frac{1}{T} \int_0^T f(\boldsymbol{x}_1, \ldots, \boldsymbol{x}_N)\, dt. \tag{1.55}$$

Simply put, ergodic theory gives a formal answer to the question: under what circumstances do the two averages converge so that $\bar{f} \approx \langle f \rangle$?

Equation (1.55) yields two immediate questions: does the limit exist and how can $\bar{f}$ be computed in finite time? This can be regarded as determining what is the relative importance of different sub-regions of phase space as the trajectory of the dynamical system moves through the whole of its phase space. (It is believed that as $N \to \infty$ these sub-regions shrink [91].)

To answer the convergence question, some classical theorems of ergodic theory are required. First, Liouville's theorem is used to guarantee that the evolution of the dynamical system is a measure preserving transformation. Specifically, the vector field defined by the dynamical system (1.1)

$$V(x, y) = \left(-\frac{\partial H}{\partial y_1}, \ldots, -\frac{\partial H}{\partial y_N}; \frac{\partial H}{\partial x_1}, \ldots, \frac{\partial H}{\partial x_N} \right),$$

preserves phase space volume i.e. $\nabla \cdot V = 0$. From this the following theorems can be applied: the mean ergodic theorem of von Neumann guaranteeing 'mean-square' (i.e. L^2 norm) convergence and the pointwise ergodic theorem of Birkhoff guaranteeing 'almost everywhere' (i.e. pointwise) convergence.

From these theorems it can be seen that as a given trajectory evolves in phase space it will, after sufficiently long times, have densely filled the entire phase space uniformly so that equal sub-regions are visited for equal times. In this case the time average $\bar{f}$ is equal to the ensemble average $\langle f \rangle$ and the system is ergodic. Assuming the system is ergodic allows the fundamental postulate of statistical mechanics to be stated: '*equal a priori probabilities*' states that all microstates with the same energy are equally probable. From this, the key concept of statistical equilibrium can be illustrated: consider a system evolving in time that has reached an equilibrium (time averages of macroscopic quantities are steady). Clearly as the system evolves the

microstate changes and hence there must be many different microstates that all give the same macrostate. As such the macroscopic equilibrium state is the one with the largest number of consistent microstates; this is termed the '*principle of maximum entropy*'. The Boltzmann entropy $S = \log W$ counts the number of microstates, meaning the maximum entropy state is the equilibrium state (see chapter 2). Further, using equal a priori probabilities, the alternative Gibbs entropy, $S = -\sum_i p_i \log p_i$, can be seen to be equivalent to the Boltzmann entropy when all the probabilities are equal to $p_i = 1/W$.

Returning to ergodic theory and equation (1.55), from a practical and computational point of view the question now becomes: how large does T have to be for $\bar{f} \approx \langle f \rangle$? Put another way, how long a run is required for the dynamical system to reach an equilibrium so that averages over the run can be justifiably be compared with predicted averages from equilibrium statistical mechanics? Onsager himself was concerned with this exact question, mentioning, in correspondence to Lin [49]

> "*I still have to find out whether the process anticipated by these considerations are rapid enough to play a dominant role in the evolution of vortex sheets*".

Numerical calculations [121] have addressed this question directly for the low $N = 6$ point vortex system, and concluded that ergodicity does not hold. Consequently, for robust verification of any statistical mechanics predictions, comparisons should be made against both the ensemble and time-averages.

In general the specific form of the function f dictates how close to ergodic the system is. For simple functions (typically with a high degree of symmetry) the convergence is rapid as most sub-regions of phase space are very similar to one another.

PL76 [95] performed approximate numerical simulations using $N = 40$ vortices in a circular domain in an attempt to verify their equilibrium predictions of the streamfunction. As will be detailed in chapter 2, equilibrium streamfunctions in this situation tend to be characterised by like-signed vortices clustering into macro configurations. However, over the length of their run (it is not explicit what their time scale is), PL76 found that while in some cases the long-time equilibrium was reached, in other cases the vortices only formed meta-stable equilibria and did not

reach the predicted long-time equilibrium.

In a more recent study [13], equilibrium statistical mechanics theories were tested using direct numerical simulations (with the same time stepping scheme as in this thesis; see section 1.2.3) of $N = 100$ vortices over a time interval of $t \approx 470N$ in the time scale used here. Four macroscopic diagnostics were used at three different energies and agreement between the runs and statistical mechanics was very good in all cases.

In this thesis dynamical runs will involve $N = 100$ vortices and are at least $t = 1000N$ time units in length. There is no justification for this other than on an empirical basis: averages taken over this time appear to reach an equilibrium (as seen from animations) and show good agreement with theoretical predictions and ensemble averages. This time interval also compares favourably with that used in other modern studies [13, 123].

1.4.2 Miller-Robert-Sommeria theory

The more fundamental question as to the validity of the point vortex model in a physical context is now considered, and a vorticity statistical mechanics theory, complementary to that of Onsager's in section 1.3, is described.

It has been shown that any smooth 2D Euler solution may be approximated arbitrarily well over a finite time interval $0 < t < T$ by the singular vorticity distribution (1.15) i.e. $\omega(\boldsymbol{x}) = \sum_{i=1}^{N} \Gamma_i \delta(\boldsymbol{x} - \boldsymbol{x}_i)$, with $\Gamma_i = \pm 1/N$ as $N \to \infty$ (see [80] and section 1.2.1). However this is not sufficient to justify equilibrium statistical mechanics where the limit $T \to \infty$ is required.

Onsager himself was fully aware of the limitations[11] of the point vortex model [49]

> "*The present theory for the formation of large vortices does not apply to all cases of unsteady flow. As a matter of fact, the phenomenon is common but not universal.*"

Onsager's main concern with the discrepancy between the point vortex model as $N \to \infty$ and the 2D Euler model is most easily explained with the following example. Consider an ideal vortex patch i.e. constant vorticity in a finite area. Due to the

[11] Onsager did remark that the point vortex model should work better for superfluids, where he correctly predicted that turbulence is genuinely discretised [6].

incompressibility of the 2D Euler equations, the area is conserved which together with the conservation of circulation implies that it is not possible for vorticity to intensify in localised regions. However if the vortex patch is approximated by N point vortices at a high energy, the vorticity could eventually evolve into a more intense localised structure and the effective area would decrease: the vortices are behaving in some respects like a compressible system with the ability to cluster or expand.

A major step in eliminating the discrepancies between the two models was made independently by Miller [84] and Robert [101], with further developments by Miller [85] and Robert & Sommeria [102]. The Miller-Robert-Sommeria theory (MRS hereafter) avoids the vortex approximation altogether and instead an equilibrium statistical mechanics theory is derived directly from the 2D Euler equations with vorticity broken into small 'patches' that are distributed using Lynden-Bell statistics [79] to find the most probable state. The solution is an equilibrium solution of the full 2D Euler equations, on which fine-scale vorticity fluctuations are superimposed.

The basic quantity of the theory is a local distribution function $n(\boldsymbol{x}, \sigma)$, which gives the probability density that the microscopic vorticity $\omega(\boldsymbol{x})$ lies between σ and $\sigma + d\sigma$ at the point $\boldsymbol{x}$. As the vorticity field evolves it mixes to very fine scales so that the neighbourhood of $\boldsymbol{x}$ will contain many values of vorticity, distributed according to $n(\boldsymbol{x}, \sigma)$. Thus at each point $\boldsymbol{x} \in \mathcal{D}$, n satisfies

$$\int_{-\infty}^{\infty} n(\boldsymbol{x}, \sigma)\, d\sigma = 1, \tag{1.56}$$

and the macroscopic vorticity is given by

$$\bar{\omega}(\boldsymbol{x}) = \int_{-\infty}^{\infty} n(\boldsymbol{x}, \sigma)\sigma\, d\sigma.$$

The function $n(\boldsymbol{x}, \sigma)$ encodes an infinite set of conserved quantities of the 2D incompressible Euler equations, namely the area occupied by each level set of the initial vorticity. If $g(\sigma)d\sigma$ is the fraction of the total area A on which occur vorticities

between σ and $d\sigma$ then

$$\frac{1}{A}\int_{\mathcal{D}} n(\boldsymbol{x},\sigma)\,d\boldsymbol{x} = g(\sigma).$$

From here the entropy associated with $n(\boldsymbol{x},\sigma)$ can be calculated using standard Maxwell-Boltzmann statistics, and is given by

$$S = -\int_{\mathcal{D}}\int_{-\infty}^{\infty} n(\boldsymbol{x},\sigma)\log n(\boldsymbol{x},\sigma)\,d\boldsymbol{x}\,d\sigma. \tag{1.57}$$

Maximising (1.57) subject to (1.56) and the fixed energy given by

$$E = -\frac{1}{2}\int_{\mathcal{D}^2}\int_{-\infty}^{\infty}\int_{-\infty}^{\infty} \sigma\sigma' G(\boldsymbol{x},\boldsymbol{x}')n(\boldsymbol{x},\sigma)n(\boldsymbol{x},\sigma')\,d\sigma\,d\sigma'\,d\boldsymbol{x}\,d\boldsymbol{x}',$$

gives

$$n(\boldsymbol{x},\sigma) = \frac{1}{Z(\boldsymbol{x})}\exp\left(-\bar{\beta}[\sigma\bar{\psi}(\boldsymbol{x}) - \mu(\sigma)]\right),$$

where $Z(\boldsymbol{x})$, $\mu(\sigma)$ and $\bar{\beta}$ are Lagrange multipliers. Finally the streamfunction is given by

$$\nabla^2\bar{\psi}(\boldsymbol{x}) = \frac{1}{Z(\boldsymbol{x})}\int_{-\infty}^{\infty}\exp\left(-\bar{\beta}[\sigma\bar{\psi}(\boldsymbol{x}) - \mu(\sigma)]\right)\,d\sigma. \tag{1.58}$$

With the infinitely many conserved quantities of the 2D Euler system, the MRS theory can be seen to reconcile the problems discussed at the start of the section relating to the point vortex approximation. However the MRS theory depends on detailed initial conditions, and in practice, because of its complexity (i.e. solving a variational problem involving an infinite number of constraints), has usually been used for simple initial distributions [12] or for linearised approximations [27]. For a more general description of vorticity (independent of detailed initial conditions) and for more for straightforward computation, the point vortex model will be studied in this thesis. Reconciling the two theories with respect to fully turbulent Navier-Stokes simulations is a continuing area of study e.g. [124].

Finally it is noted that equation (1.58) has a form that is very common to statisti-

cal theories of 2D Euler vortex models in the hydrodynamic limit (i.e. dominated by the mean flow), both from the MRS framework and the standard point vortex model. In general such equations for the equilibrium streamfunction are called 'mean-field' equations and are given by

$$\nabla^2\psi = F(\psi, \alpha),$$

where F is a function and α a variable (or variables) that depend on the specific formulation. The term mean-field equation will be used throughout this thesis, particularly when comparing different models.

1.5 Thesis outline

The research presented in this thesis is split up into four main problems, with a chapter devoted to each one. Chapter 2 focuses on the bounded 2D Euler point vortex system in the hydrodynamic limit, where the famous sinh-Poisson equation is the valid. Two different classical derivations of the sinh-Poisson equation are presented in section 2.2 and these are found to fit in neatly with a new 'vorticity mode' eigenvalue problem. Numerical techniques are discussed in section 2.3. Section 2.4 focuses on the statistical mechanics in a new left-right symmetric, 'heart'-shaped domain, including verification by direct numerical simulation of the N vortex system. Finally in section 2.5 conclusions are drawn.

Chapter 3 presents a new algorithm (VOR-MFS) for the solution of the dynamics of the generalised vortex problem. Section 3.2 introduces the algorithm, including details of the use of the method of fundamental solutions (MFS), a necessary boundary approximation and the computational cost. Section 3.3 is then devoted to a number of test-cases demonstrating the robustness of the new algorithm. Finally, in section 3.4 conclusions are presented.

The focus of chapter 4 is the general point vortex system in the thermodynamic limit. Using the reformed PL76 hierarchy presented 1.3.5, in section 4.2 the 'vorticity fluctuation equation' equation is derived (a thermodynamic analogue to the sinh-Poisson equation), which leads to statistical descriptions of the density of states

$W_t(\tilde{E})$ and the caloric curve $\beta_t(\tilde{E})$ for a general bounded system at low positive and negative energies. The vorticity fluctuation is solved in section 4.3 using the vorticity modes first introduced in chapter 2. To verify these statistical mechanics predictions, section 4.4 considers the quasi-geostrophic vortex in a pair of Neumann oval domains and uses the VOR-MFS algorithm of chapter 3 for microcanonical sampling in order to construct finite N vortex versions of $W(\tilde{E})$ and $\beta(\tilde{E})$. Finally in section 4.5 conclusions are drawn.

Chapter 5 considers the distribution of vorticity in the 2D Euler system in the Neumann oval domain. In section 5.2.2 a joint probability distribution is constructed between the energy and a suitable macroscopic diagnostic that describes the distribution of the vorticity in the domain. Cross sections of this joint PDF at fixed energies are then compared to direct numerical simulations at the same energies in section 5.2.3. In section 5.3 conclusions are made and a possible extension to the work using large deviation statistical mechanics is suggested.

Finally in chapter 6 overall conclusions are presented and possible directions for future research discussed.

Chapter 2

Statistical mechanics of point vortices in the hydrodynamic limit

2.1 Introduction

Following on from Onsager's seminal paper in 1949 [93], there was little further work done on point vortex statistical mechanics until the 1970s when the connection between the point vortex system and the 2D plasma system was made, interesting many more researchers. It can be argued that this renaissance of Onsager's theory was initialised by the derivation of the famous sinh-Poisson equation (SPE) describing the mean circulation in the domain. One reason for the continued popularity of the SPE is that it has been shown [88] that its solutions are relevant to the long-time states of turbulent 2D Navier-Stokes flows. One particularly important phenomenon in such turbulent flows is that of 'spin-up' – the spontaneous acquisition of angular momentum by the flow in a bounded domain [31, 32] – and recently the paper by Taylor, Matthias & Helander [111] has sought to link spin-up with solutions of the SPE.

For historical interest it is noted that Onsager derived a form of the SPE in the late 1940s, though never published it [49]. In terms of published work, the SPE was independently derived, first by Joyce & Montgomery [64] (JM73 hereafter) and then later by PL76 using a contrasting technique. JM73 used a maximum entropy approach, making no a priori assumption about the sign of the inverse temperature,

then later finding only negative temperature states yielded non-trivial solutions. The important point about the JM73 approach was to neglect the energy of fluctuations, in a manner consistent with the taking of the hydrodynamic limit. PL76 on the other hand used their cumulant expansion method described in section 1.3.5 in the hydrodynamic limit, immediately restricting the solutions of the SPE to negative temperature states only.

In section 2.2.1 JM73's derivation will be reviewed. In section 2.2.2, a generalised version of the SPE, termed here as the 'elliptic-sinh equation' (ESE), is derived in a similar manner to that of PL76[1]. This continues the theme, started in section 1.3.5, of using a version of the PL76 hierarchy that is valid for a more general dynamics, rather than just the 2D Euler dynamics (which would lead to the SPE).

An interesting limitation of most previous studies, e.g. [11, 113], is that it is assumed that the boundary condition of the SPE is of homogeneous Dirichlet type. Chavanis & Sommeria [27] showed that in general this is not correct and that there exists a further class of physically relevant solutions with non-zero boundary condition. This point was recently re-emphasised by Taylor et al. [111].

Naturally, finding solutions of the SPE has been a continual area of study since its derivation. Analytical solutions do exist, though only for square [113] or doubly-periodic domains [72]. The standard numerical algorithm for solving the SPE was published in 1974 by McDonald [11,82] (just one year after the first published derivation of the SPE), and continues to find applications e.g. [124]. Section 2.3 focuses on numerical solutions and introduces using a new Galerkin-type solver that handles the non-zero boundary condition mentioned above, as well as the standard homogeneous Dirichlet boundary condition.

Section 2.4 is concerned solely with the 2D Euler system and solutions of the SPE are found in a new left-right symmetric domain and verified with direct numerical simulations of the finite N vortex system as well as a small E asymptotic theory, details of which are given in appendix B.2. The domain is chosen specifically so that an energy-induced phase transition occurs in the structure of the mean flow.

[1] A related equation was derived in [38], simply termed the 'mean field equation', in the context of a two layer quasi-geostrophic point vortex system.

2.2 The sinh-Poisson/elliptic-sinh equation

2.2.1 Joyce-Montgomery maximum entropy derivation

In the first published derivation of the SPE, JM73 used a maximum entropy approach, subject to constraints determined from the conservation of energy and conservation of positive and negative vortices. This method is now reviewed.

The basic set-up is the same as in section 1.3: N point vortices in a bounded domain $\mathcal{D}$. A total of n_+N vortices have positive circulation and n_-N have negative circulation ($n_+ + n_- = 1$). The domain is then divided into M cells, each of area Δ where $1 \ll M \ll N$. The cells are large enough to contain many vortices, but there is no distinction made between the locations of individual vortices within a cell (the area of the cell will later be reduced to zero). Let $\mathfrak{n}_i^+$ ($\mathfrak{n}_i^-$) denote the number of positive (negative) vortices in the i^{th} cell. The probability of a given vortex distribution is

$$W = \left\{ (n_+N)! \prod_{i=1}^{M} \frac{\Delta^{\mathfrak{n}_i^+}}{\mathfrak{n}_i^+!} \right\} \left\{ (n_-N)! \prod_{i=1}^{M} \frac{\Delta^{\mathfrak{n}_i^-}}{\mathfrak{n}_i^-!} \right\}, \tag{2.1}$$

which can also be interpreted as the phase space volume occupied by the distribution, meaning the Boltzmann entropy is given by

$$S = \log W,$$

as in section 1.3.2. Assuming $n_\pm N$ and $\mathfrak{n}_i^\pm$ are large enough for Stirling's formula to apply to the factorials in (2.1), S is given by

$$S = -\sum_{i=1}^{M} \left(\mathfrak{n}_i^+ \log \frac{\mathfrak{n}_i^+}{\Delta} + \mathfrak{n}_i^- \log \frac{\mathfrak{n}_i^-}{\Delta} \right), \tag{2.2}$$

which, to within a constant, is the two-species Gibbs entropy. At statistical equilib-

rium it is assumed that the *principle of maximum entropy* holds i.e. the system is expected to be in the most probable macrostate – the one that is the most represented at the microscopic level (see section 1.4.1). Under the classical assumption of *equal a priori probabilities* (that all microstates are equiprobable under the uniform measure in phase space), the equilibrium distribution is obtained by maximising the Boltzmann entropy (2.2). This is done using the method of Lagrange multipliers, under the constraints of fixed energy

$$E = -\frac{1}{2}\sum_{i\neq j}(\mathfrak{n}_i^+ - \mathfrak{n}_i^-)G(\boldsymbol{x}_i,\boldsymbol{x}_j)(\mathfrak{n}_j^+ - \mathfrak{n}_j^-), \tag{2.3}$$

and fixed total number of positive and negative vortices

$$\sum_{i=1}^{M}\mathfrak{n}_i^+ = n_+N, \quad \sum_{i=1}^{M}\mathfrak{n}_i^- = n_-N.$$

This results in

$$\log\mathfrak{n}_i^+ - \log\Delta + \alpha^+ + \beta\sum_{i\neq j}G(\boldsymbol{x}_i,\boldsymbol{x}_j)(\mathfrak{n}_j^+ - \mathfrak{n}_j^-) = 0 \tag{2.5a}$$

$$\log\mathfrak{n}_i^- - \log\Delta + \alpha^- - \beta\sum_{i\neq j}G(\boldsymbol{x}_i,\boldsymbol{x}_j)(\mathfrak{n}_j^+ - \mathfrak{n}_j^-) = 0, \tag{2.5b}$$

for Lagrange multipliers α^+, α^- (often interpreted as 'chemical potentials') and β (interpreted as the inverse thermodynamic temperature). The function $G(\boldsymbol{x}_i,\boldsymbol{x}_j)$ is the Green's function of the first kind for the domain, as defined by (1.3) in section 1.2.1.

As a brief aside that will be used later, we derive alternative expression for the entropy. Substituting (2.5) into (2.2), and using the energy definition (2.3), the entropy is found to be

$$S \;=\; 2\beta E + \alpha^+ n_+ N + \alpha^- n_- N. \tag{2.6}$$

Returning to the derivation, subtracting (2.5a) from (2.5b) gives

$$\begin{aligned}\frac{\mathfrak{n}_i^+ - \mathfrak{n}_i^-}{\Delta} &= \exp\left(-\alpha^+ - \beta\sum_{i\neq j} G(\boldsymbol{x}_i,\boldsymbol{x}_j)(\mathfrak{n}_j^+ - \mathfrak{n}_j^-)\right) \\ &\quad - \exp\left(-\alpha^- + \beta\sum_{i\neq j} G(\boldsymbol{x}_i,\boldsymbol{x}_j)(\mathfrak{n}_j^+ - \mathfrak{n}_j^-)\right). \end{aligned} \tag{2.7}$$

The next step is to take the limit of zero cell size $\Delta \to 0$. In this limit the 'mean field vorticity' $\omega(\boldsymbol{x})$ (which determines the mean flow) can now be formally defined by

$$\begin{aligned}\frac{\mathfrak{n}_i^+ - \mathfrak{n}_i^-}{\Delta} &\to \omega(\boldsymbol{x}) \\ \sum_{i\neq j} G(\boldsymbol{x}_i,\boldsymbol{x}_j)(\mathfrak{n}_j^+ - \mathfrak{n}_j^-) &\to \int_{\mathcal{D}} G(\boldsymbol{x},\boldsymbol{x}')\omega(\boldsymbol{x}')\,d\boldsymbol{x}' = \tilde{\psi}(\boldsymbol{x}).\end{aligned}$$

In this limit (2.7) becomes an integral equation for the vorticity

$$\begin{aligned}\omega(\boldsymbol{x}) &= \exp\left(-\alpha^+ - \beta\int_{\mathcal{D}} G(\boldsymbol{x},\boldsymbol{x}')\omega(\boldsymbol{x}')\,d\boldsymbol{x}'\right) \\ &\quad - \exp\left(-\alpha^- + \beta\int_{\mathcal{D}} G(\boldsymbol{x},\boldsymbol{x}')\omega(\boldsymbol{x}')\,d\boldsymbol{x}'\right),\end{aligned}$$

which, using the definition of the streamfunction (1.43) i.e. $\tilde{\psi} = \int_{\mathcal{D}} G(\boldsymbol{x},\boldsymbol{x}')\omega(\boldsymbol{x}')\,d\boldsymbol{x}$, can be converted into the partial differential equation

$$\nabla^2\tilde{\psi} = \tfrac{1}{2}C_1\exp\left(\beta\tilde{\psi}\right) - \tfrac{1}{2}C_2\exp\left(-\beta\tilde{\psi}\right), \tag{2.8}$$

with normalisation constants, determined by the conservation of the number of vortices, given by

$$C_{1,2} = 2n_\pm\left(\int_{\mathcal{D}}\exp\left(\pm\beta\tilde{\psi}\right)\,d\boldsymbol{x}\right)^{-1}. \tag{2.9}$$

In this limit the energy (2.3) is given by

$$E = -\frac{1}{2}\int_{\mathcal{D}}\tilde{\psi}(\boldsymbol{x})\omega(\boldsymbol{x})\,d\boldsymbol{x} = -\frac{1}{2}\int_{\mathcal{D}}\tilde{\psi}(\boldsymbol{x})\nabla^2\tilde{\psi}(\boldsymbol{x})\,d\boldsymbol{x}, \tag{2.10}$$

which is identical to (1.17) i.e. the regular energy in 2D Eulerian fluid dynamics; see end of section 1.2.1.

At this point the results of Chavanis & Sommeria [27] (CS96 hereafter) and Taylor et al. [111] (TBH09 hereafter) are utilised to construct the sinh-Poisson equation with the correct boundary condition. In the first instance, reference will be made to later work of TBH09 due to its similarity with the notation used in this thesis and useful nomenclature. The equivalence to the original derivation by CS96 will then be noted.

Note that by writing $C_1 = \beta \exp(-\beta\psi_0)$ and $C_2 = \beta \exp(\beta\psi_0)$, (2.8) is transformed, into the canonical form of the sinh-Poisson equation

$$\nabla^2\psi = C \sinh \beta\psi, \tag{2.11}$$

where

$$\psi = \tilde{\psi} - \psi_0, \quad C = (C_1C_2)^{1/2} \quad \text{and} \quad \psi_0 = \frac{1}{2\beta}\log(C_2/C_1). \tag{2.12}$$

Note that ψ remains the streamfunction as the addition of the constant ψ_0 has no effect.

If the assumption can be made that $C_1 = C_2$ (referred to as 'type I' solutions in TBH09), $\psi_0 = 0$ and (2.11-2.12) is in the usual form, with the homogeneous Dirichlet boundary condition

$$\psi(\boldsymbol{x}) = 0, \quad \boldsymbol{x} \in \partial\mathcal{D}.$$

This is the form of the SPE that has been studied by [11] among others. However, in general $C_1 \neq C_2$ (referred to as 'type II' solutions in TBH09), and then general boundary condition is

$$\psi(\boldsymbol{x}) = -\psi_0, \quad \boldsymbol{x} \in \partial\mathcal{D}.$$

Both of these solutions are physically relevant and therefore must treated on an equal footing.

To aid in the classification of solutions of the SPE, the linearised form of (2.11)

is considered, which leads to the following eigenvalue problem

$$\nabla^2\Phi_j = \beta_j\rho_0\Phi_j, \qquad \boldsymbol{x}\in\mathcal{D}, \tag{2.13a}$$

$$\Phi_j = \text{constant}, \qquad \boldsymbol{x}\in\partial\mathcal{D}, \tag{2.13b}$$

where $\rho_0 = |\mathcal{D}|^{-1}$ is the inverse of the domain area, Φ_j are the eigenmodes (corresponding to type I and type II solution branches) and $\beta_j < 0$ are the domain size invariant eigenvalues. Note that $\int_\mathcal{D}\Phi_j\,d\boldsymbol{x} = 0$ since the system is neutral.

As mentioned, the eigenvalue problem (2.13) was first introduced by Chavanis & Sommeria [27] (CS96 hereafter), albeit in a different form: for the mean streamfunction ψ, CS96 derived the linearised problem

$$-\nabla^2\psi(\boldsymbol{x}) + \beta\psi(\boldsymbol{x}) = \beta\langle\psi(\boldsymbol{x})\rangle \qquad \boldsymbol{x}\in\mathcal{D}, \tag{2.14a}$$

$$\psi(\boldsymbol{x}) = 0, \qquad \boldsymbol{x}\in\partial\mathcal{D} \tag{2.14b}$$

for which there are two types of solution:

1. When $\langle\psi\rangle = 0$, we return to the Laplace eigenvalue problem with *zero* mean and $\{\beta_j\}$ the corresponding eigenvalues. These solutions were termed type I by TBH09.

2. When $\langle\psi\rangle \neq 0$, the eigenvalue problem is new. The corresponding eigenvalues are roots of a function $F(\beta)$ and are constructed using eigenvalues of the Laplacian with *non-zero* mean. These solutions were termed type II by TBH09.

Setting $\Phi = \psi - \langle\psi\rangle$ in the (2.14), there is equivalence with the vorticity mode eigenvalue problem (2.13).

A further property of the above eigenvalue problem is revealed by integrating (2.13a) to give

$$\int_\mathcal{D}\nabla^2\Phi_j\,d\boldsymbol{x} = \beta_j\rho_0\int_\mathcal{D}\Phi_j\,d\boldsymbol{x} = 0, \quad k = 1,2,3,\ldots. \tag{2.15}$$

The integral constraint (2.15) can be simplified further using the divergence theorem

$$\oint_{\partial\mathcal{D}}\nabla\Phi_j\cdot\boldsymbol{n}\,ds = 0, \quad \text{or} \quad \oint_{\partial\mathcal{D}}\boldsymbol{u}_k\cdot d\boldsymbol{s} = 0, \tag{2.16}$$

for $\boldsymbol{u}_k = -\nabla \times (\Phi_j \boldsymbol{k})$. If each vorticity mode Φ_j is interpreted as the streamfunction of a flow $(\boldsymbol{u}_k)$ in $\mathcal{D}$, then each can be said to satisfy 'no normal flow' and 'zero-circulation' conditions on $\partial\mathcal{D}$.

In summary

$$\nabla^2 \Phi_j = \beta_j \rho_0 \Phi_j, \qquad \boldsymbol{x} \in \mathcal{D} \tag{2.17a}$$

$$\Phi_j = \text{constant}, \qquad \boldsymbol{x} \in \partial\mathcal{D} \tag{2.17b}$$

$$\oint_{\partial\mathcal{D}} \boldsymbol{u}_k \cdot d\boldsymbol{s} = 0, \tag{2.17c}$$

which will be termed the 'vorticity mode' eigenvalue for problem with β_j the 'domain inverse temperatures' (DITs).

By the Hilbert-Schmidt theorem [37] the vorticity modes form a complete orthonormal basis and also unify both the type I and type II solutions of TBH09 as the solutions of a single eigenvalue problem. Further, the vorticity modes and DITs will be used again in chapter 4 to study the vortex system in the thermodynamic limit. This is a remarkable result: the vorticity modes are the natural basis to solve the relevant equations of the vortex system in *both* the hydrodynamic limit *and* the thermodynamic limit.

Finally the form of the solutions to the full nonlinear SPE (or in general the ESE) in (E, β) are described. There are infinitely many solution branches of the SPE and by the linear theory above, each solution branch originates at DIT $\beta = \beta_j$ at $E = 0$. As the solution becomes more nonlinear the solution branch extends towards infinite energy with the structure of the solution expected to remain qualitatively the same along the entire branch.

2.2.2 Pointin-Lundgren cumulant expansion derivation

Next we briefly outline PL76's approach for the derivation of the SPE, generalised for an appropriate linear, elliptic and self-adjoint operator $\mathcal{L}$, as described in section 1.2.1. This generalisation could equally well be done in JM73 framework outlined in the previous section.

PL76 continued the cumulant expansion method introduced in section 1.3.5, in the hydrodynamic limit where the terms of $O(1/N)$ are small, meaning

$$\partial_{\tilde{E}} = \tfrac{1}{N}\partial_E \ll \beta = O(1).$$

Setting $\epsilon = 1/N$, the following quantities are expanded in powers of ϵ

$$\omega_1 = \omega_1^{(0)} + \epsilon\omega_1^{(1)} + O(\epsilon^2) \tag{2.18}$$
$$\rho_1 = \rho_1^{(0)} + \epsilon\rho_1^{(1)} + O(\epsilon^2). \tag{2.19}$$

A natural solution to the asymptotic hierarchy is obtained if it is taken that second-order fluctuations are $O(\epsilon)$ to leading order, third order fluctuations are $O(\epsilon^2)$ etc. At leading order (1.50-1.51) become

$$\nabla\omega_1^{(0)}(\boldsymbol{x}) = \beta\rho_1^{(0)}(\boldsymbol{x})\nabla\psi_1^{(0)}(\boldsymbol{x}) \tag{2.20a}$$
$$\nabla\rho_1^{(0)}(\boldsymbol{x}) = \beta\omega_1^{(0)}(\boldsymbol{x})\nabla\psi_1^{(0)}(\boldsymbol{x}). \tag{2.20b}$$

Adding and subtracting (2.20) gives

$$\nabla\log(\omega_1^{(0)} + \rho_1^{(0)}) = \beta\nabla\psi_1^{(0)}$$
$$\nabla\log(\rho_1^{(0)} - \omega_1^{(0)}) = -\beta\nabla\psi_1^{(0)},$$

and then integrating gives

$$\omega_1^{(0)} + \rho_1^{(0)} = C_1\exp(\beta\psi_1^{(0)}) \tag{2.21a}$$
$$\rho_1^{(0)} - \omega_1^{(0)} = C_2\exp(-\beta\psi_1^{(0)}), \tag{2.21b}$$

with normalisation constants

$$C_{1,2} = 2n_\pm\left(\int_{\mathcal{D}}\exp\left(\pm\beta\psi_1^{(0)}\right)d\boldsymbol{x}\right)^{-1}. \tag{2.22}$$

Using the definition of vorticity $\mathcal{L}\psi_1 = \omega_1$, (2.21b) is subtracted from (2.21a) to give

$$\mathcal{L}\psi_1^{(0)} = \tfrac{1}{2}C_1 \exp\left(\beta\psi_1^{(0)}\right) - \tfrac{1}{2}C_2 \exp\left(-\beta\psi_1^{(0)}\right), \tag{2.23}$$

i.e. an elliptic-Boltzmann equation. Using the same transformation of TBH09 (as in section 2.2.1), (2.23) can be reformed into the elliptic-sinh equation (ESE)

$$\mathcal{L}\psi = C \sinh \beta\psi, \tag{2.24}$$

where, again,

$$\psi = \psi_1^{(0)} - \psi_0, \quad C = (C_1 C_2)^{1/2}, \quad \psi_0 = \frac{1}{2\beta}\log\left(C_2/C_1\right), \tag{2.25}$$

and the linearised version of (2.24) satisfies a generalised version of the vorticity mode eigenvalue problem

$$\mathcal{L}\Phi_k = \beta_k \rho_0 \Phi_k, \qquad \boldsymbol{x} \in \mathcal{D}, \tag{2.26a}$$

$$\Phi_k = \text{constant}, \qquad \boldsymbol{x} \in \partial\mathcal{D} \tag{2.26b}$$

$$\int_{\mathcal{D}} \mathcal{L}\Phi_j \, d\boldsymbol{x} = 0. \tag{2.26c}$$

Note that in the case of QGSW vortices ($\mathcal{L} \equiv \nabla^2 - \lambda^2$, with λ^{-1} the Rossby radius) the integral constraint (2.26c) simplifies in the same way the 2D Euler version (2.17c) does, since

$$\int_{\mathcal{D}} (\nabla^2 - \lambda^2)\Phi_k \, d\boldsymbol{x} \equiv \int_{\mathcal{D}} \nabla^2 \Phi_k \, d\boldsymbol{x}.$$

Hence the QGSW vorticity mode spectrum is simply the 2D Euler vorticity mode spectrum shifted by the constant $-\lambda^2/\rho_0$. For the SQG system the situation is more complicated and will not be considered in this thesis.

Finally it is noted that at $O(\epsilon)$ the energy (1.46) is given by

$$E = -\frac{1}{2}\int_{\mathcal{D}^2} G(\boldsymbol{x},\boldsymbol{x}')\omega_1^{(0)}(\boldsymbol{x})\omega_1^{(0)}(\boldsymbol{x}')\,d\boldsymbol{x}\,d\boldsymbol{x}' \tag{2.27a}$$

$$= -\frac{1}{2}\int_{\mathcal{D}} \psi_1^{(0)}\mathcal{L}\psi_1^{(0)}\,d\boldsymbol{x}. \tag{2.27b}$$

Following TBH09, to compute the entropy consider (1.48) and (1.49) at $O(\epsilon)$. As in PL76 the closure assumption $p_{++}(\boldsymbol{x},\boldsymbol{x}') \approx p_+(\boldsymbol{x})p_+(\boldsymbol{x}')$ etc, (known as the 'mean field approximation'; see [23]) is used. This assumption is equivalent to second order cumulants being ignored for large N. This gives

$$\log\left(\frac{p_+(\boldsymbol{x})}{C}\right) = \beta\int_{\mathcal{D}} G(\boldsymbol{x},\boldsymbol{x}')\big(n_+p_+(\boldsymbol{x}') - n_-p_-(\boldsymbol{x}')\big)\,d\boldsymbol{x}' \tag{2.28a}$$

$$\log\left(\frac{p_-(\boldsymbol{x})}{C}\right) = \beta\int_{\mathcal{D}} G(\boldsymbol{x},\boldsymbol{x}')\big(n_-p_-(\boldsymbol{x}') - n_+p_+(\boldsymbol{x}')\big)\,d\boldsymbol{x}', \tag{2.28b}$$

which when inserted into (1.35) and using (2.27a) gives the entropy

$$S = 2\beta E - \rho_0\log\frac{C}{\rho_0}, \tag{2.29}$$

which is equivalent to equation (2.6), derived for the specific 2D Euler system. Note also that for $\mathcal{L} = \nabla^2$ (and identifying $\psi_1^{(0)}$ with $\tilde{\psi}$) equations (2.24), (2.27b) are exactly consistent with (2.11) and (2.10) in the previous section.

Following PL76, it is useful to show that the two species Gibbs entropy (1.35) can also yield the inverse temperature definition (1.30) i.e. $dS/dE = \beta$, thus demonstrating equivalence between the Gibbs and Boltzmann definitions of entropy. Differentiating the Gibbs entropy (1.35) with respect to E gives

$$\frac{dS}{dE} = -\int_{\mathcal{D}}\left[\frac{dp_+(\boldsymbol{x})}{dE}\left\{1+\log\frac{p_+(\boldsymbol{x})}{\rho_0}\right\} + \frac{dp_-(\boldsymbol{x})}{\partial E}\left\{1+\log\frac{p_-(\boldsymbol{x})}{\rho_0}\right\}\right]d\boldsymbol{x}$$

$$= -\int_{\mathcal{D}}\left[\frac{dp_+(\boldsymbol{x})}{dE}\log\frac{p_+(\boldsymbol{x})}{\rho_0} + \frac{dp_-(\boldsymbol{x})}{\partial E}\log\frac{p_-(\boldsymbol{x})}{\rho_0}\right]d\boldsymbol{x}, \tag{2.30}$$

and differentiating the energy (2.27a) with respect to E gives

$$1 = -\int_{\mathcal{D}^2} G(\boldsymbol{x},\boldsymbol{x}')\left(\frac{dp_+(\boldsymbol{x})}{\partial E} - \frac{dp_-(\boldsymbol{x})}{\partial E}\right)(p_+(\boldsymbol{x}') - p_-(\boldsymbol{x}'))\,d\boldsymbol{x}\,d\boldsymbol{x}'. \tag{2.31}$$

Note that

$$\int_{\mathcal{D}} p_{\pm}(\boldsymbol{x})\, d\boldsymbol{x} = 1 \Rightarrow \int_{\mathcal{D}} \frac{dp_{\pm}(\boldsymbol{x})}{dE}\, d\boldsymbol{x} = 0.$$

Combining (2.30)-(2.31) and making use of (2.28) gives

$$\frac{dS}{dE} = \beta,$$

i.e. the definition of inverse temperature, first introduced in section 1.3.2 using the Boltzmann entropy. This result linking the inverse temperature with the two definitions of entropy allows both definitions to be used interchangeably as appropriate.

2.3 Numerical methods for the elliptic-sinh equation

2.3.1 Previous solution methods

With the SPE/ESE derived in the previous section, the next step is its numerical solution. Two algorithms for solving the system defined by (2.22), (2.24), (2.27b) (or specifically for the 2D Euler case the system defined by (2.11), (2.12), (2.10)) are now presented. The generalised PL76 ESE is defined by[2]

$$\mathcal{L}\psi = C\sinh(\beta\psi), \quad E = -\frac{1}{2}\int_{\mathcal{D}} \psi\mathcal{L}\psi\, d\boldsymbol{x}, \quad C = \left(\int_{\mathcal{D}} e^{\beta\psi}\, d\boldsymbol{x} \cdot \int_{\mathcal{D}} e^{-\beta\psi}\, d\boldsymbol{x}\right)^{-1/2},$$

which, using the substitutions $\phi = \beta\psi$ and $b = C\beta$, can be rewritten as

$$\mathcal{L}\phi = b\sinh(\phi), \quad E = -\frac{1}{2\beta^2}\int_{\mathcal{D}} \phi\mathcal{L}\phi\, d\boldsymbol{x}, \quad C = \left(\int_{\mathcal{D}} e^{\phi}\, d\boldsymbol{x} \cdot \int_{\mathcal{D}} e^{-\phi}\, d\boldsymbol{x}\right)^{-1/2}. \tag{2.32}$$

The system most amenable to numerical solution is (2.32), though to calculate physically relevant quantities we must revert back to ψ, E and β using the substitutions

[2]For clarity, we have substituted ψ for $\psi_1^{(0)}$.

described above.

McDonald [82] discovered that finding nontrivial solutions of the SPE by standard techniques such as fixed point iteration using an inverted Laplacian operator was not successful[3]. Instead, McDonald developed a new algorithm (with the results analysed in [11]) which specifically excludes the trivial solution $\psi = 0$. The method (generalised for $\mathcal{L}$ below) uses a special iteration loop that updates a 'trial solution' until a specified precision is reached.

The first step in the McDonald iteration algorithm is to define the residual function

$$R = \frac{\mathcal{L}w + b\sinh w}{\langle w, w\rangle}, \tag{2.33}$$

for a trial solution $w(\boldsymbol{x})$, where $\langle B_1, B_2\rangle$ is the inner product[4] of the functions B_1 and B_2

$$\langle B_1(\boldsymbol{x}), B_2(\boldsymbol{x})\rangle = \int_{\mathcal{D}} B_1(\boldsymbol{x})B_2(\boldsymbol{x})\, d\boldsymbol{x}.$$

The residual function (2.33) tends to zero everywhere as w approaches a non-trivial solution ϕ, but tends to infinity as w approaches a trivial solution.

The linear PDE

$$\mathcal{L}v + bv\cosh w = \langle w, w\rangle R, \quad v = 0 \text{ on the boundary} \tag{2.34}$$

is solved, and the trial solution is iteratively corrected by

$$w \to w + \frac{v\langle w, w\rangle}{2\langle v, w\rangle - \langle w, w\rangle}, \tag{2.35}$$

until a sufficiently accurate solution is found. To determine the accuracy of the solution, first the grid cells of the computational domain where the solution is being

[3] A relaxation method has recently been used successfully in [111].

[4] Note the use of angled brackets with two arguments in this section represents the inner product, while angled brackets with a single argument used in a microcanonical ensemble context (e.g. in section 1.3.5) represent ensemble averages. Hence there should be no confusion.

constructed are indexed i and j. Then the rms error norm is computed by

$$\varepsilon_r = \left(\sum_{i,j} g_1^2 \Big/ \sum_{i,j} g_2^2 \right)^{1/2},$$

where

$$g_1(i,j) = \mathcal{L}\psi(i,j) + b \sinh \psi(i,j) \tag{2.36a}$$

$$g_2(i,j) = |\mathcal{L}\psi(i,j)| + |b \sinh \psi(i,j)|. \tag{2.36b}$$

The solver described above is amenable to conformal mapping by simply scaling the elliptic operators in the manner described in appendix A. Namely, for a conformal map $z = f$, (2.33) becomes

$$R = \frac{\mathcal{L}w/|f'|^2 + b \sinh w}{\langle w, w \rangle},$$

and (2.34) becomes

$$\mathcal{L}v/|f'|^2 + bv \cosh w = \langle w, w \rangle R,$$

along with the elliptic operators in (2.36) being scaled in the same way.

The McDonald iteration method described above is straightforward to implement and has recent applications such as [124]. However, modifying the solver, particularly (2.34), in order to find solutions with a non-zero boundary condition is not straightforward. As such, a new, more flexible scheme is introduced in section 2.3.2 and implemented in section 2.4.

2.3.2 The general nonlinear solver

A new, more general method based on a Galerkin-type expansion will now be introduced to solve for ϕ in the ESE (2.32). Since the linear approximation of the ESE is given by the vorticity modes (2.26), it is natural to use the vorticity modes themselves as the basis in the construction of the solution ϕ. Specifically the vorticity mode eigenvalue problem (2.26) is related to the linearised version of (2.32)

by identifying b with $\rho_0\beta_k$ and ϕ with Φ_k. The solver, which is described next, makes use of the Chebyshev spectral methods of Trefethen [115] (see appendix A.4).

A solution $w \approx \phi$ to (2.32) is sought on a specific branch in (E, β) space denoted by $*$ i.e. the branch originating at $E = 0$ with $\beta = \beta_*$ and Φ_*. Recall from section 2.2.1 that there are infinitely many solution branches, each originating from a DIT β_j. Truncating to use a total of P vorticity modes, the solution w is approximated by

$$w = A\Phi_* + \sum_{k\neq *}^{P} a_k \Phi_k, \tag{2.37}$$

where $A = A(b)$ is the pre-specified weight of the 'dominant' mode and $\{a_k\}$ are the $P-1$ as yet undetermined weights of the remaining modes. Note that the value of b in (2.32) is also undetermined, meaning there is a total of P unknowns. To have an exactly determined system to solve, P constraints are constructed by exploiting orthogonality

$$\int_{\mathcal{D}} \left(\mathcal{L}w - b\sinh(w)\right)\Phi_q \, d\boldsymbol{x} = 0, \quad q = 1, \ldots, P. \tag{2.38}$$

Substituting (2.37) into (2.38) and using (2.26) gives the following system of P integrals of nonlinear algebraic equations

$$\int_{\mathcal{D}} \left[\rho_0 \left(A\beta_*\Phi_* + \sum_{k\neq *}^{P} a_k\beta_k\Phi_k\right) - b\sinh\left(A\Phi_* + \sum_{k\neq *}^{P} a_k\Phi_k\right)\right]\Phi_q \, d\boldsymbol{x} = 0 \quad q = 1, \ldots, P, \tag{2.39}$$

with P unknowns

$$\{\underbrace{a_1, a_2, \ldots, a_{*-1}, a_{*+1}, \ldots, a_P}_{P-1}, b\}.$$

The system (2.39) can then be solved using standard nonlinear root finding algorithms (e.g. MATLAB's *fsolve* function), thus determining the numerical solution (2.37).

The corresponding energy can be calculated using the Galerkin expansion and

the substitutions $\phi = \beta\psi$ and $b = C\beta$ as

$$E = -\frac{1}{2\beta^2}\beta_* A^2 - \frac{1}{2\beta^2}\sum_{k\neq *}^{P} a_k^2 \beta_k,$$

and can be used as an internal consistency check.

A solution branch is started at $\beta = \beta_*$ using a small dominant weight A (≈ 0.1) and remaining weights $\{a_k\} = 0$. Moving along the branch towards higher energies, A is increased and the previous $\{a_k\}$ and β are used as initial guesses. It is possible that the solution can 'jump' from one branch to another, which would be indicated by one of more of the coefficients a_k being greater than the dominant coefficient A. As such this method seems somewhat less constrained to follow a certain solution branch than the McDonald method (though this is still the most likely result).

The performance of the new method for the 2D Euler system is considered in terms of the residual (2.33). The maximum residual, $\max\{R(w)\}$, for three sizes of Galerkin expansion ($P = 400$, 800 & 1600) is computed along the first and second solution branches (i.e originating at $(E, \beta) = (0, \beta_1)$ and $(E, \beta) = (0, \beta_2)$) of the SPE in a heart-shaped domain defined by $(c, q) = (0.5, 0.55)$ (see section 2.4.3). A grid consisting of 50 radial and 100 azimuthal points is used in each case. The branch runs from $E \approx 0$ (where the solution is approximately linear i.e. very close to the dominant vorticity mode Ψ_*) to $E = 0.02$ (where the equation in strongly nonlinear). The results are shown in fig. 2.1, with solution contours from the $P = 800$ branch at $E = 0$ and $E = 0.01$ shown on the right hand side. The method performs well for 2.1(a) the zero boundary condition (TBH09's type I solution) and 2.1(b) the non-zero boundary condition (TBH09's type II solution). Similar behaviour is observed in both panels: at very low energy the method is effectively projecting exactly onto the mode Ψ_* and machine precision can be attained irrespective of the truncation number P. Moving along the branch towards higher energies the solution is projected onto more modes and the value of $\max\{R(w)\}$ grows approximately quadratically for each P. Unsurprisingly, the larger P expansions perform better. Comparing the solution contours at $E = 0$ and $E = 0.01$ in (a) and (b), intensification of the vorticity into tighter clusters is evident.

A further test of the method will demonstrate the grid size independence of the

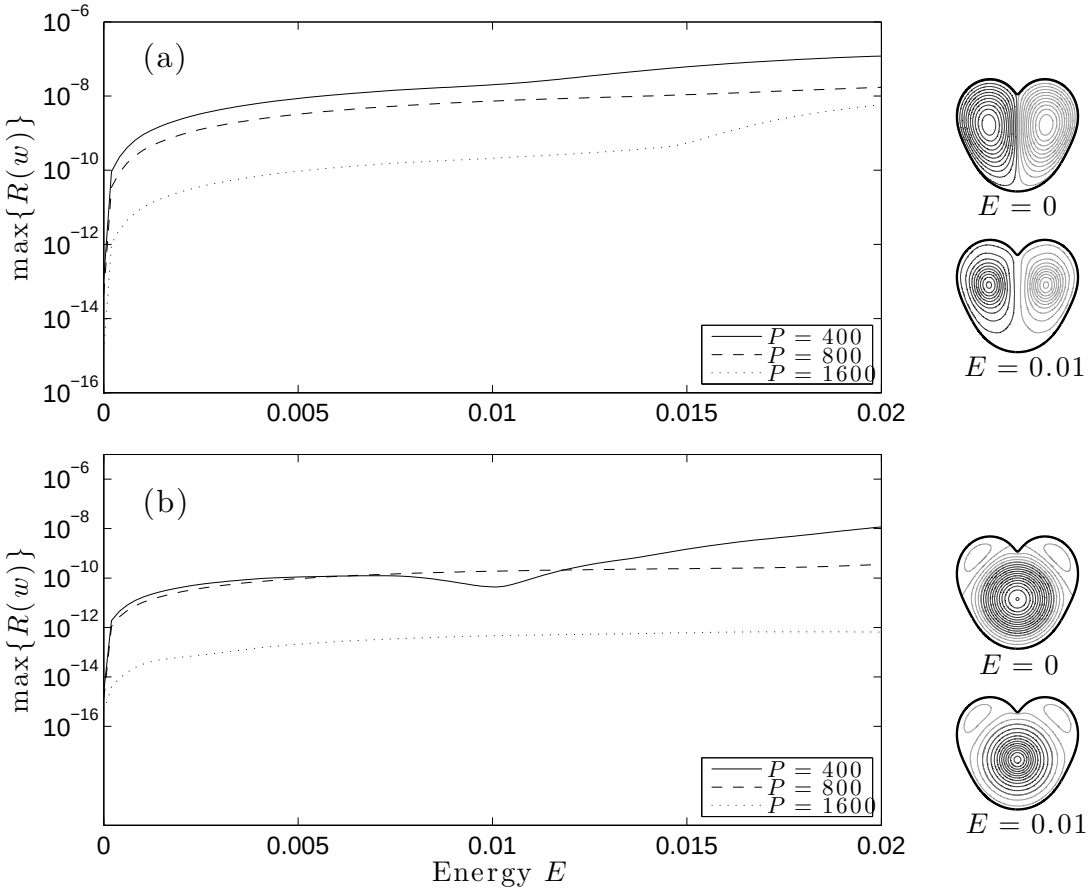

Figure 2.1: (a) Maximum residual of the first solution branch (zero boundary condition) of the sinh-Poisson equation in the heart-shaped domain defined by $(c, q) = (0.5, 0.55)$ for $E \in [0, 0.02]$, as computed by the Galerkin expansion method. Three sizes of Galerkin expansion have been used: $P = 400$ (solid), $P = 800$ (dashed) and $P = 1600$ (dotted). In each case $\mathcal{M} = 100$ azimuthal points and $\mathcal{N} = 50$ radial points. Solution contours from the $P = 800$ branch, at $E = 0$ and $E = 0.01$ are shown to the right. (b) As for (a) for the second solution branch (non-zero boundary condition).

solutions. To do this the energy is calculated for an increasing number of grid points while keeping the weight of the dominant mode A and the number of terms in the Galerkin expansion P fixed, so that the 'same' solution is found each time. As discussed in appendix A.4, using more azimuthal points $\mathcal{M}$ than radial points $\mathcal{N}$ offers greatest 'coverage' of complicated domains. Consequently the ratio of $\mathcal{M}$ to $\mathcal{N}$ will again remain fixed at 2:1, while the total number of points is increased. Figure 2.2 shows the relative error in the energy, scaled by the energy computed from a grid of $\mathcal{M} \times \mathcal{N} = 50 \times 100$, of the first solution branch sinh-Poisson solution in a heart-shaped domain with $(c, q) = (0.5, 0.55)$. Panel (a) compares the convergence of the energy error at three different energy values, all computed using $P = 400$ modes in the Galerkin expansion. Panel (b) shows the same as (a) using $P = 800$. From panel (a) it can be seen that by $\mathcal{N} \approx 35$ the energy error has plateaued and the solution is independent of the grid size. Comparing panel (a) to panel (b) it can be seen that using more than 400 Galerkin modes does not noticeably improve convergence of this particular error, either in terms of rate of convergence or final precision.

With the nonlinear solver presented in this section, numerical solutions of the ESE with the corrected boundary condition (i.e. zero *and* non-zero) can be obtained. In the next section 2D Euler dynamics are considered and the SPE equation solved in a new left-right symmetric domain. The predicted equilibrium streamfunction from the solutions of the SPE will be verified using direct numerical simulations. The low energy asymptotic theory from appendix B.2 is also verified.

2.4 Equilibrium mean flow in a left-right symmetric domain

2.4.1 'Most-probable' dynamics

Recall from section 1.4.1 that, for a general N vortex system at fixed energy, the 'most probable' equilibrium state corresponds to the maximum entropy state[5]. By definition a system not in equilibrium will always move towards a higher entropy

[5]Note that lower entropy solutions with a maximum local entropy may still be relevant to the dynamics as meta-stable states.

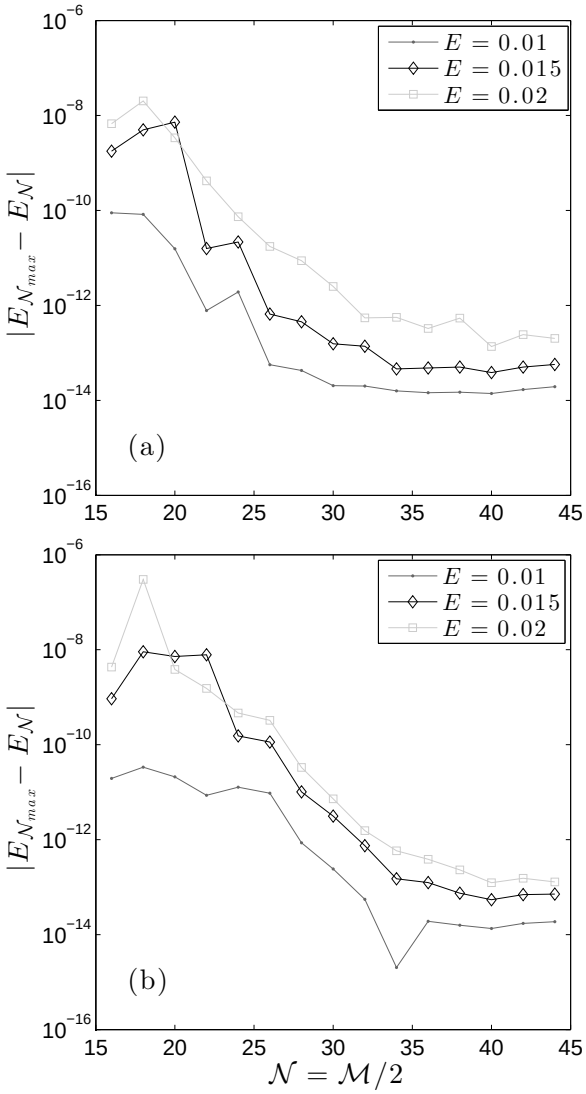

Figure 2.2: (a) Convergence of the energy (relative to energy computed with the highest resolution grid of $\mathcal{M} \times \mathcal{N} = 50 \times 100$) with the number of grid points, for the first solution branch of the sinh-Poisson in 'heart'-shaped domain (see section 2.4.3) at $E = 0.01$ (solid), $E = 0.015$ (dashed), $E = 0.02$ (dotted), using $P = 400$ Galerkin modes. (b) As for (a) using $P = 800$ Galerkin modes.

state. From section 2.2.2 the entropy S of the point vortex system is given by

$$S = 2\beta E - \rho_0 \log \frac{C}{\rho_0},$$

where E is the energy given by the Hamiltonian (1.2), β is the inverse thermodynamic temperature defined by (1.30), ρ_0 is the reciprocal of the domain area and C is the constant defined in terms of the streamfunciton ψ by

$$C = \left(\int_{\mathcal{D}} e^{\beta\psi} \, d\boldsymbol{x} \cdot \int_{\mathcal{D}} e^{-\beta\psi} \, d\boldsymbol{x} \right)^{-1/2}.$$

Recall also that in (E, β) space, the i^{th} solution branch of the sinh-Poisson equation (SPE) emerges at $E = 0$ and $\beta = \beta_i$, where $\{\beta_i\}$ are the domain inverse temperatures (DITs). Solution branches may be categorised by the number of extrema of the mean streamfunction and their relative positions within the domain. The streamfunctions corresponding to different solution branches tend to have significantly different structures from each other; see [11].

For an investigation into the maximum entropy solutions it is instructive to plot solution branches in (E, S) space, where the maximum entropy solution at a given energy will be immediately apparent. At $E = 0$ all branches have the same entropy and no global equilibrium solution exists. As the energy is increased, the maximum entropy solution is usually characterised by the branch in which the streamfunction has either one or two nodes i.e. a monopole (a cluster of vortices of one sign surrounded by vortices of the other sign) or a dipole (two well-separated clusters, each having opposite sign). The other families of solutions (i.e. branches) that are characterised by a more oscillatory streamfunction and a larger number of maxima/minima generally have lower entropies.

The question is then, at a given nonzero energy to which solution branch does the maximum entropy solution belong? In PL76 the following claim is made for a square domain

> "*It appears that the values of the reciprocal temperature* λ [β in the notation used here] *and of the entropy* $\tilde{S}$ [S here]*, corresponding to the solutions having the same value of the energy, are always in the same order among the families of solutions. In other words, the solutions corresponding to the largest value of the entropy always belongs to the family*

> *of solutions which is characterized by a single maximum or minimum of the mean streamfunction at the center of the square domain*".

This can be interpreted as stating that only the 'first' branch (i.e. the one originating from the first DIT, β_1) with a single maximum/minimum in its streamfunction has highest entropy. The implication is that the second (or higher) branch does not cross the first branch – if this did occur the maximum entropy solution would change structure and the "order among families of solutions" would be different at different energies.

PL76 considered two domains: the square and the circle. In the case of the circle the SPE (2.2.1) must be slightly modified to include the role of angular momentum. The resultant (non-degenerate) DITs[6] for the circle are well separated, and the structure of the streamfunction is drastically different across different solution branches. Consequently, the solution branches have significantly different entropies and when plotted in (E, S) space the maximum entropy branch is very apparent for all energies greater than zero. On the other hand, in the case of the square, angular momentum is not conserved and (2.2.1) is valid. The first DIT for the square, clearly distinct from lower branches, corresponds to a monopole. The next two DITs are very close, with branch 2 being characterised by a left-right (or equivalently up-down) dipolar streamfunction structure and branch 3 by a diagonal dipole structure (see their fig. 5). Other branches have a significantly more oscillatory structure. The first branch always appears to be the maximum entropy solution.

The focus of this chapter is on the (unmodified) SPE (2.2.1) and consequently the circle cannot be considered. Instead, non-rotationally symmetric domains[7] are chosen in section 2.4.3 specifically such that the first few DITs are in close proximity, and so the branches have comparable entropies, similar to the situation in the square, as described above. These new domains belong to a 1-parameter family for which, crucially, the parameter can be tuned to make the branches cross in (E, S) space[8].

[6] In the circle, DITs can be calculated analytically in terms of zeros of Bessel functions.

[7] Note that though elliptical domains seem like an obvious choice for this, there is no explicit conformal map from the interior of a circle to the interior of an ellipse; the Joukowsky map is to the exterior of an ellipse.

[8] PL76's square/rectangle could have been tuned in a similar manner (and in fact was in [111]), but verification by DNS of point vortices is more difficult in such a domain (compared to those conformal to the circle, as will be considered in section 2.4.3) as an infinite number of images are required. See footnote 1 of section 1.2.1.

A crossing means that for a fixed domain, the maximum entropy solution will be different at different energies. This type of transition will be classified in the next section as a particular type of phase transition in the statistical mechanics framework.

It is important to note that the crossing of solution branches of the SPE was considered in TBH09, where the SPE was considered as a model for the phenomenon of spin-up in 2D Navier-Stokes turbulence (the spontaneous acquisition of angular momentum in a bounded flow). As discussed in section 2.2.1, TBH09 observed that solutions of the SPE with both zero and nonzero boundary conditions are physically relevant, and they use the angular momentum as a diagnostic to distingish between the two solutions (which have drastically different structures) in a rectangular domain. They find that for a rectangle of aspect ratio 1.2, the first two solution branches of the SPE cross in (E, S) space. No DNS of the finite N vortex system was presented in TBH09, so one of the goals of sections 2.4.4 and 2.4.5 is to numerically verify this phenomena for the first time.

A final note is made about the work of Yin et al. [124]. They considered a doubly periodic domain and focused primarily on comparison between sinh-Poisson solutions and a Miller-Robert-Sommeria (MRS) sinh-Poisson analogue with various 'patch' sizes. They also noted that there can be solutions with different topologies but very similar values of entropy (though they did not pursue the idea that the maximum entropy solution can be different at different energies in the same model). Their predictions were verified with DNS of the 2D Navier-Stokes equations. They found the predicted equilibrium at a given energy had different topologies depending on whether the point or patch model was used. In fact different (finite) patch sizes were also found to give topologically different predictions for the equilibrium. For initial conditions with nearly flat vorticity patches (plus random noise), the late-time solutions of the Navier-Stokes DNS came close to the predicted maximum entropy solution of the MRS sinh-Poisson analogue for a certain patch size, but not the predicted maximum entropy solution of the point vortex sinh-Poisson equation. Relating the point vortex model (including statistical mechanics predictions such as the sinh-Poisson equation) to turbulent flows is an active area of research.

2.4.2 Phase transitions

In order to more formally characterise the potential crossings of the solution branches of the SPE in a statistical mechanics context, the concept of phase transitions is now reviewed. In general a phase transition is a change in the macroscopic behaviour (or 'phase') of the system as an external parameter is varied. An 'order parameter' can often be defined that represents the main qualitative difference between phases. In the context of entropy, a phase transition is often related to the competition between two (or more) different states for the maximum entropy state of the system.

From a general point of view [14, 57, 73] there are two main types of phase transitions:

1. **First order**

   Competing macrostates have significantly different properties and the transition between them is discontinuous. A classical example is the conversion of liquid water into water vapour where the external parameter is the temperature. In this example there is no exact order parameter.

2. **Second order/higher order**

   Competing macrostates are not drastically different and the transition between them is continuous. In fact the two competing macrostates can coalesce at a critical value. A classical example occurs in the 2D Ising model where the external parameter is again the temperature and the order parameter is the net magnetisation, with the transition occurring at temperatures below a critical 'Curie temperature'.

To further characterise the two types of phase transitions that are observed in the vortex system some new terminology is introduced. Firstly the term 'condensate' will be used to describe states (at high energies) dominated by a mean flow (i.e. macro vortices/large clusters in the point vortex model), usually in a monopolar or dipolar structure. From this two different types of phase transition can be described: The first type is classically termed 'Bose condensation' and is concerned with the onset of the formation of the condensate as energy is increased in the hydrodynamic limit.

This can be regarded as a first order, energy-induced phase transition and has been studied in 2D Navier-Stokes turbulence [29, 106, 116].

The second type of phase transition (clearly distinct from Bose condensation) shall be termed a 'condensate switch' and is characterised by drastic changes in the flow topology of a fully-realised condensate e.g. from a monopole to a dipole or an 'up-down' dipole to a 'left-right' dipole. The transition can be first or second order and can be induced by a change in the energy, geometry or net circulation (for a non-neutral system). Condensate switches have been studied in the context of the vortex system (both using point vortices and MRS theory), though under the more general term of phase transitions. Three examples will be reviewed next using the same terminology as used by the respective authors (i.e. 'phase transition' rather than 'condensate switch'), while sections 2.4.3-2.4.5 are devoted to new results.

The first theoretical study, by CS96 [27], aims to predict phase transitions in the 2D Euler equations. To do this they use MRS theory to calculate the 'mean field equilibrium state', which is analogous to the solutions of the SPE. Their problem is controlled by a set of eigenvalues, which as noted in section 2.2.1, transpire to be identical to the DITs used in this thesis. In a number of the cases investigated, the first mode is in competition with higher modes for the maximum entropy solution. At fixed energy a geometry-induced phase transition can occur in the flow topology from a monopolar vorticity distribution to a dipolar one when the aspect ratio of a rectangular domain increases above a critical value.

Complimentary to [27] is the work by Venaille & Bouchet [117, 118]. In this case the authors consider Fofonoff flows, which are steady states of the one layer unforced, non-dissipative barotropic quasi-geostrophic system. Using the MRS framework the authors uncover numerous phase transitions in this system. In a similar manner to [27], the authors formulate a problem controlled by a set of eigenvalues, from which the canonical ensemble can be calculated for a range of temperatures and hence plot classical phase diagrams between energy and circulation (acting as the order parameter). For certain geometries energy-induced phase transitions were found with two of particular note being a bifurcation from a first order phase transition to two second order phase transitions and the spontaneous and simultaneous appearance of two second order phase transitions. The effect of different Rossby radii was

also investigated in terms of area equivalence between ensembles. Interestingly, the statistical mechanics of Fofonoff flows was also studied in [90] using the methodology of [27].

The final example is from the point vortex model by Smith and Smith & O'Neil [107, 108], where a single-signed system bounded by a cylinder is considered in the hydrodynamic limit. At sufficiently high energies all the vortices congregate into a single cluster away from the centre of the domain and the rotational symmetry is spontaneously broken so that a net displacement of the system accounts for a significant fraction of the angular momentum. The transition between axisymmetric and displaced equilibria is continuous and hence resembles a second order phase transition. It is important to note that the cylinder is a special case in point vortex dynamics because of the additional invariant of angular momentum; see section 1.2.2. Further, this phase transition found in [107, 108] is unique to the circular domain – the phase transitions found in the next section are not unique to a particular domain and as such can be argued to be more fundamental.

From this section, it should be evident that the crossings of the solution branches of the SPE that result in a change in structure of maximum entropy state of the system can be formally regarded as an energy-induced condensation switch, complimentary to the other examples of phase transitions in the vortex system given above.

2.4.3 The 'heart'-shaped domain

A convenient domain in which to look for crossings of the solution branches of the SPE is the so-called 'heart'-shaped domain, introduced for the first time in this thesis. The domain is defined by the conformal map from the unit circle

$$z = F(Z) = \frac{a(c,q)Z}{(1-q^2Z)(1-icZ)}, \tag{2.40}$$

for real constants[9] a, q and c. The area of the domain defined by (2.40), which will remain fixed at π, is given by

$$\frac{1}{2\mathrm{i}}\oint_{|Z|=1}\bar{z}dz = \pi a^2\frac{1+c^4(2c^2-1)q^8+4c^2q^2(1-c^2)(q^4-1)+(1-c^2)^2q^4}{(q^4-1)^2(q^2c^2+1)^2(c^2-1)^2}.$$

Details of the modifications of the DIT eigenvalue problem/SPE in a conformal domain such as the heart are given appendix A.3.1. Modifications of the Hamiltonian (1.2) (that will be used in section 2.4.5) in such domains are given appendix A.2.1.

Note that the inverse of the map (2.40) is found by solving the following cubic in Z

$$(\mathrm{i}cq^2z)Z^3-(q^2z)Z^2-(\mathrm{i}cz-a)Z+(z)Z=0. \tag{2.41}$$

For a given z (2.41) is solved numerically using MATLAB's *roots* function, with the third root mapping the interior of the unit circle to the interior of the heart.

A convenient one-parameter family of domains may be defined by c for fixed q (and with $a=a(c,q)$). The first four vorticity modes for the domains defined by $(c,q)=(0.5,0.55)$, $(0.55,0.55)$ and $(0.65,0.55)$ are shown in fig. 2.3.

In all three domains shown in fig. 2.3 the first three DITs are clustered in the range from -44 to -54 and all the corresponding vorticity modes are characterised by a high entropy monopole or dipole structure. Altering the parameter c between 0.5 and 0.65 causes a reordering of the first three vorticity modes. For example, the 'left-right' dipole mode is Φ_1 for $c=0.5$, Φ_2 for $c=0.55$ and Φ_3 for $c=0.65$. Assuming no crossings, the maximum entropy solution will be along the branch originating from the first DIT in all three domains. Therefore, varying c from 0.5 to 0.55 causes a change in the structure of this first mode/branch from dipolar to monopolar. This change in structure can be regarded as a geometry-induced condensate switch similar to that mentioned in section 2.4.2 for an MRS system [27].

In all three domains the fourth DIT is well separated from the first three and corresponding fourth vorticity modes are all characterised by a quadrupole structure which has a lower entropy.

[9]Note that when $c=0$ the map (2.40) is identical to the Neumann oval map used in chapters 3 and 4, and when $q=c=0$ the map is simply to a circle of radius a.

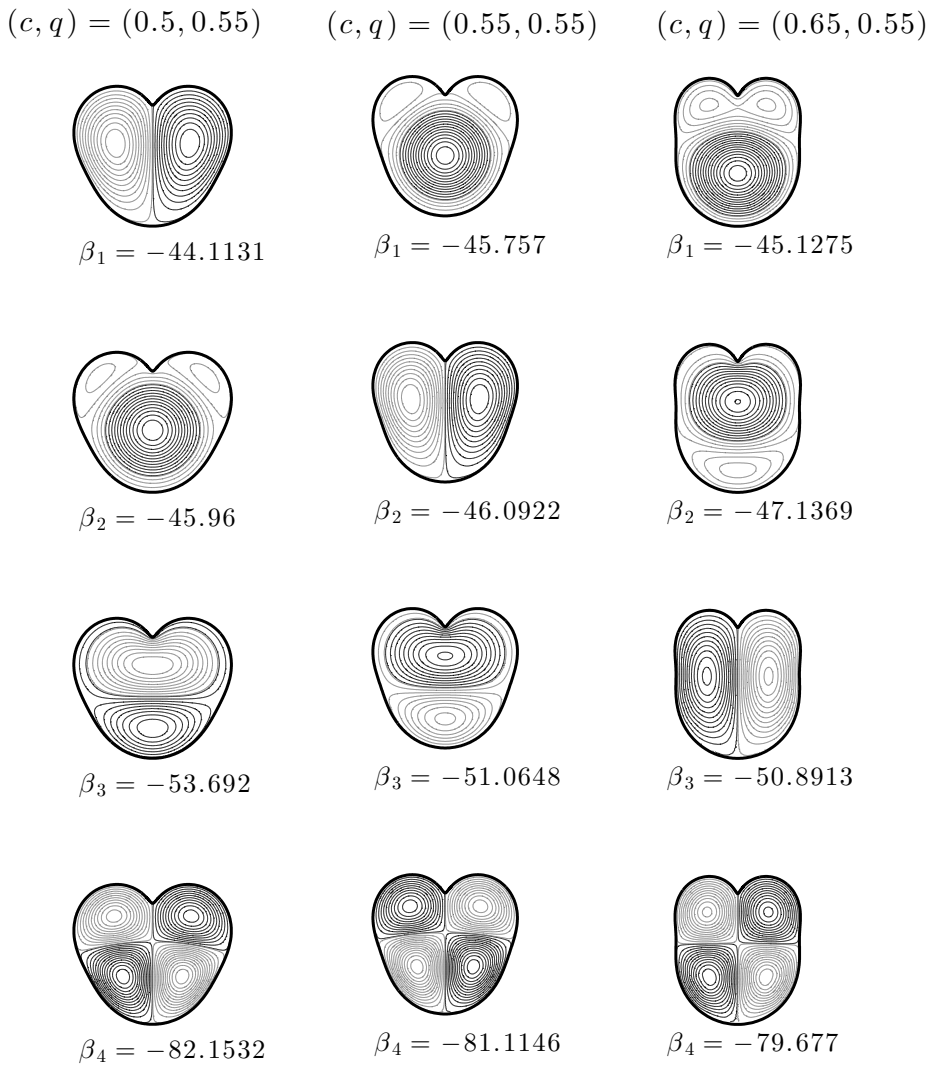

Figure 2.3: The first four vorticity modes for heart domains defined by $(c, q) = (0.5, 0.5)$ (left-hand column), $(c, q) = (0.5, 0.55)$ (centre column) and $(c, q) = (0.5, 0.65)$ (right-hand column).

Due to the close proximity of the first three DITs/similar structure of these vorticity modes, the heart domain is a good candidate for investigating potential crossings of the SPE solution branches in (E, S) space and hence an energy-induced condensate switch.

2.4.4 Solutions of the sinh-Poisson equation

To identify the specific heart domain we will use to investigate crossings of the SPE, first consider the domains defined by $(c, q) = (0.45, 0.55)$ and $(c, q) = (0.55, 0.55)$. The first two solution branches of the sinh-Poisson equation in these domains are shown in (E, β) space in figure 2.4, as computed using the nonlinear solver introduced in section 2.3.2, using $P = 800$ Galerkin modes and a grid of $\mathcal{N} \times \mathcal{M} = 50 \times 100$. Also shown in the figure are the corresponding vorticity modes that characterise each solution along the whole branch (i.e. the mode that was used as the dominant mode in the nonlinear solver in 2.3.2). Note that for $(c, q) = (0.45, 0.55)$ the first solution branch (i.e. the one originating from β_1) has a dipole structure while for $(c, q) = (0.55, 0.55)$ the first solution branch has a monopole structure. These solution branches are also plotted in (E, S) space in figure 2.5, following the approach of TBH09, [124] and others in assuming that the entire entropy of the system is in the maximum entropy solution. From figure 2.5, and for this range of energies, it is clear that the solution branches *do not* cross (E, S) space, and hence the first branch (i.e. the one originating from β_1) is always the maximum entropy solution.

From the above, we know that (over the range of energies shown) the maximum entropy solution branch for the $(c, q) = (0.45, 0.55)$ domain is always characterised by a dipole and for $(c, q) = (0.55, 0.55)$ the maximum entropy branch is always characterised by a monopole. Evidently, at some value $c \in (0.45, 0.55)$ the dipole and monopole solution branches must switch order and a crossing of the two branches is a possibility. To investigate this, the domain defined by $(c, q) = (0.51, 0.55)$ is considered. Note that a number of other suitable heart domains were found that were defined by similar values for (c, q), though the interesting behaviour occurred at energies that were not readily accessible to DNS of the vortex system (as will be

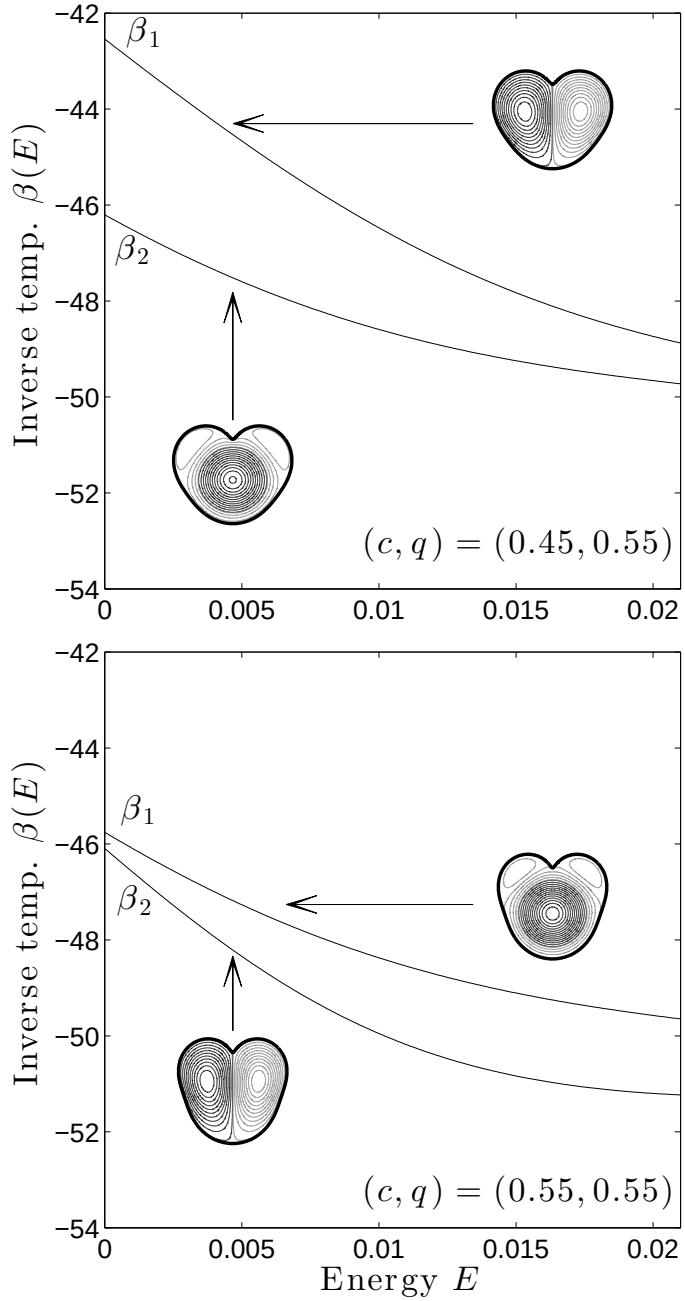

Figure 2.4: (Top) The first two solution branches, β_{1-2}, in (E, β) space of the sinh-Poisson equation for the $(c, q) = (0.45, 0.55)$ domain. The vorticity mode characterising each branch is indicated with an arrow. (Bottom) As for (a) for the $(c, q) = (0.55, 0.55)$ domain.

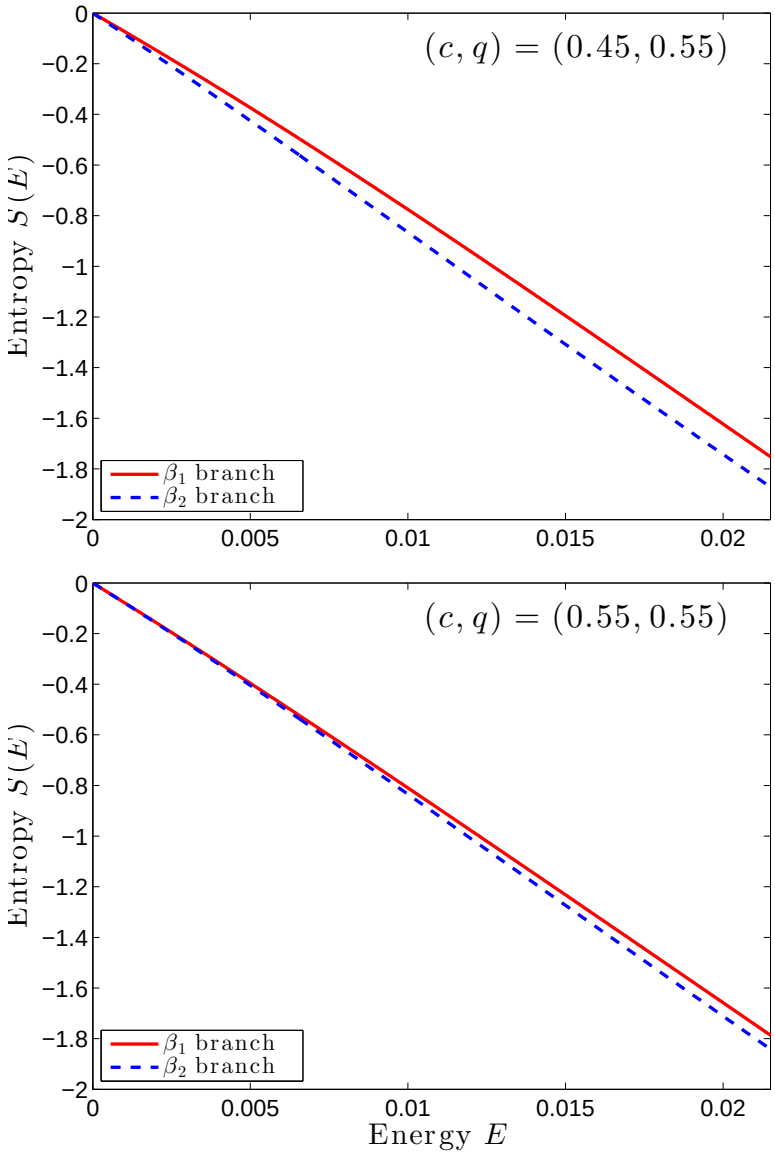

Figure 2.5: (Top) The first two solution branches in (E, S) space of the sinh-Poisson equation for the $(c, q) = (0.45, 0.55)$ heart domain. (Bottom) As top for the $(c, q) = (0.55, 0.55)$ heart domain.

performed later in section 2.4.5). There are doubtless other domains with drastically different geometries which could also be considered.

The first three solution branches (solid) of the sinh-Poisson equation in the heart domain defined by $(c, q) = (0.55, 0.51)$ are shown in (E, β) space in fig. 2.6, computed as above. For each solution branch the corresponding small E tangent approximations (dashed) derived in appendix B.2 are also shown and compare well to the numerical results. The values of the constants used to compute the approximation (B.9) were numerically determined (see appendix A) to be $D_1 = 2.296$, $D_2 = 2.529$ and $D_3 = 2.374$ (correct to 4 sig. fig.). Figure 2.7 shows the same solution branches in (E, S) space.

In contrast to figure 2.5, from figure 2.7(a-d) it is clear that the branches of the first and second vorticity mode *do* cross in (E, S) space, at $E_c \approx 0.0132$. Hence for $E < E_c$ the maximum entropy solution corresponds to the first vorticity mode, whereas for $E > E_c$ the maximum entropy solution corresponds to the second vorticity mode. In other words, in this domain an energy-induced condensate switch occurs, with $E = E_c$ being the 'double point' where the two competing maximum entropy states coexist.

It should also be stated that the entropy differences are very small throughout the energy range shown. In fact, the above analysis of merely comparing the entropies of two solutions to determine which is the maximum entropy solution lacks rigour: we could study the thermodynamic stability by computing $\frac{d^2S}{dE^2}$ and testing whether solutions are fully stable (global maximum entropy solutions), meta-stable (local maximum entropy solutions) or even unstable (saddle points).

For the purposes of this thesis, comparing entropies is deemed sufficient, though it would not be surprising if occasionally the second highest entropy solution is found for long time periods, as this could well be a meta-stable state. In fact, in [89] it was shown that the vortex system can even remain in unstable states for long periods, as the system does not spontaneously generate perturbations which would destabilise the state (after sufficiently long times the authors observed the system eventually relaxing to the stable state). Interestingly, CS96 state that secondary solutions branches of their SPE equivalent are are unstable in the linearised limit. Perhaps they become meta-stable (and even stable) for higher energies?

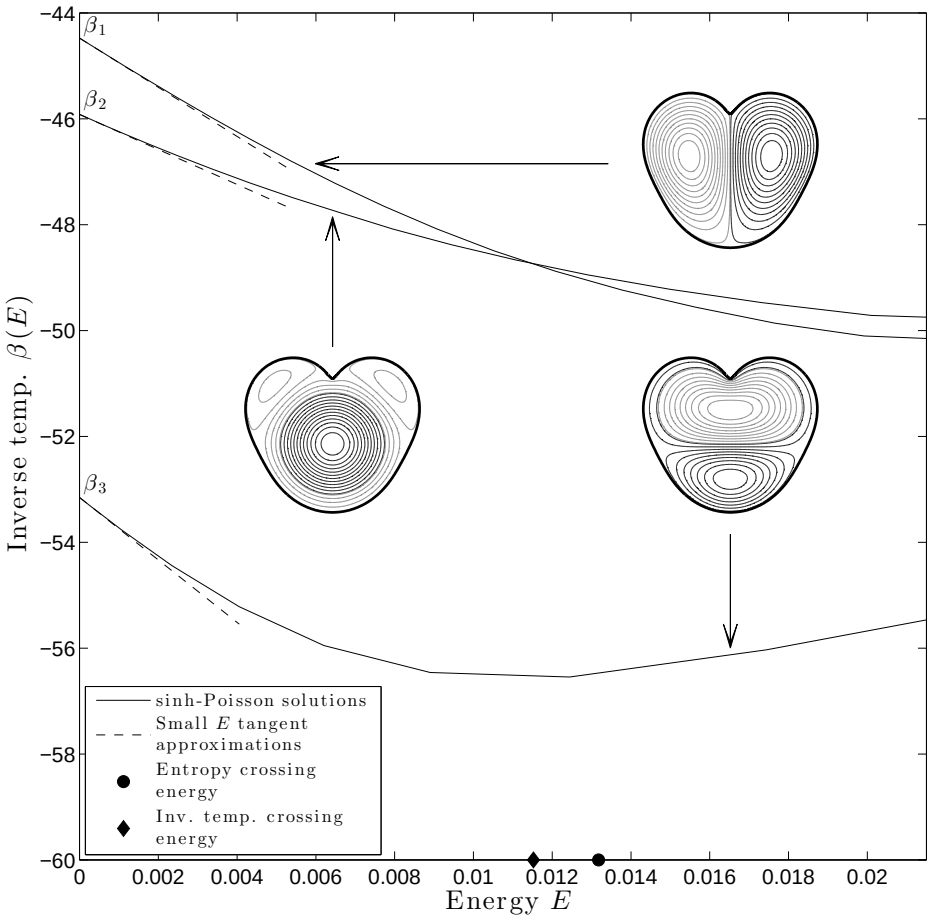

Figure 2.6: The first three solution branches, β_{1-3}, in (E, β) space of the sinh-Poisson equation (solid lines) for the $(c, q) = (0.51, 0.55)$ heart domain, along with small energy tangent approximations (dashed lines). The vorticity mode characterising each branch is indicated with an arrow. The energy at which the branches β_1 and β_2 cross is marked with a filled diamond. Also shown is the energy at which the entropy branches β_1 and β_2 of fig. 2.7 cross (filled circle).

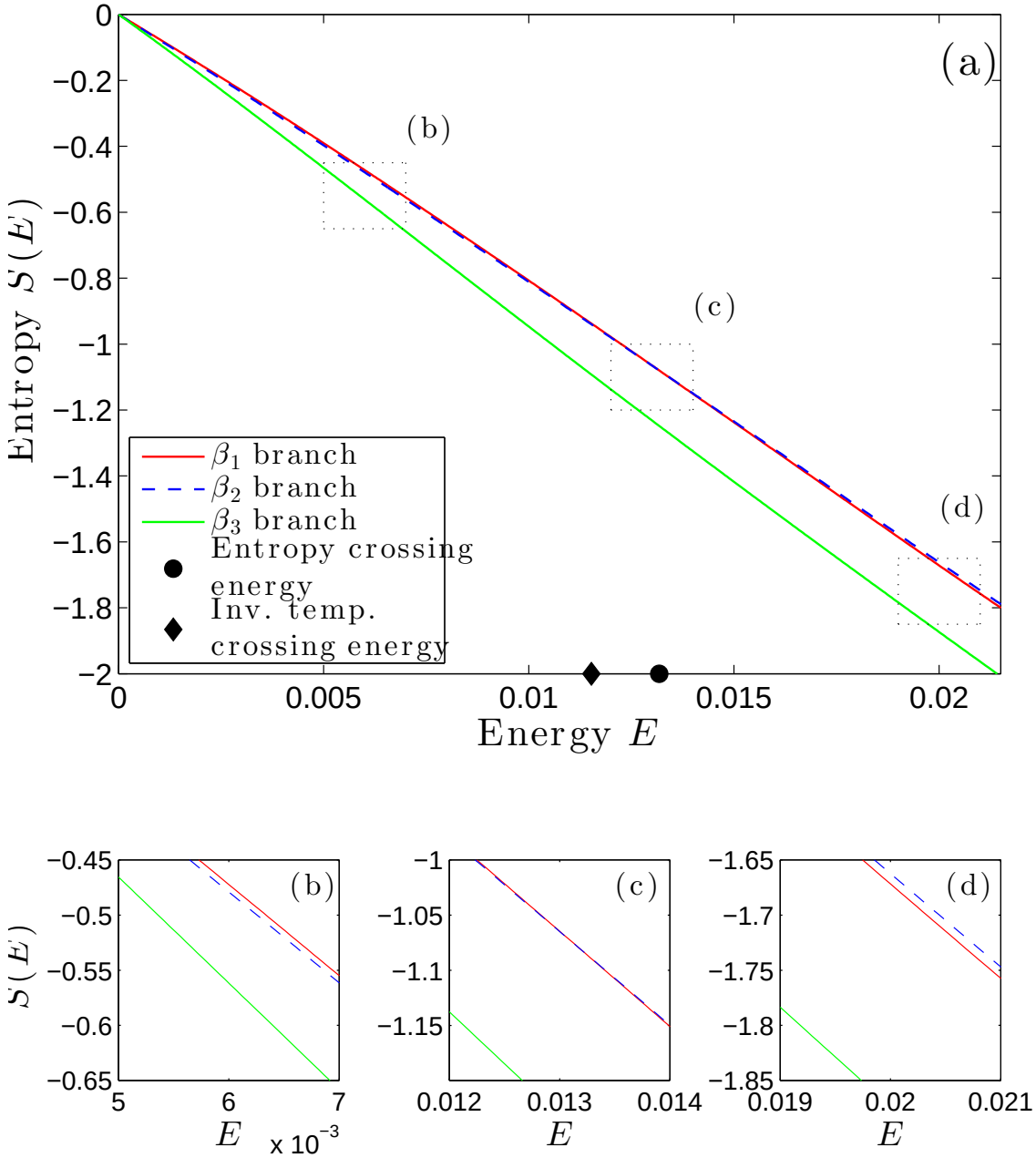

Figure 2.7: (a) The first three solution branches in (E, S) space of the sinh-Poisson equation for the $(c, q) = (0.51, 0.55)$ heart domain. The energy at which the branches β_1 and β_2 cross is marked with a filled circle. Also shown is the energy at which the inverse temperature branches of fig. 2.6 cross (filled diamond). (b)-(d) Magnified plots corresponding to the dotted boxes of (a).

It is also worth noting that the energy at which the branches cross in (E, β) space differs from the energy at which they cross in (E, S) space. This implies there is a vertical 'jump' in β at constant E from branch 1 to branch 2 in (E, β) space when the solutions cross in (E, S) space . This is unphysical and could be a property of the assumption that all the entropy of the system is in the maximum entropy solution to due to the existence of meta-stable states. The validity of this assumption is discussed in section 2.5.

The predictions for the equilibrium streamfunction based on the solutions of the SPE in this section will be tested against direct numerical simulations of the vortex system in the same domain in the next section.

2.4.5 Verification by direct numerical simulation

The statistical mechanics predictions based on the solutions of the SPE in the heart domain presented in section 2.4.4 may be tested against DNS of the finite N vortex system in the same domain. A similar verification was done by PL76 for the cylinder, using the $N = 40$ vortex system. For a high energy initial condition with zero angular momentum, PL76 observed that vortices rapidly cluster into a dipolar configuration which is the predicted maximum entropy SPE solution. For a high energy initial condition with nonzero angular momentum their results are slightly less clear, though the dipolar solution does still appear to emerge, and it is likely would be fully realised with a longer run (which the authors were unable to perform without the system becoming dissipative). In a more modern study [123] using $N \approx 7000$ vortices (also in the cylinder), the high energy initial condition again finds the dipolar solution, though surprisingly the SPE was not explicitly mentioned.

From the above, it is reasonable to conclude that the solutions of the SPE correspond well with DNS of the N vortex system. The cylinder is a particularly good system with which to compare DNS with SPE solutions since, as noted in section 2.4.1, for all energies high enough for the mean flow to dominate, the SPE maximum entropy solution is always the first branch/dipolar streamfunction. As detailed in the previous section, for the $(c, q) = (0.51, 0.55)$ heart domain the predicted maximum entropy SPE solution is different at different energies and so the goal of this section

is to test whether these solutions can still be found with DNS.

The details of the general image model used in the DNS are given in section 1.2.1 and of the modified version of the Hamiltonian (1.2) and Hamilton's equations (1.1) for a domain such as the heart are given in appendix A.2.1. From a given initial vortex configuration, prior to equilibrium there will be a 'turbulent spin-up' period where small clusters of like-signed vortices coalesce and no obvious maximum entropy solution is apparent. It is likely that the nonzero angular momentum results of PL76 mentioned at the start of this section were yet to reach the end of this spin-up period.

Using the heart domain defined by $(c, q) = (0.51, 0.55)$ (see figure 2.6), dynamical runs at five different energies are performed: $E = 0.006 \ll E_c$, $E = 0.0095 < E_c$, $E = 0.0132 = E_c$, $E = 0.0165 > E_c$ and $E = 0.02 \gg E_c$. The two extreme energy runs ($E = 0.006,\ 0.02$) are expected to correspond with high probability to a maximum entropy solution of the SPE characterised by mode 1 (dipole) and mode 2 (monopole) respectively. The situation for energies closer, and equal to E_c is likely to be harder to predict.

Accessing the initial conditions for the high energy runs mentioned above is not feasible using standard Monte Carlo uniform sampling i.e. choosing high energy configurations from a sample of randomly distributed vortex positions. The multicanonical Markov chain Monte Carlo (MCMCMC) sampling technique described in section 1.3.3 could be used, however it is possible that the initial configurations found using this method would strongly resemble a specific vorticity mode/SPE solution, and thus a dynamical run from such an initial condition could be biased to remain 'stuck' in that mode and not necessarily find the maximum entropy solution as expected (or take an impractically long time to do so).

Instead, initial conditions for the $N = 100$ system are generated as follows (see figure 2.8). First, ten cluster centres (filled diamonds) are generated inside $\mathcal{D}$ at random using the uniform distribution; see figure 1.1 in section 1.3.3. Around each cluster centre, ten like-signed vortices are randomly distributed within a radius r_c (dashed circles). The vortices in the first five clusters are all given positive circulation $\Gamma_i = 1/N$ (black plus symbols) and the vortices in the remaining five clusters negative circulation $\Gamma_i = -1/N$ (grey circles). The final energy of the configuration can then be approximately controlled by varying the cluster radius r_c.

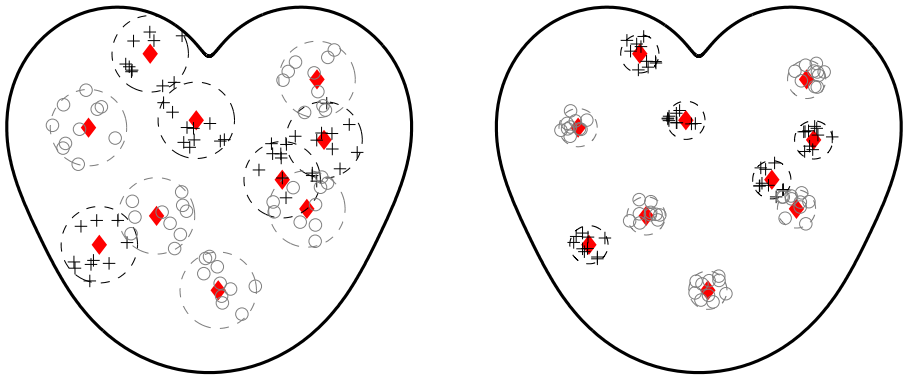

Figure 2.8: Illustration of the technique used to generate less biased, low and high energy initial conditions in the heart domain. Filled diamonds indicate uniformly distributed cluster centres and are the same in both panels. Around each cluster centre vortices are randomly distributed within a cluster radius r_c (dashed circles). The energy is controlled by varying r_c from low E on the left panel to high E on right panel. Black plus symbols represent positive vortices and grey circles negative vortices.

For the numerical experiments in this section ten different cluster centre distributions are generated and indexed with subscripts $I-X$. For each cluster centre distribution five initial conditions are found at $E = \{0.006, 0.0095, 0.0132, 0.0165, 0.02\}$ and indexed a-e respectively (a total of 50 initial conditions/runs). Hence, for example, a_I and b_I will have the have the same cluster centres and energies $E = 0.006$ and $E = 0.0095$ respectively.

It is possible that a given centroid distribution could be strongly biased towards a certain equilibrium solution, and so that equilibrium would be found for any energy $a - e$. The method described above helps to minimise this bias: consider the dynamical runs a_I and e_I i.e. same cluster centres and $E = 0.006$ & $E = 0.02$ respectively. Both these runs have qualitatively the *same* initial distribution (as same cluster centres), so if a_I found a *different* equilibrium to e_I it can only be due to the difference in energy – if there was a bias a_I and e_I would both find the same equilibrium.

The 50 initial conditions $\{a_{I-X}, b_{I-X}, c_{I-X}, d_{I-X}, e_{I-X}\}$ are integrated using the time stepping scheme described in section 1.2.3 for $t = 2000N$, $\Delta t = 0.1N$ and $\delta = 10^{-8}$. Energy was conserved to at least 6 sig. figs. over the course of each run.

At this point it is worthwhile to perform some analysis of the length of the spin-up period. Since the high energy runs start in very tight clusters (see right-hand panel of figure 2.8), the spin-up can be deemed to be over when the initial clusters have fully broken up and reformed into new, larger-scale clusters (lower energy clusters break up very rapidly). A useful diagnostic is $\overline{\mathcal{R}}$, the mean distance between the ten vortices that make up each individual cluster, as tracked for the length of the integration. The results for high energy run e_I are shown in figure 2.9. From the figure (and other runs not shown) it can be seen that by $t = 500N$, the value of $\overline{\mathcal{R}}$ for all ten clusters has increased to close to the scale of the domain implying the clusters have fully broken up. Hence averages will be taken after $t = 500N$.

One must be careful of simply taking averages from the end of spin-up to the end of the run as one feature of this system is the possible reversal or 'flip' of vorticity in an equilibrium state; see chapter 5. Note that such an event was only observed in dipolar solutions. If this does occur, averages will be taken before the reversal and after the reversal with the sign of the vorticity changed, therefore giving an average that describes only the a single equilibrium state and not the oscillation event. In practice, the energies chosen for the DNS here were sufficiently high that after the spin-up period the system remained in the same state for the rest of the integration, and no reversal of vorticity occured. Note also that the sign of the vorticity was changed in runs a_{II}, a_V and e_{III} to give consistency with the other runs.

To compare the DNS with the equilibrium streamfunction of the SPE ψ, the streamfunction ψ_N of the N vortex system is required. This is computed using the complex notation of appendix A and the grid of appendix A.4 as follows. The N vortex positions in the unit circle $\mathcal{C}$ at time t are given by $Z_i(t) \in \mathbb{C}$, $i = 1, \ldots, N$ and a grid, $Z_{\mathcal{C}} \in \mathbb{C}$ (found by mapping their actual positions in the heart domain), is generated that encloses the whole circle – this is the same grid that was used in the SPE solutions in section 2.4.4 of $\mathcal{N} \times \mathcal{M} = 50 \times 100$. The time-dependent, finite N streamfunction is then given on $Z_{\mathcal{C}}$ by

$$\psi_N(Z_{\mathcal{C}}, t) = \sum_{i=1}^{N} \Gamma_i G(Z_i(t), Z_{\mathcal{C}}) \tag{2.42}$$

where $G(\cdot, \cdot)$ is (A.5) – the domain Green's function in the circle, which for the 2D

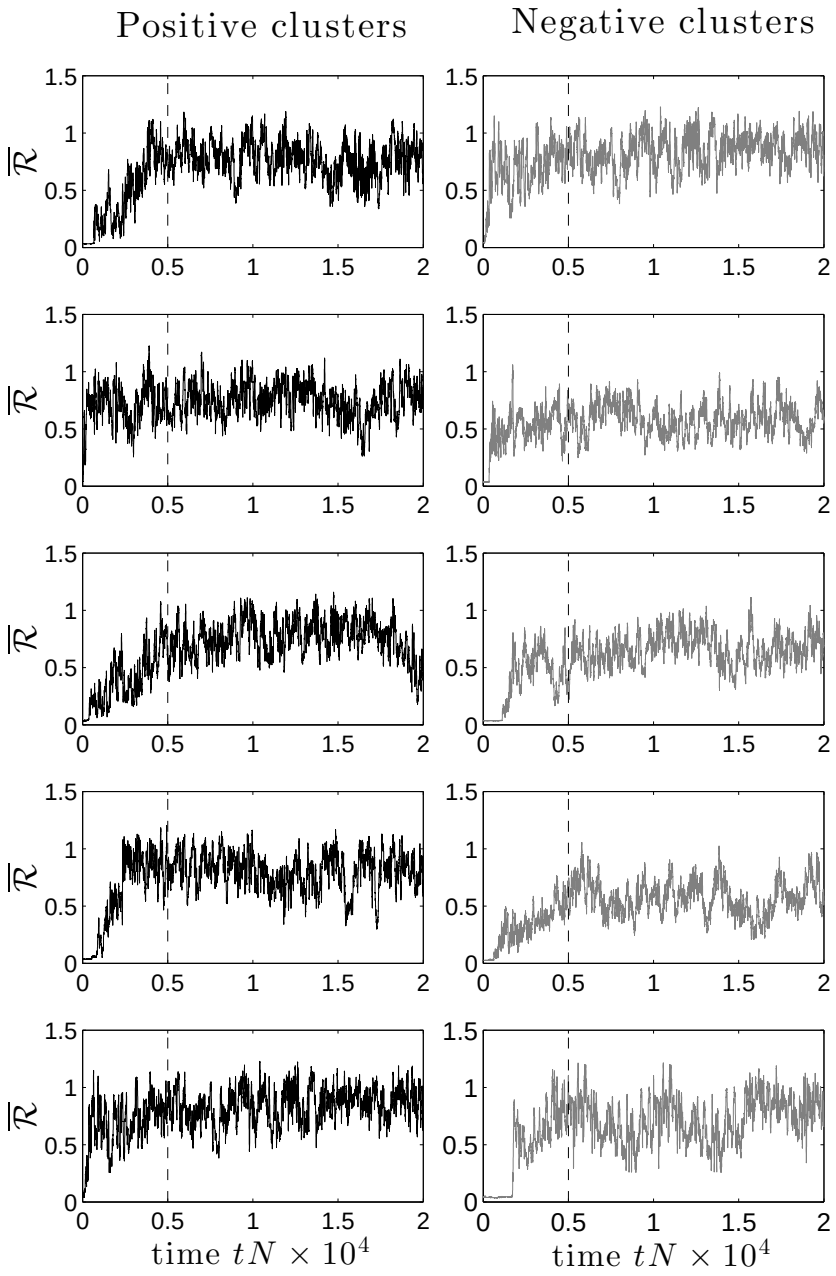

Figure 2.9: Time series of the mean distance $\overline{\mathcal{R}}$ between vortices that make up each of the initial clusters ($N = 10$) of positive vorticity (left-hand column) and negative vorticity (right-hand column) of run e_I ($E = 0.02$). The vertical dashed line at $t = 500N$ denotes the arbitrary end of the 'spin up' period when all the clusters are deemed to have broken up.

Euler system is invariant when conformally mapped. Equation (2.42) is then mapped back to the heart by (2.40) and time averages of ψ_N taken after the spin up period to compute the mean $\overline{\psi_N}$. Note that G is singular when $Z_i(t) = Z_{\mathcal{C}}$ (since G is defined by logarithms), but in reality the vortex positions Z_i will never exactly coincide with the grid points $Z_{\mathcal{C}}$, and so the singularities will be avoided.

With the details given above, we can now begin the analysis of the runs. In the first instance we consider the sets of runs at the two extreme energies where the predictions of the SPE are likely to be best. Figure 2.10 shows the results for the runs a_{I-V} i.e. at $E = 0.006 \ll E_c$ (contours intervals 1.06×10^{-5}) and figure 2.11 for runs e_{I-V} i.e. at $E = 0.02 \gg E_c$ (contour intervals 1.25×10^{-5}). On the left-hand column of both figures the initial vortex configurations are shown with the corresponding time-averaged streamfunction (2.42) shown in the centre column. On the right of both figures is shown the equilibrium streamfunction as predicted by the solution of the SPE at the appropriate energy i.e. $E = 0.006$ for fig. 2.10 and $E = 0.02$ for fig. 2.11. Snapshots of the vortex positions from runs a_I and e_I are shown in figure 2.12. Recall that corresponding run indices I-V in all figures have initial vortex configurations generated by the same cluster centre distributions.

Remarkably good agreement with the SPE maximum entropy predictions from fig 2.6 are observed in nine out of the ten dynamical runs: $E \ll E_c$ $a_{I-III,V}$ all find the dipolar solution and $E \gg E_c$ e_{I-V} all find the monopolar solution i.e. an energy-induced condensate switch has occurred between $E \ll E_c$ and $E \gg E_c$. For run a_{IV} the monopolar solution corresponding to β_2 has been found over this time interval. Based on the other runs this could be a temporary or 'meta-stable' state and eventually the dipolar state, predicted by maximum entropy, may be found. Due to the small difference in entropies between the β_1 branch and the β_2 branch (see 2.7), such an event should not be unexpected.

An important point to note from figure 2.12 is that at a given instant, the vortex positions for the 'monopole' solution do not actually look like a monopole as seen in figure 2.11 – instead the system is characterised by two large opposite-signed clusters, with one remaining approximately in the middle of the domain, while the other orbits around it. Only when a long-time average of the streamfunction is taken is the monopole structure apparent. This is not the case for the dipolar solution,

where at a given instant the vortex positions clearly resemble the dipolar structure.

Before proceeding with the analysis of the other runs with E closer to E_c, two simple diagnostics are defined to allow a more formal classification of a dynamical run (or part of one) as dipolar or monopolar. Due to the very clear structures from the low energy runs in figure 2.10 and the high energy runs in figure 2.11, these will be used as benchmarks. It should be noted that observations of the mean streamfuction were used extensively in validating these diagnostics.

The following two diagnostics will be used for the distinguishing between a dipolar and monopolar structure of the mean streamfunction ψ_N:

1. The first diagnostic is the x coordinate of the centre of vorticity and is defined by

$$X = \sum_{i=1}^{N} \Gamma_i x_i,$$

and is expected to have larger values for solutions with left-right symmetry, such as the dipole. Note that X is effectively a non-conserved linear impulse in the x direction, similar to that introduced in 1.2.2.

2. The second diagnostic is the angular momentum[10],

$$L = \frac{1}{2\pi} \sum_{i=1}^{N} \Gamma_i \left(x_i^2 + (y_i - \bar{y})^2 \right),$$

where $\bar{y}$ is the y coordinate of the centroid of the domain given by the integral

$$\bar{y} = \frac{1}{\pi} \int_{\mathcal{D}} y \, d\boldsymbol{x},$$

which is evaluated using the methods in appendix A.4. Note that by symmetry, the x coordinate of the centroid is 0. Values of L are expected to be larger for solutions with approximate rotational symmetry, such as the monopole.

The time series of X is shown for runs a_I ($E = 0.006$) and e_I ($E = 0.02$) in figure 2.13, and the absolute means for the runs a_{I-V} and e_{I-V} from figures 2.10-

[10]TBH09 effectively use angular momentum in the same way to distinguish between different types of solutions.

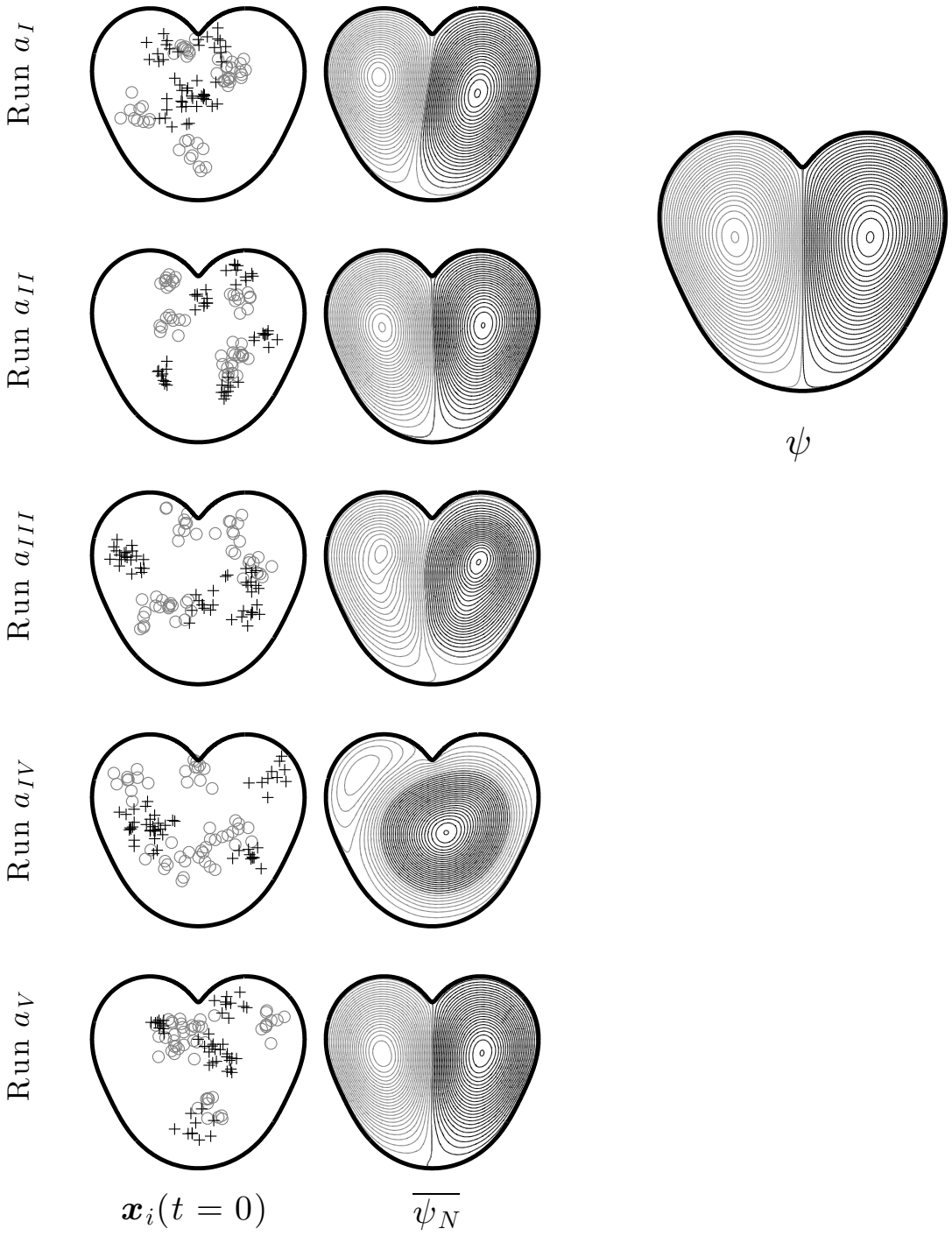

Figure 2.10: Initial $N = 100$ vortex configuration (left column) with corresponding time-averaged finite N streamfunction $\overline{\psi_N}$ (centre column), for five runs all at $E = 0.006$, in the heart domain defined by $(c, q) = (0.51, 0.55)$. The larger right-hand contour shows the maximum entropy equilibrium streamfunction ψ as predicted by the sinh-Poisson solution at $E = 0.006$. In all cases black indicates positive circulation and grey negative circulation.

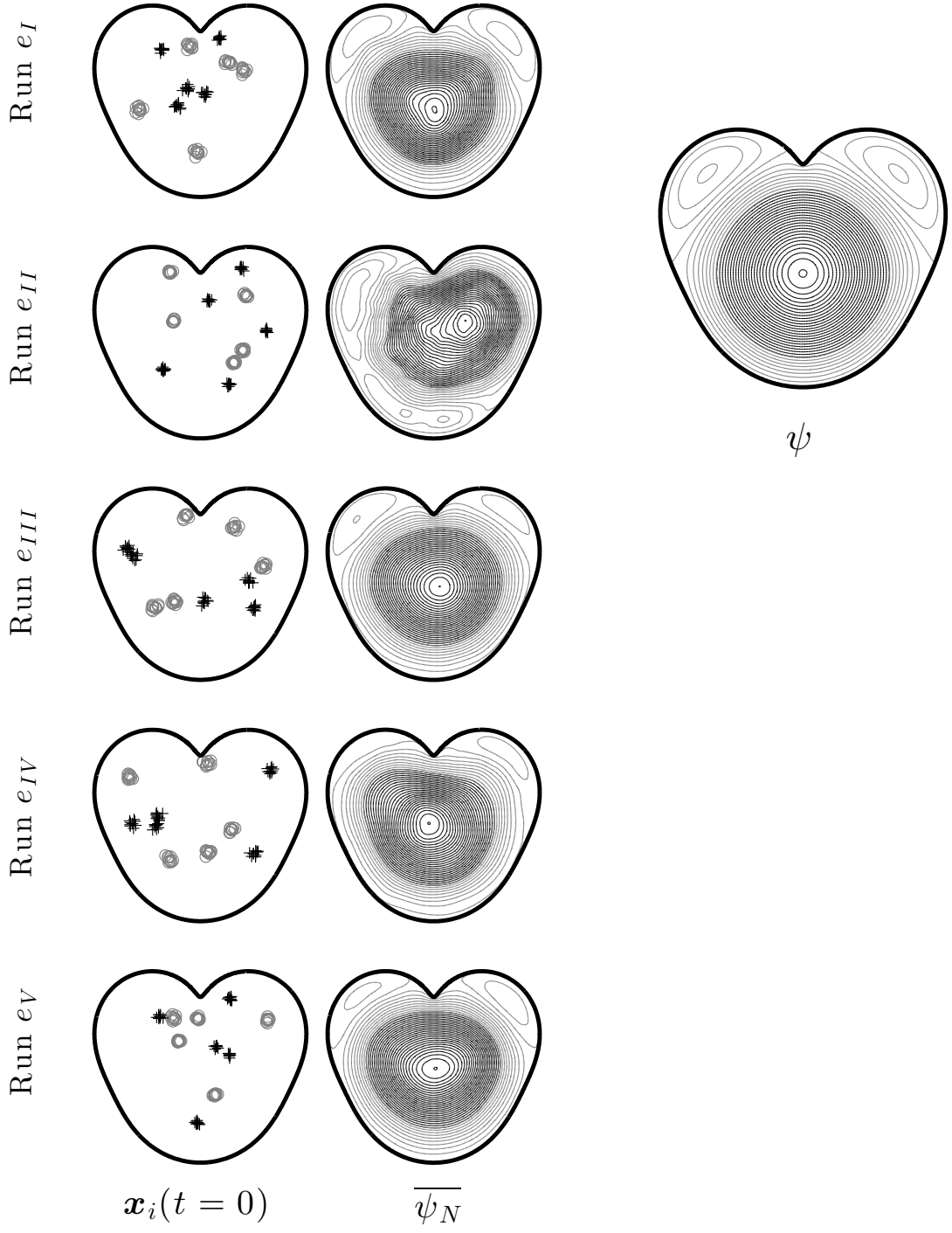

Figure 2.11: As for fig. 2.10, but for runs at $E = 0.02$. Note that runs $_{I-V}$ have the same initial cluster centres as the corresponding runs $_{I-V}$ in fig. 2.10, though the cluster radius is significantly smaller here to attain the higher energy.

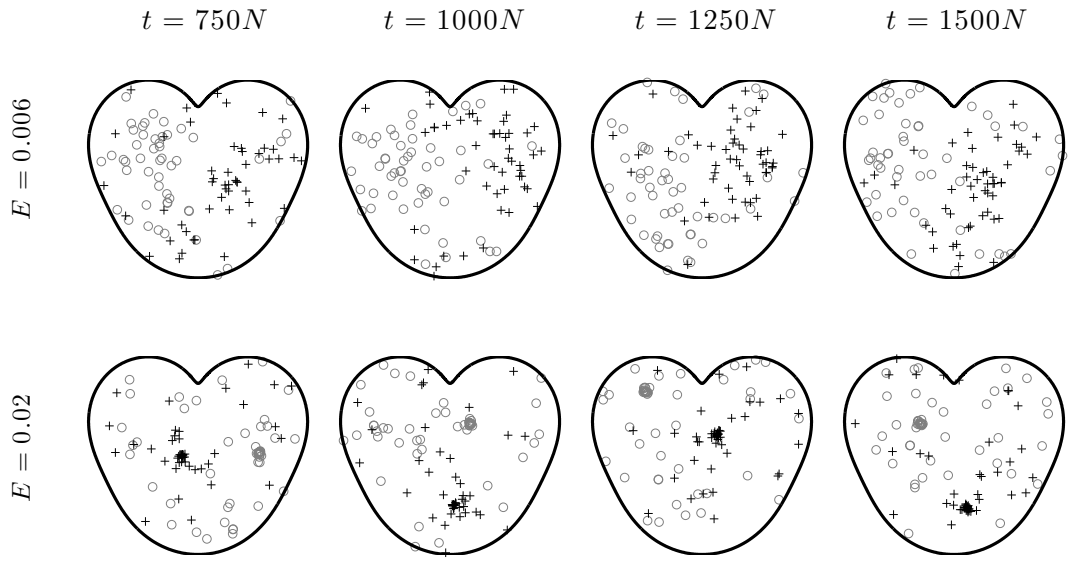

Figure 2.12: Snapshots of the N vortex positions at the times indicated of (top row) low energy Run a_I from fig. 2.10 and (bottom row) high energy Run e_I from fig. 2.11. In both cases vortices with positive circulation are denoted by black plus symbols and vortices with negative circulation by grey circles.

2.11 are shown in table 2.1. Considering figure 2.13, it is clear that X is persistently nonzero for a dipole[11], while for the monopole X oscillates frequently. In terms of the results in table 2.1, this phenomenon is characterised by the dipole runs $a_{I-III,V}$ having $|\bar{X}| \approx 2 \times 10^{-1}$ compared to $|\bar{X}| < O(10^{-1})$ for monopole runs (including the anomalous Run a_{IV} at $E = 0.006$).

$\lvert\bar{X}\rvert \times 10^{-1}$	a_- $(E = 0.006)$	e_- $(E = 0.02)$
Run I	2.402	0.7887
Run II	2.265	0.2279
Run III	2.112	0.06829
Run IV	0.5899	0.3814
Run V	1.881	0.7050

Table 2.1: Mean (to 4 sig. figs) of the absolute time averaged angular momentum $\bar{L}$ from the low energy runs shown in fig. 2.10 and high energy runs shown in fig. 2.11.

The time series of L is shown for runs a_I $(E = 0.006)$ and e_I $(E = 0.02)$ in figure

[11]This phenomenon will be further investigated for a different domain in chapter 5.

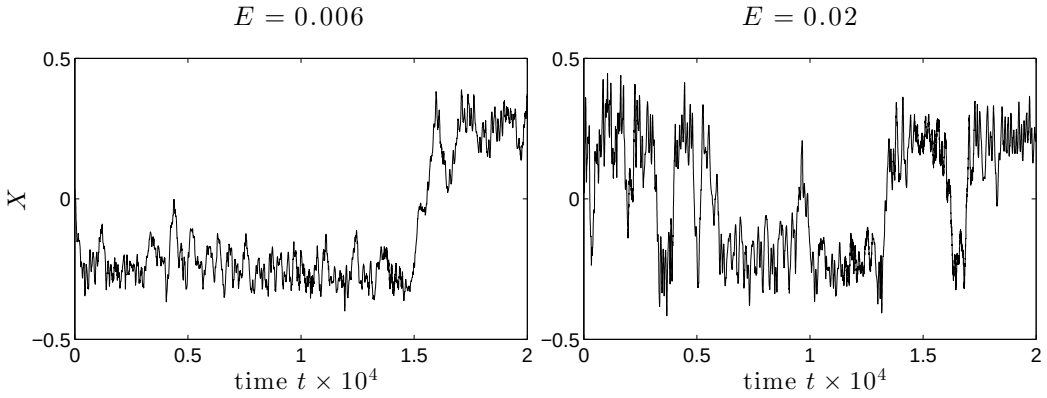

Figure 2.13: (Left) Times series of the centre of vorticity diagnostic X for run a_I ($E = 0.006$). (Right) As for left for run e_I ($E = 0.02$).

2.14, and the absolute means for the runs a_{I-V} and e_{I-V} from figure 2.10-2.11 are shown in table 2.2. From figure 2.14 it is difficult to discern how the dipole and monopole runs are different in terms of angular momentum. The results in table 2.2 shed more light on the matter, though the conclusions are weaker than those for the X diagnostic above. Considering all the dipole runs i.e. $a_{I-III,V}$ it can be seen that $|\bar{L}| = O(5 \times 10^{-3})$. However, though some monopole runs (a_{IV}, $e_{I,II,IV}$) have significantly larger $|\bar{L}|$ at $O(2 \times 10^{-2})$, the two monopolar runs $e_{III,V}$ have $|\bar{L}|$ at the same order as the dipolar runs.

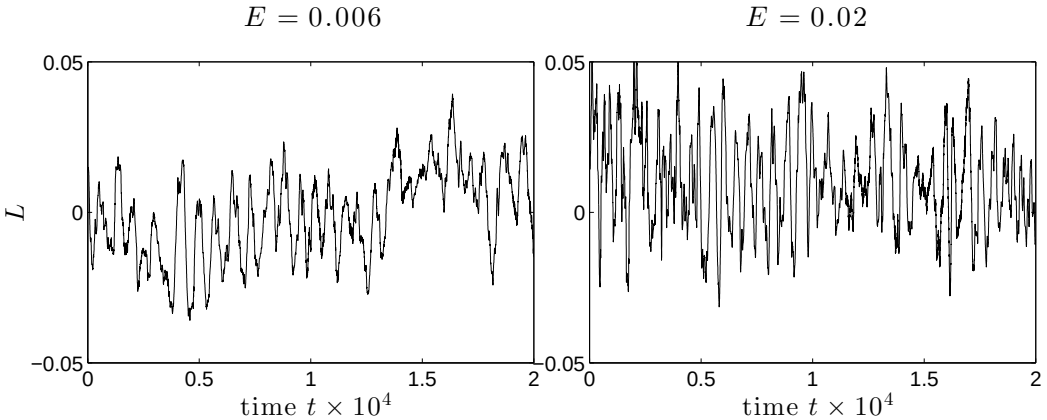

Figure 2.14: (Left) Times series of the angular momentum diagnostic L for run a_I ($E = 0.006$). (Right) As for left for run e_I ($E = 0.02$).

$\lvert\bar{L}\rvert \times 10^{-2}$	a_- $(E = 0.006)$	e_- $(E = 0.02)$
Run I	0.4627	1.177
Run II	0.2829	1.528
Run III	0.6401	0.6365
Run IV	1.845	1.784
Run V	0.4387	0.8201

Table 2.2: Means (to 4 sig. figs) of the absolute time averaged angular momentum $\bar{L}$ from the low energy runs shown in fig. 2.10 and high energy runs shown in fig. 2.11.

To further examine the two diagnostics, the runs a_{I-V} (black dots) and e_{I-V} (grey plus symbols) are plotted in $(|\bar{X}|, |\bar{L}|)$ space in figure 2.15, with dipolar and monopolar solutions grouped according to observations from figures 2.10-2.11. The dipolar runs are clearly characterised by large $|\bar{X}|$ *and* small $|\bar{L}|$, while the monopolar runs are only be characterised by small $|\bar{X}|$ and have a much wider range of $|\bar{L}|$. Consequently, a suitable classification of a solution as dipolar or monopolar is the following:

- Dipole: $|\bar{X}| > 0.2$ and $|\bar{L}| < 0.01$
- Monopole: $|\bar{X}| < 0.1$

The above analysis, though somewhat heuristic, gives a more formal framework to efficiently analyse all 50 runs. As mentioned earlier, in every case, the contour plot of the mean streamfunction (like those shown in figures 2.10 and 2.11) was used to validate the diagnostics.

Clearly there is a possibility of a run not falling into either the classification of a dipole or a monopole e.g. $|\bar{X}| > 0.2$ and $|\bar{L}| \gg 0.01$. In practice this did not occur in any of the 50 runs performed, and after a long enough integration a clear dipole or monopole was always found.

With the diagnostics above, we can now proceed with analysing the other runs with E closer to E_c. From figures 2.10 and 2.11, we can conclude that the predictions of the SPE are generally accurate for energies significantly far away from the critical energy E_c. How does this change when $E = E_c$? Is a fixed proportion of runs attracted to one state or the other, remaining in that state for the rest of time? For example does the system find the dipolar state 50% of the time and the monopolar

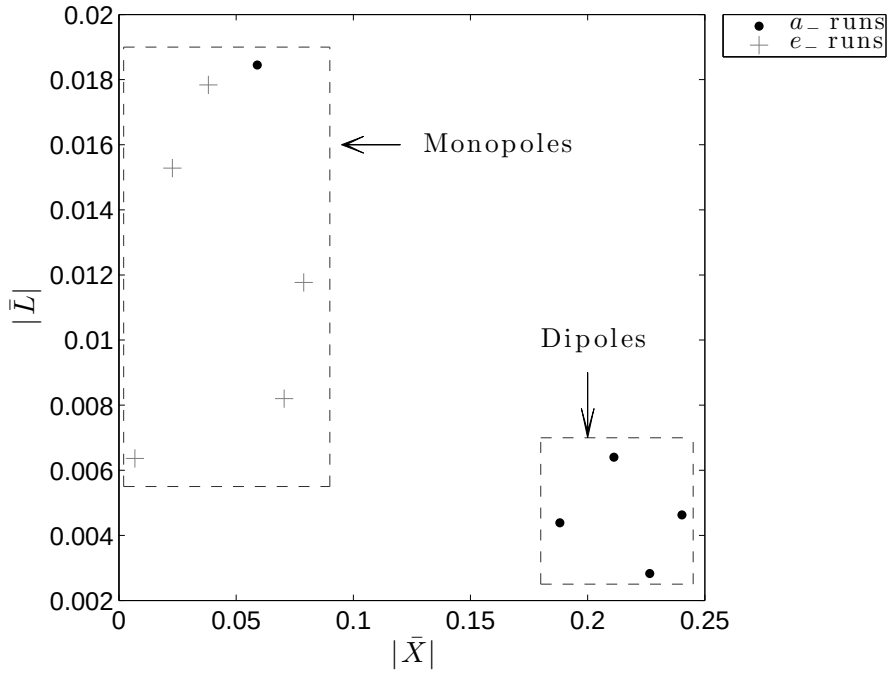

Figure 2.15: Plot showing the positions of runs a_{I-V} (black dots) and e_{I-V} (grey plus symbols) in the diagnostic space $(|\bar{X}|, |\bar{L}|)$. The runs are visually 'classified' as dipolar or monopolar based on mean streamfunctions shown in figures 2.10 and 2.11.

state the other 50% time? Or is a 'mixed mode' found where, for a given run, the system oscillates between the dipolar state and the monopolar state, spending long times in each? In other words both the states are metastable and random oscillations between dipoles and monopoles are due to a small entropy barrier. Further, how does the behaviour change for energies between E_c and the extreme energies shown in figs. 2.10-2.11?

To answer these questions the total number of dipolar and monopolar runs from all 50 simulations (10 each at $E = \{0.006, 0.0095, 0.0132, 0.0165, 0.02\}$) are displayed in a stacked bar chart in figure 2.16 using the classification $|\bar{X}| > 0.2$ & $|\bar{L}| < 0.01 \Rightarrow$ dipole, $|\bar{X}| < 0.1 \Rightarrow$ monopole, that was developed for runs a_{I-V} and e_{I-V}. To further elucidate theses results, table 2.3 shows the breakdown of all the runs – recall that for each run index I-X, the positions of the cluster centres used for the initial conditions are the same. Consequently for a given row in table 2.3, all the initial conditions are qualitatively the same.

From figure 2.16 there is a clear trend: increasing the energy leads to an increasing

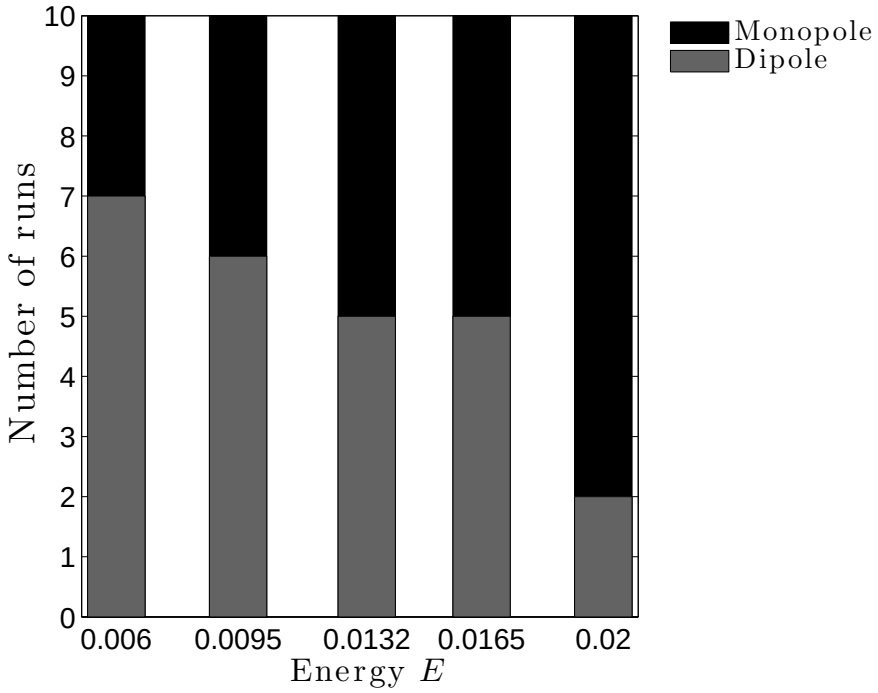

Figure 2.16: Stacked bar chart showing which equilibrium solution was found using the centre of vorticity diagnostic ($|\bar{X}| > 0.2$ & $|\bar{L}| < 0.01 \Rightarrow$ dipole, $|\bar{X}| < 0.1 \Rightarrow$ monopole) for an ensemble of dynamical runs, each of length $t = 1500N$ (after a spin-up period of $t = 500N$), at different energies.

probability of monopole/decreasing probability of dipole, in accordance with the predictions of the SPE as shown in figure 2.7. At $E = E_c$ the probability of a monopole or dipole seems to be equal for a given run, then moving to lower energies the probability of a dipolar run increases/monopolar run decreases, and moving to higher energies, the probability of a dipole decreases/monopole increases.

Table 2.3 gives an idea as to how important the cluster centre configuration is in determining whether dipole or monopole solution found in a DNS. Though some runs (e.g. I, III and VI) appear to be moderately bias towards the simulation finding a dipole or monopole, overall the initial condition, as controlled by the cluster centre configuration, does not appear to play a significant role in the which equilibrium state is found.

	$E = 0.006$	$E = 0.0095$	$E = 0.0132$	$E = 0.0165$	$E = 0.02$
Run I					
Run II					
Run III					
Run IV					
Run V					
Run VI					
Run VII					
Run VIII					
Run IX					
Run X					

Table 2.3: Breakdown of all 50 DNS. As in figure 2.16, grey boxes indicate the time-averaged streamfunction is a dipole and black boxes indicate a monopole. Across a given row, all the cluster centers and hence the initial conditions used in the DNS are qualitatively the same.

The above analysis, though indicating a clear trend, is somewhat coarse in that a lot of interesting dynamics are simply averaged out. In particular, it is noted that from animations of the all runs it is observed that the system does occasionally switch form one state to the other (i.e. dipole $\rightarrow$ monopole or vice versa), spending a short time in the new state, before switching back to the original state, where it remains for longer times. This suggests the existence of the meta-stable states mentioned earlier and it is postulated that closer to $E = E_c$ the entropy barrier is smaller meaning the meta-stable states are found more regularly. This is difficult to verify from the relatively small ensemble of dynamical runs presented in this section, though a more detailed stability analysis of the SPE solution branches in section 2.4.4 would shed more light on the matter.

2.5 Conclusion

This chapter has focussed on the sinh-Poisson equation (or more generally the elliptic-sinh equation), as a model for equilibrium statistical mechanics of the point vortex system in the hydrodynamic limit, where the system is dominated by the mean flow (i.e. condensate). Two classical derivations of the the sinh-Poisson equation were reviewed in section 2.2 and numerical techniques discussed in section 2.3.

The new results were presented section 2.4, where the type of phase transition

first identified in TBH09 was observed in a new domain and verified numerically using DNS of the point vortex system for the first time. These results are summarised by the following points:

1. Solutions of the nonlinear sinh-Poisson equation indicate that an energy-induced condensate switch (i.e. first order phase transition), where the maximum entropy solution changes from a dipolar condensate structure to a monopolar one, occurs in a heart domain defined by $(c, q) = (0.51, 0.55)$, with the two structures having equal entropy at $E_c \approx 0.0132$. Note that this condensate switch is not unique to the domain defined by these parameters, and similar energy-induced switches occur in other heart domains defined by similar parameters.

2. The predictions of the sinh-Poisson equation mentioned in 1. were verified by a time-averaged, finite-N streamfunction computed from DNS with $N = 100$ vortices, with convincing results: far from E_c the dipolar or monopolar structure is found the vast majority of the time as predicted by the maximum entropy solution of the sinh-Poisson equation. Moving closer the E_c the two competing solution structures have increasingly similar entropies and the second maximum entropy solution is found more frequently. At E_c both solutions have the same entropy, and are found with equal probability over a sample of ten dynamical runs.

Of particular interest, the predictions of the equilibrium streamfunction based on the sinh-Poisson equation are remarkably accurate when compared to DNS of a relatively low N dynamical system.

One important point that is not addressed in this chapter is related to the entropy of the solutions of the sinh-Poisson equation. As in previous studies such as TBH09 and Yin et al. [124], in this chapter it was assumed that the entire entropy of the system is solely in the maximum entropy solution. This is not strictly true, as lower entropy solutions are relevant as meta-stable states. This means that the entropy of the whole system is in fact given by a sum of the entropies of all the states, with the maximum entropy solution having the greatest weighting. In most domains the maximum entropy solution is significantly higher than the lower entropy solutions and so the lower entropy solutions can be ignored. However, in the heart domain defined

by $(c, q) = (0.51, 0.55)$ the entropies of the first two maximum entropy solutions are very close (or the same) and as such both their contributions should be considered (and possibly the contribution of other relevant lower entropy solutions as well). The partitioning of the entropy between the different solutions in a domain such as the heart awaits a future study.

As mentioned in section 2.4.4, a more rigourous study into the stability properties of the solutions of the SPE (e.g. computing $\frac{d^2S}{dE^2}$) would allow stronger conclusions to be made.

There are also a number of other possible avenues for future research. For example, as stated in section 2.4.2, the phase transition found in this chapter can be regarded as more fundamental that that found by in [107, 108] which relies on relies on conservation of angular momentum. Indeed, the heart domain defined by $(c, q) = (0.51, 0.55)$ is not the only heart domain that exhibits a condensate switch, and it is entirely likely that other, completely different, domains have similar behaviour. It would be straightforward to solve the SPE and run DNS of the vortex system in different conformal domains, and hence carry out a systematic classification of condensate switches in a variety of domains.

Finally, although the ESE corresponding to QGSW vortices was derived in section 2.2.2, it is not solved in this thesis. It is straightforward to use the algorithm described in section 2.3.2 to find the solution branches of ESE. The verification using large N DNS in section 2.4.5 could also be carried out for the QGSW system using the VOR-MFS algorithm that will be introduced in chapter 3. However, significant speed improvements would be required to the VOR-MFS as evaluating the Bessel function that governs the QGSW dynamics is typically one to two orders of magnitude slower than evaluating the logarithm that governs the 2D Euler dynamics. Further, a QGSW vortex travels slower that a 2D Euler vortex due to the QGSW vortex having a shorter range of interaction, as controlled by the Rossby radius λ^{-1}. Consequently, dynamical runs significantly longer than the $t = 2000N$ runs used in this chapter would be required to achieve equilibrium for the QGSW system. Assuming speed improvements could be made, it would be interesting to see how the condensate switch differs with the QGSW system, compared to the 2D Euler system considered in this chapter. Does the switch still occur in the heart domain defined by

$(c, q) = (0.51, 0.55)$ and what influence does the new free control parameter λ have?

Chapter 3

Generalised point vortex dynamics on arbitrary domains using the method of fundamental solutions

3.1 Introduction

As stated in section 1.2.1, a number of theoretical results (method of images, conformal mapping) allow the construction of the N vortex Hamiltonian (1.2) in a wide variety of domains for 2D Euler vortices i.e.

$$\mathcal{L} \equiv \nabla^2, \qquad G_0(\boldsymbol{x}, \boldsymbol{x}') = \frac{1}{2\pi} \log(|\boldsymbol{x} - \boldsymbol{x}'|).$$

For systems governed by operators other than the Laplacian, however, the method of images is typically restricted to domains with straight boundaries, and operator invariant conformal mapping is not possible. Consequently, the aim of this chapter is to formulate a new algorithm that constructs a numerical approximation to (1.2) for a general linear operator $\mathcal{L}$. A requirement for the rest of this chapter (and chapter 4) is that an explicit expression (or means of numerical evaluation) is available for the free space Green's function $G_0(\boldsymbol{x}, \boldsymbol{x}')$ corresponding to $\mathcal{L}$. In the case of the 2D Euler system the new algorithm has the advantage of allowing solutions in domains for which an explicit conformal map is not known.

The new algorithm (VOR-MFS hereafter) is designed to solve the generalized

point vortex problems detailed in section 1.2.1 by exploiting the method of fundamental solutions (MFS hereafter), see [50, 55] for detailed overviews. The idea of the MFS is to approximate the dynamical influence of the domain boundary at each vortex location using a linear combination of free-space (G_0) Green's function solutions (the fundamental solutions). The locations of the singularities associated with the fundamental solutions lie outside $\mathcal{D}$ on a set of points known as the MFS charge points, and the weights attached to each charge are chosen to satisfy the Dirichlet boundary condition (1.3b) on a discrete set of boundary points on $\partial\mathcal{D}$. The method is particularly simple to implement and has excellent convergence properties that will be discussed below. Apart from the recent work of Wu et al. [122], who apply MFS to the relatively straightforward problem of the motion of a single 2D Euler vortex outside an elliptical cylinder, to the authour's knowledge VOR-MFS represents the first attempt to exploit the MFS in this context.

This chapter is based on the publication by Ashbee, Esler & McDonald [4] and is structured as follows: Section 3.2 introduces the new algorithm VOR-MFS and reviews the relevant aspects of the MFS method. A protocol for choosing numerical parameters to obtain numerical solutions to a pre-determined accuracy is described. Section 3.3 describes a number of test-cases demonstrating the robustness of the new algorithm. Finally, in section 3.4 conclusions are presented along with possible directions for future research.

3.2 The VOR-MFS algorithm

3.2.1 Use of the method of fundamental solutions

A standard problem for which the MFS has been designed is the boundary value problem

$$\mathcal{L}\phi(\boldsymbol{x}) = 0 \qquad \boldsymbol{x} \in \mathcal{D}, \tag{3.1a}$$

$$\phi(\boldsymbol{x}) = b(\boldsymbol{x}) \qquad \boldsymbol{x} \in \partial\mathcal{D}, \tag{3.1b}$$

where $b(\boldsymbol{x})$ is specified on the domain boundary $\partial\mathcal{D}$.

The MFS exploits the fact that the free-space Green's function $G_0(\boldsymbol{x}, \boldsymbol{x}')$ (see equation (1.5) in section 1.2.1) satisfies $\mathcal{L}G_0(\boldsymbol{x}, \boldsymbol{x}') = 0$ everywhere in $\mathcal{D}$, provided that $\boldsymbol{x}'$ lies outside $\mathcal{D}$. The key idea of the MFS is simply to approximate $\phi(\boldsymbol{x})$ using a linear combination $\phi_M(\boldsymbol{x})$ of M free-space Green's functions, centered on a fixed set of points $\{\boldsymbol{y}_1, \ldots, \boldsymbol{y}_M\}$ located outside $\mathcal{D}$, known as the MFS charge points. In summary,

$$\phi_M(\boldsymbol{x}) = \sum_{k=1}^{M} \alpha_k G_0(\boldsymbol{x}, \boldsymbol{y}_k), \quad \boldsymbol{x} \in \mathcal{D}, \quad \boldsymbol{y}_k \notin \mathcal{D}, \tag{3.2}$$

where the $\{\alpha_k\}$ are a set of weights. The weights are determined by enforcing the boundary condition (3.1b) on a discrete set of points $\{\boldsymbol{x}_j^B\}$ located on $\partial\mathcal{D}$. (For the purposes of the discussion here, and for the VOR-MFS algorithm, it will be assumed that there are M such boundary points. In some circumstances it has been shown [109] that the use of a number greater than M can be advantageous.) The result is a M-dimensional linear system in the $\{\alpha_k\}$, i.e.

$$\mathbf{G}\boldsymbol{\alpha} = \mathbf{b}, \tag{3.3}$$

where the $M \times M$ matrix $\mathbf{G}$ has components $\{G_0(\boldsymbol{x}_j^B, \boldsymbol{y}_k)\}$, the vector $\boldsymbol{\alpha}$ components $\{\alpha_k\}$ and the vector $\mathbf{b}$ components $\{b(\boldsymbol{x}_j^B)\}$. Equation (3.3) can be solved for the $\{\alpha_k\}$ using a standard algorithm (e.g. MATLAB's *backslash* command [which is based on Gaussian elimination]). Note that the matrix $\mathbf{G}$ need only be inverted once at the beginning of a simulation.

A detailed discussion of the convergence and stability of the MFS is given in [50, 55] and references therein. For the illustrative problems of Laplace's equation and the Helmholtz equation in the unit disk, it has been shown [7, 66, 67] that if the MFS charge points are situated at radius $R > 1$ then the solution converges exponentially with M

$$\max_{\boldsymbol{x} \in \mathcal{D}} |\phi(\boldsymbol{x}) - \phi_M(\boldsymbol{x})| = O\left(R^{-M}\right),$$

provided that $R < \sqrt{\rho}$, where ρ is the radius of first singularity of the analytic

continuation of the solution in the complex plane. For other geometries, exponential convergence can also be attained, but the situation can be more complicated [7].

A possible limitation with the MFS is that the linear system (3.3) can be ill-conditioned [70,71]. However there is evidence in the literature [9,54–56] that apparent ill-conditioning of the MFS-problem presents minimal practical problems for the exponential convergence of the solution in Helmholtz and Laplace boundary value problems. The essence of the problem is that the object of interest in the MFS problem is the convergence of the quantity ϕ_M in (3.2) and not the convergence of the individual charge weights $\{\boldsymbol{\alpha}\}$ themselves. Kitagawa [70, 71] has studied precisely this problem and has found that errors are magnified by a quantity $O(M)$ relative to the error when no ill-conditioning is present (which of course decreases exponentially in M). The essential point is that those degrees of freedom in $\{\boldsymbol{\alpha}\}$ that cannot be determined accurately (due to ill-conditioning of the linear problem (3.3)) are precisely those that do not contribute significantly to ϕ_M.

In practice, the ill-conditioning is not typically found to affect the accuracy of the MFS solutions. However, for a particular set-up, it is recommended that the singular values of the matrix $\mathbf{G}$ are examined (i.e. prior to commencing a VOR-MFS integration).

To use the MFS to solve (1.1) in the absence of an explicit expression for the domain Green's function $G(\boldsymbol{x}, \boldsymbol{x}')$, note that by subtracting (1.5) from (1.3) the following equation for the residual Green's function $g(\boldsymbol{x}, \boldsymbol{x}')$ is obtained

$$\mathcal{L}g(\boldsymbol{x}, \boldsymbol{x}') = 0 \qquad \boldsymbol{x}, \boldsymbol{x}' \in \mathcal{D}, \tag{3.4a}$$

$$g(\boldsymbol{x}, \boldsymbol{x}') = -G_0(\boldsymbol{x}, \boldsymbol{x}'). \qquad \boldsymbol{x} \in \partial\mathcal{D}. \tag{3.4b}$$

Since the free-space Green's function G_0 is known everywhere, the boundary value problem (3.4) is exactly of the form (3.1) (for given $\boldsymbol{x}'$) and consequently a standard MFS routine can be straightforwardly applied to solve for an MFS approximation $g_M(\boldsymbol{x}, \boldsymbol{x}')$ to the residual Green's function, thus obtaining a corresponding approximation to $G(\boldsymbol{x}, \boldsymbol{x}')$.

The above approach can be extended to solve for an MFS approximation to the N-vortex Hamiltonian H (denoted H_M) by linearity, with still just a single MFS

calculation required. The relevant boundary value problem is

$$\mathcal{L}\phi(\boldsymbol{x}) = 0 \qquad \boldsymbol{x} \in \mathcal{D}, \tag{3.5a}$$

$$\phi(\boldsymbol{x}) = -\sum_{j=1}^{N} \Gamma_j G_0(\boldsymbol{x}, \boldsymbol{x}_j) \qquad \boldsymbol{x} \in \partial\mathcal{D}, \tag{3.5b}$$

which from (3.4) has exact solution

$$\phi(\boldsymbol{x}) = \sum_{j=1}^{N} \Gamma_j g(\boldsymbol{x}, \boldsymbol{x}_j).$$

It is straightforward to verify that an alternative expression for the Hamiltonian (1.2) is

$$H = -\sum_{i=1}^{N}\sum_{j=i+1}^{N} \Gamma_i\Gamma_j G_0(\boldsymbol{x}_i, \boldsymbol{x}_j) - \frac{1}{2}\sum_{i=1}^{N} \Gamma_i \phi(\boldsymbol{x}_i).$$

A standard application of the MFS provides an approximate expression ϕ_M for ϕ from (3.2), which allows us to define an MFS Hamiltonian

$$H_M(\boldsymbol{x}_1, \ldots, \boldsymbol{x}_N) = -\sum_{i=1}^{N}\sum_{j=i+1}^{N} \Gamma_i\Gamma_j G_0(\boldsymbol{x}_i, \boldsymbol{x}_j) - \frac{1}{2}\sum_{i=1}^{N}\sum_{k=1}^{M} \Gamma_i\alpha_k G_0(\boldsymbol{x}_i, \boldsymbol{y}_k), \tag{3.6}$$

where the $\{\alpha_k\}$ are the MFS weights obtained from the MFS solution of (3.5).

The partial derivatives of the MFS Hamiltonian can be evaluated directly from (3.6) and hence (1.1) can be integrated using the time-stepping algorithm of section 1.2.3. Note that this method bypasses the need for an explicit expression for $G(\boldsymbol{x}, \boldsymbol{x}')$. Because H is a conserved quantity, a key test of the algorithm is conservation of H_M. This will be investigated below.

3.2.2 The use of pseudo-images

One factor that strongly influences the accuracy and convergence of the MFS algorithm is the smoothness of the boundary function $b(\boldsymbol{x})$ in (3.1b) [7]. In particular, if $b(\boldsymbol{x})$ varies on spatial scales comparable to the spacing between MFS charge points (i.e. has significant spectral power at wavenumbers $\sim M|\mathcal{D}|^{-1/2}$ or greater, where $|\mathcal{D}|$ is the domain area), then the MFS solution will be unable to resolve the associated

fine scale structure in $b(\boldsymbol{x})$ near the domain boundary. Ref. [7] recommend up to 10 MFS charge points per wavelength for the case where $b(\boldsymbol{x})$ consists of a single Fourier wavenumber, to obtain solutions close to machine precision.

For the specific MFS boundary value problem (3.5) solved in VOR-MFS, the boundary function appearing on the right-hand side remains smooth everywhere on $\partial\mathcal{D}$, except where a vortex approaches the boundary. A vortex $\boldsymbol{x}_j$ located a distance ε from the domain boundary will induce a spectral peak in the boundary data at wavenumbers $\sim \varepsilon^{-1}$. If vortices are to move freely in the domain, close encounters with the boundary are inevitable, and the MFS method will fail whenever $\varepsilon^{-1} \gtrsim M|\mathcal{D}|^{-1/2}$ for the reason outlined above.

There turns out to be a simple solution of the above problem. If an additional 'pseudo-image' vortex of opposite sign is placed at a suitable point $\boldsymbol{x}_j^*$ on the opposite side of the boundary ∂D to the 'problem' vortex $\boldsymbol{x}_j$, then the spectral peak in the boundary data is smoothed and the MFS solution will retain its accuracy. There is considerable flexibility in the precise choice of $\boldsymbol{x}_j^*$, because all that is required is that as $\boldsymbol{x}_j$ approaches the domain boundary ($\varepsilon \to 0$) is that $\boldsymbol{x}_j^* \to \tilde{\boldsymbol{x}}_j$, (more precisely it is required that $\lim_{\varepsilon\to 0} |\boldsymbol{x}_j^* - \tilde{\boldsymbol{x}}_j|/\varepsilon = 0$), where $\tilde{\boldsymbol{x}}_j$ is the reflected point generated by the nearest point on $\partial\mathcal{D}$ to $\boldsymbol{x}_j$, as illustrated in Fig. 3.1(a). For example, the locations of the exact 2D Euler images in the unit circle $\boldsymbol{x}_j^* = \boldsymbol{x}_j/|\boldsymbol{x}_j|^2$ are easily shown to converge towards the reflection point $\tilde{\boldsymbol{x}}_j$, as required. It is to be emphasised that the pseudo-image is not (necessarily) an exact image of the vortex at $\boldsymbol{x}_j$ (which is not, in general, available), merely an approximate image that becomes exact in the limit $\varepsilon \to 0$.

One possible choice for the pseudo-image position $\boldsymbol{x}_j^*$ is the boundary reflection point $\tilde{\boldsymbol{x}}_j$ itself. However, in some relatively simple geometries $\tilde{\boldsymbol{x}}_j$ is a discontinuous function of $\boldsymbol{x}_j$, which can lead to computationally undesirable jumps in the pseudo-image position as $\boldsymbol{x}_j$ evolves in time. In the examples below, knowledge of an explicit conformal map to the unit circle is exploited to choose $\boldsymbol{x}_j^*$; see below for details. Alternative methods of selecting $\boldsymbol{x}_j^*$ are no doubt possible. In practice pseudo-images are introduced smoothly as a vortex approaches the boundary. For example, in a

circular domain with unit radius the pseudo-image strength is set by the function

$$\hat{\Gamma}_j = -\Gamma_j \begin{cases} 0, & 0 \leq |\boldsymbol{x}_j| \leq R_1 \\ \left(\frac{|\boldsymbol{x}_j|-R_1}{R_2-R_1}\right)^2, & R_1 < |\boldsymbol{x}_j| \leq R_2 \\ 1, & R_2 < |\boldsymbol{x}_j| \leq 1. \end{cases} \tag{3.7}$$

In domains that are conformal to the unit circle a similar approach can be taken (see below). Fig. 3.1(b) illustrates schematically the three regions in (3.7), some vortices and pseudo-images, and the MFS charge points.

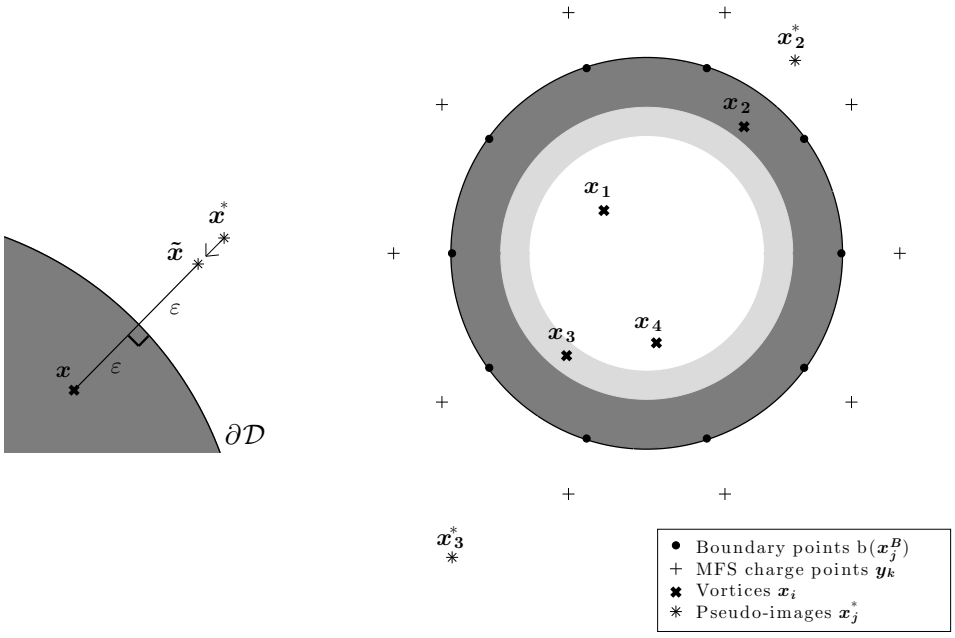

(a) (b)

Figure 3.1: (a) Schematic illustrating the boundary reflection point $\tilde{\boldsymbol{x}}$ and a possible pseudo-image location $\boldsymbol{x}^*$ associated with a vortex at $\boldsymbol{x}$. (b) Schematic illustrating a typical configuration of vortices and pseudo-images in the unit circle domain (with $N = 4$). For vortices in central white region $|\boldsymbol{x}_j| \leq R_1$ no pseudo-images are used. In the dark grey region $|\boldsymbol{x}_j| > R_2$ a full strength pseudo-image is present, whereas in the light grey region $R_1 < |\boldsymbol{x}_j| \leq R_2$ the strength of the pseudo-image is gradually increased as the vortex moves closer to the boundary.

In the case where there are $P \leq N$ pseudo-images, the MFS Hamiltonian is

$$H_M(\boldsymbol{x}_1, \ldots, \boldsymbol{x}_N) = -\sum_{i=1}^{N}\sum_{j=i+1}^{N} \Gamma_i \Gamma_j G_0(\boldsymbol{x}_i, \boldsymbol{x}_j) - \frac{1}{2}\sum_{i=1}^{N}\sum_{k=1}^{M} \Gamma_i \tilde{\alpha}_k G_0(\boldsymbol{x}_i, \boldsymbol{y}_k) - \frac{1}{2}\sum_{i=1}^{N}\sum_{j=1}^{P} \Gamma_i \hat{\Gamma}_j(\boldsymbol{x}_j) G_0(\boldsymbol{x}_i, \boldsymbol{x}_j^*), \quad (3.8)$$

where $\{\tilde{\alpha}_k\}$ are the weights obtained from the MFS solution of

$$\mathcal{L}\phi(\boldsymbol{x}) = 0 \qquad \boldsymbol{x} \in \mathcal{D}, \quad (3.9a)$$

$$\phi(\boldsymbol{x}) = -\sum_{j=1}^{N} \Gamma_j G_0(\boldsymbol{x}, \boldsymbol{x}_j) - \sum_{j=1}^{P} \hat{\Gamma}_j G_0(\boldsymbol{x}, \boldsymbol{x}_j^*) \qquad \boldsymbol{x} \in \partial\mathcal{D}. \quad (3.9b)$$

Placement of pseudo-images can become complicated (or even impossible) when parts of the domain are very thin (e.g. a flat plate or protrusion), such as in [92]. Further, the convergence properties of the algorithm in this context will also be severely reduced, as will be noted in the next section.

3.2.3 Selection of the location and number of MFS charge points in VOR-MFS

The optimal positioning of the MFS charge points $\{\boldsymbol{y}_k\}$ and boundary points $\{\boldsymbol{x}_k^B\}$ is a topic that has received considerable attention in the literature (see e.g. [7]). The optimal distance of the curve on which the charge points are situated from the domain boundary $\partial\mathcal{D}$ depends in general upon the nature of the boundary data $b(\boldsymbol{x})$ in equation (3.1b), as well as the curvature of the domain boundary $\partial\mathcal{D}$. A detailed analysis of the optimal location of $\{\boldsymbol{y}_k\}$ specific to the VOR-MFS problem awaits a future study. The spacing of the charge points $\{\boldsymbol{y}_k\}$ along the chosen curve must reflect the curvature of $\partial\mathcal{D}$ itself. Unsurprisingly, the best results are obtained if the charge points are concentrated near regions of high curvature.

As mentioned in section 3.2.2, vortex motion around thin obstacles will lead to severely reduced convergence properties. When the spacing between charge points exceeds the thickness of the obstacle, VOR-MFS is likely to have the more modest

quadratic convergence properties of a boundary integral method such as was used in [92]. VOR-MFS is evidently not suited to this specific problem and as such the focus of the paper will be on domains with no thin sections.

Good results have been obtained in the unit circle domain by placing the charge points uniformly at radius $R = 1.1$. In other domains, a conformal map from the unit circle domain to $\mathcal{D}$ can be used to determine the positions of $\{\boldsymbol{y}_k\}$ based on a simple distribution around the circle. The boundary points $\{\boldsymbol{x}_k^B\}$ are placed uniformly around the circle $R = 1$ and then mapped onto $\partial\mathcal{D}$. The use of the conformal map, where available, ensures that the charge points are concentrated in the desired regions [7], however heuristic methods may well work where no conformal map is available.

Once an optimal curve for the MFS charge points $\{\boldsymbol{y}_k\}$ has been chosen, a crucial issue in optimizing the performance of VOR-MFS is the choice of the number M of charge points. Recall that the adaptive time-stepping algorithm described in section 1.2.3 requires convergence of the mean vortex position to within a tolerance δ (see equation 1.26) over a time interval Δt. For given δ, the optimal choice of M will be $M_*(\delta)$, defined to be the minimum value of M for which the accumulated error due to the MFS approximation over the interval $[t_n, t_n + \Delta t]$ is less than $\epsilon\delta$. Here $\epsilon < 1$ is a constant chosen to ensure that MFS errors at $M = M_*(\delta)$ remain sufficiently small compared with the errors associated with the adaptive time-stepping scheme itself.

For a specific set-up, the value of $M_*(\delta)$ can be estimated prior to a dynamical integration by the following procedure. A set of random vortex positions $\{\boldsymbol{x}_i\}$ is first generated. The mean error in velocity $\boldsymbol{u}_i$ at the vortex locations due to the MFS is then defined to be

$$E(M) = \frac{1}{N}\sum_{i=1}^{N}\left|\boldsymbol{u}_i^{(M)} - \boldsymbol{u}_i\right|, \tag{3.10}$$

where $\boldsymbol{u}_i^{(M)}$ is the MFS estimate of $\boldsymbol{u}_i$. Next, the fact that MFS solutions converge exponentially in M, is exploited to write the following estimate for $E(M)$

$$E(M) \approx \frac{1}{N}\sum_{i=1}^{N}\left|\boldsymbol{u}_i^{(M)} - \boldsymbol{u}_i^{(M_{max})}\right| = Ae^{-\alpha M}, \tag{3.11}$$

where M_{max} is the maximum number of points for which the MFS problem can be conveniently solved. Estimates for the real constants A and α are found by using (3.11) to calculate $E(M)$ for several values of $M < M_{max}$ and making a least squares fit to $\log E(M)$. The values of A and α thus obtained are specific to the problem being solved, and also depend to a certain extent on numerical choices such as the locations of $\{\boldsymbol{y}_k\}$, the values of R_1, R_2 etc. In practice a number of realisations of $\{\boldsymbol{x}_i\}$ are tested and the 'worst case' values of A and α are used below.

Provided Δt is sufficiently small, the MFS error in mean vortex position over the time interval Δt can be estimated to be $E(M)\,\Delta t$. The requirement that

$$E(M)\,\Delta t \leq \epsilon\delta, \tag{3.12}$$

is sufficient for the estimated MFS error to be less than the time-stepping error (by a factor ϵ). Our estimate of $M_*(\delta)$ is defined by equality in the above relation, and using (3.11) is found to be

$$M_*(\delta) = -\frac{1}{\alpha}\log\left(\frac{\epsilon\delta}{A\Delta t}\right). \tag{3.13}$$

The important point evident from (3.13) is that $M_*(\delta)$ has logarithmic dependence on δ. Consequently, provided the constant α is not too small, appropriately small values of δ can be targeted at little additional cost in terms of MFS charge points. A conservative choice of $\epsilon = 10^{-3}$ is made in all integrations described below, to ensure that time-stepping errors dominate over MFS errors.

The dependence of $E(M)$ on N is shown in Fig. 3.2 for the neutral system (equal numbers of positive and negative vortices) for (a) 2D Euler vortices ($\lambda = 0$) and (b) the QGSW vortices ($\lambda = 1$), with $N = 4$, $N = 8$ and $N = 16$ in a unit circle. Charge points are placed at a radius of 1.1, $\Delta t = 0.1$ and $\Gamma_i = \pm 1$. Ten realisations of the vortex positions are used for each calculation. It is clear from Fig. 3.2 that the mean error $E(M)$ in the vortex velocities depends, at most, weakly on N and on λ.

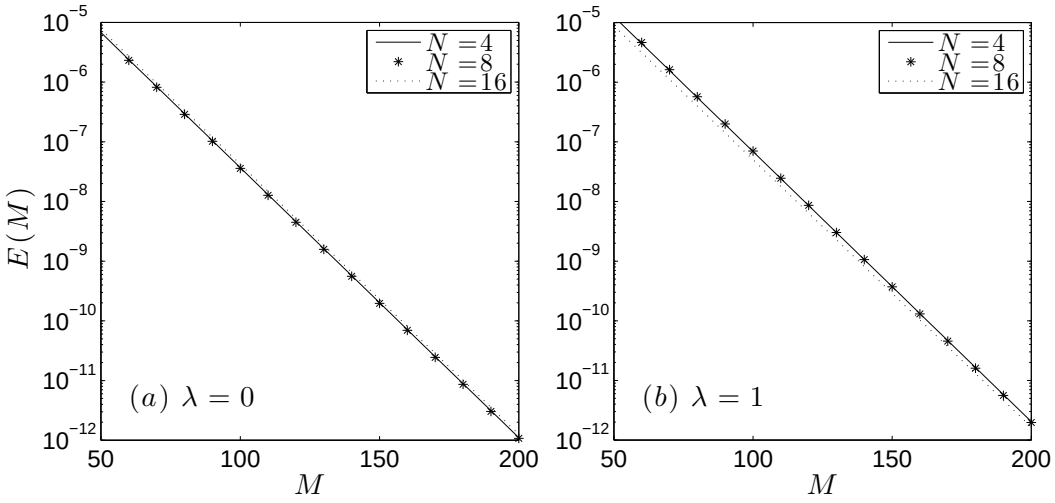

Figure 3.2: MFS mean velocity error $E(M)$ for (a) the 2D Euler system and (b) the QGSW system, with $N = 4$, $N = 8$ and $N = 16$ in the unit circle. The results are calculated from the 'worst' case outcome of ten uniformly distributed random configurations of the N vortices.

3.2.4 Computational cost of VOR-MFS

The structure of the MFS Hamiltonian (3.8) makes possible simple scaling estimates for the computational costs of VOR-MFS in comparison with an explicit numerical scheme designed to solve the same problem. How, for example, does the VOR-MFS algorithm scale with vortex number N and the accuracy controlling (tolerance) parameter δ?

First note that a single evaluation of the linear problem (3.3) requires $[M_*(\delta)]^2$ multiplication operations. It follows that the costs associated with solving the linear problem are overwhelmed by the costs associated with the evaluations of the derivatives of the Hamiltonian (3.8) in (1.1), which (as argued below) requires at least $[M_*(\delta)]^2$ evaluations of the derivatives of the free space Green's function. Hence the additional costs of solving the linear system (3.3) can be safely neglected.

Comparing the costs of evaluating the derivatives of an image model Hamiltonian (eqn. 1.2, with $G(\boldsymbol{x}, \boldsymbol{x}')$ given in appendix A.2.1) to the VOR-MFS Hamiltonian (3.8), the former requires $4N^2$ evaluations of the derivatives of G_0 and the latter $(N + M_*(\delta) + \bar{P})^2$ evaluations, where $\bar{P} < N$ is the average number of pseudo-images

in use. For $N \gg M_*(\delta)$ VOR-MFS therefore becomes *cheaper* than the corresponding image model (since $\bar{P}$ is roughly proportional to N). VOR-MFS is therefore very well-suited to large N super-computer simulations of the type performed by [123]. Note that there is evidently an optimisation problem, which has not yet been explored in detail, concerning how best to choose the pseudo-image protocol to minimize $M_*(\delta) + \bar{P}$ in VOR-MFS.

The costs associated with decreasing the tolerance parameter δ are primarily associated with the underlying adaptive time-stepping scheme described above in section 1.2.3. For the present fourth-order (RK4) scheme, a decrease in δ by a factor of sixteen results in a doubling of the number of substeps ($m_* \to m_* + 1$) needed over each integration interval Δt. In VOR-MFS there is an additional cost associated with an increase in the number of MFS points $M_*(\delta)$ but, because this increase is logarithmic in δ the additional cost is relatively small, particularly if N is large.

A further cost for VOR-MFS, which applies when the system being integrated is no longer the 2D Euler system, is the additional cost of evaluating e.g. modified Bessel functions (see eqn. 1.7), when calculating the gradients of H. This cost can be considerable, and the use of fast Bessel function routines is recommended.

3.3 Test cases for VOR-MFS

3.3.1 Test case I: Multiple 2D Euler vortices in a circular domain

The first test for VOR-MFS will consider the dynamics of N 2D Euler vortices in a unit circle domain. The performance of VOR-MFS will be tested against an exact 'image' model to be described.

The exact Hamiltonian H for the motion of N 2D Euler vortices in a unit circle is given by (1.2) with

$$G(\boldsymbol{x}, \boldsymbol{x}') = \frac{1}{2\pi} \log |\boldsymbol{x} - \boldsymbol{x}'| - \frac{1}{4\pi} \log \left(1 - 2\boldsymbol{x} \cdot \boldsymbol{x}' + |\boldsymbol{x}|^2 |\boldsymbol{x}'|^2\right), \tag{3.14}$$

where the first term can be recognised to be $G_0(\boldsymbol{x}, \boldsymbol{x}')$ and the second is therefore

$g(\boldsymbol{x}, \boldsymbol{x}')$. Viewed as a function of $\boldsymbol{x}$, (3.14) is equivalent (up to a dynamically irrelevant function of $\boldsymbol{x}'$) to the streamfunction induced in an unbounded domain by a vortex of circulation $+1$ at $\boldsymbol{x}'$ plus a vortex of circulation -1 at the image location $\boldsymbol{x}^* = \boldsymbol{x}'/|\boldsymbol{x}'|^2$. The exact expression for $G(\boldsymbol{x}, \boldsymbol{x}')$ allows (1.1) to be solved directly using the adaptive time-stepping routine described in section 1.2.3. We refer to this model henceforth as the image model.

Two tests used to assess VOR-MFS are conservation of the Hamiltonian H and of angular momentum

$$L = \frac{1}{2\pi} \sum_{i=1}^{N} \Gamma_i |\boldsymbol{x}_i|^2. \tag{3.15}$$

Conservation of L follows from the rotational symmetry of the unit circle domain; see section 1.2.2. The relative error measures

$$\delta_H(t) = \left| \frac{H(t) - H(0)}{H_r} \right|, \qquad \delta_L(t) = \left| \frac{L(t) - L(0)}{L_r} \right|, \tag{3.16}$$

are adopted as the principal means of evaluation of VOR-MFS accuracy. Here H_r and L_r are reference magnitudes for the Hamiltonian and angular momentum, chosen to be their mean and standard deviation respectively, as calculated from 100 samples based on uniformly distributed vortex positions. Recall that VOR-MFS uses convergence of mean vortex position as its criterion for advancement (see eqn. 1.26), hence conservation of H and L are not targetted directly. Numerical control over the error measures δ_H and δ_L is therefore an important internal consistency check for the algorithm.

To compare results between the image model and VOR-MFS, the equations of motion (1.1) are integrated for 100 non-dimensional time units with $N = 4$ vortices (with circulations $\Gamma_i = +1, +1, -1, -1$), using each model. The motion of four vortices in a bounded domain is known to be chaotic in general [91] and consequently provides a robust test. Results for three different values of the tolerance δ are compared ($\delta = 10^{-6}, 10^{-8}, 10^{-10}$) with the integration interval set to be $\Delta t = 0.1$. For VOR-MFS, the MFS charge points are located at $R = 1.1$, and the procedure detailed in section 2.4 is followed to set the number of MFS charge points to be

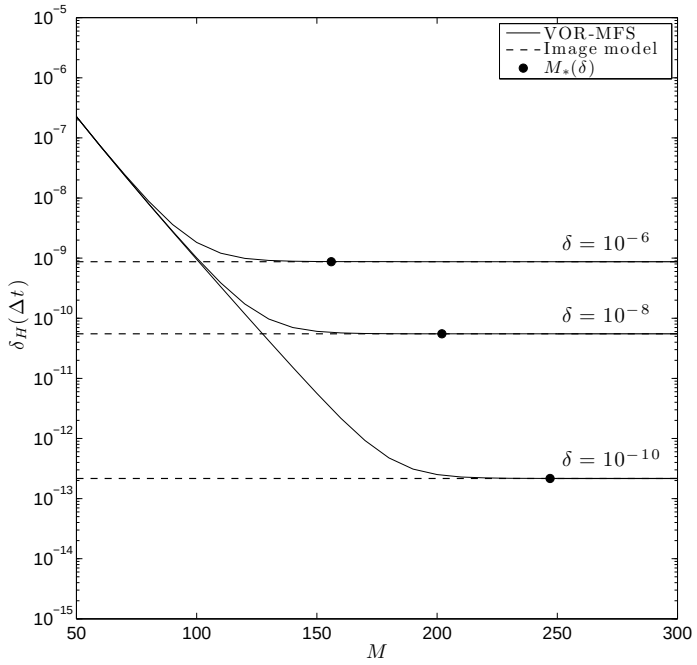

Figure 3.3: Dependence of relative numerical error $\delta_H(\Delta t)$ in the Hamiltonian H, at the end of a single integration interval Δt, upon the number of MFS charge points M used by VOR-MFS (solid curves). The largest errors over 100 realisations of uniformly distributed random initial conditions are shown and results are given for several values of the adaptive time-stepping tolerance ($\delta = 10^{-6}, 10^{-8}, 10^{-10}$). Dashed lines show the corresponding error in the image model. The values $M = M_*(\delta)$ obtained from equation (3.13) are illustrated as solid points on each curve.

$M = M_*(\delta) = 156, 202, 248$ respectively. Pseudo-images are introduced smoothly for radii greater than $R_1 = 0.8$ and with $R_2 = 0.9$ (see eqn. 3.7) at positions $\boldsymbol{x}_j^* = \boldsymbol{x}_j/|\boldsymbol{x}_j|^2$.

To confirm that the number of MFS points $M = M_*(\delta)$ is adequate in each case, Fig. 3.3 shows $\delta_H(\Delta t)$ ($H_r = -0.366$, 3 sig. fig.) as a function of M for VOR-MFS (solid curves), and the corresponding error in the image model (dashed lines). The results are taken from the worst case of 100 short integrations (length $t = \Delta t = 0.1$) with uniformly distributed random initial vortex placements as initial conditions. Fig. 3.3 confirms that the method of section 3.2 is broadly successful in selecting the minimum value $M = M_*(\delta)$ for which errors due to MFS are significantly less than errors due to the adaptive time-stepping scheme (dashed curves).

Fig. 3.4 illustrates vortex trajectories calculated using both the image model and VOR-MFS over 20 nondimensional time units. Numerical parameters are $\delta = 10^{-8}$ and $M_*(\delta) = 202$, as in the middle case above. The same initial conditions are used

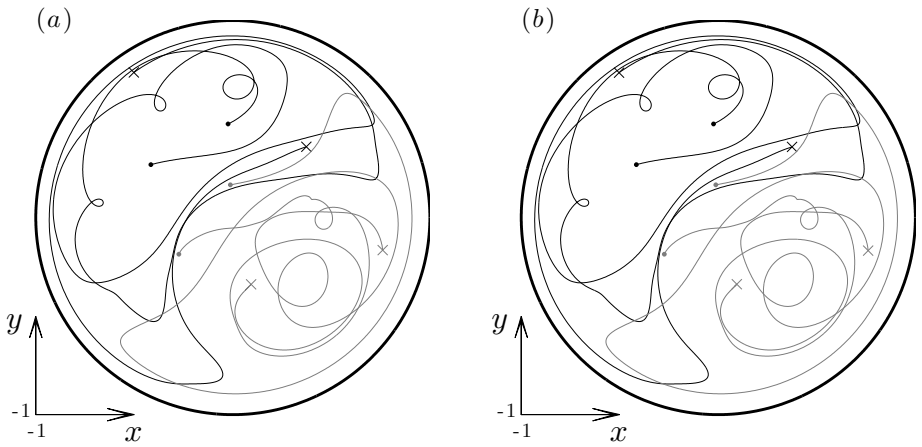

Figure 3.4: (a) Vortex trajectories as calculated using the image model over 20 nondimensional time units with tolerance parameter $\delta = 10^{-8}$. Black curves show positive vortices and grey curves negative vortices. Initial positions are plotted as filled circles and final positions as crosses. (b) As (a) but for VOR-MFS with $M_*(\delta) = 202$.

in each case and it is clear from the figure that VOR-MFS accurately reproduces the image model trajectories during a period in which the vortices make multiple circuits of the domain. The mean difference in vortex positions between the two runs at $t = 20$ is 1.3×10^{-4}. Due to the chaotic nature of the vortex evolution the mean difference grows exponentially and is 6.7×10^{-1} at $t = 40$. Beyond this time the two integrations diverge completely. Note that vortices are within the full pseudo-image region $|\boldsymbol{x}_j| > R_2 = 0.9$ (see eqn. 3.7) for just 7% of the integration.

Fig. 3.5 shows the time evolution of $\delta_H(t)$ and $\delta_L(t)$ ($L_r = 0.593$, 3 sig. fig.) over the full duration of the VOR-MFS model integrations (solid curves, with $M = M_*(\delta)$ in each case) and image model integrations (dashed curves), where again $\delta = 10^{-6}, 10^{-8}, 10^{-10}$ and $M = M_*(\delta) = 156, 202, 248$. It is evident that in both models $\delta_H(t)$ and $\delta_L(t)$ are controlled (linearly) by the tolerance parameter δ. Fig. 3.5 demonstrates that the growth of numerical errors in both H and L is comparable in each model.

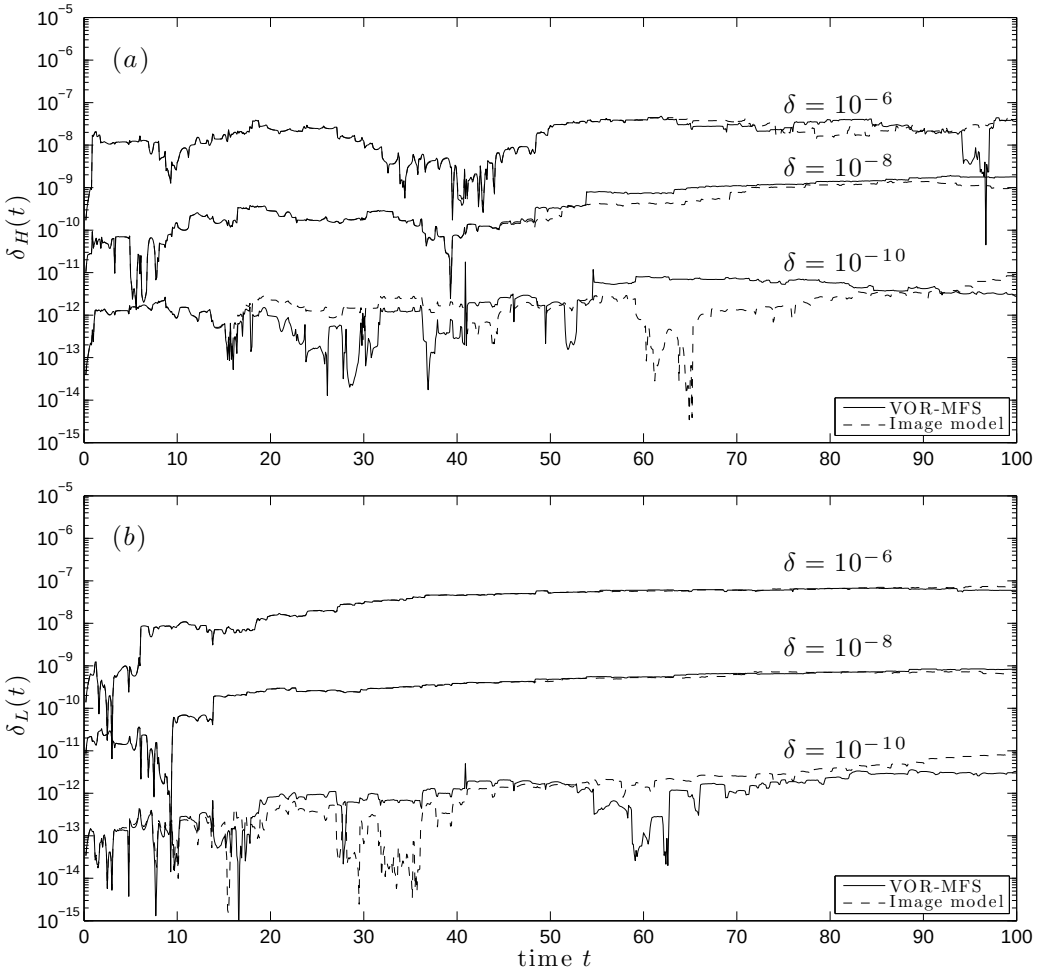

Figure 3.5: Time evolution of the error measures (a) $\delta_H(t)$ (Hamiltonian error) and (b) $\delta_L(t)$ (angular momentum error) during VOR-MFS model integrations (solid curves) and the image model integrations (dashed curves). Three values of the tolerance parameter $\delta = 10^{-6}, 10^{-8}, 10^{-10}$ are shown with $M = M_*(\delta) = 156, 202, 248$ the respective number of MFS charge points.

3.3.2 Test case II: Multiple 2D Euler vortices in a Neumann oval

A more challenging test for VOR-MFS is to simulate point vortex dynamics in a domain with less symmetry than the unit circle. Next VOR-MFS is therefore validated against an image model for 2D Euler dynamics in a domain bounded by a Neumann oval [78]. Neumann ovals, constrained here to have equal area (π), are a one-parameter family of curves defined by the conformal map from the unit circle

$$z = F(Z) = \frac{aZ}{1 - q^2 Z^2}, \qquad a = a_\pi(q) = \frac{1 - q^4}{(1 + q^4)^{1/2}}. \tag{3.17}$$

The usual correspondence between the complex plane $\mathbb{C}$ and $\mathbb{R}^2$ is assumed, i.e. $z = x + \mathrm{i}y$ is identified with coordinates $\boldsymbol{x} = (x\ y)^T$ in the Neumann oval domain and $Z = X + \mathrm{i}Y$ with coordinates $\boldsymbol{X} = (X\ Y)^T$ in the unit circle image domain. The parameter q ($0 \leq q < 1$) controls the shape of the Neumann oval. Here $q = 0.7$ is chosen ($q = 0$ maps the circle to itself). Further details of the image model for any conformally mapped domain are given in appendix A.2.1 and the specific case of the Neumann oval defined by the mapping (3.17) is used as an example in appendix A.2.2.

A numerical image model designed to solve (1.1) for the Neumann oval has been implemented using the adaptive method of section 1.2.3. The numerical image model was validated by verifying conservation of H (see below).

The VOR-MFS model is designed as follows. According to [7], MFS charge points in conformal domains are optimally placed when they do not enclose singularities of the Schwarz function associated with $\partial\mathcal{D}$. The Schwarz function $\bar{z} = S(z)$ is a complex form of the equation determining $\partial\mathcal{D}$, i.e. if $h(x, y) = 0$ defines $\partial\mathcal{D}$ in $\mathbb{R}^2$, then $\bar{z} = S(z)$ follows from resolving the equation $h((z + \bar{z})/2, (z - \bar{z})/2\mathrm{i}) = 0$ in favour of $\bar{z}$. It is assumed here that $S(z)$ is analytic in the neighborhood of $\partial\mathcal{D}$. For the particular case of (3.17) it can be shown that $S(z)$ has singularities at

$$z_\pm = \pm\mathrm{i}\frac{a_\pi(q)^2 q(1 + q^2)}{2(1 - q^4)^2}, \tag{3.18}$$

which lie on the imaginary axis outside $\partial\mathcal{D}$. Taking these locations into account, a suitable curve for the charge points, illustrated in Fig. 3.6, was found to be the Neumann oval with parameters $q = 0.73$ and $a = (1.3)^{1/2}a_\pi(q)$. The spacing of the MFS charge points on this curve follows the 'constant conformal radius' method [7], i.e. the M charge points are equally spaced on the unit circle and then mapped to their Neumann oval by (3.17). Fig. 3.6 shows that charge points are concentrated near the regions of maximum curvature of $\partial\mathcal{D}$. Calculations of $M = M_*(\delta)$ following the method of section 3.2.3 reveal that a significantly greater number of charge points (approximately twice as many for the same δ) are required for the oval as compared to the circle.

Pseudo-images are introduced much as for the unit circle. First define inner and outer Neumann ovals by (3.17) with $q_1 = 0.86$ and $a_1 = (0.6)^{1/2}a_\pi(q_1)$ and $q_2 = 0.78$ and $a_2 = (0.76)^{1/2}a_\pi(q_2)$ respectively. Denoting the polar equations of the inner and outer ovals by $r = R_1(\theta)$ and $r = R_2(\theta)$ respectively, the pseudo-image formula (c.f. eqn. 3.7) used is

$$\hat{\Gamma}_j = -\Gamma_j = \begin{cases} 1 & |\boldsymbol{x}_j| \geq R_2(\theta_j) \\ \left(\frac{|\boldsymbol{x}_j| - R_1(\theta_j)}{R_2(\theta_j) - R_1(\theta_j)}\right)^2 & R_1(\theta_j) \leq |\boldsymbol{x}_j| < R_2(\theta_j) \\ 0 & |\boldsymbol{x}_j| < R_1(\theta_j). \end{cases} \tag{3.19}$$

where $\theta_j = \tan^{-1}(y_j/x_j)$. Pseudo-images are placed at the exact image point in the unit circle image domain and mapped back to the Neumann oval. That is, if a vortex at $\boldsymbol{x}_j$ maps to $\boldsymbol{X}_j$ in the image domain then the pseudo-image is placed at $\boldsymbol{x}_j^* = \boldsymbol{f}(\boldsymbol{X}_j/|\boldsymbol{X}_j|^2)$; see appendix A.2.1.

Fig. 3.7 shows the time evolution of the error measure $\delta_H(t)$ (calculated using H_M) during separate integrations with $N = 4$, $N = 8$ and $N = 16$ vortices and $H_r = -0.441$, -0.895 and -1.70 to 3 sig. fig. respectively. Equal numbers of positive and negative vortices are used in each case with circulations $\Gamma_i = \pm 1$. The numerical parameters used are integration interval $\Delta t = 0.1$, tolerance $\delta = 10^{-8}$ and number of MFS charge points $M_*(\delta) = 348$. Good conservation properties are evident for all three integrations.

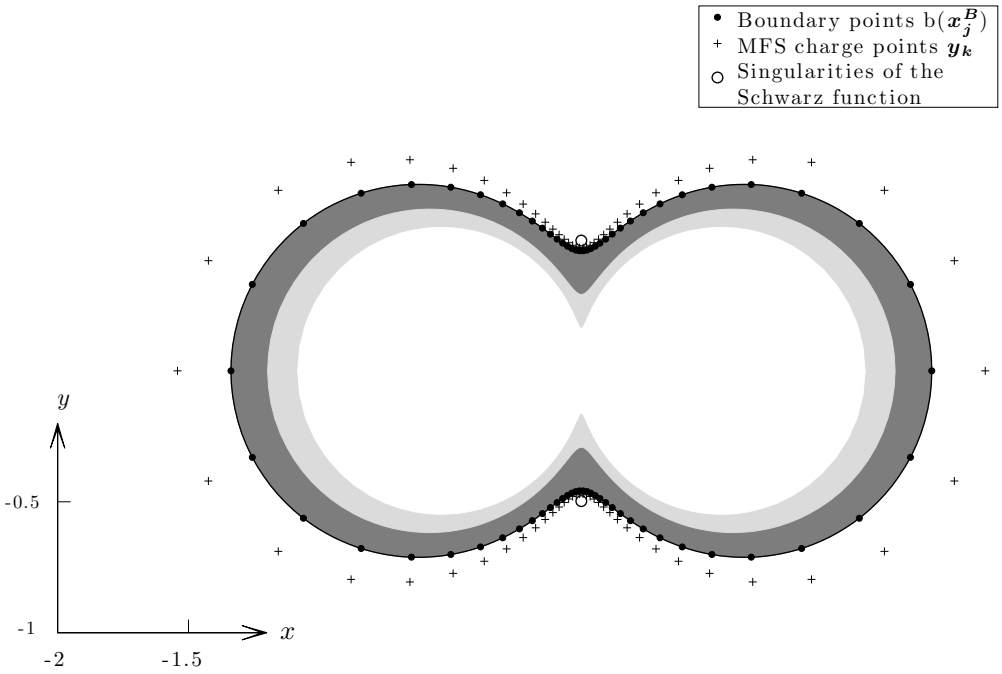

Figure 3.6: Geometry of VOR-MFS for the Neumann oval integrations with 70 MFS charge points illustrated. Partial pseudo-images are used in the light grey region and full pseudo-images in the dark grey region. Unfilled circles show the singularities $z_\pm$ of the Schwarz function given by (3.18).

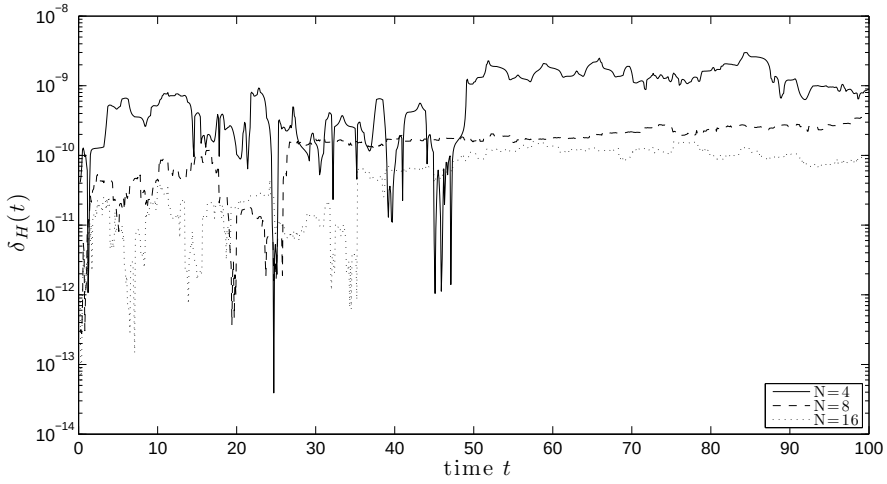

Figure 3.7: Time evolution of error measure $\delta_H(t)$ for VOR-MFS integrations of $N = 4, 8$ and 16 2D Euler vortices (solid, dashed and dotted curves respectively.) The value of the tolerance parameter was $\delta = 10^{-8}$ with $M = M_*(\delta) = 348$.

3.3.3 Test case III: A solitary QGSW vortex in a Neumann oval

Arguably the main strength of VOR-MFS is its capacity to simulate point vortex dynamics in systems other than the 2D Euler equations. One example of such a system is the quasi-geostrophic shallow water (QGSW) model discussed in section 1.2.1, see (1.7) for its free space Green's function. Next VOR-MFS will be used to simulate the motion of a single QGSW vortex in the Neumann oval.

The motion of a single vortex governed by (1.1) is well-known to be confined to isolines of the Hamiltonian H [91], which in the case of a single vortex in a domain $\mathcal{D}$ is given by

$$H(\boldsymbol{x}_1) = -\frac{1}{2}\Gamma_1^2 g(\boldsymbol{x}_1, \boldsymbol{x}_1),$$

where $g(\boldsymbol{x}, \boldsymbol{x}')$ is the residual Green's function for $\mathcal{D}$. The Hamiltonian H can be approximated at any point $\boldsymbol{x}_1$ using the MFS (by H_M, see eqn. 3.8). An MFS estimate of the isolines of H can therefore be obtained by evaluating H_M on a grid over $\mathcal{D}$, and contouring the resulting function of $\boldsymbol{x}_1$.

The isolines of H for a QGSW vortex with Rossby radius $\lambda^{-1} = 1$ and circulation $\Gamma_1 = +1$, calculated using the above method with $M = 374$ charge points, is shown in Fig. 3.8a. The isolines can be contrasted with those for a 2D Euler vortex shown in Fig. 3.8b. The main difference between the two systems is that the (boundary-induced) velocity field experienced by the vortex is much weaker in the QGSW system towards the center of the domain. (Recall from (1.1) that $\boldsymbol{u}_1 = \Gamma_1^{-1}\boldsymbol{k} \times \nabla_{\boldsymbol{x}_1} H$ and therefore vortex velocities are proportional to the gradient of H). The weaker velocities can be explained by the fact that the dynamical influence of the QGSW vortex decays exponentially at distances $\gtrsim \lambda^{-1}$, due to the modified Bessel dependence in (1.7). A QGSW vortex placed a distance $\gg \lambda^{-1}$ from a domain boundary therefore moves as if the boundary is absent.

The thick dashed lines on Fig. 3.8 show dynamical trajectories calculated explicitly using VOR-MFS (for the QGSW vortex) and the image model (for the 2D Euler vortex) for 35 non-dimensional time units. The initial condition is identical for both runs $\boldsymbol{x}_1(0) = (0.805 \;\; 0)^T$. However, the behavior is different due to the different dy-

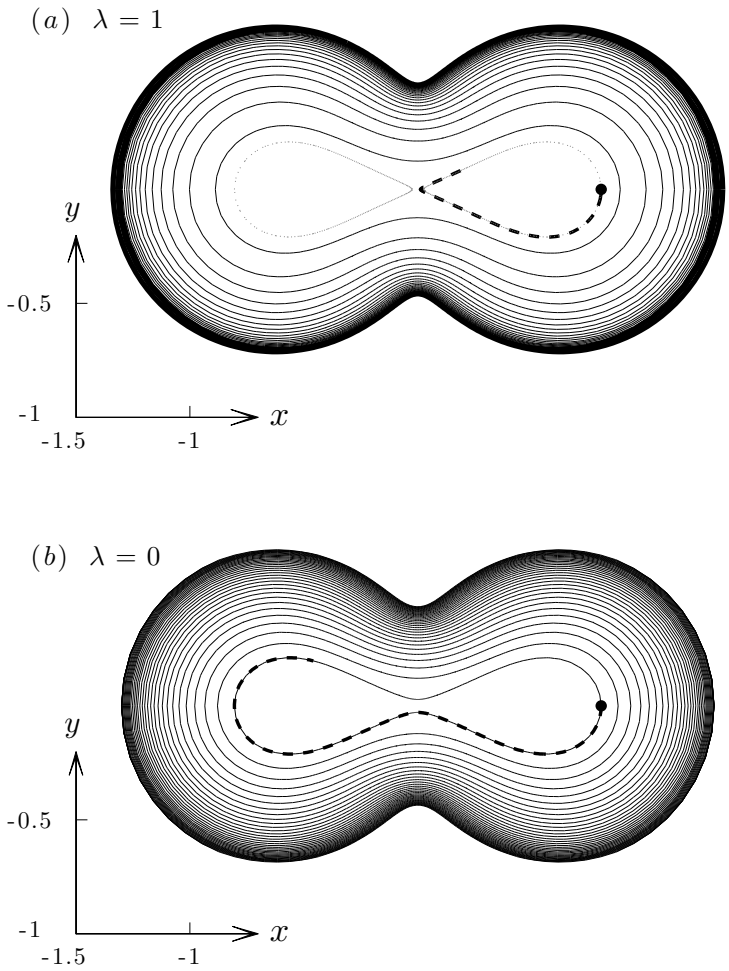

Figure 3.8: Isolines of $H(\boldsymbol{x}_1)$ for (a) a solitary QGSW vortex with $\lambda^{-1} = 1$ and $\Gamma_1 = 1$ (calculated as H_M with $M = 374$), and (b) a solitary 2D Euler vortex, in the Neumann oval given by (3.17) with $q = 0.7$. The thick dashed lines in each panel show the dynamically calculated trajectory of a vortex with initial position $\boldsymbol{x}_1(0) = (0.805\ 0)^T$ over 35 time units, with $\delta = 10^{-8}$. The contour interval is 0.078 in both panels except for the grey dotted contour in (a) (at level 0.097) plotted to illustrate the predicted trajectory.

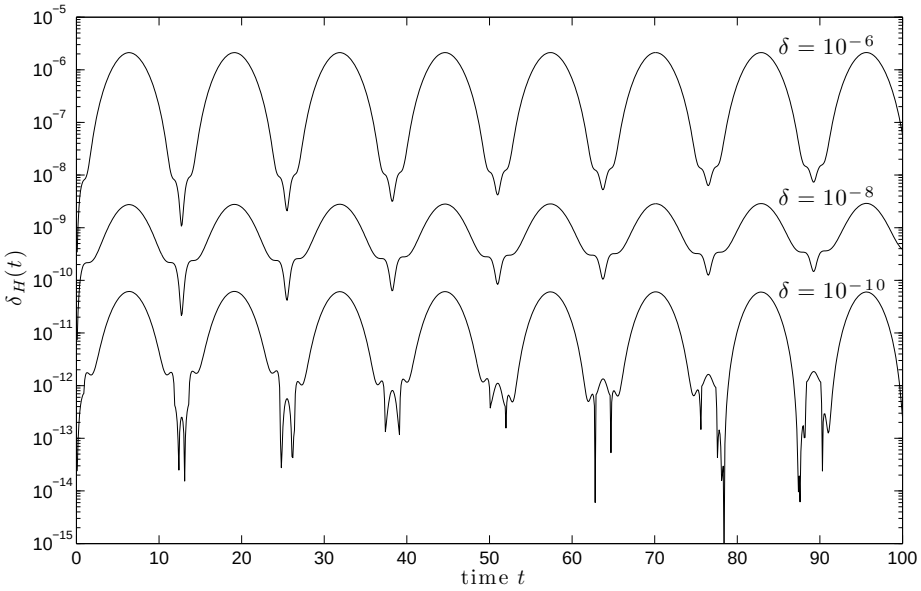

Figure 3.9: Time evolution of the error measure $\delta_H(t)$ (where H is estimated by H_M) over 100 non-dimensional time units (corresponding to approximately four complete circuits of the domain) for an QGSW vortex with $\lambda = 1$. Three values of the tolerance parameter $\delta = 10^{-6}, 10^{-8}, 10^{-10}$ are shown with $M = M_*(\delta) = 290, 374, 460$ the respective number of MFS charge points.

namics: the QGSW vortex recirculates within the same lobe, whereas the 2D Euler vortex circulates between the two lobes. It is also clear that, as expected, the 2D Euler vortex travels considerably further during the same time period.

Fig. 3.9 shows the time evolution of $\delta_H(t)$ ($H_r = 0.216$, 3 sig. fig.) during a further QGSW integration with $\boldsymbol{x}_1(0) = (0 \quad 0.3)^T$, over 100 non-dimensional time units, or approximately four complete circuits of the domain. Results are shown for three different values of the tolerance parameter $\delta = 10^{-6}, 10^{-8}$ and 10^{-10}, with corresponding numbers of MFS charge points $M_*(\delta) = 290, 374, 460$. The Hamiltonian error measure $\delta_H(t)$ is evidently linearly controlled by the tolerance parameter δ.

A further test will consider the errors in the trajectory of the vortex after one complete circuit of the Neumann oval, as computed dynamically using VOR-MFS. Consider the solitary QGSW vortex initially located at $\boldsymbol{x}_1(0) = (0 \quad 0.2)^T$ inside the Neumann oval. The vortex takes t_f time units to complete one circuit, after which it comes back to its starting position to within a tolerance $\Delta y = |0.2 - y(t_f)|$, the size of which gives an indication of the accuracy VOR-MFS when used dynamically in this situation.

The value of t_f is found with the decomposition

$$t_f = t_I + t_{II},$$

used as follows: the system is first integrated from $t = 0 \rightarrow t_I$ with $\Delta t = 0.1$ fixed, where t_I is chosen such that slightly less than one circuit is completed. Then the system is integrated for a final step from $t = t_I \rightarrow t_I + t_{II}$ with $\Delta t = t_{II}$, where t_{II} is found (to machine precision) using a shooting method combined with the secant method. The majority of the error in Δy, after t_f, will be from the steps where $\Delta t = 0.1$ with the final step (where $\Delta t < 0.1$) having a much smaller contribution. Note that δ will be the same for all steps.

With t_f found, the model is solved for various values of δ (and corresponding M_* predicted from (3.13), [not shown]) and a relationship between Δy and δ determined, and shown in figure 3.10; the dots are the numerical values and the solid line is a least squares fit. Again an exponential relationship is observed, with VOR-MFS performing accurately even at low precision.

3.3.4 Test Case IV: Multiple QGSW vortices in a Neumann oval

A final test for VOR-MFS is the simulation of the dynamics of many QGSW vortices in a Neumann oval. The dynamics of two or more vortices are chaotic and therefore more challenging numerically. As above, the main means of validating the algorithm is by verifying conservation of H (calculated as H_M from eqn. 3.8).

Fig. 3.11 shows the evolution of the error measure $\delta_H(t)$ for the Hamiltonian for three different runs with $N = 2, 4$ and 8 vortices and $H_r = -0.366, -0.719$ and -1.16, to 3 sig. fig. respectively. Numerical parameters are as for the 2D Euler calculations described in section 3.2. As in the 2D Euler case good convergence properties are evident.

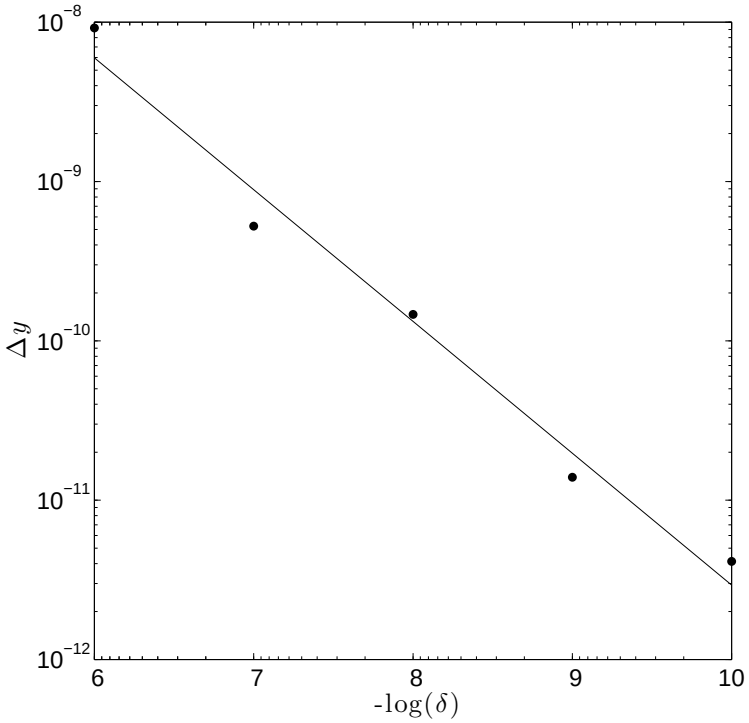

Figure 3.10: Relationship between Δy and δ (with M chosen by the M_*-δ protocol) for a single QGSW vortex after exactly one circuit of a Neumann oval. The dots are numerical values and the solid line a least-squares fit.

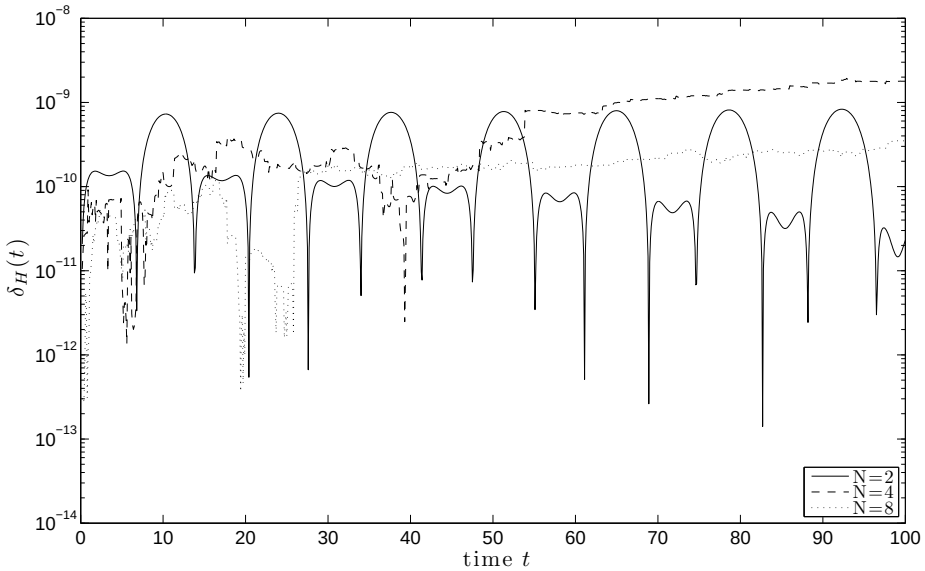

Figure 3.11: Time evolution of error measure $\delta_H(t)$ (where H is estimated by H_M) for VOR-MFS integrations with $N = 2, 4$ and 8 QGSW vortices (solid, dashed and dotted curves respectively). The value of the tolerance parameter was $\delta = 10^{-8}$ with $M = M_*(\delta) = 348$.

3.4 Conclusion

A new algorithm VOR-MFS has been presented above. It is designed to solve generalized point vortex models in arbitrary two-dimensional domains. The main advantages of the new algorithm are:

1. VOR-MFS requires knowledge of only the free-space ($\mathbb{R}^2$) Green's function $G_0(\boldsymbol{x}, \boldsymbol{x}')$ of the point vortex model in question, as opposed to the domain-adapted Green's function (required e.g. by image-based models). VOR-MFS can therefore be used to investigate the alternative point vortex models of geophysical interest discussed in chapter 1 (QGSW, SQG, etc.). Additionally, VOR-MFS can be used to solve the 2D Euler system in domains for which the Green's function $G(\boldsymbol{x}, \boldsymbol{x}')$ is not known explicitly or is expensive to calculate.

2. Subject to certain caveats [7], the MFS algorithm converges exponentially with the number of charge points M. Hence it is practical to choose M in order that the error associated with using the VOR-MFS algorithm is comparable to that of the underlying adaptive time-stepping scheme (see section 3.2.3).

3. The number M of MFS charge points required converges as the number of vortices $N \to \infty$. Consequently, for sufficiently large N, VOR-MFS becomes no more expensive (and eventually cheaper) to integrate than an image model adapted to the same problem.

One difficulty for the MFS method occurs when parts of the domain $\mathcal{D}$ are very thin (e.g. a flat plate or protrusion). In such domains VOR-MFS is likely to perform more like a boundary-integral method, similar to that in [92]. A further caveat, is that complicated domains that require a large number of MFS charge points could result in numerical difficulties, due to limitations associated with the size and apparent conditioning of the linear system (3.3). As discussed in section 3.2.1, this presents minimal practical problems.

The VOR-MFS algorithm opens up a number of interesting pathways for future research. In chapter 4 VOR-MFS will be used to test statistical mechanics predictions of the behaviour of the geophysical point vortex models mentioned chapter 1.

Some further possibilities for future research which are not addressed in this thesis are as follows. Chen [28] has demonstrated that MFS is effective in multiply connected domains, hence (for example) VOR-MFS could be used to validate and extend recent results describing vortex trajectories around islands [36]. Another possibility is that, with a few minor adaptations, VOR-MFS could be extended to study the dynamics of point vortex 'hetons' [62], i.e. two-layer quasi-geostrophic vortices of relevance in oceanography [38, 74, 75]. Further, the dynamics of large ensembles of three-dimensional quasi-geostrophic vortices has also prompted considerable interest [119], including numerical simulations of single-signed point vortices in an unbounded domain [63, 86]. There is potential for VOR-MFS to be extended to study the three-dimensional system in bounded domains, permitting the study of 'neutral' systems in which vortices of both signs are present.

Finally, it is interesting to speculate on whether or not the MFS algorithm could be used effectively to implement boundary conditions in dynamical models with piece-wise constant vorticity (contour dynamics, e.g. [41]) or even in models aiming to represent continuous vorticity distributions. In both cases the effective treatment of the continuous analogue of the 'pseudo-images' discussed in section 3.2.2 above will be paramount.

Chapter 4

Statistical mechanics of point vortices in the thermodynamic limit

4.1 Introduction

Two well-known scaling limits exist in the point vortex system: the hydrodynamic limit, valid only for positive energies, was studied in chapter 2, while the focus of this chapter is on the thermodynamic limit, valid for low positive and negative energies.

Here we will take the 'non-classical' thermodynamic limit $N \to \infty$, $\tilde{E} = NE \to$ constant, $|\mathcal{D}| =$ constant. This limit was considered for 2D Euler vortices by PL76, using the hierarchy introduced in section 1.3.5. PL76 considered the thermodynamic limit at sufficiently low energy (positive and negative) where the mean flow $\omega_1(\boldsymbol{x}) = 0$ is negligible and can be ignored, leaving the fluctuations described by the correlation function $\omega_2(\boldsymbol{x}, \boldsymbol{x}')$ as the key quantity. In a manner analogous to the derivation of the sinh-Poisson equation/elliptic-sinh equation for the statistical description of the mean flow in the hydrodynamic limit, PL76 derived an equation (c.f. eqn. 35) for the statistical description of the fluctuations in their thermodynamic limit. In this chapter, a variant of PL76's equation, referred to as the *vorticity fluctuation equation*, is derived and solved for a generalised dynamics.

To demonstrate an application of the VOR-MFS algorithm of chapter 3, the

statistics of a system of quasi-geostrophic shallow water (QGSW) vortices will be tested against the theoretical predictions of the vorticity fluctuation equation.

This chapter is a generalisation and extension of the publication by Esler, Ashbee & McDonald [45] (EAM13 hereafter) and is structured as follows. The vorticity fluctuation equation is derived in section 4.2 and solved in section 4.3. In section 4.4 the theoretical predictions of the vorticity fluctuation equation are compared with numerical experiments using QGSW vortices. In section 4.5 conclusions are drawn and further work is considered. Finally, in appendix 4.A some details of ongoing work are given.

Before proceeding, a point made in section 1.3.4 is re-emphasised. The standard 'classical' thermodynamic limit is to take $|\mathcal{D}| \to \infty$ and $N \to \infty$ while $N/|\mathcal{D}| \to$ constant, and for a classical system such as an ideal gas, this limit gives domain independent results. However domain-independence is inconsistent with the long-ranged interaction of 2D Euler vortices governed by the Laplacian (1.6) and QGSW vortices (with moderate Rossby radius) governed by the modified Helmholtz operator (1.7), where the influence of the boundary cannot be scaled away. Further, in this limit it has been proved [52] that Onsager's predicted negative temperatures (see section 1.3.2) cannot exist, contradicting numerical evidence [18, 45]. Evidently it is more interesting to take the non-classical thermodynamic limit $N \to \infty$, $\tilde{E} \to$ constant as will be done here.

4.2 Derivation of the vorticity fluctuation equation

The following treatment will be presented for a generalised vortex dynamics, as defined for an linear, elliptic and self-adjoint operator $\mathcal{L}$ (introduced in section 1.2.1) with corresponding Green's function $G(\boldsymbol{x}, \boldsymbol{x}')$ and dynamics governed by

$$\mathcal{L}G(\boldsymbol{x}, \boldsymbol{x}') = \delta(\boldsymbol{x} - \boldsymbol{x}').$$

Recall that the dynamics of 2D Euler vortices are defined by

$$\mathcal{L} \equiv \nabla^2, \qquad G_0(\boldsymbol{x}, \boldsymbol{x}') = \frac{1}{2\pi} \log(|\boldsymbol{x} - \boldsymbol{x}'|),$$

and QGSW dynamics are defined by

$$\mathcal{L} \equiv \nabla^2 - \lambda^2, \qquad G_0(\boldsymbol{x}, \boldsymbol{x}') = -\frac{1}{2\pi} K_0(\lambda|\boldsymbol{x} - \boldsymbol{x}'|),$$

where is λ^{-1} the Rossby radius and controls the range of the interaction.

In this section, theoretical expressions for the density of states $W_t(\tilde{E})$ and the inverse thermodynamic temperature $\beta_t(\tilde{E})$, valid at small energies in the non-classical thermodynamic limit $N \to \infty$, $\tilde{E} \to$ constant will be derived for a generalised vortex i.e one governed by the the linear, elliptic and self-adjoit operator $\mathcal{L}$. As detailed in section 1.3.3, it is straightforward to construct finite N estimates of the density of states $W(\tilde{E})$ using histogram methods. It was shown in [18] that for a certain domain $\mathcal{D}$ (a parallelogram) the density of states converges as

$$\lim_{N\to\infty} \frac{1}{N} W(\tilde{E}/N) = W_t(\tilde{E}), \tag{4.1}$$

with similar behaviour expected for a general domain. From EAM13 it appears that convergence is apparent for as few as $N = 100$ vortices. A corresponding limiting form of $\beta(\tilde{E})$ is also expected

$$\beta_t(\tilde{E}) = \frac{W_t'(\tilde{E})}{W_t(\tilde{E})}.$$

The starting point for determining these theoretical expressions is to derive the vorticity fluctuation equation. This is done by considering the PL76 cumulant hierarchy in the thermodynamic limit, $N \to \infty$, $\tilde{E} \to$ constant. As in sections 1.3.5 and 2.2.2, this theory is presented for a generalised vortex dynamics, though at a number of junctures reference will be made to the 2D Euler system to allow for direct comparisons with PL76 and EAM13.

When taking the thermodynamic limit, PL76 simultaneously truncate the infinite hierarchy of cumulant equations that were introduced in section 1.3.5. No formal

justification of this truncation is given, other citing the success of a similar approach for other problems in physics. As in EAM13, here we conjecture that the cumulant equations (e.g. (1.48-1.50)) admit asymptotic solutions in the small parameter $\epsilon = N^{-1/2}$. If this conjecture were proved, it would provide formal justification of PL76's truncation.

Consequently, the existence of an asymptotic hierarchy satisfying the cumulant equations in the thermodynamic limit will be assumed. As mentioned in section 4.1 it is also assumed that energy of the system is sufficiently low so that there is no mean flow (i.e. $\omega_1 = 0$). The absence of a mean flow, along with the symmetry of the microcanonical ensemble dictates that other odd vorticity moments are also zero, that is $\omega_3 = \omega_5 = \ldots = 0$ and consequently cross-correlations involving odd vorticity modes are also zero, e.g. $c_2 = 0$, see (1.53)). It is natural then to look for asymptotic series solutions for the remaining nonzero terms in the hierarchy that are of the form

$$\begin{aligned} \rho_1(\boldsymbol{x}) &= \rho_0 + \epsilon^2 \rho_1^{(1)} + \ldots \\ \omega_2(\boldsymbol{x}, \boldsymbol{x}') &= \epsilon^2 \left(\omega_2^{(0)} + \epsilon^2 \omega_2^{(1)} + \ldots \right) \\ \rho_2(\boldsymbol{x}, \boldsymbol{x}') &= \epsilon^4 \left(\rho_2^{(0)} + \epsilon^2 \rho_2^{(1)} + \ldots \right) \\ &\text{etc.} \end{aligned} \tag{4.2}$$

Here $\rho_0 = |\mathcal{D}|^{-1}$, the inverse of the domain area, is the leading term in the vortex density expansion in this scaling regime. Note that an exactly uniform distribution of vortices corresponds to $\rho_1(\boldsymbol{x}) = \rho_0$.

Inserting the expansions (4.2) into the second order cumulant equation for $\nabla\omega_2(\boldsymbol{x}, \boldsymbol{x}')$, i.e. (1.52), and equating terms of order ϵ^2 leads to the following equation

$$\nabla\omega_2^{(0)}(\boldsymbol{x}, \boldsymbol{x}') = \rho_0 \left(\partial_{\tilde{E}} + \beta \right) \left(\nabla\psi_2^{(0)}(\boldsymbol{x}, \boldsymbol{x}') + \rho_0 \nabla G(\boldsymbol{x}, \boldsymbol{x}') \right), \tag{4.3}$$

which is satisfied by the leading-order vorticity fluctuations. Here $\omega_2^{(0)}$ is symmetric in its arguments, and is subject to an integral constraint

$$\int_{\mathcal{D}} \omega_2^{(0)}(\boldsymbol{x}, \boldsymbol{x}') \, d\boldsymbol{x} = -\rho_0, \tag{4.4}$$

obtained by inserting the expansion (4.2) into the definition of the second order cumulant $c_2(\boldsymbol{x},\boldsymbol{x}')$, see (1.41). Similarly, the leading order correction to the mean vortex density is found to be given by

$$\nabla\rho_1^{(1)}(\boldsymbol{x}) = \left(\partial_{\tilde{E}} + \beta\right)\int_{\mathcal{D}} \nabla G(\boldsymbol{x},\boldsymbol{x}')\omega_2^{(0)}(\boldsymbol{x},\boldsymbol{x}')\,d\boldsymbol{x}' + \frac{1}{2}\beta\rho_0\nabla g(\boldsymbol{x},\boldsymbol{x}). \tag{4.5}$$

The energy equation (1.46) at $O(\epsilon^2)$ (and in the absence of a mean flow) is given by

$$\tilde{E} = -\frac{1}{2}\int_{\mathcal{D}} \psi_2^{(0)}(\boldsymbol{x},\boldsymbol{x})\,d\boldsymbol{x} - \frac{g_0}{2}, \tag{4.6}$$

where $g_0 = \rho_0\int_{\mathcal{D}} g(\boldsymbol{x},\boldsymbol{x})\,d\boldsymbol{x}$. To obtain a general solution to the system (4.3-4.6), it turns out to be necessary to integrate (4.3) rather than take its divergence as done by PL76[1]. This gives the integro-differential equation

$$\begin{aligned}\omega_2^{(0)}(\boldsymbol{x},\boldsymbol{x}') &= -\rho_0^2 + \rho_0\left(\partial_{\tilde{E}} + \beta\right)\left(\psi_2^{(0)}(\boldsymbol{x},\boldsymbol{x}') - \rho_0\int_{\mathcal{D}}\psi_2^{(0)}(\boldsymbol{x},\boldsymbol{x}')\,d\boldsymbol{x}\right)\\ &\quad +\beta\rho_0^2\left(G(\boldsymbol{x},\boldsymbol{x}') - \rho_0 G_0(\boldsymbol{x}')\right).\end{aligned} \tag{4.7}$$

Using the integral constraint (4.4), (4.7) can be expressed as

$$\omega_2^{(0)} = -\rho_0^2 + \rho_0\left(\partial_{\tilde{E}} + \beta\right)\mathcal{K}\omega_2^{(0)} + \beta\rho_0^2\mathcal{K}\delta(\boldsymbol{x}-\boldsymbol{x}'), \tag{4.8}$$

where $\mathcal{K}$ is the integral operator defined by

$$\begin{aligned}\mathcal{K}\phi(\boldsymbol{x}) &\equiv \int_{\mathcal{D}} K(\boldsymbol{x},\bar{\boldsymbol{x}})\,\phi(\bar{\boldsymbol{x}})\,d\bar{\boldsymbol{x}},\\ \text{where}\quad K(\boldsymbol{x},\bar{\boldsymbol{x}}) &= G(\boldsymbol{x},\bar{\boldsymbol{x}}) - \bar{G}(\boldsymbol{x}) - \bar{G}(\bar{\boldsymbol{x}}),\\ \bar{G}(\boldsymbol{x}) &= \rho_0\int_{\mathcal{D}} G(\boldsymbol{x},\bar{\boldsymbol{x}})\,d\bar{\boldsymbol{x}}.\end{aligned} \tag{4.9}$$

Equation (4.8) is the *vorticity fluctuation equation*: the key equation of the thermodynamic scaling regime, analogous to the elliptic-sinh equation in the hydrody-

[1]Considering the 2D Euler system, note that upon taking the divergence of (4.3), the resulting equation, together with (4.5-4.6) can be seen to be related to equations appearing in PL76. Specifically, the divergence of (4.3) and (4.6) are identical to eqns. 35 and 37 of PL76, upon identifying $\omega_2^{(0)}$ with PL76's $F(1,2)-1$, and rescaling $\beta \to 8\pi\lambda$, and (4.5) is analogous to PL76's eqn. 36.

namic regime (see chapter 2). Its solution will be described in the next section.

As will be detailed in the next subsection, the operator (4.9) yields an eigenvalue problem that is identical to the vorticity mode eigenvalue problem (2.26), first introduced in chapter 2 through linearising the sinh-Poisson equation (2.11). The vorticity modes are a natural basis with which to solve (4.8). This is a remarkable result: the vorticity modes are the key to determining the statistics of the vortex system in *both* the thermodynamic limit *and* the hydrodynamic limit.

4.3 Solution of the vorticity fluctuation equation

4.3.1 Vorticity modes

As stated in the previous section, the operator (4.9) can yield the vorticity mode eigenvalue problem (2.26) from chapter 2 i.e.

$$\begin{aligned} \mathcal{L}\Phi_k &= \beta_k \rho_0 \Phi_k, && \boldsymbol{x} \in \mathcal{D}, \\ \Phi_k &= \text{constant}, && \boldsymbol{x} \in \partial\mathcal{D} \\ \int_{\mathcal{D}} \mathcal{L}\Phi_j \, d\boldsymbol{x} &= 0. \end{aligned}$$

To show the equivalence between (4.9) and (2.26) the following calculations are required: first, note that from the symmetry of the kernel $K(\boldsymbol{x}, \bar{\boldsymbol{x}})$, and the close relationship between K and the Dirichlet kernel $G(\boldsymbol{x}, \bar{\boldsymbol{x}})$, that the operator $\mathcal{K}$ is self-adjoint. The Hilbert-Schmidt theorem [37] then states that the eigenvalue problem

$$\mathcal{K}\Phi_j = \frac{1}{\beta_j \rho_0}\Phi_j, \quad j = 0, 1, 2, \ldots, \tag{4.11}$$

generates a set of real eigenvalues $\{\beta_j\}$ (the *domain inverse temperatures* [DITs]) with corresponding eigenfunctions $\{\Phi_j\}$ (the *vorticity modes*) that form a complete orthonormal basis for the function space $L^2[\mathcal{D}]$, i.e. the $\{\Phi_j\}$ can be normalised so

that

$$\int_{\mathcal{D}} \Phi_j(\boldsymbol{x})\Phi_k(\boldsymbol{x})\, d\boldsymbol{x} = \delta_{jk}.$$

Importantly the first eigenfunction is given by $\Phi_0(\boldsymbol{x}) =$ constant, hence the remaining modes satisfy

$$\int_{\mathcal{D}} \Phi_j(\boldsymbol{x})\, d\boldsymbol{x} = 0, \quad j = 1, 2, 3, \ldots. \tag{4.12}$$

At this point it is still not clear how the eigenvalue problem (4.11) is equivalent to the original vorticity mode eigenvalue problem (2.26) introduced in chapter 2. Three further calculations reveal the equivalence:

1. Applying the general linear, elliptic and self-adjoint operator $\mathcal{L}$ with corresponding Green's function $G(\boldsymbol{x}, \boldsymbol{x}')$ (re-introduced in section 4.1) to both sides of (4.11) gives

   $$\beta_j\rho_0 \left(\Phi_j - \rho_0 \int_{\mathcal{D}} \Phi_j\, d\boldsymbol{x} \right) = \mathcal{L}\Phi_j, \quad j = 0, 1, 2, 3, \ldots,$$

   and it follows from (4.12) that the vorticity modes (for $j \geq 1$) satisfy the eigenvalue problem

   $$\mathcal{L}\Phi_j = \beta_j\rho_0\Phi_j, \quad j = 1, 2, 3, \ldots, \tag{4.13}$$

   which is identical to (2.26a).

2. On the boundary i.e. $\boldsymbol{x} \in \partial\mathcal{D}$

   $$\Phi_j(\boldsymbol{x}) = -\beta_j\rho_0 \int_{\mathcal{D}} \bar{G}(\bar{\boldsymbol{x}})\Phi_j(\bar{\boldsymbol{x}})\, d\bar{\boldsymbol{x}} = \text{constant}, \tag{4.14}$$

   since $G(\boldsymbol{x}, \boldsymbol{x}') = \bar{G}(\boldsymbol{x}) = 0$ for $\boldsymbol{x} \in \partial\mathcal{D}$. Equation (4.14) is identical to (2.26b).

3. Integrating (4.13), gives

   $$\int_{\mathcal{D}} \mathcal{L}\Phi_k\, d\boldsymbol{x} = \beta_j\rho_0 \int_{\mathcal{D}} \Phi_k\, d\boldsymbol{x} = 0, \quad k = 1, 2, 3, \ldots, \tag{4.15}$$

   which is identical to the boundary integral constraint (2.26c).

In summary, (4.13), (4.14) and (4.15) are identical to (2.26a), (2.26b) and (2.26c) respectively. In other words, (4.11) is identical to the original DIT eigenvalue problem (2.26).

For the special case of QGSW vortices, as governed by the modified Helmholtz operator (introduced in 1.2.1 and reintroduced in section 4.2), the vorticity mode eigenvalue problem is

$$(\nabla^2 - \lambda^2)\Phi_j = \beta_j \rho_0 \Phi_j, \qquad \boldsymbol{x} \in \mathcal{D} \tag{4.16a}$$

$$\Phi_j = \text{constant}, \qquad \boldsymbol{x} \in \partial\mathcal{D} \tag{4.16b}$$

$$\oint_{\partial\mathcal{D}} (\boldsymbol{k} \times \nabla\Phi_j) \cdot d\boldsymbol{s} = 0, \tag{4.16c}$$

where the integral constraint (4.16c) has been simplified using the divergence theorem; see section 2.2. This is the system that will be used in section 4.4.

Vorticity modes are computed using a grid in the circular domain of $\mathcal{N} \times \mathcal{M} = 50 \times 100$ points in the radial and azimuthal directions respectively – the same grid used in the sinh-Poisson equation solutions of section 2.4.4. Further details on conformal grids are given in appendix A.4.

4.3.2 Analytical solution

Returning to our goal to solve the vorticity fluctuation equation (4.8), it makes sense to seek solutions in the form of an expansion in the vorticity mode basis functions $\{\Phi_k\}$, as introduced in 4.3.1. Namely

$$\omega_2^{(0)}(\boldsymbol{x}, \boldsymbol{x}') = -\rho_0^2 + \rho_0 \sum_{j=1}^{\infty} \sum_{k=1}^{\infty} a_{jk}(\tilde{E}) \Phi_j(\boldsymbol{x}) \Phi_k(\boldsymbol{x}'). \tag{4.17}$$

The ansatz (4.17) automatically satisfies the integral constraint (4.4) because the first moment (4.12) of each vorticity mode vanishes. Inserting (4.17) into (4.8) and equating coefficients leads to

$$\beta_j a_{jk} = (\partial_{\tilde{E}} + \beta)\, a_{jk} + \beta \delta_{jk} \quad (j, k \geq 1). \tag{4.18}$$

Solutions of the homogeneous equation for a_{jk} are unphysical, i.e. they are unbounded as $\tilde{E} \to -\infty$, hence only the diagonal elements are non-zero. It follows that the solution is consistent with the $\boldsymbol{x} \leftrightarrow \boldsymbol{x}'$ symmetry implicit in the definition of $c_2(\boldsymbol{x}, \boldsymbol{x}')$, see (1.41).

Evidently the inverse temperature β in (4.18) must be regarded as a function of the scaled energy in the thermodynamic scaling limit, i.e. $\beta = \beta_t(\tilde{E})$ in (4.18). The diagonal terms in (4.18) can be obtained in terms of the corresponding entropy

$$S_t(\tilde{E}) = \int^{\tilde{E}} \beta_t(\hat{E})\, d\hat{E},$$

by direct integration, giving

$$a_{jj}(\tilde{E}) = -1 - \beta_j \exp\Big(-(S_t(\tilde{E}) - \beta_j \tilde{E})\Big) \int_{-\infty}^{\tilde{E}} \exp\Big(S_t(\hat{E}) - \beta_j \hat{E}\Big)\, d\hat{E}. \tag{4.19}$$

Inserting (4.17) into the energy equation (4.6), results in

$$\begin{aligned} -\frac{1}{2}\sum_{j=1}^{\infty} \frac{a_{jj}}{\beta_j} &= \tilde{E} - \tilde{E}_0, \qquad (4.20)\\ \text{where } \tilde{E}_0 &= \frac{G_{00} - g_0}{2} \text{ and } G_{00} = \rho_0^2 \int_{\mathcal{D}^2} G(\boldsymbol{x}, \bar{\boldsymbol{x}})\, d\boldsymbol{x}\, d\bar{\boldsymbol{x}}. \end{aligned}$$

Inserting (4.19) into the sum in (4.20) results in the linear integral equation

$$\tilde{E} - \tilde{E}_0 = \frac{1}{2}\sum_{j=1}^{\infty} \left(\frac{1}{\beta_j} + \exp\Big(-S(\tilde{E})\Big) \int_{-\infty}^{\tilde{E}} \exp\Big(S(\hat{E}) + \beta_j(\tilde{E} - \hat{E})\Big)\, d\hat{E} \right). \tag{4.21}$$

Following PL76, we substitute $W_t = \exp(S_t)$ into (4.21) to give

$$\Big(\tilde{E} - \tilde{E}_0\Big) W_t(\tilde{E}) = \frac{1}{2}\sum_{j=1}^{\infty} \left(\frac{W_t(\tilde{E})}{\beta_j} + \int_{-\infty}^{\tilde{E}} W_t(\hat{E}) \exp\Big(\beta_j(\tilde{E} - \hat{E})\Big)\, d\hat{E} \right). \tag{4.22}$$

Taking the Fourier transform of (4.22) gives the first order ordinary differential equation in the transform variable k

$$\mathrm{i}\frac{d\widehat{W}_t(k)}{dk} - \tilde{E}_0 \widehat{W}_t(k) = -\frac{1}{2}\left(\sum_{j=1}^{\infty} \frac{\mathrm{i}k}{\beta_j(\beta_j - \mathrm{i}k)} \right) \widehat{W}_t(k), \tag{4.23}$$

which can be integrated to give

$$\widehat{W_t}(k) = W_0 \exp\left[-\mathrm{i}\tilde{E}_0 k - \sum_{j=1}^{\infty} \frac{1}{4}\log\left(1+\frac{k^2}{\beta_j^2}\right) + \frac{\mathrm{i}}{2}\left(\frac{k}{\beta_j} - \tan^{-1}\left(\frac{k}{\beta_j}\right)\right)\right], \tag{4.24}$$

where W_0 is a normalising constant. Taking the inverse Fourier transform of (4.24) gives

$$W_t(\tilde{E}) = \frac{W_0}{\sqrt{2\pi}} \int_{-\infty}^{\infty} f_1(k;\beta_j) \exp\Big(\mathrm{i}(\tilde{E}-\tilde{E}_0)k - \mathrm{i}f_2(k;\beta_j)\Big)\, dk, \tag{4.25}$$

where f_1 and f_2 are real valued functions given by

$$f_1(k;\beta_j) = \prod_{j=1}^{\infty}\left(1+\frac{k^2}{\beta_j^2}\right)^{-1/4}, \tag{4.26}$$

$$f_2(k;\beta_j) = \frac{1}{2}\sum_{j=1}^{\infty}\left(\frac{k}{\beta_j} - \tan^{-1}\left(\frac{k}{\beta_j}\right)\right). \tag{4.27}$$

The corresponding inverse temperature can be written in a form convenient for numerical quadrature as the ratio of the two real integrals

$$\beta_t(\tilde{E}) = \frac{W_t'(\tilde{E})}{W_t(\tilde{E})} = -\frac{\displaystyle\int_0^{\infty} k f_1(k;\beta_j)\sin\Big(k(\tilde{E}-\tilde{E}_0) - f_2(k;\beta_j)\Big)\, dk}{\displaystyle\int_0^{\infty} f_1(k;\beta_j)\cos\Big(k(\tilde{E}-\tilde{E}_0) - f_2(k;\beta_j)\Big)\, dk}. \tag{4.28}$$

It is evident from (4.28) that the limiting thermodynamic curve is completely determined, up to a shift in the ordinate due to a change[2] in $\tilde{E}_0$, by the distribution of DITs $\{\beta_j\}$. The amplitude function $f_1(k)$ decays exponentially as $k \to \infty$ rendering numerical quadrature of (4.28) straightforward.

Using $W_t = \exp(S_t)$, (4.25) is inserted into (4.19), and evaluating the $\hat{E}$-integral

[2]For 2D Euler vortices, a change in domain size by a factor $\mu \in \mathbb{R}$ i.e. $\mathcal{D} \to \mu\mathcal{D}$ results in a shift $\tilde{E}_0 \to \tilde{E}_0 - (1/4\pi)\log\mu$. A similar result is expected for QGSW vortices. In both cases the DITs, be definition, remain unchanged.

results allows the diagonal coefficients a_{jj} to be evaluated as

$$a_{jj}(\tilde{E}) = -\frac{1}{\int_0^\infty f_1(k)\cos\Big(k(\tilde{E}-\tilde{E}_0)-f_2(k)\Big)\,dk}\int_0^\infty f_1(k)(k^2+\beta_j^2)^{-1}\times \\ \Big(k^2\cos\Big(k(\tilde{E}-\tilde{E}_0)-f_2(k)\Big)+\beta_j k\sin\Big(k(\tilde{E}-\tilde{E}_0)-f_2(k)\Big)\Big)\,dk. \tag{4.29}$$

The coefficients $\{a_{jj}\}$ determine the partitioning of the energy into fluctuations associated with each vorticity mode. In section IV. C. of EAM13 it was shown that $\{a_{jj}\}$ have a simple dynamical interpretation in terms of the time-variance of the projection of the vorticity field $\omega(\boldsymbol{x})$ onto the corresponding vorticity mode $\Phi_j(\boldsymbol{x})$. Changes in energy partitioning between the vorticity modes, as $\tilde{E}$ increases, were shown to give insight into the nature of the transition between states with and without a mean flow.

The theoretical results of sections 4.2-4.3 are compared to numerical results for the QGSW system. To allow for direct comparisons between the QGSW system considered here and the 2D Euler system considered in EAM13, the same domains are used in both cases. Consequently, much of the details are the same for both systems.

The final point in this section concerns (4.25) and (4.28) for large values of λ^2. Recal that the PL76 hierarchy introduced in section 1.3.5 is based on the small parameter $\epsilon = 1/N$, $N \to \infty$ and thus is only valid when terms smaller than $O(1/N)$ can be ignored. In particular we require

$$\frac{1}{N} \ll \frac{\rho_0}{\lambda^2}, \tag{4.30}$$

to be satisfied in order to justifiably use the PL76 hierarchy. So, for example, let us say we require $1/N$ to be an order of magnitude smaller than ρ_0/λ^2 for (4.30) to be satisfied. Thus, for $\lambda^2 = 4$ approximately $N = 100$ vortices are required, while for $\lambda^2 = 100$ approximately $N = 3000$ vortices are needed

4.4 Comparison of the vorticity fluctuation equation with numerical experiments: QGSW vortices

4.4.1 Domain inverse temperatures in Neumann ovals

The theoretical results presented in the previous section will now be tested against numerical results for the QGSW vortex system. Recall from section 1.2.1, that QGSW dynamics are defined by $\mathcal{L} \equiv \nabla^2 - \lambda^2, G_0(\boldsymbol{x}, \boldsymbol{x}') = -\frac{1}{2\pi} K_0(\lambda|\boldsymbol{x} - \boldsymbol{x}'|)$, with the Rossby radius λ^{-1} controlling the range of the interaction. For $\lambda \neq 0$, QGSW dynamics are shorter ranged than the dynamics of 2D Euler vortices, which are defined by $\mathcal{L} \equiv \nabla^2, \quad G_0(\boldsymbol{x}, \boldsymbol{x}') = \frac{1}{2\pi} \log(|\boldsymbol{x} - \boldsymbol{x}'|)$. In the limit $\lambda \to 0$ the modified Helmholtz operator $\mathcal{L} \equiv \nabla^2 - \lambda^2$ governing QGSW vortices, becomes the Laplace operator $\mathcal{L} \equiv \nabla^2$ governing 2D Euler vortices. Note that there is a degree of freedom in the choice of the free space Green's function G_0 for the 2D Euler system in that one can add an arbitrary constant – we will exploit this in section 4.4.3. In EAM13 the 2D Euler system was considered and it will also be used in this chapter as a reference point to investigate the QGSW system.

The first step to compute the theoretical prediction for the density of states (4.25) and the inverse temperature curve (4.28) for QGSW or 2D Euler vortices is to calculate[3] the DITs $\{\beta_i\}$ (introduced in section 2.2.1 and reintroduced in section 4.3.1) as was done for the heart domain (2.40) in chapter 2. The domains chosen in this chapter are from the one-parameter family of Neumann ovals, introduced in section 3.3.2 and first used in [100] in the context of Hele-Shaw flows. Details of the modifications of the vorticity mode eigenvalue problem (4.16) for a general conformal domain are given in appendix A.3.1.

[3]The DITs may be calculated analytically for the disk (given by zeros of Bessel functions), but the microcanonical ensemble, defined by the PDF (1.31), is not correct in this case as the additional invariant of angular momentum has not been incorporated (though could be done so relatively straightforwardly).

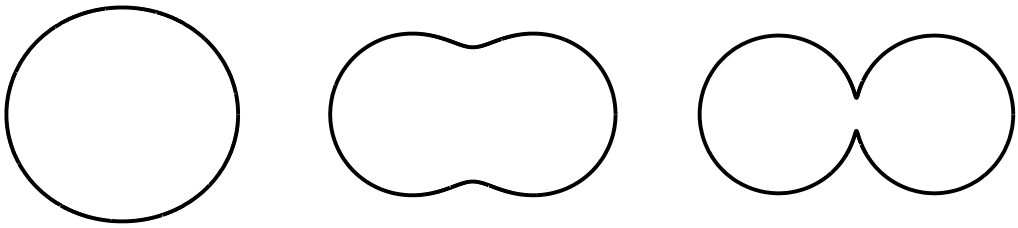

$q = 0.2$ $q = 0.6$ $q = 0.9$

Figure 4.1: Examples of the family of Neumann oval domains of area π, generated by the conformal map (A.11) for $q = 0.2$, 0.6 and 0.9.

Recall from section 3.3.2 that the conformal map from the unit circle $\mathcal{C}$ in the Z-plane to the Neumann oval $\mathcal{D}$ in the z-plane is given by (3.17), namely

$$z = F(Z) = \frac{a(q)Z}{1 - q^2 Z^2}, \quad a \in \mathbb{R}.$$

This family of domains varies, as shown in figure 4.1, from a single cylinder, centre the origin (when $q \to 0$), to two separate cylinders touching at the origin (when $q \to 1$). As expected, varying the parameter q alters the distribution of DITs. The two domains used in this chapter are defined by $q = 0.3$ and $q = 0.8$, and contour plots of these vorticity modes and corresponding DITs for the 2D Euler system (i.e. $\lambda^2 = 0$) are shown in figure 4.2. Recall that for the QGSW system (i.e. $\lambda \neq 0$) the DIT spectrum is shifted by $-\lambda^2/\rho_0$ relative to the 2D Euler system DIT spectrum. The vorticity modes remain unchanged. The significantly different distributions of DITs in the $q = 0.3$ domain compared to the $q = 0.8$ domain will be key in explaining the different structures of density of states and inverse temperature curve that will be seen later in this chapter.

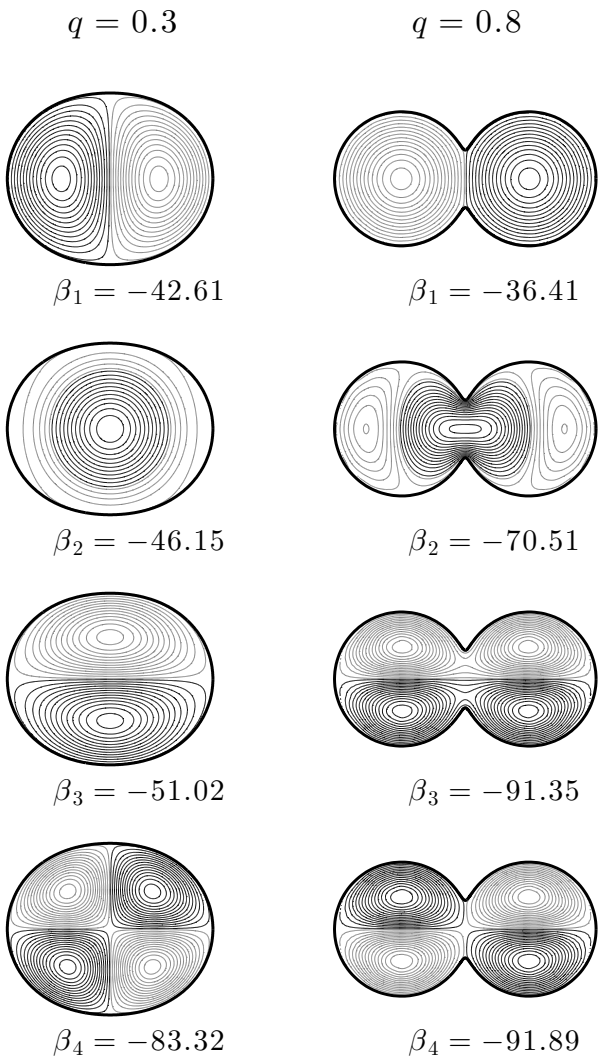

Figure 4.2: Left: Contour plots of the first four vorticity modes $\Phi_j(\boldsymbol{x})$ $(j = 1, 2, 3, 4)$ and corresponding DITs β_j (to 4 sig. figs.) for the $q = 0.3$ Neumann oval domain. Right: as left for the $q = 0.8$ Neumann oval domain. In both cases black contours are positive and grey contours are negative.

4.4.2 Calculation of the constants G_{00} and g_0

With the DITs calculated in the previous section, the next step in evaluating (4.25) and (4.28) is to calculate the constant $\tilde{E}_0$, as defined by G_{00} and g_0

$$G_{00} = \rho_0^2 \int_{\mathcal{D}^2} G(\boldsymbol{x}, \bar{\boldsymbol{x}})\, d\boldsymbol{x}\, d\bar{\boldsymbol{x}}, \tag{4.31}$$

$$g_0 = \rho_0 \int_{\mathcal{D}} g(\boldsymbol{x}, \boldsymbol{x})\, d\boldsymbol{x}, \tag{4.32}$$

where G is Green's function of the first kind for the domain (defined by (1.3)) and g is the residual Green's function (defined by (1.4)). The double integral (4.31) is straightforward to compute for both the 2D Euler system and the QGSW system using the appropriate vorticity mode basis and the completeness relation definition of the Green's function

$$G(\boldsymbol{x}, \bar{\boldsymbol{x}}) = \sum_{j=0}^{\infty} \frac{\Phi_j(\boldsymbol{x})\Phi_j(\bar{\boldsymbol{x}})}{\rho_0 \beta_j},$$

which leads to

$$G_{00}(\boldsymbol{x}, \bar{\boldsymbol{x}}) = \sum_{j=0}^{\infty} \frac{\rho_0}{\beta_j} \left(\int_{\mathcal{D}} \Phi_j(\boldsymbol{x})\, d\boldsymbol{x} \right)^2. \tag{4.33}$$

To demonstrate convergence of the above calculation figure 4.4 shows the error relative to the highest resolution computed of G_{00} for $q = 0.8$, $\lambda^2 = 0$ (dark grey dots), 4 (black diamonds), 100 (light grey squares). Note that after $\mathcal{N} \approx 35$ the errors in all three curves in figure 4.4 are very similar. This is as expected since all three calculations for (4.33) are effectively the same, since the DITs $\{\beta_j\}$ for $\lambda \neq 0$ are simply shifted by $-\lambda^2/\rho_0$ relative to the $\lambda = 0$ DITs. The differences for $\mathcal{M} \lesssim 35$ are evidently due to the non-convergence of the DITs at these resolutions (see appendix A.4). The final values of (4.33) for the domains and values of λ^2 considered in this chapter are given in table 4.1.

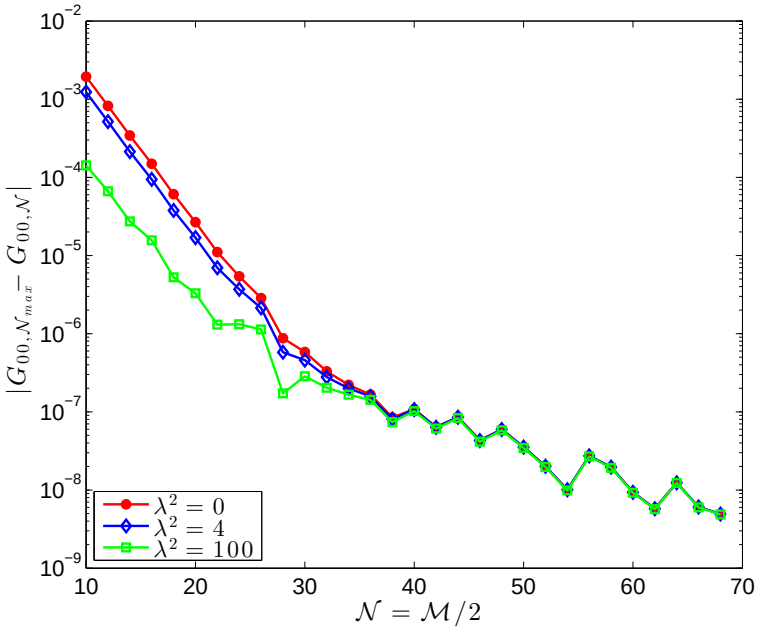

Figure 4.3: Convergence of the constant G_{00} (relative to G_{00} calculated with the highest resolution grid of $\mathcal{N} \times \mathcal{M} = 70 \times 140$) with the number of grid points for the $q = 0.8$ Neumann oval for $\lambda^2 = 0$ (dark grey dots), $\lambda^2 = 4$ (black diamonds), and $\lambda^2 = 100$ (light grey squares).

G_{00}	$\lambda^2 = 0$	$\lambda^2 = 4$	$\lambda^2 = 36$	$\lambda^2 = 100$
$q = 0.3$	-0.03926	-0.02384	-0.006133	-0.002574
$q = 0.8$	-0.02342	-0.01701	-0.005529	-0.002437

Table 4.1: Values of the constant G_{00} (to 4 sig. figs.) for $\lambda^2 = 0$, 4, 36, 100 in Neumann ovals defined by $q = 0.3$, 0.8.

For the QGSW system considered in this chapter, the function g appearing in the integrand (4.32) may be evaluated using the VOR-MFS algorithm, as was done in section 3.3.3. Namely

$$g(\boldsymbol{x}, \boldsymbol{x}) = -2 \sum_{k=1}^{M} \alpha_k G_0(\boldsymbol{x}, \boldsymbol{y}_k), \tag{4.34}$$

where $\boldsymbol{y}_k$ are the MFS charge points (see section 3.2.3), $\{\alpha_k\}$ are the weights determined by the MFS and $\boldsymbol{x}$ is a grid in the Neumann oval $\mathcal{D}$ (including boundary points on $\partial\mathcal{D}$). Note that the pseudo-image method is used for points $\boldsymbol{x}$ near the boundary – see section 3.2.2 for details.

The integral (4.32) cannot yet be evaluated as the integrand (i.e. (4.34)) is

singular as $|\boldsymbol{x}| \to \partial\mathcal{D}$. This is dealt with in the following way: first, (4.34) is transformed[4] to the unit disc $\mathcal{C}$ via the map $z = F(Z)$ with Jacobian $|F'(Z)|^2 = J(R,\theta)$, i.e.

$$g_0(\boldsymbol{x},\boldsymbol{x}) = \rho_0 \int_{\mathcal{C}} g(\boldsymbol{x}(\boldsymbol{X}),\boldsymbol{x}(\boldsymbol{X}))|F'(Z)|^2\, d\boldsymbol{X}, \tag{4.35}$$

where $R \in [0,1]$ and $\theta \in [0,2\pi]$ are, respectively, the radial and azimuthal coordinates in $\mathcal{C}$. The singularity in the integrand of (4.35) is now at the boundary of $\mathcal{C}$ (i.e. $|\boldsymbol{X}| = 1$), but can be removed using an 'image' approximation for $|\boldsymbol{X}| \to 1$. This is done by assuming the contribution to g at the boundary can be approximated by the logarithmic function $\tilde{g}_{\mathcal{C}}(R) = -\frac{1}{2\pi}\log(1-R^2)$, justified since near the boundary the Bessel function G_0 in (4.34) will have a small argument and so the approximation

$$K_0(z) \approx -\log(z/2) - \gamma, \quad \gamma = 0.5772\ldots, \tag{4.36}$$

is valid for small z and can be used. Hence, adding and subtracting $\tilde{g}_{\mathcal{C}}(R)|F'(Z/|Z|)|^2$ to the integrand of (4.35) gives

$$\begin{aligned} g_0(\boldsymbol{x},\boldsymbol{x}) &= \rho_0 \int_{\mathcal{C}} g(\boldsymbol{x}(\boldsymbol{X}),\boldsymbol{x}(\boldsymbol{X}))|F'(Z)|^2 - \tilde{g}_{\mathcal{C}}(R)|F'(Z/|Z|)|^2\, d\boldsymbol{X} \\ &\quad + \rho_0 \int_{\mathcal{C}} \tilde{g}_{\mathcal{C}}(R)|F'(Z/|Z|)|^2\, d\boldsymbol{X}, \end{aligned}$$

then switching to polar coordinates $Z = Re^{i\theta}$ in $\mathcal{C}$ gives

$$\begin{aligned} g_0(\boldsymbol{x},\boldsymbol{x}) &= \rho_0 \int_0^{2\pi}\int_0^1 \left[g(R,\theta)J(R,\theta) - \tilde{g}_{\mathcal{C}}(R)J(1,\theta)\right] R\, dR\, d\theta \\ &\quad + \frac{\rho_0}{2}\int_0^{2\pi} J(1,\theta)\, d\theta, \end{aligned} \tag{4.37}$$

where the radial part of the second integral in (4.37) has been evaluated using $\int_0^1 -\log(1-R^2)\, R\, dR = 1/2$. The remaining integrals in (4.37) are now regular and can be evaluated using the numerical techniques described in appendix A.4.

As for the G_{00} calculation, to demonstrate the convergence of the g_0 calculation figure 4.4 shows the error relative to the highest resolution computed of g_0 for $q = 0.8$,

[4]Note that the modified Helmholtz operator used in calculating g is not invariant when conformally mapped.

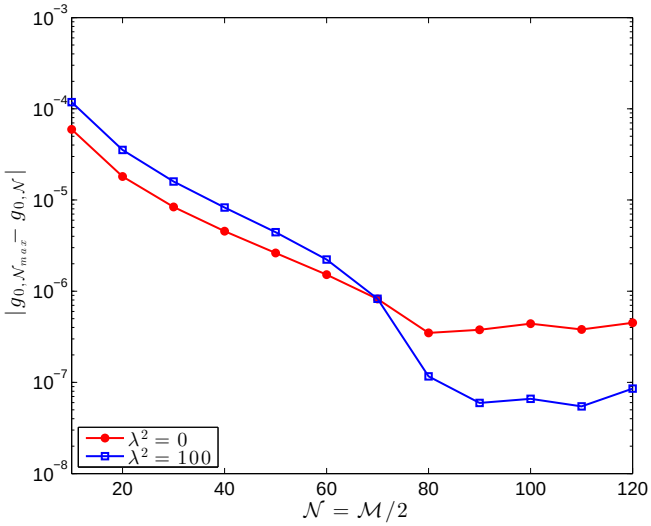

Figure 4.4: Convergence of the constant g_0 (relative to g_0 calculated with the highest resolution grid of $\mathcal{N} \times \mathcal{M} = 130 \times 260$) with the number of grid points for the $q = 0.8$ Neumann oval for $\lambda^2 = 0$ (dark grey dots), 100 (light grey squares). All calculations are done using $M = 314$ MFS charge points.

g_0	$\lambda^2 = 0$	$\lambda^2 = 4$	$\lambda^2 = 36$	$\lambda^2 = 100$
$q = 0.3$	0.1604	0.09012	0.03898	0.02343
$q = 0.8$	0.1995	0.1129	0.04487	0.02585

Table 4.2: Values of the constant g_0 (to 4 sig. figs.) for $\lambda^2 = 0$, 4, 36, 100 in Neumann ovals defined by $q = 0.3$, 0.8.

$\lambda^2 = 0$ (dark grey dots), $\lambda^2 = 100$ (light grey squares). The values of g_0 for the domains and values of λ^2 used in this chapter are shown in table 4.2. For the $q = 0.3$ values $M = 220$ MFS charge points were used and for $q = 0.8$, $M = 314$. Both these values of M were determined using the techniques of section 3.2.3.

Note that in the case of 2D Euler vortices, the integrand of (4.32) does not need to be approximated using VOR-MFS as it can be conformally mapped to $\mathcal{C}$ (see (A.7) in appendix A.2.1) to give

$$g_0 = \rho_0 \int_{\mathcal{C}} \left(g_{\mathcal{C}}(\boldsymbol{X}, \boldsymbol{X}) - \frac{1}{2\pi} \log |F'(Z)| \right) |F'(Z)|^2 \, d\boldsymbol{X}, \tag{4.38}$$

instead of (4.35). The singularity at the boundary is dealt with in the same manner

as above i.e. by adding and subtracting $\tilde{g}_{\mathcal{C}}(R)|F'(Z)/|Z|)|^2$ to (4.38), which leads to

$$\begin{aligned} g_0 &= \rho_0 \int_0^{2\pi} \int_0^1 \left[\tilde{g}_{\mathcal{C}}(R)(J(R,\theta) - J(1,\theta)) - \frac{1}{4\pi} J(R,\theta) \log J(R,\theta) \right] R\, dR\, d\theta \\ &\quad + \frac{\rho_0}{4\pi} \int_0^{2\pi} J(1,\theta)\, d\theta, \end{aligned}$$

instead of (4.37), which again can be evaluated using the numerical techniques in appendix A.4.

With the above, $W_t(\tilde{E})$ and $\beta_t(\tilde{E})$ can now be evaluated.

4.4.3 Statistical sampling of the microcanonical ensemble using VOR-MFS

We now proceed with the numerical construction of statistical estimates for $W(\tilde{E})$ and $\beta(\tilde{E})$ so that they can be compared to $W_t(\tilde{E})$ and $\beta_t(\tilde{E})$ as computed in section 4.4.1. The $N = 100$ vortex system will be considered for $\lambda^2 = 0$ (i.e. 2D Euler vortices, whose energy may be computed exactly using the conformally mapped Hamiltonian (A.12)) and $\lambda^2 = 4$, 100 (i.e. QGSW vortices whose energy may be computed approximately using the VOR-MFS algorithm, as in section 3.3.4). As mentioned in section 4.4.1, in the limit $\lambda \to 0$ the 2D Euler dynamics should be recovered from the QGSW system and the energies should be the same. However, a subtlety arises due to the fact that when $\lambda \to 0$ the free space Green's function of the QGSW vortex, given by (1.7) i.e.

$$G_0(\boldsymbol{x}, \boldsymbol{x}') = -\frac{1}{2\pi} K_0(\lambda |\boldsymbol{x} - \boldsymbol{x}'|),$$

does not equal the free space Green's function for the 2D Euler vortex, given by (1.6) i.e.

$$G_0(\boldsymbol{x}, \boldsymbol{x}') = \frac{1}{2\pi} \log(|\boldsymbol{x} - \boldsymbol{x}'|).$$

In fact

$$\lim_{\lambda\to 0} -\frac{1}{2\pi}K_0(\lambda|\boldsymbol{x}-\boldsymbol{x}'|) = \frac{1}{2\pi}\left[\log\left(\frac{\lambda|\boldsymbol{x}-\boldsymbol{x}'|}{2}\right)+\gamma\right],$$

where the small argument Bessel function approximation (4.36) has been used. Consequently, the energy computed with (1.7) would be different to the energy computed with (1.6) in the limit $\lambda \to 0$.

Evidently, the meaning of energy in the 2D Euler system is subtlety different to its meaning in the QGSW system. This is not a dynamically important issue, but in order to directly compare the QGSW results with the 2D Euler results, an *ad hoc* modification must be made to (1.6). The new version of (1.6) will be termed the '2D Euler approximation Green's function' and is defined as

$$G_0^\lambda(\boldsymbol{x},\boldsymbol{x}') = \frac{1}{2\pi}\log(|\boldsymbol{x}-\boldsymbol{x}'|) + \frac{1}{2\pi}\left(\log\frac{\lambda}{2}+\gamma\right). \tag{4.39}$$

Clearly (4.39) still describes 2D Euler dynamics, since it satisfies $\nabla^2 G_0(\boldsymbol{x},\boldsymbol{x}') = \delta(\boldsymbol{x}-\boldsymbol{x}')$ i.e. adding a constant to the streamfunction of 2D Euler vortices does not change the dynamics.

When (4.39) is used to calculate the energy in (1.2), the final result is that the domain independent constant C^λ is added to H i.e.

$$\begin{aligned} H &\rightarrow H + C^\lambda \\ \text{where}\quad C^\lambda &= \Gamma_i^2 N\frac{1}{2\pi}\left(\log\frac{\lambda}{2}+\gamma\right), \end{aligned}$$

(recall Γ_i is the circulation of the i^{th} vortex, taken to be $\pm 1/N$ in this thesis). Consequently, in the limit $\lambda \to 0$ the QGSW energy tends to the 2D Euler energy, as required. Clearly $C^\lambda \to -\infty$ as $\lambda \to 0$, though logarithmically: for $\lambda = 10^{-16}$, $C^\lambda \approx -0.03$. Note that now 2D Euler energies can only be given relative to a single QGSW energy, as C^λ is calculated for a certain value of λ.

Before proceeding with the statistical sampling of vortices, note that, as mentioned in section 2.5, the evaluation of Bessel functions on most workstations, as performed by MATLAB, is approximately one to two orders of magnitude slower than the evaluation of logarithmic functions. Consequently, calculations for the QGSW

systems are not as well-converged as those for the 2D Euler system. As will be seen later, reasonably strong conclusions can still be drawn.

4.4.4 Constructing probability density functions from the microcanonical ensemble

With the information given above and general details in section 1.3.3, statistical sampling of the uniform distribution can be approached. Calculation of probability density function (PDFs) of the density of states has been done previously in [18] and EAM13 for 2D Euler vortices, and convergence has been observed for relatively low numbers of vortices ($O(100)$ or less). The approach here is as follows: a sample of N vortex configurations is repeatedly taken out of a very large number of uniformly random positions within $\mathcal{D}$ (50 vortices have $\Gamma_i = 1/N$ and 50 have $\Gamma_i = -1/N$). For each sample the energy is calculated, and hence W and W' are constructed using kernel density estimation [105]: for Q samples of the energy $\{E_i\}$ $(i = 1, \ldots, Q)$, the estimates are constructed using Gaussian kernels (i.e. $K(x) = \frac{1}{\sqrt{2\pi}} \int_{-\infty}^{\infty} e^{-x^2/2}\, dx$) and are given by

$$W(\tilde{E}) = \frac{1}{\sigma Q\sqrt{2\pi}} \sum_{i=1}^{Q} \exp\left(-\frac{(\tilde{E}-\tilde{E}_i)^2}{2\sigma^2}\right), \tag{4.40}$$

$$W'(\tilde{E}) = -\frac{1}{\sigma Q\sqrt{2\pi}} \sum_{i=1}^{Q} \frac{(\tilde{E}-\tilde{E}_i)}{\sigma^2} \exp\left(-\frac{(\tilde{E}-\tilde{E}_i)^2}{2\sigma^2}\right), \tag{4.41}$$

where σ is the kernel 'bandwidth'. There is a considerable body of literature (e.g [105, 120]) on the choice of σ, though a heuristic method is sufficient for many purposes. Clearly too large a value of σ can obscure important features of the PDF ('oversmoothing'), while too small a value leads to random fluctuations in the PDF due to variations between particular samples and not the underlying structure of the data ('undersmoothing'). A suitable strategy is to start with a large σ, and the decrease it until fluctuations that are more 'random' than 'structural' start to appear.

In some cases it is desirable to have a more automated technique for choosing σ (e.g. based on the sample size and standard deviation), though even then it is still

worthwhile to try smaller values of σ and perform the visual checks described above. One well-established technique for automatically determining σ is the so-called 'normal scale' (NS) bandwidth selector [105], which assumes that the underlying data has a Gaussian structure, then the 'ideal' normal scale bandwidth, σ_{NS}, is given by

$$\sigma_{NS} = \left[\frac{8\sqrt{\pi}R(K)}{3[\mu_2(K)]^2}\frac{1}{Q}\right]^{1/5} \mathrm{std}(\{\tilde{E}_i\}), \tag{4.42}$$

where $\mathrm{std}(\{\tilde{E}_i\})$ is the standard deviation of the sample energies $\{E_i\}$, and $R(K)$ and $\mu_2(K)$ are defined, for a given the kernel K, by

$$\begin{aligned} R(K) &= \int_{-\infty}^{\infty} [K(x)]^2\, dx, \\ \mu_2(K) &= \int_{-\infty}^{\infty} x^2 K(x)\, dx. \end{aligned}$$

For the Gaussian kernels used here, $R(K) = 1/2\sqrt{\pi}$ and $\mu_2(K) = 1$, meaning (4.42) becomes

$$\sigma_{NS} \approx 1.06\ Q^{-1/5}\ \mathrm{std}(\{\tilde{E}_i\}). \tag{4.43}$$

Equation (4.43) is widely accepted as a good first choice for the bandwidth (with further alterations done 'by eye') for unimodal, approximately normal distributions, such as those we are expecting for the density of states (4.40).

To understand the significance of σ_{NS}, consider the microcanoncial ensemble consisting of $Q = 1.6 \times 10^5$ samples of $N = 100$ 2D Euler vortices ($\lambda^2 = 0$) in the $q = 0.3$ Neumann oval. The left hand panel of figure 4.5 shows the density of states PDFs (4.40) for 2D Euler vortices as computed from all 1.6×10^5 samples, and bandwidths $\sigma = \sigma_{NS}$ (black) and $\sigma = \sigma_{NS}/8$ (grey) – in other words, Q and $\mathrm{std}\{\tilde{E}_i\}$ are the same for both PDFs. Though there are noticeable random fluctuations for $\sigma = \sigma_{NS}/8$, the qualitative structure of the PDF is the same as for $\sigma = \sigma_{NS}$. The right hand panel of figure 4.5 shows the same as the left panel for the microcanonical ensemble of $\lambda^2 = 100$ QGSW vortices (again $N = 100$, $Q = 1.6 \times 10^5$ and $q = 0.3$). Similar conclusions may be drawn as for the left panel. Further, comparing the two panels of figure 4.5, reducing σ seems to have a similar affect in terms of the relative

size of the random fluctuations for both values of λ^2. Similar behaviour is observed for $N = 200$, $N = 1000$ and for intermediate values of λ^2, as well as for the $q = 0.8$ Neumann oval.

The practical consequence of the above analysis is that using $Q = O(10^5)$ and $\sigma = \sigma_{NS}$ as a starting point for 'by eye' smoothing gives PDFs of (4.40) that are sufficiently convergent for our purposes. Tables 4.3 and 4.4 show the values of σ_{NS} (to 4 sig. figs.) that will be used for the PDFs later in this section. Note that there has been significantly less work done on techniques to automatically choose σ for distributions like $\beta_t = W_t'/W_t$. Consequently, for figure 4.10 values of σ were chosen on a more empirical basis.

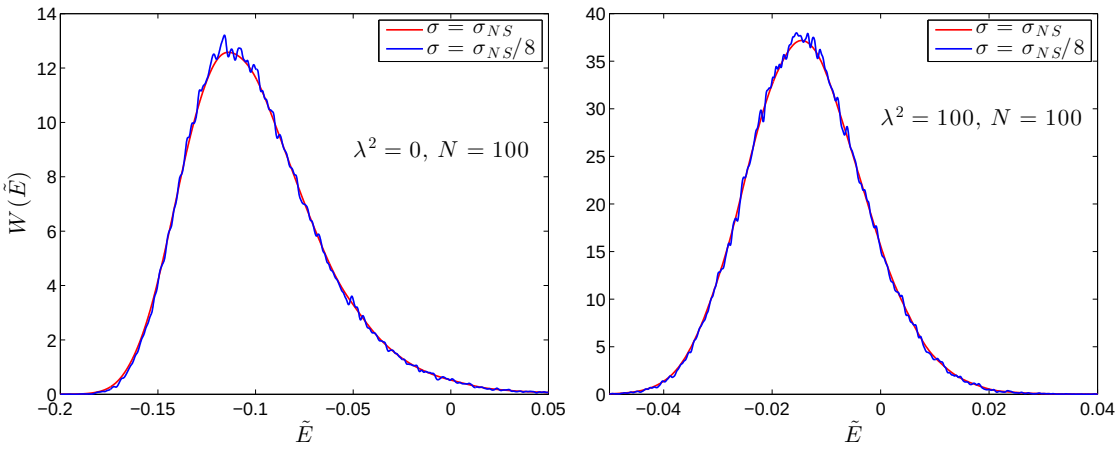

Figure 4.5: (Left) The density of states PDF (4.40) for the 2D Euler system with $N = 100$ in the $q = 0.3$ Neumann oval, computed from $Q = 1.6 \times 10^5$ samples and smoothed using $\sigma = \sigma_{NS}$ (black) and $\sigma = \sigma_{NS}/8$ (grey). (Right) As for left for the QGSW system with $\lambda^2 = 100$.

		$\max\{\sigma_{NS}\} \times 10^{-3}$
$\lambda^2 = 0$	$N = 100$	3.221
	$N = 200$	3.178
	$N = 1000$	3.158
$\lambda^2 = 4$	$N = 100$	2.643
	$N = 200$	2.625
	$N = 1000$	2.623
$\lambda^2 = 36$	$N = 100$	1.478
	$N = 200$	1.453
	$N = 1000$	1.441
$\lambda^2 = 100$	$N = 100$	0.9983
	$N = 200$	0.9600
	$N = 1000$	0.9485

Table 4.3: The normal scale bandwidth values for Gaussian kernels σ_{NS} (4.43) that were used for the PDFs for the Neumann oval defined by $q = 0.3$, for $\lambda^2 = 0$, 4, 36 and 100.

		$\max\{\sigma_{NS}\} \times 10^{-3}$
$\lambda^2 = 0$	$N = 100$	2.929
	$N = 200$	2.912
	$N = 1000$	2.904
$\lambda^2 = 4$	$N = 100$	2.545
	$N = 200$	2.521
	$N = 1000$	2.511

Table 4.4: As for table 4.3 for $q = 0.8$ Neumann ovals.

4.4.5 Results

Figure 4.6(a) compares the theoretical predictions $W_t(\tilde{E})$ (4.25) (dashed grey) with the numerical reconstructions $W(\tilde{E})$ (4.40) using $N = 100$ (red), $N = 200$ (blue) and $N = 1000$ (green), for the 2D Euler system and the QGSW system with $\lambda^2 = 4$ as indicated, for the $q = 0.3$ Neumann oval (shown). Figure 4.6(b) is the same as Figure 4.6(a) for the $q = 0.8$ Neumann oval (also shown). In each case, (4.25) is a plausible limiting curve for the convergence of the (4.40) as N increases.

Figures 4.7-4.9 compare the theoretical prediction $W_t(\tilde{E})$ (grey dashed) with numerical reconstruction $W(\tilde{E})$ for the QGSW system for $N = 100$ (black), $N = 200$ (blue) and $N = 1000$ (green), in the $q = 0.3$ Neumann oval. In particular, figure 4.7 shows $\lambda^2 = 100$, figure 4.8 shows $\lambda^2 = 4$ and figure 4.9 is the intermediate value $\lambda^2 = 36$. Also shown in all three figures are the theoretical curves $W_{ET}(\tilde{E})$ (4.58)

(black) as derived in appendix 4.A (using theory from [43]), which are valid for large λ. Note the different axes in all three figures.

Before analysing figures 4.7-4.9, recall from section 4.3.2 that for a given value of λ^2, the validity of $W_t(\tilde{E})$ as a limiting expression for $W(\tilde{E})$ depends on the value of N used to calculate $W(\tilde{E})$. In particular, we require the condition (4.30) (namely $1/N \ll \rho_0/\lambda^2$) to be satisfied. For $\lambda^2 = 100$ (figure 4.7), at $N = 1000$ (green), $1/N$ is only approximately three times smaller than ρ_0/λ^2 (for $N = 100$, $1/N$ is actually greater than ρ_0/λ^2), and so, as expected, $W_t(\tilde{E})$ fails to predict $W(\tilde{E})$. It should be noted that the rate of convergence of $W(\tilde{E})$ in terms of N is significantly slower for the $\lambda^2 = 100$ shown in figure 4.7 compared to that for $\lambda^2 = 4$, as shown in figure 4.8. Consequently, in the case of $\lambda^2 = 100$, computing $W(\tilde{E})$ using $N > 1000$ would be expected to give results increasingly closer to $W_t(\tilde{E})$.

Figure 4.8 shows the results for $\lambda^2 = 4$. In this case, even at $N = 100$ (red) the condition (4.30) is easily satisfied, with $1/N$ begin approximately ten times smaller than ρ_0/λ^2. Consequently, as should be expected $W_t(\tilde{E})$ is a good candidate limiting curve of $W(\tilde{E})$.

Figure 4.9 is the intermediate case with $\lambda^2 = 36$. At $N = 100$ (red), the condition (4.30) is not satisfied as $1/N \approx \rho_0/\lambda^2$ and $W_t(\tilde{E})$ is a poor prediction for $W(\tilde{E})$. At $N = 1000$ (green), $1/N$ is approximately ten times smaller than ρ_0/λ^2 and $W_t(\tilde{E})$ is a plausible limiting curve for $W(\tilde{E})$.

From figures 4.7-4.9, we can postulate that for a given λ^2, the number of vortices N required in computing $W(\tilde{E})$ such that the theoretical prediction $W_t(\tilde{E})$ is a plausible limiting curve is

$$N \approx 10\frac{\lambda^2}{\rho_0}. \tag{4.44}$$

For $\lambda^2 = 4$, (4.44) suggests as few as $N \approx 100$ vortices are required, while for $\lambda^2 = 100$, $N \approx 3000$.

The large λ theoretical curves $W_{ET}(\tilde{E})$ (4.58) (black), as derived in appendix 4.A, behave as expected. From figure 4.8 we see that at $\lambda^2 = 4$, $W_{ET}(\tilde{E})$ is not valid. As shown in figure 4.7, for $\lambda^2 = 100$ $W_{ET}(\tilde{E})$ has become an improved prediction for $W(\tilde{E})$.

Comparing the density of states for $\lambda^2 = 0,\ 4,\ 36$ and 100 in figures 4.6-4.7 in both domains, it is evident that the median energy is shifting to a higher positive value and the standard deviation is reducing as λ^2 increases. This is due to the decreasing range of interaction of the QGSW system, as controlled by λ^2. In the case of $\lambda^2 = 100$ the system is so short ranged that each vortex is only interacting with other vortices that are in very close proximity, and thus the influence of images (i.e. the boundary) is drastically reduced. Consequently most of the vortices behave as if they are in an unbounded domain, which is consistent with the close-to-Gaussian PDFs with median tending to zero, shown in figure 4.7.

An alternative test is to compare theoretical results for the inverse temperature curve (4.28) with the numerical reconstruction given by the quotient (4.41)/[$N\times$(4.40)]. This is shown in figure 4.10 for the same four configurations ($\lambda^2 = 0,\ 4$ and $q = 0.3,\ 0.8$) as in figure 4.6. There is reasonable agreement in all four cases, for low positive and negative energy. For large positive energy where the number of samples is scarce, the kernel bandwidth σ causes significant bias to the curves, as can be seen by the oscillatory structure.

4.5 Conclusion

In this chapter the point vortex system was studied in the thermodynamic limit. The theoretical results of [45] have been generalised for any (appropriate) type of dynamics and the VOR-MFS algorithm of chapter 3 has been employed to verify theoretical predictions for the case of the QGSW vortex.

The main results are summarised by the following points.

1. In section 4.2 new analytical expressions for the density of states $W_t(\tilde{E})$ (equation (4.25)) and the inverse thermodynamic temperature $\beta_t(\tilde{E})$ (equation (4.28)) were derived for a generalised vortex. These expressions are valid for low positive and negative energies where there is no mean flow and the distribution of vortices is close to uniform. Numerical evaluation of these analytical expressions were carried out in section 4.3.

2. To investigate the analytical expressions described in point 1, statistical sam-

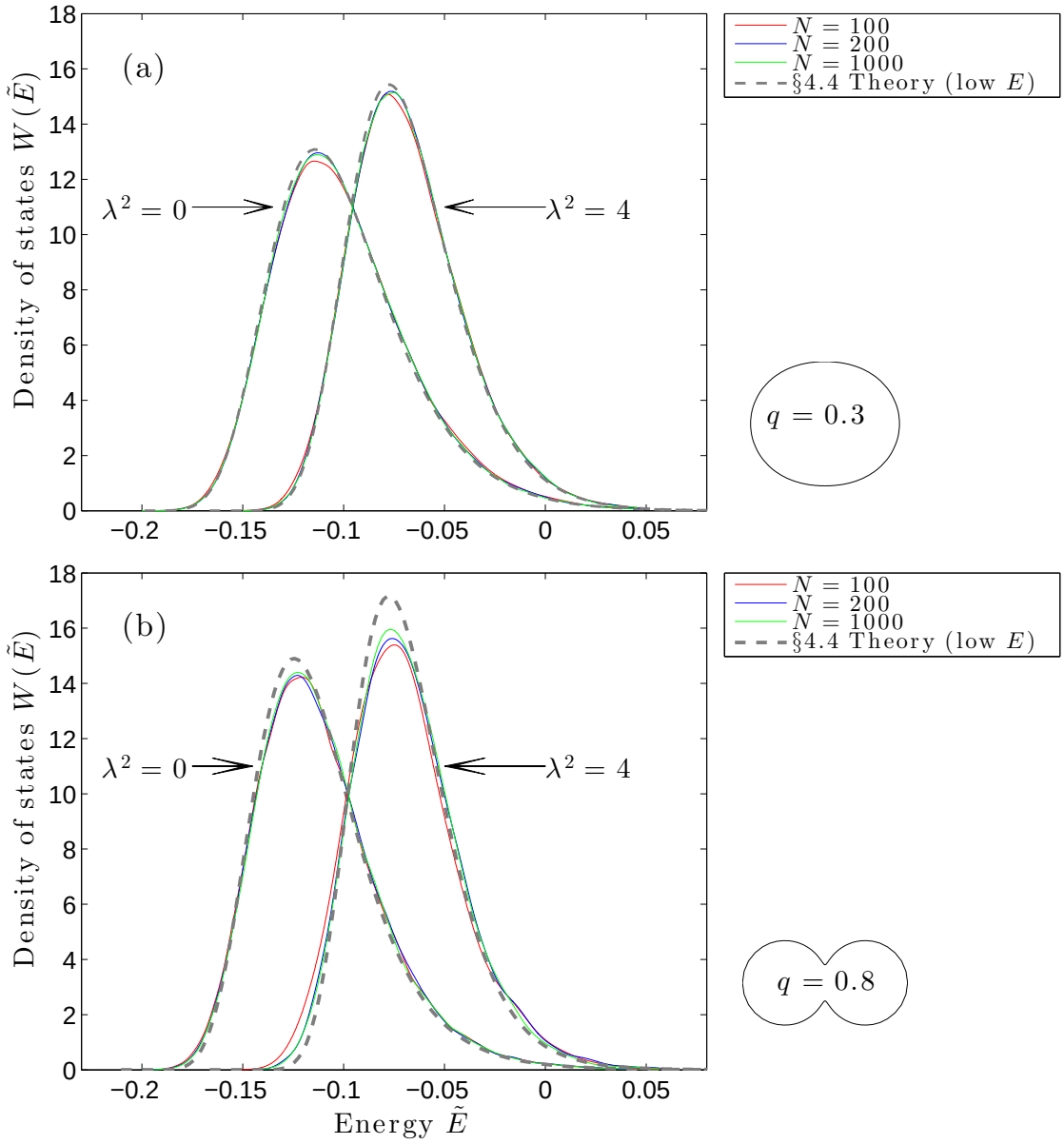

Figure 4.6: (a) Statistical reconstruction of the density of states $W(\tilde{E})$ (4.40) with $N = 100$ (red), $N = 200$ (blue), $N = 1000$ (green) and the corresponding low E theoretical prediction $W_t(\tilde{E})$ (4.25) (grey dashed) for the 2D Euler system i.e. $\lambda^2 = 0$ and QGSW vortices at $\lambda^2 = 4$ as indicated for the $q = 0.3$ Neumann oval shown to the right. (b) as for (a) for the $q = 0.8$ Neumann oval (shown).

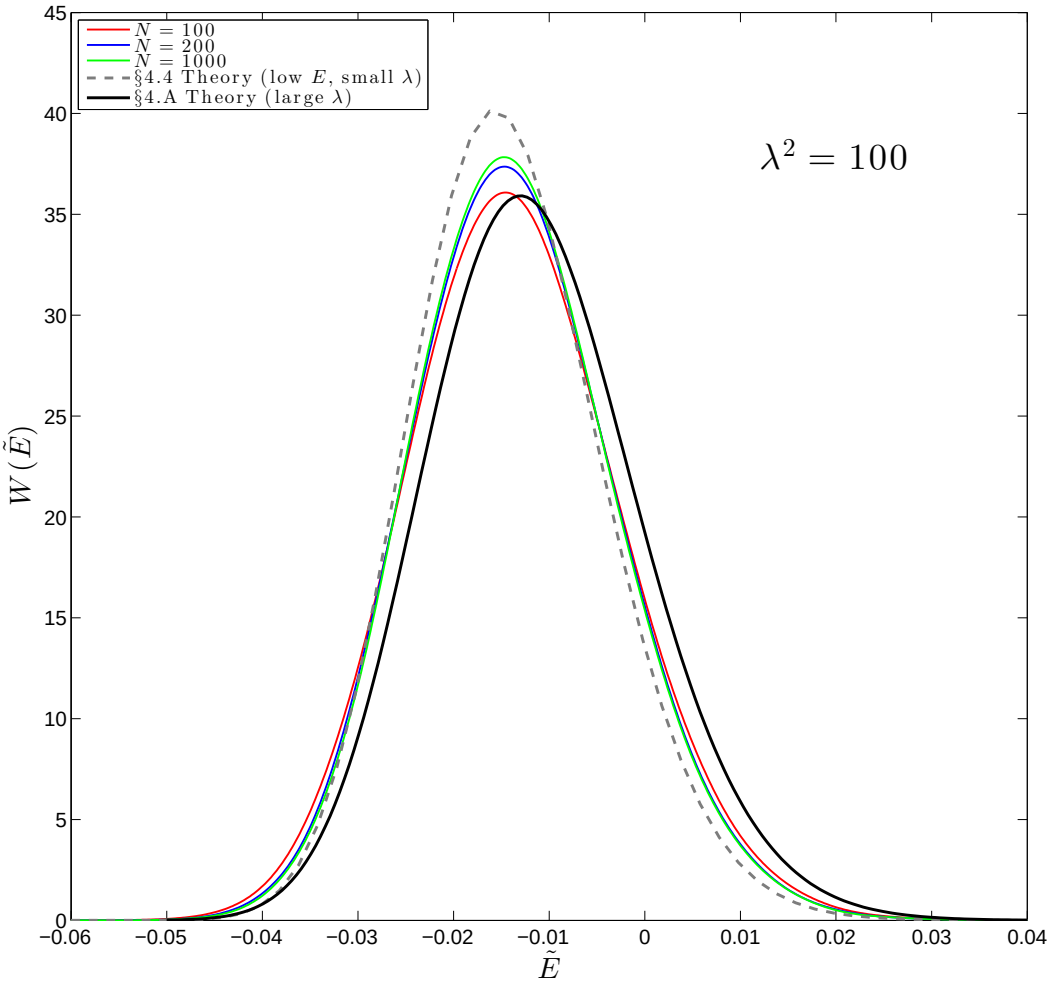

Figure 4.7: Statistical reconstruction of the density of states $W(\tilde{E})$ (4.40) for $N = 100$ (black), $N = 200$ (blue) and $N = 1000$ (green) QGSW vortices at $\lambda^2 = 100$, along with corresponding low E theoretical predictions $W_t(\tilde{E})$ (4.25) (grey dashed) from section 4.4 and the Edwards-Taylor large λ^2 theoretical predictions $W_{ET}(\tilde{E})$ (4.58) (red) from appendix 4.A, for the $q = 0.3$ Neumann oval.

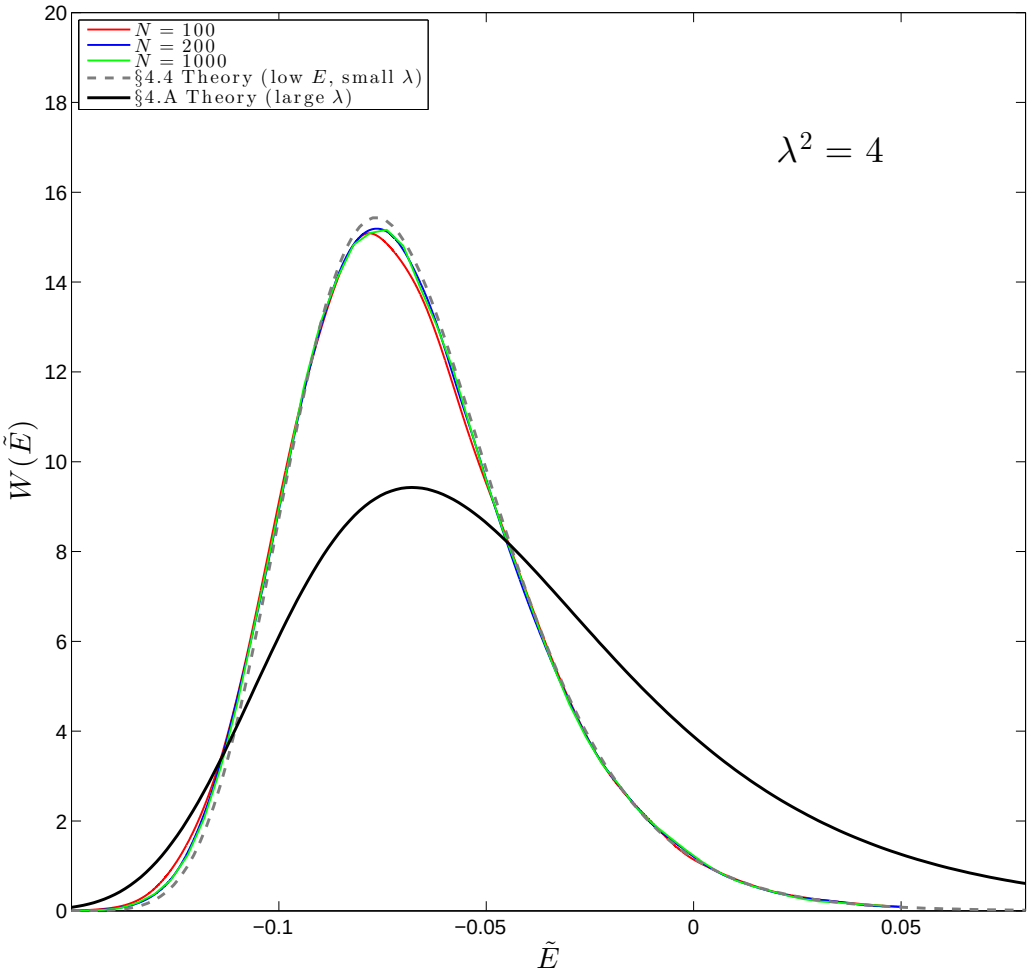

Figure 4.8: As for figure 4.7 for $\lambda^2 = 4$. Note that the axes differ from figure 4.7.

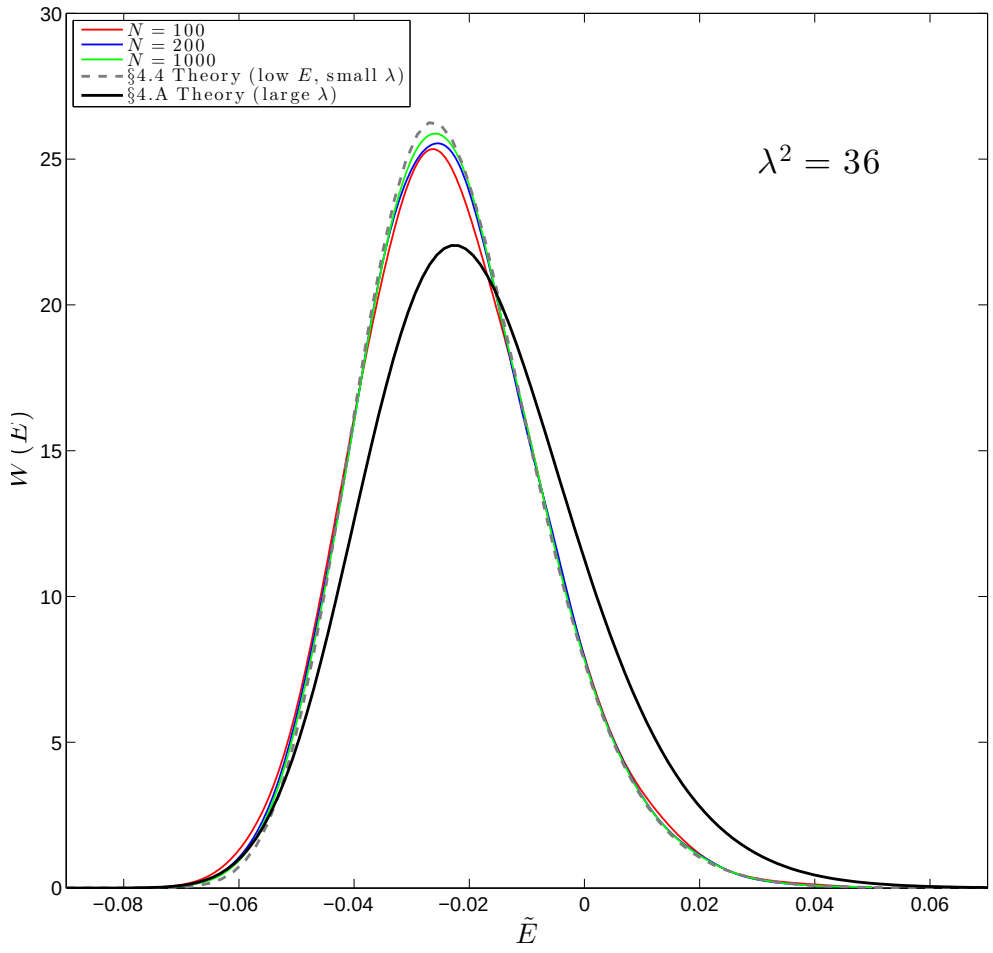

Figure 4.9: As for figures 4.7 and 4.8 for $\lambda^2 = 36$. Note that the axes differ from figures 4.7 and 4.8.

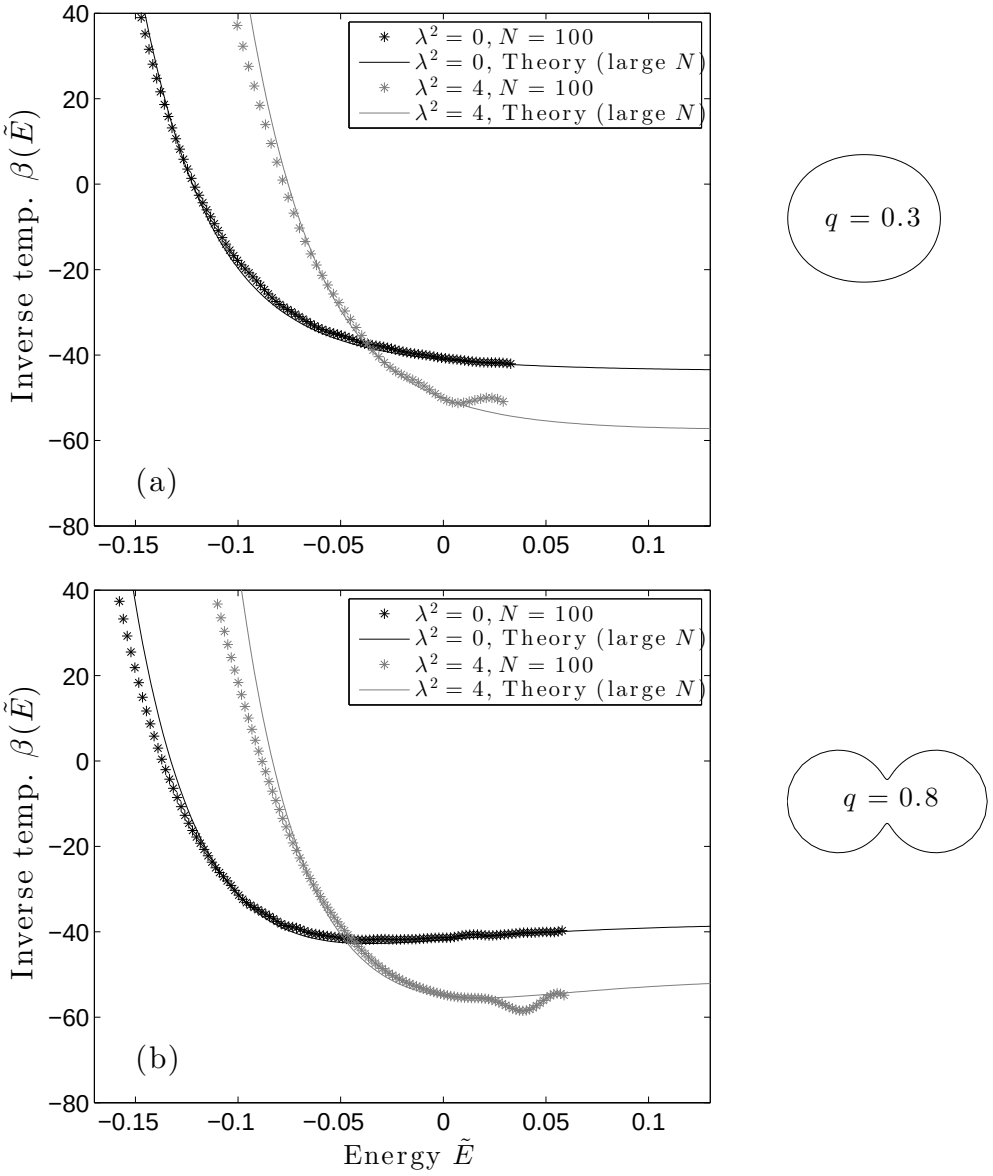

Figure 4.10: (a) Statistical reconstructions of $\beta(\tilde{E})$ for $N = 100$ vortices (stars) and corresponding theoretical predictions (solid lines) for a 2D Euler vortex (black) and a QGSW vortex ($\lambda^2 = 4$, grey) for the $q = 0.3$ Neumann oval shown to the right. (b) as for (a) for the $q = 0.8$ Neumann oval.

pling of the QGSW system was effected in section 4.4. The VOR-MFS algorithm of chapter 3 proved to be an effective method with which to construct finite N statistical estimates of the density of states and the inverse temperature curve. Note that the validity of the analytical expressions for a given Rossby radius λ^{-1} depends on the number of vortices N used in constructing the statistical estimates. In particular, the results form figures 4.7-4.9 and the condition (4.30) (namely $1/N \ll \rho_0/\lambda^2$), imply that the statistical estimates should be computed using (4.44), i.e. using $N \approx 10\lambda^2/\rho_0$ vortices, in order for the theoretical expression $W_t(\tilde{E})$ to be valid. For $\lambda^2 = 4$, $N \approx 100$ is sufficient, while for $\lambda^2 = 100$, $N \approx 3000$ would be required. As described in section 3.2.4, there are significant computational costs to using larger N (though parallelisation would help), though this is something that could be pursued in future work.

3. Alternative theoretical expressions for the density of states $W_{ET}(\tilde{E})$ (equation (4.58)) and inverse thermodynamic temperature $\beta_{ET}(\tilde{E})$ (equation (4.59)) are derived in appendix 4.A, based on the work of Edwards & Taylor [43]. These expressions are valid in the limit of large λ, and were also tested against the finite N statistical estimates of the density of states for various values of λ, and by $\lambda^2 = 100$ are becoming an increasing plausible limiting curve.

4. The importance of the DITs, $\{\beta_i\}$, in describing the system is demonstrated again, following on from their key role in the solutions of the elliptic-sinh equation in the hydrodynamic limit as considered in chapter 2. Comparing the two Neumann oval domains for the 2D Euler system ($\lambda^2 = 0$) the significantly different structures of the inverse temperature curves $\beta_t(\tilde{E})$ (and to a less striking extent the density of states $W_t(\tilde{E})$) are controlled by the different DIT distributions. For the QGSW system, the DITs of a certain domain are simply shifted by the constant $-\lambda^2/\rho_0$ relative to 2D Euler DITs for the same domain. Therefore, for a given domain and moderate value of λ^2, the distribution of 2D Euler DITs is similar to the distribution of QGSW DITs. Hence, as might be expected, the qualitative properties of the curves, such as the inverse thermodynamic temperature achieving a minimum for the $q = 0.8$ Neumann oval (see

figure 4.10), are the same for the QGSW system and for the 2D Euler system. In other words, since the qualitative properties of the theoretical curves are controlled by the distribution of DITs, and since the distributions are similar for the QGSW $\lambda^2 = 4$ and the 2D Euler vortex, the theoretical curves for these two systems are qualitatively similar.

For very large values of λ^2, the influence of the domain is drastically reduced and the QGSW DIT distribution is significantly different than the distribution for the 2D Euler system. An investigation into the affect this has on the density of states and the inverse thermodynamic temperature is underway and some theoretical details are given in appendix 4.A.

In EAM13, the 2D Euler version of the theoretical results of sections 4.2 and 4.3 compare well with DNS of the $N = 100$ vortex system. It is not straightforward to construct the inverse temperature curve $\beta_t(\tilde{E})$ from a set of runs at fixed $\tilde{E}$. Instead the vorticity fluctuation ω_2 can be projected onto the vorticity modes and comparisons were made between dynamical runs, the microcanonical ensemble and theoretical predictions. As mentioned in section 2.5, even at moderate value of N (e.g. $N = 100$) DNS of the QGSW system using VOR-MFS would require significant speed improvements to the algorithm, due to (a) Bessel functions being slower to evaluate than logarithmic functions and (b) longer integration times required to achieve equilibrium for the QGSW system as a result of slower vortex speeds. If these improvements could be made, the QGSW theory could be further compared with the DNS in the same manner as EAM13.

While the theoretical results of this chapter were derived for a generalised dynamics, verification was performed using the QGSW system introduced in section 1.2.1. The flexibility of the VOR-MFS algorithm should allow the SQG system, also introduced in section 1.2.1, to be considered in the same manner.

It is also noted that the theoretical results of Edwards & Taylor [43] and Taylor [110] have relevance to the QGSW system considered in this chapter. In the context of 2D plasmas, they consider a 'finite-range' Coulomb potential i.e. using the free space Green's function $G_0(\boldsymbol{x}, \boldsymbol{x}) = K_0(\lambda|\boldsymbol{x} - \boldsymbol{x}'|)$. For fixed λ they take the limit $|\mathcal{D}| \to \infty$, to give a system independent of the boundary. It can be seen that this

is equivalent to fixing $|\mathcal{D}|$ and taking the limit $\lambda \to \infty$ i.e. a system with such short-ranged interactions that it is not influenced by the boundary. They derive a number of thermodynamic quantities including an equation of state (analogous to the ideal gas equation in classical statistical mechanics) and hence an expression for the inverse thermodynamic temperature. A brief overview of the modifications required to the theory in [43] so that it can be used in the framework presented here is given in appendix 4.A.

4.A Edwards-Taylor theory

In this appendix an overview of the modified version of the theory of Edwards & Taylor [43] is given, which is valid for QGSW vortices in the large λ limit. Expressions in this limit will be denoted by the subscript ET below.

The key part of the theory of [43] that we are interested in involves approximating the summation in their eqn. 13 by an integral (which can be evaluated analytically). In the framework used here, this translates to approximating the infinite sum on the right hand side of the ordinary differential equation for the density of states (4.23) i.e.

$$\mathrm{i}\frac{d\widehat{W}_t(k)}{dk} - \tilde{E}_0\widehat{W}_t(k) = -\frac{1}{2}\left(\sum_{j=1}^{\infty}\frac{\mathrm{i}k}{\beta_j(\beta_j - \mathrm{i}k)}\right)\widehat{W}_t(k).$$

This may be done using Weyl's law [3] (stated explicitly below for the Laplacian operator) which can be used to determine the asymptotic distribution of the QGSW DITs for large λ: first consider the standard Laplace eigenvalue problem in a domain $\mathcal{D}$ (area $|\mathcal{D}|$),

$$\nabla^2\Psi_j = -\alpha_j\Psi_j, \quad \Psi_j = \text{constant on } \partial\mathcal{D}, \tag{4.45}$$

with eigenvalues $\alpha_j > 0$. Weyl's law [3] states that, at leading order, the asymptotic distribution of Laplace eigenvalues satisfies

$$\lim_{j\to\infty}\frac{j}{\alpha_j} = \frac{|\mathcal{D}|}{4\pi}. \tag{4.46}$$

Next consider the QGSW vorticity mode eigenvalue problem

$$(\nabla^2 - \lambda^2)\Phi_j = \beta_j \Phi_j, \quad \Phi_j = \text{constant on } \partial\mathcal{D}, \tag{4.47}$$

with DITs $\beta_j < 0$. The two eigenvalue problems (4.45) and (4.47) are related (see section 4.3.1) by

$$\beta_j = -\pi(\alpha_j + \lambda^2),$$

which when combined with (4.46) gives the asymptotic distribution of the DITs in the QGSW problem (with domain area $|\mathcal{D}| = \pi$) to be

$$\lim_{j\to\infty} \beta_j = -\pi(4j + \lambda^2). \tag{4.48}$$

Figure 4.11 compares (4.48) to the DITs of the $q = 0.3$ Neumann oval computed at resolutions $\mathcal{N}\times\mathcal{M} = 20\times40$, 30×60 and 40×80. The 'dropping off' of the computed DITs relative to the Weyl's law is due to a lack of resolution in the computational grids.

For large λ, the sum in (4.23) will be dominated by large β_j and using (4.48) we can replace the sum with an integral, retaining accuracy at leading order i.e.

$$\mathrm{i}\frac{d\widehat{W}_{ET}(k)}{dk} - \tilde{E}_0\widehat{W}_{ET}(k) = -\frac{\mathrm{i}k}{2}\widehat{W}_{ET}(k)\int_1^\infty \frac{1}{(4\pi s + \pi\lambda^2)(4\pi s + \pi\lambda^2 - \mathrm{i}k)}\,ds. \tag{4.49}$$

Note that the lower limit of the integral in (4.49) is only correct to leading order: considering the next order term in the Weyl's expansion could give a more accurate approximation of the summation.

The integral on the right hand side of (4.49) is evaluated to give

$$\mathrm{i}\frac{d\widehat{W}_{ET}(k)}{dk} - \tilde{E}_0\widehat{W}_{ET}(k) = -\frac{1}{8\pi}\widehat{W}_{ET}(k)\log\left(1 + \frac{\mathrm{i}k}{\Lambda}\right), \tag{4.50}$$

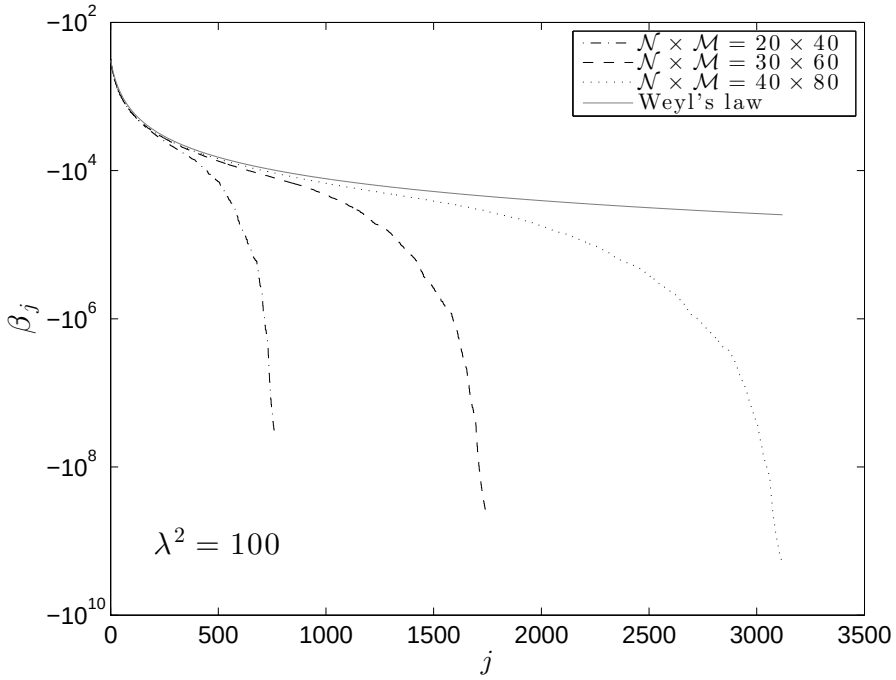

Figure 4.11: Comparison of DIT version of Weyl's law (4.48) (solid grey) for the asymptotic distribution of DITs to the DITs calculated numerically at resolutions $\mathcal{N} \times \mathcal{M} = 20 \times 40$ (black dash-dot), 30×60 (black dash) and 40×80 (black dot), for $\lambda^2 = 100$.

where $\Lambda = \pi(4+\lambda^2)$. The ordinary differential equation (4.50) is solved to give

$$\widehat{W}_{ET}(k) = \tilde{W}_0 \exp\Lambda\left(-\mathrm{i}\left(\tilde{E}_0 + \frac{1}{8\pi}\right)\frac{k}{\Lambda} + \frac{1}{8\pi}\left(1+\frac{\mathrm{i}k}{\Lambda}\right)\log\left(1+\frac{\mathrm{i}k}{\Lambda}\right)\right), \quad (4.51)$$

where $\tilde{W}_0$ is a normalisation constant. Taking the inverse Fourier transform of (4.51) gives

$$\begin{aligned} W_{ET}(\tilde{E}) &= \frac{\tilde{W}_0}{\sqrt{2\pi}}\int_{-\infty}^{\infty}\exp\Bigg[\Lambda\Bigg(\mathrm{i}\left(\tilde{E}-\tilde{E}_0-\frac{1}{8\pi}\right)\frac{k}{\Lambda} \\ &\qquad + \frac{1}{8\pi}\left(1+\frac{\mathrm{i}k}{\Lambda}\right)\log\left(1+\frac{\mathrm{i}k}{\Lambda}\right)\Bigg)\Bigg]\,dk \\ &= W_0\int_{-\infty}^{\infty}\exp\left[\tilde{\Lambda}\big(\mathrm{i}(\tilde{e}-1)z + (1+\mathrm{i}z)\log(1+\mathrm{i}z)\big)\right]\,dz, \end{aligned} \quad (4.52)$$

where $\tilde{e} = 8\pi(\tilde{E}-\tilde{E}_0)$, $\tilde{\Lambda} = \Lambda/8\pi$ and $z = k/\Lambda$. Equation (4.52) is identical to eqn. 14 in [43], and as in [43], can be evaluated using the method of steepest descents. To do this we use the following result for integrals involving analytic functions

$$I(\Lambda) = \int_C e^{\Lambda g(z)}\,dz,$$

for some analytic function $g(z)$. If $g(z)$ has a saddle point at z_0, where $g'(z_0)$, and the contour C can be deformed to pass through z_0 on the steepest descent path (on which $\Im\{g(z)\}$=constant), then the asymptotic form for I is

$$\lim_{\Lambda\to\infty} I(\Lambda) = \left(\frac{2\pi}{\Lambda}\right)^{1/2}\frac{e^{\Lambda g(z_0)}}{(-g''(z_0))^{1/2}}\left(1+O(\Lambda^{-1})\right). \quad (4.53)$$

For our specific case (i.e. (4.52)),

$$g(z) = \mathrm{i}(\tilde{e}-1)z + (1+\mathrm{i}z)\log(1+\mathrm{i}z), \quad (4.54)$$

and so the first task in evaluating (4.53) is to calculate z_0. This is done by

$$\begin{aligned} g'(z_0) &= \mathrm{i}(\tilde{e}-1) + \mathrm{i} + \log(1+\mathrm{i}z_0) = 0 \\ \Rightarrow z_0 &= \mathrm{i}(1-e^{-\tilde{e}}). \end{aligned} \quad (4.55)$$

Substituting (4.55) into z in (4.54) gives

$$g(z_0) = 1 - e^{-\tilde{e}} - \tilde{e}, \tag{4.56}$$

and similarly for the second derivative

$$g''(z_0) = -\frac{1}{1 + \mathrm{i}z_0} = -e^{\tilde{e}}. \tag{4.57}$$

Substutiting (4.56) and (4.57) into (4.53) gives the leading order behaviour of (4.52) to be

$$W_{ET}(\tilde{E}) = W_1 \exp\Big(\tilde{\Lambda}\left(1 - e^{-\tilde{e}} - \tilde{e}\right) - \tilde{e}/2\Big),$$

or, in terms of our original variables

$$W_{ET}(\tilde{E}) = W_2 \exp\left(\frac{4+\lambda^2}{8}\left(1 - e^{-8\pi(\tilde{E}-\tilde{E}_0)} - 8\pi(\tilde{E}-\tilde{E}_0)\right) - 4\pi(\tilde{E}-\tilde{E}_0)\right), \tag{4.58}$$

(where W_1 and W_2 are normalisation constants) and hence the inverse thermodynamic temperature is

$$\beta_{ET}(\tilde{E}) = (4+\lambda^2)\pi\left(e^{-8\pi(\tilde{E}-\tilde{E}_0)} - 1\right) - 4\pi. \tag{4.59}$$

Both (4.58) and (4.59) are valid for large λ. These expressions are tested against numerical reconstructions in section 4.4.3.

Chapter 5

Oscillations of the point vortex system between meta-stable states

5.1 Introduction

For the point vortex system at equilibrium there are *two*[1] equivalent states of vorticity, both of which are maximum entropy solutions and are identical but for a switch in the sign of vorticity i.e. equilibrium solutions occur in plus/minus pairs. Consider a bounded vortex system in the hydrodynamic limit, dominated by the mean flow with two equivalent equilibrium states (referred to as *meta-stable* states), such as that shown for the Neumann oval shown in figure 5.1. Since the two meta-stable states are both maximum entropy solutions they are both equally likely to be realised in a dynamical simulation. For extremely long-time simulations the system is assumed to be ergodic (see section 1.4.1) and thus it is expected to spend equal times in each meta-stable state meaning the vorticity of the system must theoretically flip from one state to the other. However, in certain cases the time scale over which these flips occur will be too long to be observed in a simulation.

[1]This is excluding the results of chapter 2, where in the heart domain, at $E = E_c$ there are four equally likely equilibrium states: two corresponding to the dipolar solutions and two corresponding to the monopolar solution.

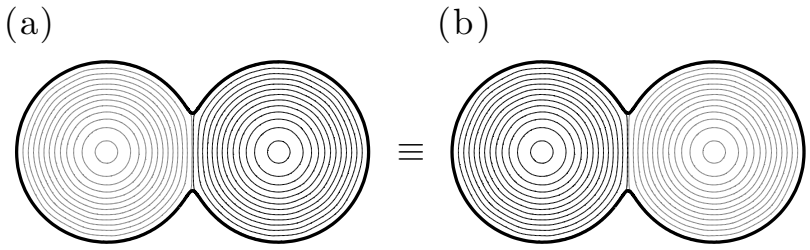

Figure 5.1: Two equivalent streamfunctions in the Neumann oval domain defined by $q = 0.8$. Positive contours are black and negative contours are grey.

This short chapter will investigate the oscillation of vorticity between meta-stable states in the Neumann oval domain. Similar phenomena was predicted in [27] and verified numerically in [89], though a different approach is taken here. Although the oscillatory phenomena will occur in the heart-shaped domain studied in chapter 2 (and likely other domains as well), the high curvature of the Neumann oval as the parameter $q \to 1$ leads to particularly clear results. The system will be investigated using microcanonical sampling in section 5.2.2 and using direct numerical simulations in section 5.2.3. In section 5.3 conclusions are drawn and possible extensions to the work are suggested.

5.2 Meta-stable states in the Neumann oval

5.2.1 The centre of vorticity diagnostic

Before proceeding with the calculations, recall from section 1.3.2 how the macroscopic behaviour of the point vortex system changes as energy is increased: starting at high negative energies (i.e. $E \to -\infty$), the system is characterised by opposite-signed pairs. As energy increases towards $E = 0$ the opposite-signed pairs break up until the vorticity is uniform across the domain. Then, as energy increases ($E \to \infty$) like-signed clusters form, with the size of the cluster increasing as the energy increases. Oscillations of vorticity between meta-stable states occur in this high positive energy

state and can be characterised using the following macroscopic diagnostic[2]

$$X = \sum_{i=1}^{N} \Gamma_i x_i = \frac{1}{N} \sum_{i=1}^{N} \mathrm{sgn}(\Gamma_i) x_i, \tag{5.1}$$

with $X > 0$ corresponding to positive vorticity in the right-hand lobe and negative vorticity in the left-hand lobe (i.e. figure 5.1(a)) and vice-versa for $X < 0$ (figure 5.1(b)). Below it will be seen that when X persistently remains bounded away from zero, the system is in one of the two meta-stable states and a change in sign indicates an oscillation from one state to the other. On the other hand, when X is persistently close to zero the vorticity distribution is close to uniform and there are no large-scale oscillations of vorticity between the lobes. The variable X can be regarded as the x-coordinate of the centre of vorticity of the system and was previously used in section 2.4.5 to diagnose DNS in the heart domain at dipolar (effectively the same use as in this chapter). Also, as stated in section 2.4.5, (5.1) is effectively a non-conserved version of the linear impulse in the x direction, referred to as P in section 1.2.2.

A final point is made about how ensemble averages relate to the time averages of the diagnostic X. To verify equilibrium statistical mechanics, it is usually desirable to run DNS for the longest time that is feasible, and then take averages of macroscopic quantities which can be compared to microcanonical ensemble averages. However, one must be careful of doing so here as even if the system is at a sufficiently high energy for large scale oscillations between meta-stable states to occur, for sufficiently long-time DNS the time average of (5.1) i.e. $\overline{X(t)}$ will be zero, as the system will have spent equal times in each meta-stable state. What we are actually interested in here are intermediate-time averages that correspond to the system being stuck in one meta-stable state or the other.

[2]The projection of the vortex positions onto the maximum entropy vorticity mode could also be used.

5.2.2 Statistical sampling of the microcanonical ensmble

As described in section 1.3.3, joint probability density functions can be constructed to show the correlation between two macroscopic quantities. Here it is most instructive to calculate the joint PDF between the two macroscopic quantities E and X, both of which require scaling. Let $\tilde{X} = \sqrt{N}X$. We then postulate that

$$\lim_{N\to\infty} p_{0,N}(\tilde{X}, \tilde{E}) = p_0(\tilde{X}, \tilde{E}). \tag{5.2}$$

The scaling on E (i.e. $\tilde{E} = NE$) is the same thermodynamic scaling that was used in chapter 4 and was previously verified numerically in [18, 45]. The scaling on X may be justified by assuming that the x-coordinates of the vortices are independently and identically distributed (iid) on $\mathcal{D}$ (note that bounded variance is guaranteed as $\mathcal{D}$ is finite). For moderate values of $|E|$ the iid assumption is valid and the central limit theorem can be applied: consider $\hat{N}$ vortices placed inside a sub-domain of the domain $\mathcal{D}$. Under the iid assumption, by the central limit theorem [98] the distribution of x-coordinates of the vortices is normal and hence the diagnostic X is also normal, meaning the quantity $\sqrt{\hat{N}}X$ tends to a fixed distribution as $\hat{N} \to \infty$. Consequently, we postulate that over the whole domain the quantity

$$\tilde{X} = \frac{1}{\sqrt{N}} \sum_{i=1}^{N} \operatorname{sgn}(\Gamma_i) x_i$$

also tends to a fixed distribution as $N \to \infty$. Note that for very large positive energies the iid assumption is not valid as the vortices are strongly biased to form into tight clusters – the energies considered in this chapter are not high enough for this to occur meaning the iid assumption and hence the use of the central limit theorem are valid in justifying the scaling $\tilde{X} = \sqrt{N}X$.

Figure 5.2 shows the joint probability density function $p_{0,N}(\tilde{X}, \tilde{E})$ for $N = 100$ vortices in the Neumann oval defined by $q = 0.8$, as computed using Gaussian kernels [105] from 10^7 samples generated by Monte Carlo sampling with bandwidths $\sigma_{\tilde{X}} = 8 \times 10^{-3}$ and $\sigma_{\tilde{E}} = 4 \times 10^{-3}$ (see section 4.4.4). The contour spacing is quadratic for

clarity. Also shown are the maxima of the PDF (thick black line). From the figure there are clearly two regimes: for $\tilde{E} \lesssim -0.05$ the PDF is unimodal ($\tilde{X} = 0$) and for $\tilde{E} \gtrsim 0.05$ the PDF is bimodal ($\tilde{X} \neq 0$). In the bimodal regime, as energy increases, larger like-signed clusters form in each lobe and the distance between the two modes of the PDF increases.

Assuming ergodicity, i.e. that the microcanonical ensemble can predict the average of intermediate-time DNS (see section 5.2.1), the increasing distance between the two modes of the PDF as the energy increases signifies the decreasing probability of a switch between the two meta-stable states in a DNS as energy increases. As expected, since the two modes are symmetric about $\tilde{E} = 0$, both meta-stable states are equally likely to be realised.

Figure 5.3 shows cross sections of the PDF $p_{0,N}(\tilde{X}, \tilde{E})$ at $\tilde{E} = -0.05, 0, 0.05$ for $N = 10, 20, 50$ and 100 vortices, all computed with 10^7 samples. Convergence to the invariant function (5.2) is evident, even at this relatively low N.

The change in regime from unimodal (corresponding to no oscillations in a DNS) to bimodal (corresponding to oscillations in a DNS) shown in figures 5.2 and 5.3 is consistent with second order phase transitions, as introduced in section 2.4.2. In this case, $\tilde{X}$ is the order parameter that defines the different phases: as energy is increased $\tilde{X}$ changes smoothly from zero in the unimodal phase to non-zero in the bimodal phase.

In fact in most domains the phase transition from a unimodal regime to a bimodal regime as the energy is increased will happen, for an appropriate order parameter. Consider the vortex system in an arbitrary domain: at low energy the distribution of vorticity will be close to uniform and hence unimodal (order parameter zero). At high energy the system is forced into one of the two equivalent bimodal configurations comprising of two well-separated clusters, one of either sign (order parameter non-zero). As energy increases the like-signed clusters become larger and further apart from each other. In the $q = 0.8$ Neumann oval this means that a cluster of one sign will naturally occupy one lobe while the cluster of the other sign occupies the other lobe. Due to the high curvature of this Neumann oval, these clusters become trapped in their respective lobes leading to the situation where the probability of the clusters switching lobes is unlikely even at relatively low energies. In a domain

such as the heart, like-signed clusters will still become trapped in localised regions of the domain in the same manner as the Neumann oval, though only at significantly higher energies.

The critical energy at which the two symmetric states occur in an arbitrary domain is related to the first DIT β_1, as introduced in section 2.4.1. In domains such as the heart, $\beta_{2,3}$ are close to β_1 leading to a less clear emergence of the two symmetric states, as mentioned above. There are a number of subtleties to this phenomena, which are detailed in [44].

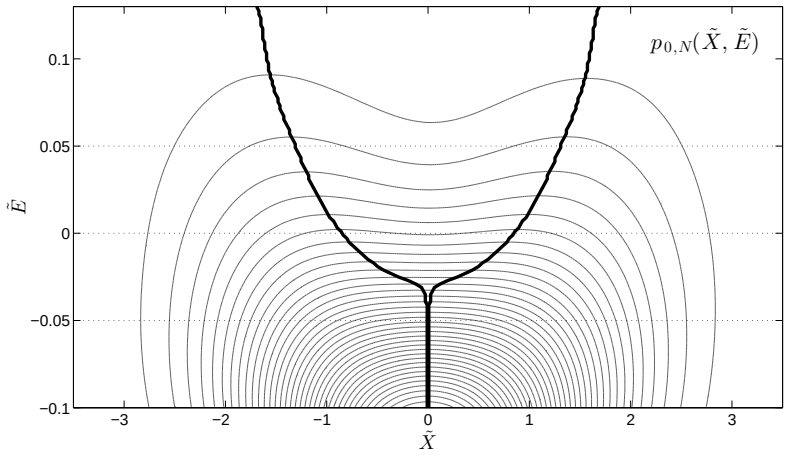

Figure 5.2: Joint $\tilde{X}$-$\tilde{E}$ PDF for the $q = 0.8$ Neumann oval with $N = 100$ vortices. The contour spacing is quadratic and the thick black line indicates the maximum of the PDF.

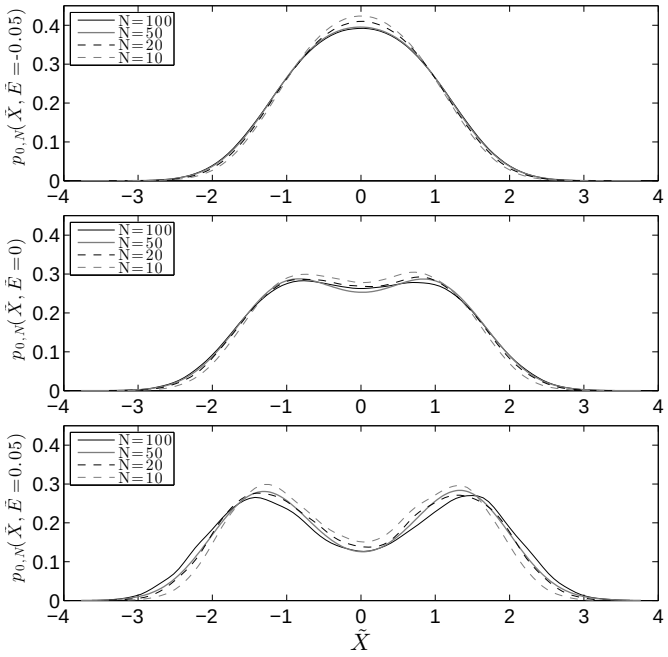

Figure 5.3: Cross sections of the joint $\tilde{X}$-$\tilde{E}$ PDF for the $q = 0.8$ Neumann oval at $\tilde{E} = -0.05$ (top), $\tilde{E} = 0$ (middle) and $\tilde{E} = 0.05$ (bottom), using $N = 100$ (solid black), $N = 50$ (solid grey), $N = 20$ (dashed black) and $N = 10$ (dashed grey).

5.2.3 Direct numerical simulation

The predictions from the joint PDF $p_{0,N}(\tilde{X}, \tilde{E})$ of the previous subsection can be verified using direct numerical simulations of the vortex system in the same domain[3]. Four integrations of $N = 100$ vortices are performed each at $\tilde{E} = -0.05$, $\tilde{E} = 0$, $\tilde{E} = 0.05$, using the parameters $t = 6000N$, $\Delta t = 0.1N$ and $\delta = 10^{-8}$; see section 1.2.3 for details. Initial conditions are generated using the Monte Carlo method described in section 1.3.3.

Figure 5.4 shows the DNS PDFs $p_D(\tilde{X})$ (solid black lines) at $\tilde{E} = -0.05$ (top), $\tilde{E} = 0$ (middle), and $\tilde{E} = 0.05$ (bottom). Each PDF is based on the average of four DNS runs. Also shown are the normalised cross sections of the joint PDF (dashed grey lines) from the microcanonical ensemble shown in figure 5.2 at the same energies i.e. $p_{0,N}(\tilde{X}, \tilde{E} = -0.05)$, $p_{0,N}(\tilde{X}, \tilde{E} = 0)$, $p_{0,N}(\tilde{X}, \tilde{E} = 0.05)$. Qualitative agreement

[3]This is not verification as in chapters 2 and 4 where DNS and microcanonical sampling were used to verify the predictions from statistical mechanics. Here the DNS is only confirming the ergodicity of the system – possible statistical mechanics predictions are discussed in section 5.3.

between the DNS PDFs and microcanonical ensemble PDFs is observed at all three energies.

Figure 5.5 shows typical time series of the DNS at $\tilde{E} = -0.05$ (top), $\tilde{E} = 0$ (middle), and $\tilde{E} = 0.05$ (bottom). As the energy increases the period of the oscillations also increases, in agreement with the microcanoncial predictions from the previous section.

5.3 Discussion

This chapter has presented numerical evidence, based on statistical sampling of the microcanonical ensemble and direct numerical simulations, that oscillations of the centre of vorticity between meta-stable states can occur in the point vortex system dominated by the mean flow in the $q = 0.8$ Neumann oval domain. It was noted that there are two phases of this system: a high energy phase where vorticity oscillates between the lobes of the Neumann oval, as characterised by a bimodal vorticity distribution and a low energy phase where the vorticity is uniform, as characterised by a unimodal vorticity distribution.

The next step in this problem would be to place the above result more formally in a statistical mechanics context and hence derive statistical mechanics predictions for the vorticity that also exhibit the same oscillatory behaviour at the appropriate energy. Equilibrium statistical mechanics models only provide a basis for calculations of the *probability* of the oscillations, while offering no information about their evolution in time. A suitable alternative way to model the time evolution of an N particle system is using *large deviation statistical mechanics*, as reviewed by Touchette [114]. As detailed by Touchette, the outcome of a given macrostate (such as X) should concentrate around certain meta-stable values (observed in this chapter) and the probability of oscillations between meta-stable states should decay exponentially with the number of vortices.

Touchette outlines a 'phenomenological' model for the evolution of the fluctuations in time of a general N particle system. Touchette's model (summarised below) is phenomenological in the sense that the dynamics are postulated on the basis of a number of mathematical and physical principles, rather than being derived directly

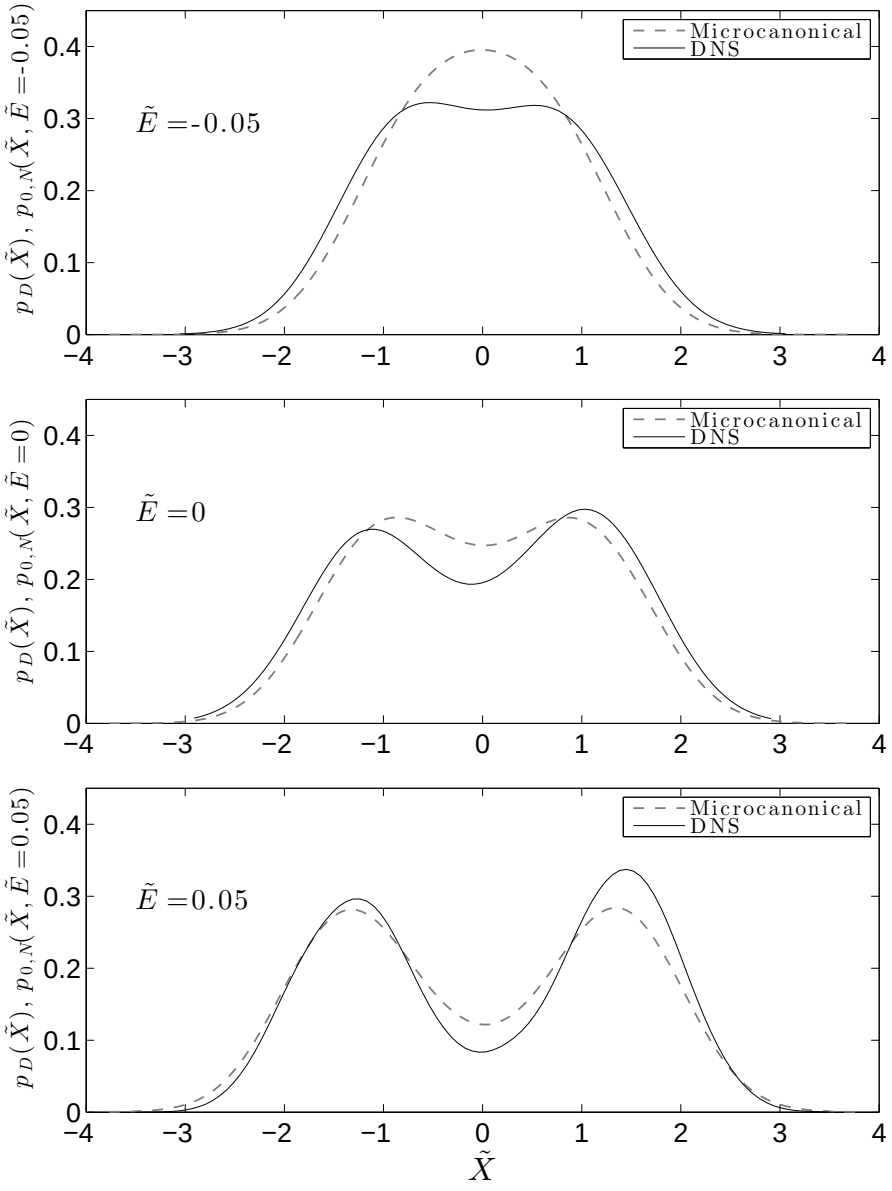

Figure 5.4: Comparison of the PDFs of centre of vorticity X as computed from direct numerical simulations (solid black lines) and the microcanonical ensemble (dashed grey lines) at $\tilde{E} = -0.05$ (top panel), $\tilde{E} = 0$ (middle panel) and $\tilde{E} = 0.05$ (bottom panel).

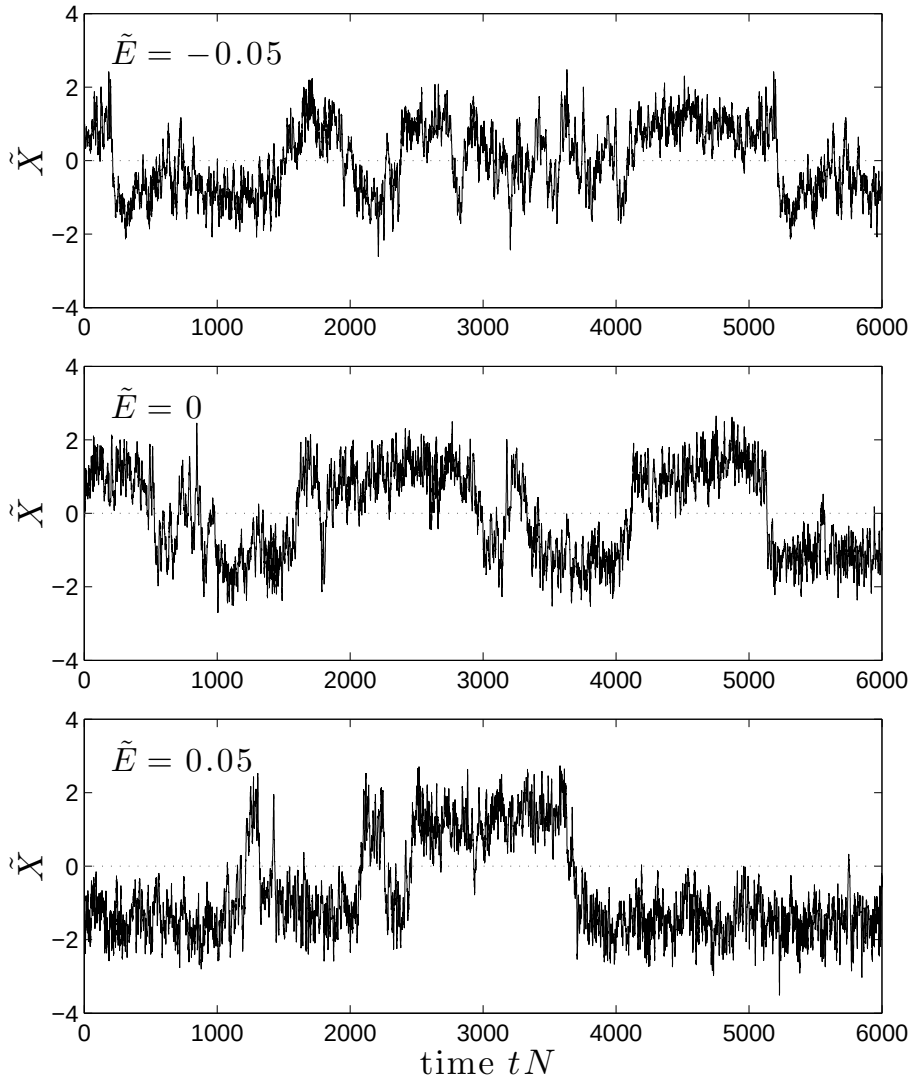

Figure 5.5: Typical time series of the centre of vorticity X from direct numerical simulations at $\tilde{E} = -0.05$ (top panel), $\tilde{E} = 0$ (middle panel) and $\tilde{E} = 0.05$ (bottom panel).

from the N-particle system – an extremely difficult (if not impossible) task.

Touchette's proposed model for the time evolution of a macrostate X_N, assumes that the dynamics satisfy a stochastic differential equation of the form

$$\frac{d}{dt}X_N(t) = b(X_N) + \xi_N(t), \tag{5.3}$$

where $b(X_N)$ is a restorative force field computed from the statistics of the system and $\xi_N(t)$ is a noise term that models the oscillations of $X_N(t)$. Some of the key mathematical and physical principles used in the derivation of (5.3) are:

1. The intensity of the noise $\xi_N(t)$ should vanish as $N \to \infty$ to reflect the fact that the oscillations of X_N vanish as $N \to \infty$.

2. Assuming the oscillations of X_N arise from the short-time correlated interactions of the N particles, the noise $X_N(t)$ should be chosen to be a Gaussian white noise with zero mean. In fact the noise term can be decomposed as

$$\xi_N(t) = r\frac{dB(t)}{dt},$$

   where r models the size of the fluctuations (as estimated from the statistics of the system) and $dB(t)/dt$ are increments of a Wiener process, which automatically gives Gaussian white noise [53].

3. The stationary probability distribution of (5.3) should match the equilibrium probability distribution of X_N determined from the microcanonical ensemble of the N particle system.

Recall that in chapter 4, equilibrium statistical mechanics predictions were derived for the density of states which were valid in the limit $N \to \infty$. These predictions were then verified by observing the convergence, as N increases, of the density of states computed from the microcanonical ensemble towards the theoretical predictions. Equation (5.3) is a similar type of theoretical prediction and so would be tested against the DNS of the vortex system (as in figure 5.5) for increasing N, where the decay of the oscillations, as N increases, should be observable.

In fact, a stochastic model very similar to (5.3) was used to model oscillations of vorticity between meta-stable states in the vortex system in [89], though in a less physically relevant domain than was used in this chapter.

Another interesting avenue of research would be investigating the 'entropy barrier' between the two dipole states of the Neumann oval. The two dipole states correspond to the first branch of the sinh-Poisson equation and they must be separated by an entropy minimum (or saddle point) creating a barrier of entropy ΔS. Is would be interesting to find out which state creates the entropy barrier: presumably the second solution branch of the sinh-Poisson equation. Further, ΔS could be computed as a function of E, then the lifetime of meta-stable states should scale as $e^{N\Delta s}$ and the probability of an oscillation as $e^{N\Delta s}$. Such behaviour was predicted in [21] and could be verified by DNS of the system considered in this chapter. The finite N effects a long-ranged system, similar to the vortex mode considered here, were considered in the context of the canonical ensemble in [26].

Chapter 6

Conclusions and future work

The work presented in this thesis concerns the dynamics and statistical mechanics of N point vortex systems in a variety of bounded domains. Broadly speaking four main problems have been approached. Chapter 2 considered the 2D Euler vortex system in the hydrodynamic limit. Chapter 3 introduced a new numerical algorithm which was subsequently used in chapter 4 to study the QGSW vortex system in the thermodynamic limit. Chapter 5 used the 2D Euler system to numerically demonstrate how vorticity can oscillate between localised regions in a left-right symmetric domain. At the end of chapters 2, 3, 4 and 5 detailed summaries are given and suggestions for future work that is closely related to the chapter has been discussed. This chapter will provide a broader overview of the work and also suggest some future problems that, while still being complementary, differ significantly from those already considered in the previous chapters.

In chapter 2 the vortex system in the hydrodynamic limit, dominated by the mean flow, was considered. The focus of the chapter was on 2D Euler dynamics where the well-known sinh-Poisson equation (SPE), an elliptic partial differential equation for the streamfunction, is the key statistical mechanics result. The SPE has infinitely many solution branches, each with a different streamfunction structure and each originating at zero energy from a 'domain inverse temperature' (DIT); the branches are found as solutions to a 'vorticity mode' eigenvalue problem derived by linearising the SPE. The entropy of the statistical mechanics predictions can also be calculated from the solution branches and hence the most probable maximum entropy solution can be predicted. The full nonlinear SPE was solved, using a new

numerical technique based on a Galerkin-type expansion, in a domain chosen such that the solution branches have the potential to cross. It was found that the two highest entropy solution branches did cross as the energy of the system increased; hence the topological structure of the most probable solution changed (from a dipole to a monopole) as the energy increased. This was classified as a condensate switch phase transition, where the condensate is simply the state of the system dominated by the mean flow. In order to verify this condensate switch, the $N = 100$ vortex system, from which the SPE is derived in the limit $N \to \infty$, E=constant, was considered in the same domain. An ensemble of long-time direct numerical simulations at different energies was carried out and the time-averaged equilibrium streamfunction of these simulations were compared with the predicted equilibrium streamfunction from the SPE solutions. Reasonably Convincing results were observed, verifying the condensate switch: at low energies the dipolar solution was found and at high energies the monopolar solution; both as predicted by the SPE. Additionally, at the critical energy where the two solution branches of the SPE cross, and hence have equal entropy, the dipolar solution was found in half of the runs and the monopolar solution was found for the other half.

In chapter 3, a new algorithm (VOR-MFS) was introduced for the calculation of the dynamics of a generalised vortex. VOR-MFS utilised the method of fundamental solutions (MFS) to construct a highly accurate numerical approximation of the dynamical influence of the boundary on the dynamics of vortices inside a domain, using a weighted sum of M fundamental solutions (charges) placed outside the domain. With appropriate placing of charges, the MFS (and hence VOR-MFS) achieves exponential convergence, even in complicated domains. Consequently, the solutions constructed using VOR-MFS are highly accurate, with verification being carried out using the invariance of the analytical Hamiltonian if available or the numerical Hamiltonian (and angular momentum in the case of the disk). This was done for four test cases, including the dynamics of N quasi-geostrophic shallow water (QGSW) vortices in a Neumann oval domain.

In chapter 4 the vortex system in the thermodynamic limit was considered. In particular, in the absence of a mean flow the 'vorticity fluctuation equation' was derived which is the thermodynamic analogue of the SPE. It transpires that solutions

of the vorticity fluctuation equation may be constructed using the vorticity modes introduced in chapter 2 as a basis. Solutions of the vorticity fluctuation equation allow low positive and negative energy equilibrium predictions to be made for the density of states and hence for the inverse thermodynamic temperature. In order to verify these statistical mechanics predictions, and further demonstrate the effectiveness of the VOR-MFS algorithm introduced in chapter 3, the QGSW system in a Neumann oval was considered. Using statistical sampling of the microcanonical ensemble, finite N estimates of the density of states and inverse thermodynamic temperature were constructed and compared with the statistical mechanics predictions, with convincing results.

In chapter 5, the 2D Euler system in the Neumann oval was considered. Using a suitable macroscopic diagnostic for the distribution of vorticity in the domain, a joint probability density function with the energy was constructed from the microcanonical ensemble and it was found that, as the energy increases, the vorticity distribution changes from unimodal to bimodal where a vortex cluster of one sign becomes increasingly likely to be trapped in one lobe of the Neumann oval while a cluster of the other sign becomes trapped in the other lobe. This behaviour was verified using direct numerical simulations where, due to ergodicity, the clusters switch lobes in an oscillatory manner. The higher the energy the greater the clustering and hence the longer the period of oscillation. The change in the behaviour of the system as the energy is increased (and the vorticity distribution changes from unimodal to bimodal) is classified as an energy-induced second order phase transition in statistical mechanics.

From chapters 2 and 4, it should be evident that the vorticity modes and DITs are a remarkably useful tool for statistical mechanics calculations in a variety of limits and their significance should be emphasised. The distribution of DITs varies depending on the shape of the domain and this distribution controls the form of solutions in the hydrodynamic and thermodynamic limits. Hence, one clear avenue for future research would be a rigorous mathematical investigation into the behaviour of the distribution of DITs in general domains. This would likely use techniques from spectral theory and progress in this area could allow very general observations to be made regarding the behaviour of the system in multiple limits.

There are also a number of other possibilities for future research. For example, as noted in section 1.3.4, in addition to the hydrodynamic and thermodynamic limits, other limits could conceivably exist which have yet to be explored. Complementary to the work in chapters 2 and 4, it would be interesting to investigate the transition from when the system is best described by the thermodynamic limit where the vorticity fluctuation equation (4.8) applies to when it is best described by the hydrodynamic limit where the sinh-Poisson equation/elliptic-sinh equation (2.23) applies. This spontaneous, symmetry breaking as the mean flow emerges has been observed in 2D turbulence and described as Bose condensation; see section 2.4.2. As noted by PL76, this 'intermediate scaling regime' must involve asymptotic matching of the hydrodynamic limit as $E \to 0$ with the thermodynamic limit as $\tilde{E} \to \infty$.

The Miller-Robert-Sommeria (MRS) theory [84, 85, 101, 102], as introduced in section 1.4.2, also offers a number of possibilities for future work. The MRS theory dispenses with the point vortex approximation and instead breaks up the vorticity into patches which are distributed using Lynden-Bell statistics [79] to find the most probable state. Unlike the point vortex approximation, the MRS approach enables all the invariants of the 2D Euler equations to be included, though it is debatable whether they *should* be included if we are interested in generic properties of the system [111]. Interestingly, a number of MRS studies such as [27, 117, 118] also rely on a set of eigenvalues, analogous to the DITs mentioned above. In the paper by Yin et al. [124], the following MRS sinh-Poisson analogue was derived and solved in a doubly periodic domain

$$\nabla^2\psi = D\left[\frac{2\sinh(\beta\psi)}{e^{-\alpha} + 2\cosh(\beta\psi)}\right], \tag{6.1}$$

where D^{-1} is the (arbitrary) patch size, α is a Lagrange multiplier and β and ψ are, respectively, the inverse temperature and the streamfunction, as defined in chapter 2. It would be interesting to find out if the crossings of solution branches of the SPE in the heart-shaped domain considered in section 2.4, and the resulting condensate switch, also correspond to crossings in the branches of (6.1). Yin et al. also noted that the structure of the maximum entropy solutions of (6.1) varies depending on patch size D^{-1}. How this relates to the SPE maximum entropy solutions, particularly

at the critical energy where two solution branches have the same entropy, would be of interest.

Another potential extension to the work presented in this thesis would be 'direct' comparisons between point vortex statistical mechanics and 2D turbulence. Yin et al. verified their solutions of the SPE and (6.1) in the doubly periodic domain using DNS of the full Navier-Stokes equations. Though technically challenging, similar calculations for the heart domain in chapter 2, and for the Neumann oval in chapter 4, would provide a stringent test as to the validity of point vortex statistical mechanics as a model for 2D turbulence.

Finally, it would be interesting to relate the equilibrium statistical mechanics results presented in this thesis to *non-equilibrium* statistical mechanics. In equilibrium statistical mechanics, statistics of macroscopic quantities are stationary in time, whereas in non-equilibrium statistical mechanics, time-dependent statistics are derived based on a 'kinetic theory' approach. Though equilibrium statistical mechanics has demonstrated to be an effective model for 2D turbulence, its clear shortcoming is that this model ignores the dynamical mechanisms that lead to equilibrium, which can dominate the flow for long times. This shortcoming can be addressed using non-equilibrium statistical mechanics where the relaxation of point vortices towards equilibrium is governed by an energy conserving integro-differential equation; see [25] and references therein[1]. It would be interesting to use a similar equation to model the non-equilibrium 'turbulent spin-up' period described in section 2.4.5. Here the non-equilibrium state was simply ignored and a heuristic approach was used to determine when it was over and hence when the equilibrium statistical mechanics could be justifiably used (see figure 2.9). It would be desirable to have a more complete description of the system, using both non-equilibrium and equilibrium statistical mechanics.

[1]Note that the evolution of the non-energy conserving system of a single test vortex in a bath of field vortices is governed by the Fokker-Plank equation [22]; incidentally, the evolution of Brownian vortices as a whole is also governed by the Fokker-Plank equation [24].

Appendix A

Conformal mapping techniques

A.1 Introduction

Conformal mapping techniques have been used throughout this thesis to study Hamiltonian vortex dynamics (1.2) and elliptic partial differential equations (e.g. the sinh-Poisson equation (2.11)) in two different families of domains: chapter 3 introduced the Neumann oval (also used in chapter 4) and chapter 2 introduced the heart-shaped domain. Details of the transformation of the Hamiltonian from the unit disk to any simply connected domain are given in section A.2.1, with the Neumann oval used as an example in section A.2.2. In section A.3.1 the mapping theory for a general elliptic PDE is given, and in section A.3.2 two examples are presented using the Laplace eigenvalue problem for domains not used in this thesis. Finally section A.4 details the conformal grids themselves, with respect to their 'coverage' of the domain and their performance in terms of numerical quadrature.

A.2 Green's function/Hamiltonian

A.2.1 The map

Consider a unit disk domain $\mathcal{C}$ in the complex Z-plane with the usual correspondence between $\mathbb{C}$ and $\mathbb{R}^2$ is taken so that $Z = X + \mathrm{i}Y \in \mathbb{C}$ is identified with $\boldsymbol{X} = (X\ Y)^T \in \mathbb{R}^2$. As mentioned in section 3.3.1, the exact Hamiltonian H for the

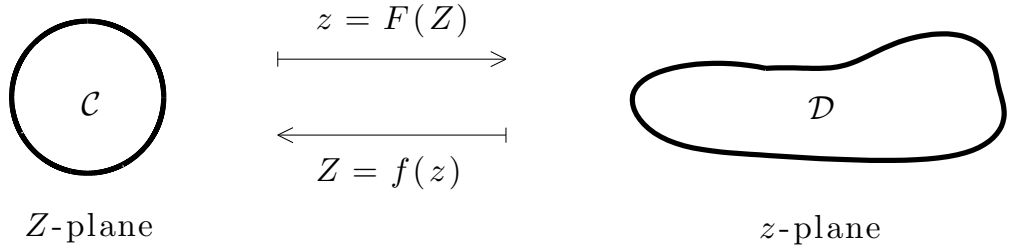

Figure A.1: The conformal map from a unit circle $\mathcal{C}$ in the Z-plane to another simply connected domain $\mathcal{D}$ in the z-plane.

motion of N 2D Euler vortices in $\mathcal{C}$ is given by (1.2) with

$$G(Z,Z') = G_{\mathcal{C}}(Z,Z') = \frac{1}{2\pi}\log|Z-Z'| - \frac{1}{4\pi}\log\left|Z - \frac{Z'}{|Z'|^2}\right|, \tag{A.1}$$

where the first term is $G_0(Z,Z')$ (alternatively, the free space interaction of a vortex of circulation $+1$ at Z') and the second term the de-singularised function $g_{\mathcal{C}}(Z,Z')$ (alternatively, the contribution due to image vortex of circulation -1 at $Z^* = Z'/|Z'|^2$).

Switching to complex conjugate notation and inserting (A.1) into the Hamiltonian (1.2) leads to the familiar N vortex Hamiltonian for $\mathcal{C}$

$$\begin{aligned} H_{\mathcal{C}}\left(Z,\overline{Z}\right) = & -\frac{1}{4\pi}\sum_{i=1}^{N}\sum_{j=i+1}^{N}\Gamma_i\Gamma_j\log\left((Z_i-Z_j)\overline{(Z_i-Z_j)}\right) \\ & +\frac{1}{4\pi}\sum_{i=1}^{N}\Gamma_i^2\log\left(1-Z_i\overline{Z_i}\right) \\ & -\frac{1}{4\pi}\sum_{i=1}^{N}\sum_{j=i+1}^{N}\Gamma_i\Gamma_j\log\left(\left(1-Z_i\overline{Z_i}\right)\left(1-Z_j\overline{Z_j}\right)+(Z_i-Z_j)\overline{(Z_i-Z_j)}\right). \end{aligned} \tag{A.2}$$

The first term in the right hand side of (A.2) corresponds to the free space vortex-vortex interaction, the second term is the self-interaction for each vortex with its own image and the third term is the interaction of each vortex with the images of all the other vortices.

We are concerned here with how the Hamiltonian (A.2) transforms when the

domain $\mathcal{C}$ is conformally mapped to another simply-connected domain $\mathcal{D}$ in the z-plane by the map

$$Z = f(z), \tag{A.3}$$

with inverse

$$z = f^{-1}(Z) = F(Z), \tag{A.4}$$

see fig. A.1. As with the Z-plane, in the z-plane $\mathbb{C}$ corresponds to $\mathbb{R}^2$, and $z = x + \mathrm{i}y$ corresponds to $\boldsymbol{x}$.

As proved in [77] and reviewed in [91,104], in order to construct the Hamiltonian in the z-plane $H_{\mathcal{D}}$, the Green's function $G_{\mathcal{D}}$ and the de-singularising function $g_{\mathcal{D}}$ are required. The invariance of the Laplace equation under the map (A.3) guarantees the Green's function itself is also invariant

$$G_{\mathcal{D}}(\boldsymbol{x}, \boldsymbol{x}') = G_{\mathcal{C}}(\boldsymbol{f}(\boldsymbol{x}), \boldsymbol{f}(\boldsymbol{x}')) \tag{A.5}$$

where the vector-valued function $\boldsymbol{X} = \boldsymbol{f}(\boldsymbol{x})$ is the $\mathbb{R}^2$ expression of (A.3).

The function $g_{\mathcal{D}}$ does, however, change under the mapping (A.3). By definition

$$\begin{aligned} g_{\mathcal{D}}(\boldsymbol{x}, \boldsymbol{x}') &= G_{\mathcal{D}}(\boldsymbol{x}, \boldsymbol{x}') - \frac{1}{2\pi} \log |\boldsymbol{x} - \boldsymbol{x}'| \\ &= g_{\mathcal{C}}(\boldsymbol{f}(\boldsymbol{x}), \boldsymbol{f}(\boldsymbol{x}')) + \frac{1}{2\pi} \log \left| \frac{f(z') - f(z)}{z' - z} \right|. \end{aligned} \tag{A.6}$$

To find the function $g_{\mathcal{D}}(\boldsymbol{x}, \boldsymbol{x})$, as required in (1.2) (where it is denoted at $g(\boldsymbol{x}, \boldsymbol{x})$), take the limit $z \to z'$ in (A.6) giving

$$g_{\mathcal{D}}(\boldsymbol{x}, \boldsymbol{x}) = g_{\mathcal{C}}(\boldsymbol{f}(\boldsymbol{x}), \boldsymbol{f}(\boldsymbol{x})) - \frac{1}{2\pi} \log |F'(Z)|, \tag{A.7}$$

where the Taylor expansion

$$f(z') = f(z) + (z' - z) f'(z) + O\left((z' - z)^2\right),$$

has been used.

Note that both (A.5) and (A.7) are given only in terms of Z coordinates, allowing the so-called Kirchhoff-Routh formula to also be defined purely in terms of Z coordinates as

$$H_{\mathcal{D}}(z,\overline{z}) = H_{\mathcal{C}}\left(Z,\overline{Z}\right) + \sum_{i=1}^{N} \frac{\Gamma_i^2}{4\pi} \log\left|F'(Z_i)\right|, \tag{A.8}$$

a result first given for $N = 1$ by Routh [103] in 1881 and generalised for any N by Lin [77] in 1941.

The dynamics governed by (A.8) are found as follows: first note that $x = (z+\bar{z})/2$ and $y = (z-\bar{z})/2\mathrm{i}$ and so

$$\begin{aligned} \frac{\partial H_{\mathcal{D}}}{\partial z} &= \frac{\partial H_{\mathcal{D}}}{\partial x}\frac{\partial x}{\partial z} + \frac{\partial H_{\mathcal{D}}}{\partial y}\frac{\partial y}{\partial z} \\ &= \frac{1}{2}\left(\frac{\partial H_{\mathcal{D}}}{\partial x} - \mathrm{i}\frac{\partial H_{\mathcal{D}}}{\partial y}\right), \end{aligned}$$

then the complex form of Hamilton's equations (1.1) is

$$\begin{aligned} \Gamma_i \dot{\overline{z_i}} &= 2\mathrm{i}\frac{\partial H_{\mathcal{D}}}{\partial z_i} \\ &= 2\mathrm{i}\left(\frac{\partial H_{\mathcal{D}}}{\partial Z_i}\frac{\partial Z_i}{\partial z_i} + \frac{\partial H_{\mathcal{D}}}{\partial \overline{Z_i}}\frac{\partial \overline{Z_i}}{\partial z_i}\right) \\ &= 2\mathrm{i}\frac{\partial H_{\mathcal{D}}}{\partial Z_i}\left(\frac{\partial z_i}{\partial Z_i}\right)^{-1}, \end{aligned} \tag{A.9}$$

since $\partial\overline{Z_i}/\partial z_i = 0$ as the conformal map (A.4) is not a function of $\overline{Z}$. Using (A.4), the left hand side of (A.9) can also be expressed in terms of Z coordinates, giving

$$\Gamma_i \dot{\overline{F(Z_i)}} = 2\mathrm{i}\frac{\partial H_{\mathcal{D}}}{\partial Z_i}\left(\frac{\partial z_i}{\partial Z_i}\right)^{-1}. \tag{A.10}$$

Hence the dynamics are computed in $\mathcal{C}$ using (A.10) then mapped to $\mathcal{D}$ using (A.4); see next section.

A.2.2 Example

The Hamiltonian in the Neumann oval domain that is used in chapters 3 and 4 is examined in detail in this subsection. The domain is defined by the conformal map

$$z_i = F(Z_i) = \frac{aZ_i}{1 - q^2 Z_i^2}, \tag{A.11}$$

(for real constants a and q) and was first used to investigate Hele-Shaw blob growth near a wall in [100]. The area is given by

$$\frac{1}{2\mathrm{i}} \oint_{\mathcal{D}} \bar{z}\, dz = \pi a^2 \frac{(1+q^4)}{(1-q^4)^2},$$

which when fixed defines a one-parameter family of Neumann ovals in q.

Using (A.8) (and hence (A.2)) the Hamiltonian for N point vortices in the Neumann oval $\mathcal{D}$ is

$$H_{\mathcal{D}}\left(Z, \overline{Z}\right) = H_{\mathcal{C}} + \frac{1}{4\pi} \sum_{i=1}^{N} \Gamma_i^2 \log \left| \frac{a(1+q^2 Z_i^2)}{(1-q^2 Z_i^2)^2} \right|. \tag{A.12}$$

Using the conjugate of (A.11) we can compute, by directly differentiating with respect to time,

$$\dot{\overline{z_i}} = a\dot{\overline{Z_i}} \frac{1 + q^2 \overline{Z_i}^2}{\left(1 - q^2 \overline{Z_i}^2\right)^2},$$

and also

$$\frac{\partial z_i}{\partial Z_i} = \frac{a(1+q^2 Z_i^2)}{(1-q^2 Z_i^2)^2},$$

which when substituted into (A.9) gives

$$\Gamma_i \dot{\overline{Z_i}} = \frac{2i}{a^2 |1 - q Z_i|^2} \frac{\partial H_{\mathcal{D}}}{\partial Z_i}.$$

Thus the equations of motion for the i^{th} vortex are

$$\dot{X}_i = \frac{-1}{2\pi a^2|1-qZ_i|^2}\left\{\sum_{i=1,i\neq j}^{N}\frac{\Gamma_j(Y_i-Y_j)}{|Z_i-Z_j|^2}+\sum_{j=1}^{N}\frac{\Gamma_j(Y_j^*-Y_i)}{|Z_i-Z_j^*|^2} + 2q^2\left[\frac{Y_iQ_2-X_iQ_3}{|1+q^2Z_i^2|^2}+2\frac{Y_iQ_1+X_iQ_3}{|1-q^2Z_i^2|^2}\right]\right\} \tag{A.13a}$$

$$\dot{Y}_i = \frac{1}{2\pi a^2|1-qZ_i|^2}\left\{\sum_{i=1,i\neq j}^{N}\frac{\Gamma_j(X_i-X_j)}{|Z_i-Z_j|^2}-\sum_{j=1}^{N}\frac{\Gamma_j(X_i-X_j^*)}{|Z_i-Z_j^*|^2} - 2q^2\left[\frac{X_iQ_2+Y_iQ_3}{|1+q^2Z_i^2|^2}+2\frac{X_iQ_1-Y_iQ_3}{|1-q^2Z_i^2|^2}\right]\right\}, \tag{A.13b}$$

where the image vortices denoted by stars are

$$Z_j^* = X_j^* + \mathrm{i}Y_j^* = (X_j+\mathrm{i}Y_j)\frac{1}{X_j^2+Y_j^2},$$

and

$$\begin{aligned} Q_1(Z_i) &= \Re\{1-q^2Z_i^2\} \\ Q_2(Z_i) &= \Re\{1+q^2Z_i^2\} \\ Q_3(Z_i) &= \Im\{1-q^2Z_i^2\} \equiv \Im\{1+q^2Z_i^2\}, \end{aligned}$$

where $\Re\{\cdot\}$ and $\Im\{\cdot\}$ denote the real and imaginary parts of the relevant expression. The differential equations (A.13) can then be integrated to give Z coordinates for the motion in the z-plane. These coordinates can then be mapped to the z-plane by substituting $z_i = x_i + \mathrm{i}y_i$ and $Z_i = X_i + \mathrm{i}Y_i$ into (A.11) and equating real and imaginary coefficients to give

$$\begin{aligned} x_i &= a\frac{X_iQ_1-Y_iQ_3}{|1-q^2Z_i^2|^2} \\ y_i &= a\frac{Y_iQ_1+X_iQ_3}{|1-q^2Z_i^2|^2}. \end{aligned}$$

A.3 Elliptic operators

A.3.1 The map

Consider the elliptic PDE

$$\nabla^2 u_{\mathcal{D}}(x,y) = h(u_{\mathcal{D}}(x,y)) \tag{A.14}$$

in the same domain $\mathcal{D}$ as described in section A.2.1. The function h on the right hand side of (A.14) was effectively $\sinh(u_{\mathcal{D}})$ in chapter 2 and simply the eigenvalue problem $-\lambda_i u_{\mathcal{D}}$ in chapter 4. The question is, again, how is the equation (in this case (A.14)) transformed when mapped to $\mathcal{C}$ via (A.3), i.e. $Z = f(z)$? Note that Dirichlet or vorticity mode boundary conditions associated with a partial differential equation such as (A.14) are unchanged when mapped to $\mathcal{C}$.

Following [1], the answer to the above question is now reviewed. First note that

$$u_{\mathcal{D}}(x,y) \equiv u_{\mathcal{C}}(X(x,y), Y(x,y)), \tag{A.15}$$

meaning the right hand side of (A.14) remains unchanged when mapped to $\mathcal{C}$. Consequently the task is to find the multiplying factor A in

$$\nabla_z^2 u_{\mathcal{D}}(x,y) = A \nabla_Z^2 u_{\mathcal{C}}(X,Y), \tag{A.16}$$

where $\nabla_z^2 = \partial^2/\partial x^2 + \partial^2/\partial y^2$ and $\nabla_Z^2 = \partial^2/\partial X^2 + \partial^2/\partial Y^2$. The first step is to take the second derivatives of (A.15) with respect to X and with respect to Y

$$\frac{\partial^2 u_{\mathcal{C}}}{\partial X^2} = \frac{\partial^2 u_{\mathcal{D}}}{\partial x^2}\left(\frac{\partial x}{\partial X}\right)^2 + 2\frac{\partial^2 u_{\mathcal{D}}}{\partial x \partial y}\frac{\partial x}{\partial X}\frac{\partial y}{\partial X} + \frac{\partial^2 u_{\mathcal{D}}}{\partial y^2}\left(\frac{\partial y}{\partial X}\right)^2 + \frac{\partial u_{\mathcal{D}}}{\partial x}\frac{\partial^2 x}{\partial X^2} + \frac{\partial u_{\mathcal{D}}}{\partial y}\frac{\partial^2 y}{\partial X^2} \tag{A.17}$$

$$\frac{\partial^2 u_{\mathcal{C}}}{\partial Y^2} = \frac{\partial^2 u_{\mathcal{D}}}{\partial x^2}\left(\frac{\partial x}{\partial Y}\right)^2 + 2\frac{\partial^2 u_{\mathcal{D}}}{\partial x \partial y}\frac{\partial x}{\partial Y}\frac{\partial y}{\partial Y} + \frac{\partial^2 u_{\mathcal{D}}}{\partial y^2}\left(\frac{\partial y}{\partial Y}\right)^2 + \frac{\partial u_{\mathcal{D}}}{\partial x}\frac{\partial^2 x}{\partial Y^2} + \frac{\partial u_{\mathcal{D}}}{\partial y}\frac{\partial^2 y}{\partial Y^2}. \tag{A.18}$$

Using the Cauchy-Riemann equations

$$\frac{\partial x}{\partial X} = -\frac{\partial y}{\partial Y}, \quad \frac{\partial y}{\partial X} = \frac{\partial x}{\partial Y},$$

(A.17) and (A.18) are combined to give

$$\nabla_z^2 u_{\mathcal{D}}(X) = |F'(Z)|^{-2} \nabla_Z^2 u_{\mathcal{C}}(Z),$$

and hence when (A.14) is mapped to $\mathcal{C}$ it is transformed into

$$|F'(Z)|^{-2} \nabla_Z^2 u_{\mathcal{C}}(Z) = h(u_{\mathcal{C}}(Z)). \tag{A.19}$$

Equation (A.19) can then be solved in $\mathcal{C}$ using, for example, Chebyshev spectral methods [115] (see appendix A.4) and then mapped back to the $\mathcal{D}$ via (A.4).

To compute the scaling for a non-Laplacian operator by the same map, a similar calculation to that given above for the Laplacian operator is required. For example in the case of the modified Helmholtz operator considered in chapter 4, $(\nabla^2 - \lambda^2)u(z) = f(z)$ is also transformed into (A.19) with $h \equiv \lambda^2 u_c - h^*$.

Before proceeding with some examples, a final point about (A.14) & (A.19) and their relation to conformal mapping of the Hamiltonain as discussed in section A.2.1 is made. In section A.2.1 we demonstrated the changes of the Laplace Green's function $G_{\mathcal{D}}(\boldsymbol{x}, \boldsymbol{x}')$ with conformally mapped to domain $\mathcal{C}$. In order words we showed how Laplace's equation $\nabla_z^2 G_{\mathcal{D}}(\boldsymbol{x}, \boldsymbol{x}') = 0$ changes when conformally mapped i.e. (A.14) with zero right hand side. However, vortex dynamics is not defined by Laplace's equation, but by the Poisson equation with Dirac delta function on the right hand side i.e. $\nabla_z^2 G_{\mathcal{D}}(\boldsymbol{x}, \boldsymbol{x}') = \delta_z(\boldsymbol{x} - \boldsymbol{x}')$ or equivalently

$$\nabla_z^2 G_{\mathcal{D}}(z, z') = \delta_z(z - z'), \tag{A.20}$$

where $\delta_z(\cdot)$ is the delta function in the z-plane. Therefore, for the results of section A.2.1 to be valid we must prove the conformal invariance of the delta function, a point frequently missed in many analyses and only proven recently in [42]. The argument is as follows. Consider the delta function in the z-plane, for some arbitrary function

$h(z)$

$$\int_{z\in\mathbb{R}^2} \delta_z(z-z')h(z)\,dz = h(z') \tag{A.21}$$

Applying the conformal map (A.3) to (A.21) gives

$$\int_{Z\in\mathbb{R}^2} \delta_Z(F(Z)-F(Z'))h(F(Z))|F'(Z)|^{-2}\,dZ = h(F(Z')), \tag{A.22}$$

where $\delta_Z(\cdot)$ is the delta function in the Z-plane. From (A.22) it can be seen that

$$\delta_Z(F(Z)-F(Z'))|F'(Z)|^{-2} = \delta_Z(Z-Z'). \tag{A.23}$$

Using (A.19), (A.20) becomes

$$\frac{\nabla_Z^2}{|F'(Z)|^2}G(F(Z),F(Z')) = \delta_Z(F(Z)-F(Z')), \tag{A.24}$$

then using (A.23) gives

$$\nabla_Z^2 G(F(Z),F(Z')) = \delta_Z(Z-Z').$$

Hence we conclude that (A.14) with delta function on the right hand side is conformally invariant, meaning no additional factors are required to the changes in the Green's function described in section A.2.1.

A.3.2 Examples

To further demonstrate the mapping of elliptic problems (beyond that used for the heart-shaped domain considered in chapter 2 and the Neumann oval considered in chapter 4), the Laplace eigenvalue problem

$$\nabla^2 u_i = -\alpha_i^2 u_i,$$

where u_i is the i^{th} eigenmode and α_i^2 is the i^{th} eigenvalue, is considered for two domains that were not used elsewhere in this thesis. The calculations are done using

Chebyshev spectral methods [115]; further details are given in section A.4. The first domain considered is the cardioid which may be defined by

$$z = F(Z) = qZ\left(1 - \frac{a(q)Z}{2}\right) \tag{A.25}$$

which is a map from $\mathcal{C}$ to a family of limaçons in $\mathcal{D}$ defined by a and q. The area is given by

$$\pi a^2(1 + 2q^2),$$

and the domain varies from a circle (as $q \to 1$, $a \to 0$) to a cardioid (as $q \to \sqrt{2/3}$, $a \to 1$). To compute the eigenmodes of the cardioid the scaling factor in (A.19) is required

$$|F'(Z)|^2 = a^2(1 - 4qR\cos\theta + 4q^2R^2), \quad Z = Re^{\mathrm{i}\theta}.$$

The solution is then mapped back to $\mathcal{D}$ using

$$\begin{aligned} x &= qR\left(\cos\theta - \frac{aR}{2}\cos 2\theta\right) \\ y &= qR\left(\sin\theta - \frac{aR}{2}\sin 2\theta\right). \end{aligned}$$

The eigenmodes u_i and eigenvalues α_i^2 for the cardioid of area π are shown in fig. A.2. This calculation was done using $\mathcal{N} \times \mathcal{M} = 50 \times 100$ radial and azimuthal points respectively; see section A.4. Eigenvalues are shown to six significant figures, though at this resolution they have converged to better than 10^{-12}.

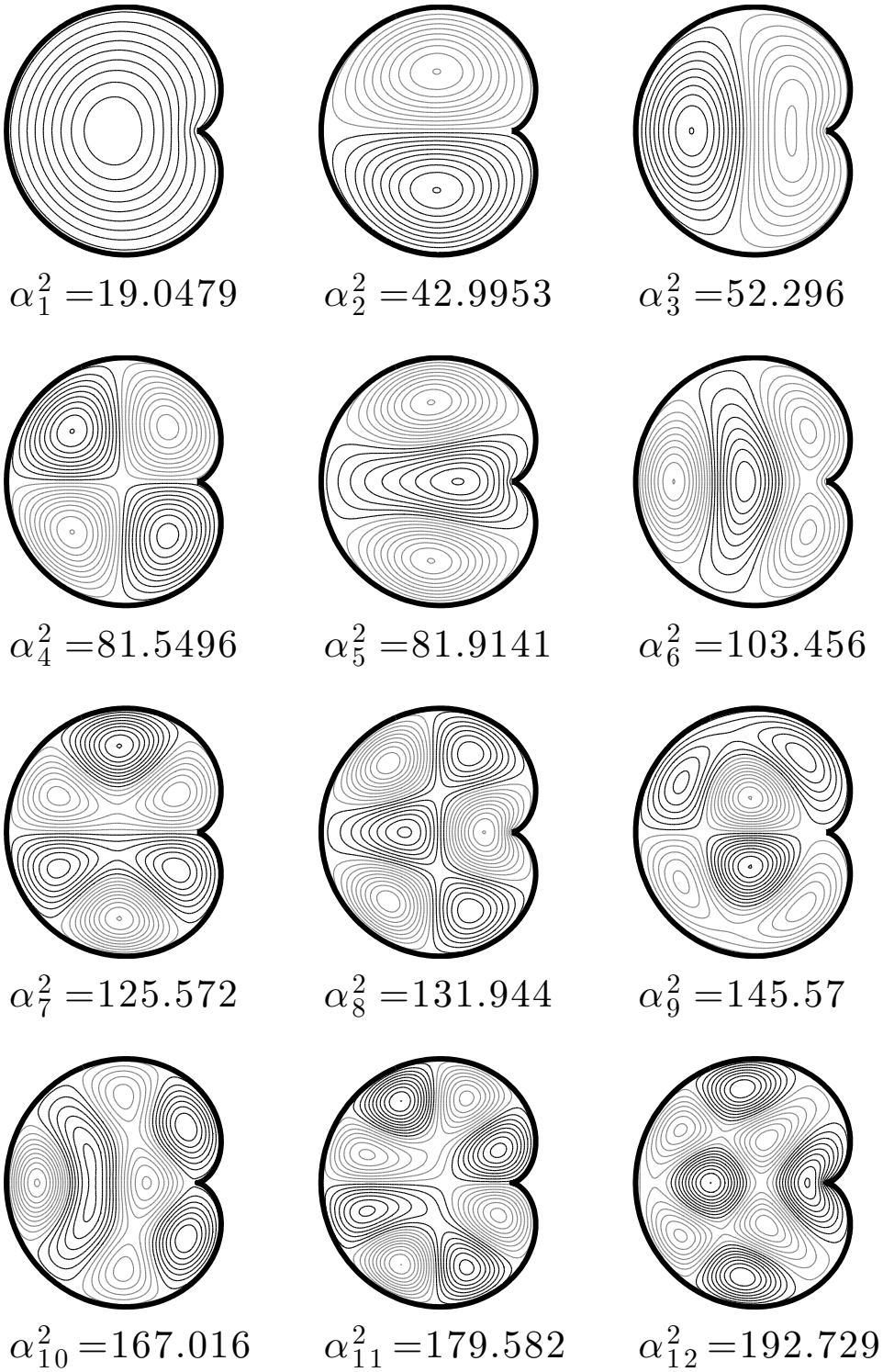

Figure A.2: First 12 Laplace eigenmodes and eigenvalues of the cardioid defined by the conformal map (A.25), $a = 1$, $q = \sqrt{2/3}$.

The next domain considered is a generalised version of the Neumann oval, where the two lobes are allowed to be of different size. The domain is defined by the map

$$z = F(Z) = \frac{a(q,\gamma)Z + \gamma Z^2}{1 - q^2 Z^2}, \tag{A.26}$$

with area given by

$$\pi \frac{2\gamma^2 + a^2 + q^4 a^2}{(1-q^4)^2}$$

and

$$|F'(Z)|^2 = \frac{a^2(1 + 2q^2R^2\cos 2\theta + q^4R^4) + 4\gamma r(a\cos\theta(R^2+1) + \gamma r)}{(1 - 2q^2R^2\cos 2\theta + q^4R^4)^2}, \quad Z = Re^{\mathrm{i}\theta}$$

with

$$\begin{aligned} x &= \frac{Ra\cos\theta(1-q^2R^2) + R^2\gamma(\cos 2\theta + R\beta^2)}{1 - 2q^2R^2\cos(2\theta) + q^4R^4} \\ y &= \frac{Ra\sin\theta(1-q^2R^2) + R^2\gamma\sin 2\theta}{1 - 2q^2R^2\cos(2\theta) + q^4R^4}. \end{aligned}$$

The domain (A.26) has three parameters a, q and γ. Fixing the area gives $a = a(q,\gamma)$, with γ then controlling the size of the smaller, left-hand lobe, and q the 'pinching' between the lobes, as for the Neumann oval considered in chapters 3 and 2. It is noted that domain can vary from a Neumann oval ($\gamma \to 0$), to a circle by reducing the size of the left-hand lobe ($\gamma \to 1$).

The eigenmodes for the uneven Neumann oval of area π are given in fig. A.3. Again the radial $\times$ azimuthal resolution used in the computation is $\mathcal{N}\times\mathcal{M} = 50\times100$.

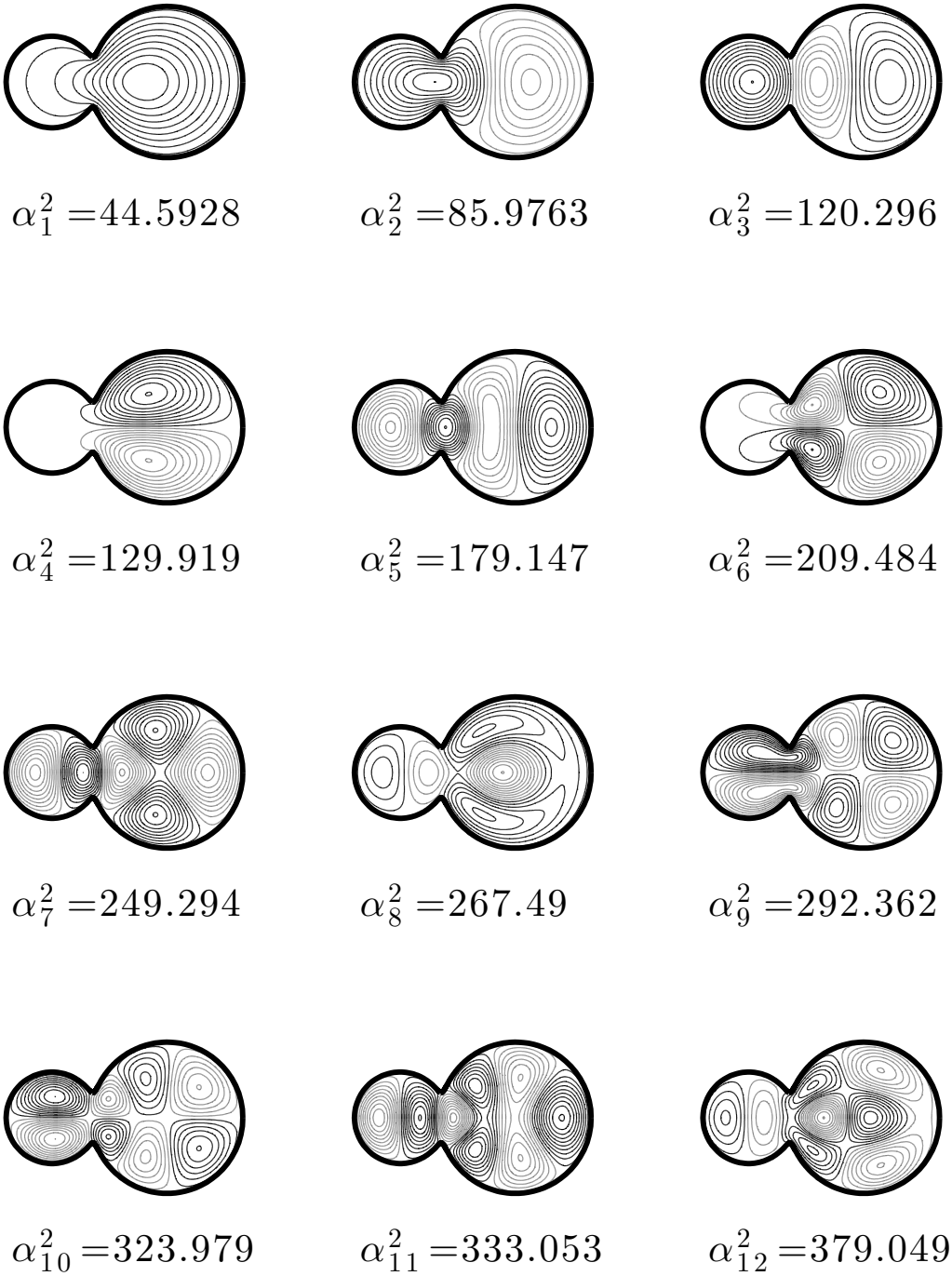

Figure A.3: First 12 Laplace eigenmodes and eigenvalues of the uneven Neumann oval defined by the conformal map (A.26), $q = 0.8$, $\gamma = 0.1$, $a = 0.4828$ (4 sig. figs.).

A.4 Conformal grids and numerical quadrature

Throughout this thesis Chebyshev spectral methods based on the work of Trefethen [115] have been used. Two examples, which also use the conformal mapping techniques of A.3.1, are

1. Eigenvalue solvers for the vorticity mode eigenvalue problem introduced in the context of the hydrodynamic limit in section 2.2 (and further used in the thermodynamic limit in section 4.3.1).

2. Expressions for the Laplacian and quadrature routines used in the sinh-Poisson solver of section 2.3.2.

A brief overview of Chebyshev spectral methods will now be presented and the convergence of the method demonstrated in terms of numerical quadrature for the domains used in this thesis.

Chebyshev methods are best introduced by considering the standard problem of approximating the derivative of some function $u(x)$ on a non-periodic 1D grid $x = \{x_1, \ldots, x_{\mathcal{N}}\}$. A standard way to do this would be using a finite difference formula [15]. Finite difference approximations are often derived by considering Taylor expansions, though in this case it is more instructive to consider their derivation using local interpolation: first we fit a unique polynomial of low degree (e.g. ≤ 4) to our function $u(x)$ at each grid point $\{x_i\}$, from which algebraic expressions for the derivative $u'(x)$ on all grid points can be calculated, leading to a matrix differential operator called a *differentiation matrix* $D_{\mathcal{N}}$. The degree of the polynomials used for this local interpolation determines the rate of convergence of the approximation of $u'(x)$. In general, uniform grids are used in this case. This method is effective, though in situations where high accuracy is required (e.g. calculation of eigenvalues), we are often stymied by computational difficulties relating to the size of the $D_{\mathcal{N}}$.

Chebyshev spectral methods take a more global approach: given $\mathcal{N}+1$ grid points $\{x_i\}$, a polynomial of order $\mathcal{N}$ is fitted to our function $u(x)$ on all grid points, which can then be differentiated to give an algebraic expression for the derivative $u'(x)$

and hence a differentiation matrix $D_{\mathcal{N}}$ (with different entries to the finite difference version). For a suitably smooth function $u(x)$, the Chebyshev spectral approximation of $u'(x)$ has remarkably fast 'spectral' convergence rates, in some cases exponential in $\mathcal{N}$. This allows high-accuracy approximations of the derivative to be computed using fewer grid points and hence a smaller $D_{\mathcal{N}}$ than would be required using the finite difference method described above.

Uniformally-spaced grids often have poor stability properties with Chebyshev spectral methods, so non-uniform grids are frequently used – a convenient one being that comprised of Chebyshev points, which are projections onto the x axis of equally spaced points on the unit circle. Consequently, 1D Chebyshev grids are naturally defined for $x \in [-1, 1]$, with points clustered near $x = \pm 1$. It is straightforward to alter such grids to have different ranges in 1D e.g. $R = (x + 1)/2$ gives $R \in [0, 1]$ with points clustered near $R = 0,\ 1$.

First and higher order[1] ordinary differential equations as can be solved by simply inverting the appropriate differentiation matrix and solving the resulting system linear of equations, usually using MATLAB's *backslash* command. Similarly, the eigenvalue problem $u'' = \lambda u$ (eigenvalues λ_i) can be solved by simply computing the eigenvalues of the differentiation matrix $[D_{\mathcal{N}}]^2$, easily done using MATLAB's *eig* routine[2]. In chapter 12 of Trefethen, the evaluation of integrals (numerical quadrature) on Chebyshev grids was demonstrated, with the so-called *Clenshaw-Curtis quadrature* shown to also have exponential convergence with the number of grid points.

The methods described above for solving differential equations/eigenvalue problems and calculating integrals can be extended to 2D problems. For square or rectangular domains Chebyshev grids can be used in both directions and the extensions are straightforward. However, in this thesis a grid is required in the unit disk $\mathcal{C}$ with $Z = Re^{i\theta}$ (see figure A.1). Such a grid was defined in chapter 11 of Trefethen that consisted of Chebyshev points in the radial direction R and periodic, regularly-spaced points in the azimuthal direction θ. The 2D Laplacian ∇^2 can be defined on this grid and hence partial differential equations and eigenvalue problems solved.

[1]The n^{th} derivative $u^{(n)}(x)$ is simply given the of the first order differentiation matrix raised to the power n i.e. $[D_{\mathcal{N}}]^n$.

[2]Note that the higher eigenvalues (when the number of grid points per wavelength of the eigenfunction is low) will not be spectrally accurate.

Numerical quadrature may also be performed using Clenshaw-Curtis quadrature in the radial direction and the periodic trapezoid rule in the azimuthal direction (which also converges exponentially fast).

For any grid and numerical quadrature scheme, integrals may be evaluated in the conformal domain $\mathcal{D}$ (see fig. A.1) using

$$\int_{\mathcal{D}} d\boldsymbol{x} = \int_{\mathcal{C}} J(R,\theta)\, d\boldsymbol{X}, \tag{A.27}$$

where $J(R,\theta) = |F'(Z)|^2$ is the Jacobian of the domain, also used in sections A.2.1 and A.3.1.

With the tools based on Chebyshev spectral methods described above, all the types of problems mentioned at the start of this section can be solved. To demonstrate the effectiveness of these methods, the convergence of integrals in the conformally mapped domains used in this thesis is considered. The error norm used is simply

$$e_{\mathcal{D}} = \left| \int_{\mathcal{D}} d\boldsymbol{x} - |\mathcal{D}| \right|, \tag{A.28}$$

where $|\mathcal{D}|$ is the domain area, equal to π in this thesis. The evaluation of the integral $\int_{\mathcal{D}} d\boldsymbol{x}$ is performed as described above i.e. mapping to $\mathcal{C}$ using (A.27) and then using Clenshaw-Curtis quadrature in the radial direction and periodic trapezoid rule in the azimuthal direction.

Before proceeding, the choice of the number of grid points must be considered. The work of Banjai [5] is particularly relevant here as he used the same conformal mapping techniques of section A.3.1 and the same spectral methods described above to calculate the Laplace eigenvalues and eigenmodes in a domain $\mathcal{D}$ with a fractal boundary. Of note, he found that having significantly more azimuthal points $\mathcal{M}$[3] than radial points $\mathcal{N}$ in $\mathcal{C}$ gave the best 'coverage' when the grid was mapped to the domain of interest $\mathcal{D}$. This approach is also adopted here, though on a less extreme scale than [5]. Specifically twice as many azimuthal points as radial points in $\mathcal{C}$ will be used. Figure A.4 shows the coverage of two grids with approximately

[3] $\mathcal{M}$ should not be confused with M the number of MFS charge points as used in chapter 3 and similarly $\mathcal{N}$ should not be confused with N the number of vortices as used throughout this thesis.

the same total number of grid points ($\mathcal{M}\mathcal{N} \approx 3000$) in the Neumann oval defined by $q = 0.8$. The grid in A.4(a) is constructed using $\mathcal{N} = \mathcal{M}/2$ and can be seen to offer significantly better coverage then the grid in A.4(b) that is constructed with $\mathcal{N} = \mathcal{M}$.

Note that the wasteful crowding of grid points near the regions of highest curvature in the domains shown in figure A.4 is a property of conformally mapping the Chebyshev grid in the disk to this domain. A new gird with more even spacing in the Neumann oval that reduces the crowding could be defined, but the exponential convergence properties of the spectral methods described above would be lost. As will be shown next, the use of spectral methods gives highly accurate results even with crowded grids.

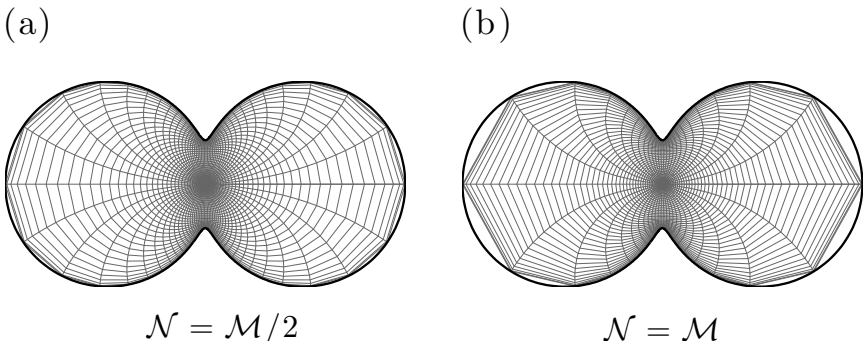

Figure A.4: Chebyshev grids in a Neumann oval for (a) twice as many azimuthal $\mathcal{M}$ as radial points $\mathcal{N}$ and (b) equal number of azimuthal and radial points. Both grids have approximately equal number of total grid points (3000).

With the above we are now able to demonstrate the effectiveness of the spectral methods. Figure A.5 shows the performance of the error norm (A.28) as the number of grid points increases while the ratio of twice as many azimuthal to radial points is maintained, for the two Neumann oval domains considered in chapter 4. Shown to the left are typical grids for both Neumann ovals. Machine precision ($\epsilon_{mach} \approx 10^{-15}$) in the error norm (A.28) is achieved in both cases, though convergence is significantly faster for the $q = 0.3$ Neumann oval due to the close-to-regular grid spacing in $\mathcal{D}$.

Figure A.6 shows the same as figure A.5 for two heart-shaped domains as used in chapter 2. Machine precision is achieved rapidly in both cases, again due to close-to-regular grid spacing in $\mathcal{D}$.

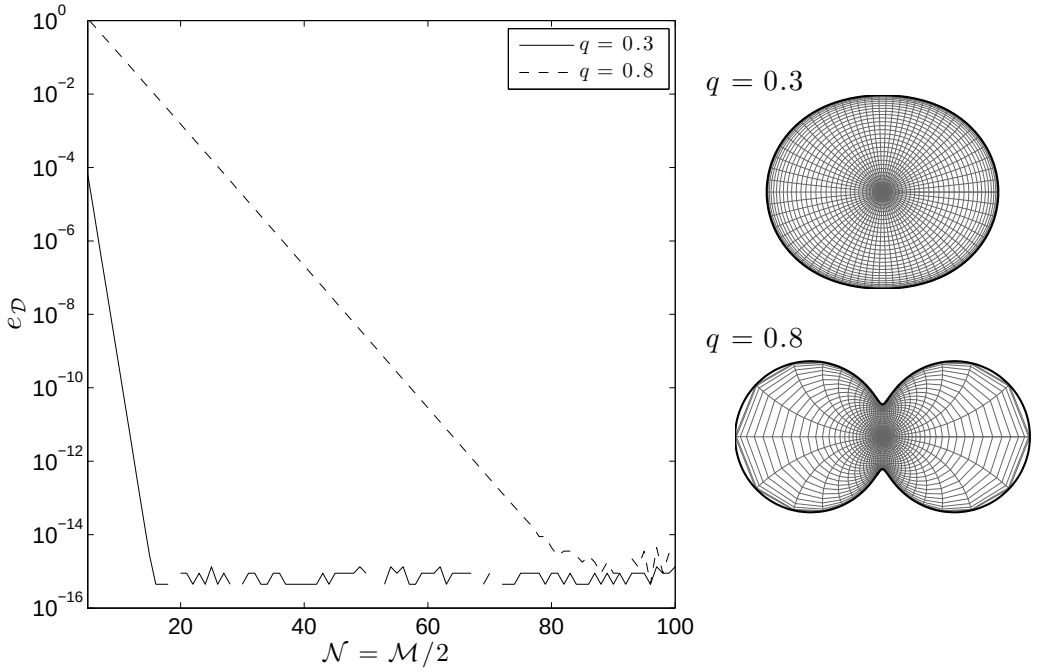

Figure A.5: Convergence of the integral error norm (A.28) as the number of grid points increases for the two Neuman oval domains shown to the right (shown with typical grids). The ratio of azimuthal points to radial points remains fixed at 2:1.

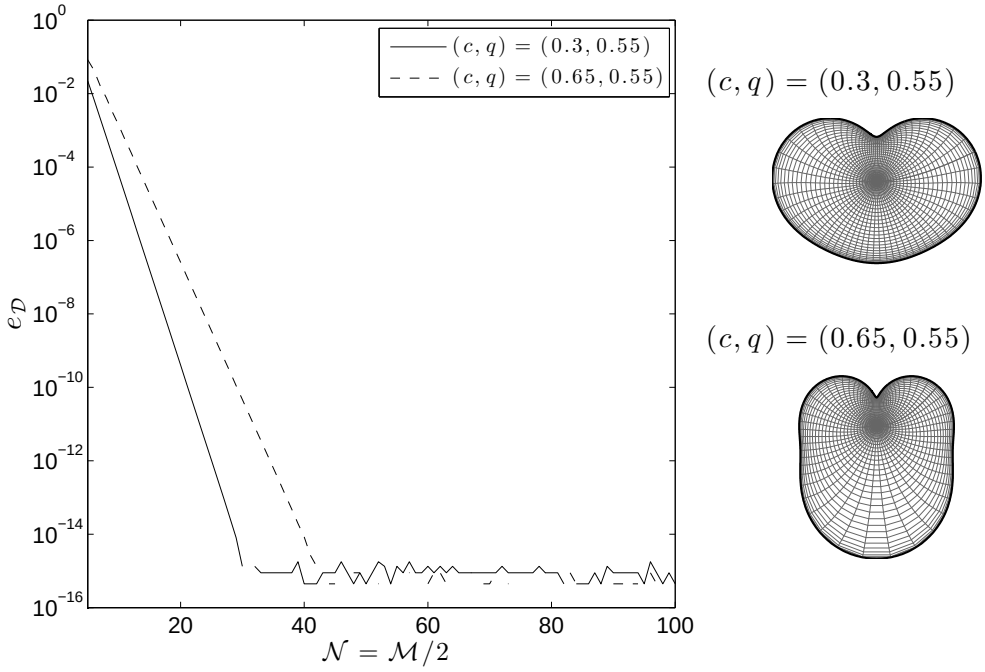

Figure A.6: As for figure A.5 for the heart-shaped domains shown to the right.

Appendix B

Further results from the Pointin-Lundgren hierarchy

B.1 Derivation of the second-order cumulant equations

In this section the missing detail in the derivation of (1.50-1.51) is supplied and a full account of the derivation of the second-order cumulant equations (1.52-1.54) is given.

Careful application of the same procedure as in section 1.3.5 to the marginal density p_{++} leads to

$$\begin{aligned}\nabla p_{++}(\boldsymbol{x},\boldsymbol{x}') = \left(\partial_{\tilde{E}}+\beta\right)\Bigg(&\frac{1}{2}\int_{\mathcal{D}}\nabla G(\boldsymbol{x},\boldsymbol{x}'')\big(p_{+++}(\boldsymbol{x},\boldsymbol{x}',\boldsymbol{x}'')-p_{++-}(\boldsymbol{x},\boldsymbol{x}',\boldsymbol{x}'')\big)\,d\boldsymbol{x}''\\ &-\frac{2}{N}\int_{\mathcal{D}}\nabla G(\boldsymbol{x},\boldsymbol{x}'')p_{+++}(\boldsymbol{x},\boldsymbol{x}',\boldsymbol{x}'')\,d\boldsymbol{x}''\\ &+\frac{1}{N}\nabla G(\boldsymbol{x},\boldsymbol{x}')p_{++}(\boldsymbol{x},\boldsymbol{x}')+\frac{1}{2N}\nabla g(\boldsymbol{x},\boldsymbol{x})p_{++}(\boldsymbol{x},\boldsymbol{x}')\Bigg).\end{aligned}\tag{B.1}$$

Similarly

$$\begin{aligned}\nabla p_{+-}(\boldsymbol{x},\boldsymbol{x}') = \Big(\partial_{\tilde{E}}+\beta\Big)\Big(&\frac{1}{2}\int_{\mathcal{D}}\nabla G(\boldsymbol{x},\boldsymbol{x}'')\big(p_{+-+}(\boldsymbol{x},\boldsymbol{x}',\boldsymbol{x}'')-p_{+--}(\boldsymbol{x},\boldsymbol{x}',\boldsymbol{x}'')\big)\,d\boldsymbol{x}''\\ &-\frac{1}{N}\int_{\mathcal{D}}\nabla G(\boldsymbol{x},\boldsymbol{x}'')\left(p_{+-+}(\boldsymbol{x},\boldsymbol{x}',\boldsymbol{x}'')-p_{+--}(\boldsymbol{x},\boldsymbol{x}',\boldsymbol{x}'')\right)\,d\boldsymbol{x}''\\ &-\frac{1}{N}\nabla G(\boldsymbol{x},\boldsymbol{x}')p_{+-}(\boldsymbol{x},\boldsymbol{x}')+\frac{1}{2N}\nabla g(\boldsymbol{x},\boldsymbol{x})p_{+-}(\boldsymbol{x},\boldsymbol{x}')\Big)\end{aligned}\tag{B.2}$$

$$\begin{aligned}\nabla p_{-+}(\boldsymbol{x},\boldsymbol{x}') = \Big(\partial_{\tilde{E}}+\beta\Big)\Big(&-\frac{1}{2}\int_{\mathcal{D}}\nabla G(\boldsymbol{x},\boldsymbol{x}'')\big(p_{-++}(\boldsymbol{x},\boldsymbol{x}',\boldsymbol{x}'')-p_{-+-}(\boldsymbol{x},\boldsymbol{x}',\boldsymbol{x}'')\big)\,d\boldsymbol{x}''\\ &+\frac{1}{N}\int_{\mathcal{D}}\nabla G(\boldsymbol{x},\boldsymbol{x}'')\left(p_{-++}(\boldsymbol{x},\boldsymbol{x}',\boldsymbol{x}'')-p_{-+-}(\boldsymbol{x},\boldsymbol{x}',\boldsymbol{x}'')\right)\;\;d\boldsymbol{x}''\\ &-\frac{1}{N}\nabla G(\boldsymbol{x},\boldsymbol{x}')p_{-+}(\boldsymbol{x},\boldsymbol{x}')+\frac{1}{2N}\nabla g(\boldsymbol{x},\boldsymbol{x})p_{-+}(\boldsymbol{x},\boldsymbol{x}')\Big)\end{aligned}\tag{B.3}$$

$$\begin{aligned}\nabla p_{--}(\boldsymbol{x},\boldsymbol{x}') = \Big(\partial_{\tilde{E}}+\beta\Big)\Big(&\frac{1}{2}\int_{\mathcal{D}}\nabla G(\boldsymbol{x},\boldsymbol{x}'')\big(p_{---}(\boldsymbol{x},\boldsymbol{x}',\boldsymbol{x}'')-p_{--+}(\boldsymbol{x},\boldsymbol{x}',\boldsymbol{x}'')\big)\,d\boldsymbol{x}''\\ &-\frac{2}{N}\int_{\mathcal{D}}\nabla G(\boldsymbol{x},\boldsymbol{x}'')p_{---}(\boldsymbol{x},\boldsymbol{x}',\boldsymbol{x}'')\;\;d\boldsymbol{x}''\\ &+\frac{1}{N}\nabla G(\boldsymbol{x},\boldsymbol{x}')p_{--}(\boldsymbol{x},\boldsymbol{x}')+\frac{1}{2N}\nabla g(\boldsymbol{x},\boldsymbol{x})p_{--}(\boldsymbol{x},\boldsymbol{x}')\Big).\end{aligned}\tag{B.4}$$

To obtain the equation for $\nabla\omega_2$ take

$$\frac{1}{4}\Big(\big((B.1)-p_+(\boldsymbol{x}')(1.48)\big)-\big((B.2)-p_-(\boldsymbol{x}')(1.48)\big)-\big((B.3)-p_+(\boldsymbol{x}')(1.49)\big)+\big((B.4)-p_-(\boldsymbol{x}')(1.49)\big)\Big)-\frac{1}{2N}\big((B.1)+(B.4)\big)$$

and for ∇c_2

$$\frac{1}{4}\Big(\big((B.1)-p_+(\boldsymbol{x}')(1.48)\big)-\big((B.2)-p_-(\boldsymbol{x}')(1.48)\big)+\big((B.3)-p_+(\boldsymbol{x}')(1.49)\big)-\big((B.4)-p_-(\boldsymbol{x}')(1.49)\big)\Big)-\frac{1}{2N}\big((B.1)-(B.4)\big)$$

with a similar calculation for $\nabla\rho_2$ leading to (1.54). In the latter case, the second-order cumulant

$$\begin{aligned}\phi_2(\boldsymbol{x},\boldsymbol{x}') &= \int_{\mathcal{D}} c_2(\boldsymbol{x},\boldsymbol{x}'')G(\boldsymbol{x}'',\boldsymbol{x}')\,d\boldsymbol{x}''\\ &= \langle(\rho(\boldsymbol{x})-\rho_1(\boldsymbol{x}))\,(\psi(\boldsymbol{x}')-\psi_1(\boldsymbol{x}'))\rangle-\frac{1}{N}\omega_1(\boldsymbol{x})G(\boldsymbol{x},\boldsymbol{x}')\end{aligned}$$

has been introduced. The third-order de-singularised cumulants are defined to be

$$\begin{aligned}
\omega_3(\boldsymbol{x},\boldsymbol{x}',\boldsymbol{x}'') &= \langle(\omega(\boldsymbol{x})-\omega_1(\boldsymbol{x}))(\omega(\boldsymbol{x}')-\omega_1(\boldsymbol{x}'))(\omega(\boldsymbol{x}'')-\omega_1(\boldsymbol{x}''))\rangle \\
&\quad - \frac{1}{N}\Big(\delta(\boldsymbol{x}''-\boldsymbol{x})c_2(\boldsymbol{x},\boldsymbol{x}')+\delta(\boldsymbol{x}-\boldsymbol{x}')c_2(\boldsymbol{x}',\boldsymbol{x}'')+\delta(\boldsymbol{x}'-\boldsymbol{x}'')c_2(\boldsymbol{x}'',\boldsymbol{x})\Big) \\
&\quad + \frac{2}{N^2}\delta(\boldsymbol{x}'-\boldsymbol{x})\delta(\boldsymbol{x}''-\boldsymbol{x})\omega_1(\boldsymbol{x}) \\
c_3(\boldsymbol{x},\boldsymbol{x}',\boldsymbol{x}'') &= \langle(\rho(\boldsymbol{x})-\rho_1(\boldsymbol{x}))(\omega(\boldsymbol{x}')-\omega_1(\boldsymbol{x}'))(\omega(\boldsymbol{x}'')-\omega_1(\boldsymbol{x}''))\rangle \\
&\quad - \frac{1}{N}\Big(\delta(\boldsymbol{x}'-\boldsymbol{x}'')\rho_2(\boldsymbol{x},\boldsymbol{x}')+\delta(\boldsymbol{x}-\boldsymbol{x}')\omega_2(\boldsymbol{x},\boldsymbol{x}'')+\delta(\boldsymbol{x}-\boldsymbol{x}'')\omega_2(\boldsymbol{x},\boldsymbol{x}')\Big) \\
&\quad + \frac{2}{N^2}\delta(\boldsymbol{x}'-\boldsymbol{x})\delta(\boldsymbol{x}''-\boldsymbol{x})\rho_1(\boldsymbol{x}).
\end{aligned}$$

and can be introduced into the calculation by means of the identities

$$\begin{aligned}
&\omega_3(\boldsymbol{x},\boldsymbol{x}',\boldsymbol{x}'')+\omega_1(\boldsymbol{x})\omega_2(\boldsymbol{x}',\boldsymbol{x}'')+\omega_1(\boldsymbol{x}')\omega_2(\boldsymbol{x}'',\boldsymbol{x})+\omega_1(\boldsymbol{x}'')\omega_2(\boldsymbol{x},\boldsymbol{x}') \\
&\qquad\qquad +\omega_1(\boldsymbol{x})\omega_1(\boldsymbol{x}')\omega_1(\boldsymbol{x}'') \\
&= \frac{1}{8}\Big(p_{+++}(\boldsymbol{x},\boldsymbol{x}',\boldsymbol{x}'')-p_{[++-]}(\boldsymbol{x},\boldsymbol{x}',\boldsymbol{x}'')+p_{[--+]}(\boldsymbol{x},\boldsymbol{x}',\boldsymbol{x}'')-p_{---}(\boldsymbol{x},\boldsymbol{x}',\boldsymbol{x}'')\Big) \\
&\quad - \frac{1}{4N}\Big(3p_{+++}(\boldsymbol{x},\boldsymbol{x}',\boldsymbol{x}'')-p_{[++-]}(\boldsymbol{x},\boldsymbol{x}',\boldsymbol{x}'')+p_{[--+]}(\boldsymbol{x},\boldsymbol{x}',\boldsymbol{x}'')-3p_{---}(\boldsymbol{x},\boldsymbol{x}',\boldsymbol{x}'')\Big) \\
&\quad + \frac{1}{N^2}\big(p_{+++}(\boldsymbol{x},\boldsymbol{x}',\boldsymbol{x}'')-p_{---}(\boldsymbol{x},\boldsymbol{x}',\boldsymbol{x}'')\big)
\end{aligned}$$

$$\begin{aligned}
&c_3(\boldsymbol{x},\boldsymbol{x}',\boldsymbol{x}'')+\rho_1(\boldsymbol{x})\omega_2(\boldsymbol{x}',\boldsymbol{x}'')+\omega_1(\boldsymbol{x}')c_2(\boldsymbol{x},\boldsymbol{x}'')+\omega_1(\boldsymbol{x}'')c_2(\boldsymbol{x},\boldsymbol{x}') \\
&\qquad\qquad +\rho_1(\boldsymbol{x})\omega_1(\boldsymbol{x}')\omega_1(\boldsymbol{x}'') \\
&= \frac{1}{8}\Big(p_{+++}(\boldsymbol{x},\boldsymbol{x}',\boldsymbol{x}'')+p_{(-++)}(\boldsymbol{x},\boldsymbol{x}',\boldsymbol{x}'')+p_{(+--)}(\boldsymbol{x},\boldsymbol{x}',\boldsymbol{x}'')+p_{---}(\boldsymbol{x},\boldsymbol{x}',\boldsymbol{x}'')\Big) \\
&\quad - \frac{1}{4N}\Big(3p_{+++}(\boldsymbol{x},\boldsymbol{x}',\boldsymbol{x}'')+p_{(-++)}(\boldsymbol{x},\boldsymbol{x}',\boldsymbol{x}'')+p_{(+--)}(\boldsymbol{x},\boldsymbol{x}',\boldsymbol{x}'')+3p_{---}(\boldsymbol{x},\boldsymbol{x}',\boldsymbol{x}'')\Big) \\
&\quad + \frac{1}{N^2}\big(p_{+++}(\boldsymbol{x},\boldsymbol{x}',\boldsymbol{x}'')-p_{---}(\boldsymbol{x},\boldsymbol{x}',\boldsymbol{x}'')\big)
\end{aligned}$$

where the shorthand $p_{[++-]}=p_{++-}+p_{-++}+p_{+-+}$ and $p_{(-++)}=p_{-++}-p_{+-+}-p_{++-}$ has been used.

B.2 Small E asymptotic theory

This section follows on from the cumulant expansion in the hydrodynamic limit in section 2.2.2 with an asymptotic analysis of the elliptic-sinh equation (ESE) in the small (positive) energy limit. Further properties of the EPE are revealed including a linear approximation to the inverse temperature $\beta(E)$.

Consider solutions to the ESE in the limit $E \to 0$. A new small parameter $\varepsilon = E^{1/2}$ is introduced and the key quanities in the PL76 framework are expanded in terms of it

$$\psi_1^{(0)} = \varepsilon \left(\Psi_0 + \varepsilon^2 \Psi_2 + \ldots\right), \tag{B.5a}$$

$$\omega_1^{(0)} = \mathcal{L}\psi_1^{(0)} = \varepsilon \left(\Omega_0 + \varepsilon^2 \Omega_2 + \ldots\right), \tag{B.5b}$$

$$\beta = B_0 + \varepsilon^2 B_2 + \ldots . \tag{B.5c}$$

As $E \to 0$ solutions of the ESE are known to bifurcate from critical values of the inverse temperature β; in other words from B_0 in (B.5c). These critical values are a property of the domain and it will be shown that they are given by the DITs defined is chapters 2 and 4. The aim of this asymptotic analysis is to determine B_0 (to obtain the critical temperatures of bifurcation) and further B_2 (to obtain a linear approximation to β, valid for small E). To simplify the calculation, the elliptic-Boltzmann-Poisson equation (2.23) will be considered instead of the elliptic-sinh equation (2.24).

Inserting the expansions (B.5a-B.5c) into the integral expression for C_1 given by

(2.22) gives

$$\begin{aligned}
C_1 &= \left(\int_{\mathcal{D}} \exp(\beta\psi)\ d\boldsymbol{x}\right)^{-1} \\
&= \rho_0 \left(1 + \varepsilon B_0\rho_0 \int_{\mathcal{D}} \Psi_0\ d\boldsymbol{x} + \varepsilon^2 \frac{B_0^2\rho_0}{2} \int_{\mathcal{D}} \Psi_0^2\ d\boldsymbol{x}\right. \\
&\quad \left. + \varepsilon^3 B_2\rho_0 \int_{\mathcal{D}} \Psi_0\ d\boldsymbol{x} + \varepsilon^3 B_0\rho_0 \int_{\mathcal{D}} \Psi_2\ d\boldsymbol{x} + \varepsilon^3 \frac{B_0^3\rho_0}{6} \int_{\mathcal{D}} \Psi_0^3\ d\boldsymbol{x} + O(\epsilon^4)\right)^{-1} \\
&= \rho_0 \left[1 - \varepsilon B_0\rho_0 \int_{\mathcal{D}} \Psi_0\ d\boldsymbol{x} + \varepsilon^2 B_0^2\rho_0 \left(\rho_0 \left(\int_{\mathcal{D}} \Psi_0\ d\boldsymbol{x}\right)^2 - \tfrac{1}{2}\int_{\mathcal{D}} \Psi_0^2\ d\boldsymbol{x}\right)\right. \\
&\quad - \varepsilon^3 B_2\rho_0 \int_{\mathcal{D}} \Psi_0\ d\boldsymbol{x} - \varepsilon^3 B_0\rho_0 \int_{\mathcal{D}} \Psi_2\ d\boldsymbol{x} \\
&\quad - \varepsilon^3 B_0^3\rho_0 \left(\rho_0^2 \left(\int_{\mathcal{D}} \Psi_0\ d\boldsymbol{x}\right)^3 - \right. \\
&\quad \left.\left. \rho_0 \left(\int_{\mathcal{D}} \Psi_0\ d\boldsymbol{x}\right)\left(\int_{\mathcal{D}} \Psi_0^2\ d\boldsymbol{x}\right) + \tfrac{1}{6}\int_{\mathcal{D}} \Psi_0^3\ d\boldsymbol{x}\right) + O(\varepsilon^4)\right].
\end{aligned}$$

The corresponding expression for C_2, also given by (2.22), is obtained by mapping $\beta \to -\beta$, hence

$$\begin{aligned}
\frac{C_1 - C_2}{2} &= -\varepsilon B_0\rho_0^2 \int_{\mathcal{D}} \Psi_0\ d\boldsymbol{x} - \varepsilon^3 B_2\rho_0^2 \int_{\mathcal{D}} \Psi_0\ d\boldsymbol{x} - \varepsilon^3 B_0\rho_0^2 \int_{\mathcal{D}} \Psi_2\ d\boldsymbol{x} \\
&\quad - \varepsilon^3 B_0^3\rho_0^2 \left[\rho_0^2 \left(\int_{\mathcal{D}} \Psi_0\ d\boldsymbol{x}\right)^3\right. \\
&\quad \left. - \rho_0 \left(\int_{\mathcal{D}} \Psi_0\ d\boldsymbol{x}\right)\left(\int_{\mathcal{D}} \Psi_0^2\ d\boldsymbol{x}\right) + \tfrac{1}{6}\int_{\mathcal{D}} \Psi_0^3\ d\boldsymbol{x}\right] + O(\varepsilon^5), \\
\frac{C_1 + C_2}{2} &= \rho_0 + \varepsilon^2 B_0^2\rho_0^2 \left[\rho_0 \left(\int_{\mathcal{D}} \Psi_0\ d\boldsymbol{x}\right)^2 - \tfrac{1}{2}\int_{\mathcal{D}} \Psi_0^2\ d\boldsymbol{x}\right] + O(\varepsilon^4).
\end{aligned}$$

Decomposing the Boltzmann-Poisson equation (2.23) into

$$\mathcal{L}\psi_1^{(0)} = \tfrac{1}{2}(C_1 - C_2)\cosh(\beta\psi_1^{(0)}) + \tfrac{1}{2}(C_1 + C_2)\sinh(\beta\psi_1^{(0)})$$

and inserting the above expansions, gives to leading order in ε,

$$\mathcal{L}\Psi_0 = B_0\rho_0 \left(\Psi_0 - \rho_0 \int_{\mathcal{D}} \Psi_0\ d\boldsymbol{x}\right), \tag{B.6}$$

together with boundary condition, and associated integral constraint

$$\Psi_0 = \text{const. on } \partial\mathcal{D}, \qquad \int_{\mathcal{D}} \mathcal{L}\Psi_0 \; d\boldsymbol{x} = 0.$$

These are the exact conditions that specify the vorticity mode eigenvalue problem (4.13) in chapter 4. Evidently, by definition, the possible eigenvalues are $B_0 = \beta_j$, with Ω_0 proportional to Φ_j. Further, since $\mathcal{L}\Phi_j = \beta_j \rho_0 \Phi_j$, and Φ_j satisfies no-normal flow boundary conditions, Ψ_0 is proportional to Φ_j (up to an irrelevant constant). The maximum entropy solution will be the one with largest inverse temperature, i.e. $j = 1$. Considering the energy (2.27b) at leading order gives the constraint

$$-\frac{1}{2}\int_{\mathcal{D}} \Psi_0 \mathcal{L}\Psi_0 \; d\boldsymbol{x} = 1$$

which is used to normalise Ψ_0, giving

$$\Psi_0(\boldsymbol{x}) = \left(-\frac{2}{\beta_1 \rho_0}\right)^{1/2} \Phi_1(\boldsymbol{x}).$$

To determine the specific heats of the modes of excitation in the limit $E \to 0$, we must proceed to higher order. At $O(\varepsilon^3)$ the elliptic-Boltzmann equation can be written as

$$\begin{aligned}
\left(\mathcal{L} - B_0\rho_0 + B_0\rho_0^2 \int_{\mathcal{D}} \cdot \; d\boldsymbol{x}\right)\Psi_2 = \\
&- B_0^3\rho_0^2\left(\rho_0^2\left(\int_{\mathcal{D}} \Psi_0 \; d\boldsymbol{x}\right)^3 - \rho_0\left(\int_{\mathcal{D}} \Psi_0 \; d\boldsymbol{x}\right)\left(\int_{\mathcal{D}} \Psi_0^2 \; d\boldsymbol{x}\right) + \tfrac{1}{6}\int_{\mathcal{D}} \Psi_0^3 \; d\boldsymbol{x}\right) \\
&- \tfrac{1}{2}B_0^3\rho_0^2\Psi_0^2\left(\int_{\mathcal{D}} \Psi_0 \; d\boldsymbol{x}\right) \\
&+ \tfrac{1}{6}\rho_0 B_0^3\Psi_0^3 + B_0^3\rho_0^2\Psi_0\left(\rho_0\left(\int_{\mathcal{D}} \Psi_0 \; d\boldsymbol{x}\right)^2 - \tfrac{1}{2}\int_{\mathcal{D}} \Psi_0^2 \; d\boldsymbol{x}\right) \\
&+ B_2\rho_0\Psi_0 - B_2\rho_0^2\left(\int_{\mathcal{D}} \Psi_0 \; d\boldsymbol{x}\right).
\end{aligned}$$

Inserting for Ψ_0 and B_0, and using the fact that

$$\int_{\mathcal{D}} \Phi_1 \; d\boldsymbol{x} = 0$$

results in

$$\left(\mathcal{L} - B_0\rho_0 + B_0\rho_0^2 \int_{\mathcal{D}} \cdot \; d\boldsymbol{x}\right) \Psi_2 = \left(-\frac{2}{\beta_1\rho_0}\right)^{1/2} \left(-\frac{\beta_1^2}{3}\left(\Phi_1^3 - \rho_0 \int_{\mathcal{D}} \Phi_1^3 \; d\boldsymbol{x}\right) + \left(\beta_1^2 + B_2\right)\rho_0\Phi_1\right). \quad \text{(B.7)}$$

The solvability condition for (B.7) is that the inner product of the forcing terms on the right-hand side with Φ_1 must be zero. Evaluating this inner product returns B_2,

$$\begin{aligned} B_2 &= -\beta_1^2\left(1 - \frac{D_1}{3}\right), \\ \text{where} \quad D_1 &= \rho_0^{-1}\int_{\mathcal{D}} \Phi_1^4 \; d\boldsymbol{x}. \end{aligned} \quad \text{(B.8)}$$

Hence, in the hydrodynamic scaling regime the inverse temperature in the limit $E \to 0$ has the form

$$\beta(E) = \beta_1 - \beta_1^2\left(1 - \frac{D_1}{3}\right)E + O(E^2). \quad \text{(B.9)}$$

Expressions analogous to (B.9) can be derived corresponding to the higher branches β_i, $i > 1$.

Figure 2.6 shows the linear approximations (B.9) and the corresponding full non-linear sinh-Poisson solutions for the first three branches for the heart domain defined by $(c, q) = (0.51, 0.55)$. Good agreement at low energies it evident between the full solution and (B.9).

It is interesting to understand how the values of D_1 (and $D_{2,3,\ldots}$) vary depending on the geometry of the domain $\mathcal{D}$. Table B.1 shows $D_1/3$ for a variety of domains; further details of the Neumann oval are in section 3.3.2 and of the heart in section 2.4.3. Despite the domains being drastically different from one another, $D_1/3 \in [0.7, 0.78]$ for all domains shown. This prompts two questions: how fundamental to the system is this range of values? Further, is $1 < D_1/3$ for every domain i.e. is the gradient of (B.9) always negative? These questions, along with others relating to how the geometry controls the distribution of DITs, await further study.

Domain (area $= \pi$)	$D_1/3$
Circle	0.7758
Neumann oval, $q = 0.3$	0.7553
Neumann oval, $q = 0.8$	0.7007
Heart, $(c, q) = (0.51, 0.55)$	0.7634
Heart, $(c, q) = (0.65, 0.55)$	0.7484

Table B.1: Values of the integral constraint (B.8) (to 4 sig. figs.) for various domains.

Bibliography

[1] M. J. Ablowitz and A. S. Fokas. *Complex Variables: Introduction and Applications*. Cambridge Univ. Press, Cambridge, 2003.

[2] H. Aref, editor. *150 years of vortex dynamics: Proceedings of an IUTAM symposium held at the Technical University of Denmark (October 12-16 2008)*. Springer, 2010.

[3] W. Arendt, R. Nittka, W. Peter, and F. Steiner. Weyl's law: Spectral properties of the Laplacian in mathematics and physics. In W. Arendt and W. P. Schleich, editors, *Mathematical Analysis of Evolution, Information, and Complexity*, pages 1–71. Wiley-VCH Verlag GmbH & Co. KGaA, Weinheim, 2009.

[4] T. L. Ashbee, J. G. Esler, and N. R. McDonald. Generalized Hamiltonian point vortex dynamics on arbitrary domains using the method of fundamental solutions. *J. Comput. Phys.*, 246:289–303, 2013.

[5] L. Banjai. Eigenfrequencies of fractal drums. *J. Comput. Appl. Math.*, 198(1):1–18, 2007.

[6] C. F. Barenghi, R. J. Donnelly, and W. F. Vinen. *Quantized vortex dynamics and superfluid turbulence*. Springer-Verlag, Berlin, 2001.

[7] A. H. Barnett and T. Betcke. Stability and convergence of the method of fundamental solutions for Helmholtz problems on analytic domains. *J. Comput. Phys.*, 227(14):7003–7026, 2008.

[8] B. A. Berg. Introduction to multicanonical Monte Carlo simulations. *Fields Inst. Commun.*, 26:124, 2000.

[9] A. Bogomolny. Fundamental solutions method for elliptic boundary value problems. *SIAM J. Numer. Anal.*, 22(4):644–669, 1985.

[10] L. E. Boltzmann. *Lectures on Gas Theory*. Dover Publications, Mineola, 1995.

[11] D. L. Book, S. Fisher, and B. E. McDonald. Steady-state distributions of interacting discrete vortices. *Phys. Rev. Lett.*, 34:4–8, 1975.

[12] F. Bouchet and J. Sommeria. Emergence of intense jets and Jupiter's Great Red Spot as maximum-entropy structures. *J. Fluid Mech.*, 464:165–207, 2002.

[13] O. Bühler. Statistical mechanics of strong and weak point vortices in a cylinder. *Phys. Fluids*, 14(7):2139–2149, 2002.

[14] O. Bühler. *A brief introduction to classical, statistical and quantum mechanics*. Amer. Math. Soc., Providence, 2006.

[15] R. L. Burden and J. D. Faires. *Numerical Analysis*. Brooks Cole, Stamford, 1988.

[16] E. Caglioti, P. L. Lions, C. Marchioro, and M. Pulvirenti. A special class of stationary flows for two-dimensional Euler equations: A statistical mechanics description. Part I. *Commun. Math. Phys.*, 143(3):501–525, 1992.

[17] E. Caglioti, P. L. Lions, C. Marchioro, and M. Pulvirenti. A special class of stationary flows for two-dimensional Euler equations: A statistical mechanics description. Part II. *Commun. Math Phys.*, 174(2):229–260, 1995.

[18] L. J. Campbell and K. O'Neil. Statistics of two-dimensional point vortices and high-energy vortex states. *J. Stat. Phys.*, 65:495–529, 1991.

[19] S. Chandrasekhar. *Principles of stellar dynamics*. Dover Publications, Mineola, 1942.

[20] J. G Charney. On the scale of atmospheric motions. *Geofys. Publ. Oslo*, 17:1–17, 1948.

[21] P.-H. Chavanis. On the lifetime of metastable states in self - gravitating systems. *Astron. Astrophys.*, 432:117.

[22] P.-H. Chavanis. Systematic drift experienced by a point vortex in two-dimensional turbulence. *Phys. Rev. E*, 58:1199–1202, 1998.

[23] P.-H. Chavanis. *Statistical mechanics of two-dimensional vortices and stellar systems*. Lecture Notes in Physics, Vol. 602, Springer, 2002.

[24] P.-H. Chavanis. Two-dimensional Brownian vortices. *Physica A*, 387(28):6917–6942, 2008.

[25] P.-H. Chavanis. Kinetic theory of Onsager's vortices in two-dimensional hydrodynamics. *Physica A*, 391(14):3657–3679, 2012.

[26] P.-H. Chavanis and L. Delfini. Random transitions described by the stochastic smoluchowski poisson system and by the stochastic Keller-Segel model. *Phys. Rev. E*, In press.

[27] P.-H. Chavanis and J. Sommeria. Classification of self-organized vortices in two-dimensional turbulence: The case of a bounded domain. *J. Fluid Mech.*, 314:267–297, 1996.

[28] K. H. Chen, J. H. Kao, J. T. Chen, D. L. Young, and M. C. Lu. Regularized meshless method for multiply-connected-domain Laplace problems. *Eng. Anal. Bound. Elem.*, 30(10):882–896, 2006.

[29] M. Chertkov, C. Connaughton, I. Kolokolov, and V. Lebedev. Dynamics of energy condensation in two-dimensional turbulence. *Phys. Rev. Lett.*, 99:084501, 2007.

[30] I. P. Christiansen. Numerical simulation of hydrodynamics by the method of point vortices. *J. Comput. Phys.*, 13(3):363 – 379, 1973.

[31] H. J. H. Clercx, S. R. Maassen, and G. J. F. van Heijst. Spontaneous spin-up during the decay of 2d turbulence in a square container with rigid boundaries. *Phys. Rev. Lett.*, 80:5129–5132, 1998.

[32] H. J. H. Clercx, A. H. Nielsen, D. J. Torres, and E. A. Coutsias. Two-dimensional turbulence in square and circular domains with no-slip walls. *Eur. J. Mech. B-Fluid*, 20(4):557–576, 2001.

[33] P. Constantin, A. J. Majda, and E. Tabak. Formation of strong fronts in the 2D quasigeostrophic thermal active scalar. *Nonlinearity*, 7:1495–1533, 1994.

[34] T. E. Cravens. *Physics of Solar System Plasmas*. Cambridge Univ. Press, Cambridge, 1997.

[35] D. G. Crowdy and J. S. Marshall. Analytical formulae for the Kirchhoff-Routh path function in multiply connected domains. *Proc. R. Soc. Lond. A*, 461(2060):2477–2501, 2005.

[36] D. G. Crowdy and J. S. Marshall. The motion of a point vortex around multiple circular islands. *Phys. Fluids*, 17(5):056602, 2005.

[37] L. Debnath and P. Mikusiński. *Introduction to Hilbert spaces with applications*. Elsevier, Amsterdam, 2005.

[38] M. T. DiBattista and A. J. Majda. Equilibrium statistical predictions for baroclinic vortices: The role of angular momentum. *Theor. Comp. Fluid Dyn.*, 14:293–322, 2001.

[39] R. J. Donnelly. *Quantized vortices in Helium II*. Cambridge Univ. Press, Cambridge, 1991.

[40] T. A. Driscoll and K. L. Maki. Searching for rare growth factors using multicanonical Monte Carlo methods. *SIAM Rev.*, 49:673 – 692, 2007.

[41] D. G. Dritschel. Contour dynamics and contour surgery: Numerical algorithms for extended, high-resolution modelling of vortex dynamics in two-dimensional, inviscid, incompressible flows. *Comp. Phys. Rep.*, 10(3):77–146, 1989.

[42] D. G. Dritschel and S. Boatto. The motion of point vortices on compact surfaces. *Proc. R. Soc. A*, In press.

[43] S. F. Edwards and J. B. Taylor. Negative temperature states of two-dimensional plasmas and vortex fluids. *Proc. R. Soc. A*, 336(1606):257–271, 1974.

[44] J. G. Esler and T. L. Ashbee. The critical condensation temperature of a neutral point vortex gas. *Phys. Rev. Lett.*, In press.

[45] J. G. Esler, T. L. Ashbee, and N. R. McDonald. Statistical mechanics of a neutral point-vortex gas at low energy. *Phys. Rev. E*, 88:012109, 2013.

[46] L. Euler. Principes généraux du mouvement des fluides. *Mémoires de l'Académie des Sciences de Berlin*, 11:274–315, 1757.

[47] P. P. Ewald. Die Berechnung optischer und elektrostatischer Gitterpotentiale. *Ann. Phys. (Berlin)*, 369(3):253–287, 1921.

[48] G. L. Eyink and H. Spohn. Negative-temperature states and large-scale, long-lived vortices in two-dimensional turbulence. *J. Stat. Phys.*, 70:833–886, 1993.

[49] G. L. Eyink and K. R. Sreenivasan. Onsager and the theory of hydrodynamic turbulence. *Rev. Mod. Phys.*, 78:87–135, 2006.

[50] G. Fairweather and A. Karageorghis. The method of fundamental solutions for elliptic boundary value problems. *Adv. Comput. Math.*, 9:69–95, 1998.

[51] M. Flucher and B. Gustafsson. *Vortex motion in two dimensional hydrodynamics*. Springer, New York, 1999.

[52] J. Fröhlich and D. Ruelle. Statistical mechanics of vortices in an inviscid two-dimensional fluid. *Comm. Math. Phys.*, 87:1–36, 1982.

[53] C. Gardiner. *Stochastic Methods: A Handbook for the Natural and Social Sciences*. Springer-Verlag, Berlin, 2004.

[54] M. A. Golberg and C. S. Chen. *Discrete Projection Methods for Integral Equations*. Computational Mechanics Publications, Boston, 1996.

[55] M. A. Golberg and C. S. Chen. The method of fundamental solutions for potential, Helmholtz and diffusion problems. In M. A. Golberg, editor, *Boundary Integral Methods - Numerical and Mathematical Aspects*, pages 103–176. Computational Mechanics Publications, Boston, 1999.

[56] M. A. Golberg, C. S. Chen, and S. R. Karur. Improved multiquadric approximation for partial differential equations. *Eng. Anal. Bound. Elem.*, 18(1):9–17, 1996.

[57] W. Greiner, N. Ludwig, and H. Stöcker. *Thermodynamics and statistical mechanics*. Springer-Verlag, New York, 1995.

[58] N. Grønbech-Jensen. Summation of logarithmic interactions in nonrectangular periodic media. *Comput. Phys. Commun.*, 119(2-3):115–121, 1999.

[59] A. Hasegawa and K. Mima. Pseudo-three-dimensional turbulence in magnetized nonuniform plasma. *Phys. Fluids*, 21(1):87–92, 1978.

[60] I. M. Held, R. T. Pierrehumbert, S. T. Garner, and K. L. Swanson. Surface quasi-geostrophic dynamics. *J. Fluid Mech.*, 282:1–20, 1995.

[61] H. v. Helmholtz. Über integrale der hydrodynamischen Gleichungen, welche den wirbelbewegungen entsprechen. *J. Reine Agnew. Math.*, 55:25–55, 1858.

[62] N. G. Hogg and H. M. Stommel. Hetonic explosions: The breakup and spread of warm pools as explained by baroclinic point vortices. *J. Atmos. Sci.*, 42:1465–1476, 1985.

[63] S. Hoshi and T. Miyazaki. Statistics of quasi-geostrophic point vortices. *Fluid Dyn. Res.*, 40(9):662 – 678, 2008.

[64] G. Joyce and D. Montgomery. Negative temperature states for a two-dimensional guiding center plasma. *J. Plasma Phys.*, 10:107–121, 1973.

[65] M. N. Juckes. Quasigeostrophic dynamics of the tropopause. *J. Atmos. Sci.*, 51:2756–2779, 1994.

[66] M. Katsurada. A mathematical study of the charge simulation method. II. *J. Fac. Sci. Univ. Tokyo Sect. IA Math.*, 36(1):135–162, 1989.

[67] M. Katsurada and H. Okamoto. A mathematical study of the charge simulation method. I. *J. Fac. Sci. Univ. Tokyo Sect. IA Math.*, 35(3):507–518, 1988.

[68] M. K.-H. Kiessling and J. L. Lebowitz. The micro-canonical point vortex ensemble: Beyond equivalence. *Lett. Math. Phys.*, 42:43–56, 1997.

[69] G. R. Kirchhoff. *Vorlesungen über mathematische Physik*. Teubner, Leipzig, 1876.

[70] T. Kitagawa. On the numerical stability of the method of fundamental solution applied to the Dirichlet problem. *Japan J. Appl. Math.*, 5(1):123–133, 1988.

[71] T. Kitagawa. Asymptotic stability of the fundamental solution method. *J. Comp. Appl. Math.*, 38:263–269, 1991.

[72] B. N. Kuvshinov and T. J. Schep. Double-periodic arrays of vortices. *Phys. Fluids*, 12(12):3282–3284, 2000.

[73] L. D. Landau and E. M. Lifshitz. *Statistical Physics: Part 1.* Pergamon Press, Oxford, Third edition, 1980.

[74] S. Legg and J. Marshall. A heton model of the spreading phase of open-ocean deep convection. *J. Phys. Oceanogr.*, 23:1040–1056, 1993.

[75] S. Legg and J. Marshall. The influence of the ambient flow on the spreading of convective water masses. *J. Mar. Res.*, 56:107–139, 1998.

[76] C. C. Lin. On the motion of vortices in two dimensions–I. Existence of the Kirchhoff-Routh function. *Proc. Natl Acad. Sci.*, 27:570–575, 1941a.

[77] C. C. Lin. On the motion of vortices in two dimensions–II. Some further investigations on the Kirchhoff-Routh function. *Proc. Natl Acad. Sci.*, 27:575–577, 1941b.

[78] E. Lundberg. Laplacian growth, elliptic growth, and singularities of the Schwarz potential. *J. Phys. A: Math. Theor.*, 44(13):135202, 2011.

[79] D. Lynden-Bell. Statistical mechanics of violent relaxation in stellar system. *GMon. Not. R. astr. Soc.*, 136:101, 1967.

[80] C. Marchioro and M. Pulvirenti. *Mathematical theory of incompressible and non viscous fluids.* Springer-Verlag, New York, 1994.

[81] H. Marmanis. The kinetic theory of point vortices. *Proc. R. Soc. Lond. A*, 454(1970):587–606, 1998.

[82] B. E. McDonald. Numerical calculation of nonunique solutions of a two-dimensional sinh-Poisson equation. *J. Comput. Phys.*, 16(4):360 – 370, 1974.

[83] A. Miguel. Adaptive geometric numerical integration for point vortex dynamics. *Phys. Rev. E*, 74(4):046706, 2006.

[84] J. Miller. Statistical mechanics of the Euler equation in two dimensions. *Phys. Rev. Lett.*, 65:2137–2140, 1990.

[85] J. Miller, P. B. Weichman, and M. C. Cross. Statistical mechanics, Euler's equation and Jupiter's Red Spot. *Phys. Rev. A*, 45:2328–2359.

[86] T. Miyazaki, T. Sato, and N. Takahashi. Maximum entropy states of quasi-geostrophic point vortices. *Phys. Fluids*, 24(5):056601, 2012.

[87] D. Montgomery and G. Joyce. Statistical mechanics of "negative temperature" states. *Phys. Fluids*, 17(6):1139–1145, 1974.

[88] D. Montgomery, W. H. Matthaeus, W. T. Stribling, D. Martinez, and S. Oughton. Relaxation in two dimensions and the 'sinh-Poisson' equation. *Phys. Fluids*, 4:3–6, 1992.

[89] A. Naso, P.-H. Chavanis, and B. Dubrulle. Statistical mechanics of two-dimensional euler flows and minimum enstrophy states. *Eur. Phys. J. B*, 77(2):187–212, 2010.

[90] A. Naso, P.-H. Chavanis, and B. Dubrulle. Statistical mechanics of Fofonoff flows in an oceanic basin. *Eur. Phys. J. B*, 80(4):493–517, 2011.

[91] P. K. Newton. *The N-Vortex Problem: Analytical Techniques*. Springer-Verlag, New York, 2001.

[92] R. S. Nilawar, E. R. Johnson, and N. R. McDonald. Finite Rossby radius effects on vortex motion near a gap. *Phys. Fluids*, 24(6):066601, 2012.

[93] L. Onsager. Statistical hydrodynamics. *Il Nuovo Cimento (1943-1954)*, 6:279–287, 1949.

[94] J. Pedlosky. *Geophysical Fluid Dynamics*. Springer-Verlag, New York, 1987.

[95] Y. B. Pointin and T. S. Lundgren. Statistical mechanics of two-dimensional vortices in a bounded container. *Phys. Fluids*, 19(10):1459–1470, 1976.

[96] D. I. Pullin and P. G. Saffman. Long-time symplectic integration: The example of four-vortex motion. *Proc. R. Soc. A*, 432(1886):481–494, 1991.

[97] E. M. Purcell and R. V. Pound. A nuclear spin system at negative temperature. *Phys. Rev.*, 81:279–280, 1951.

[98] J. A. Rice. *Mathematical Statistics and Data Analysis*. Brooks Cole, Stamford, 1988.

[99] P. L. Richardson, A. S. Bower, and W. Zenk. A census of meddies tracked by floats. *Prog. Oceanogr.*, 45(2):209 – 250, 2000.

[100] S. Richardson. Some Hele-Shaw flows with time-dependent free boundaries. *J. Fluid Mech.*, 102:263–278, 1981.

[101] R. Robert. A maximum entropy principle for two-dimensional Euler equations. *J. Stat. Phys.*, 65:531–553, 1991.

[102] R. Robert and J. Sommeria. Statistical equilibrium states for two-dimensional flows. *J. Fluid Mech.*, 229:291–310, 1991.

[103] E. J. Routh. Some applications of conjugate functions. *Proc. Lond. Math. Soc.*, 12:73–89, 1881.

[104] P. G. Saffman. *Vortex dynamics*. Cambridge Univ. Press, Cambridge, 1992.

[105] B. W. Silverman. *Density estimation for statistics and data analysis*. Chapman and Hall, London, 1986.

[106] L. M. Smith and V. Yakhot. Bose condensation and small-scale structure generation in a random force driven 2D turbulence. *Phys. Rev. Lett.*, 71:352–355, 1993.

[107] R. A. Smith. Phase transition behavior in a negative-temperature guiding-center plasma. *Phys. Rev. Lett.*, 63:1479–1482, 1989.

[108] R. A. Smith and T. M. O'Neil. Nonaxisymmetric thermal equilibria of a cylindrically bounded guiding-center plasma or discrete vortex system. *Phys. Fluids B*, 2(12):2961–2975, 1990.

[109] Y.-S. Smyrlis and A. Karageorghis. Efficient implementation of the MFS: The three scenarios. *J. Comput. Appl. Math.*, 227(1):83–92, 2009.

[110] J. B. Taylor. Turbulence in two-dimensional plasmas and fluids. *Plasma Phys. Conrt. F.*, 39(5A):A1, 1997.

[111] J. B. Taylor, M. Borchardt, and P. Helander. Interacting vortices and spin-up in two-dimensional turbulence. *Phys. Rev. Lett.*, 102:124505, 2009.

[112] J. B. Taylor and B. McNamara. Plasma diffusion in two dimensions. *Phys. Fluids*, 14(7):1492–1499, 1971.

[113] A. C. Ting, H. H. Chen, and Y. C. Lee. Exact solutions of a nonlinear boundary value problem: The vortices of the two-dimensional sinh-Poisson equation. *Physica D*, 26:37 – 66, 1987.

[114] H. Touchette. The large deviation approach to statistical mechanics. *Phys. Rep.*, 478(1-3):1–69, 2009.

[115] L. N. Trefethen. *Spectral Methods in MATLAB*. SIAM, Philadelphia, 2000.

[116] G. J. F. Van Heijst, H. J. H. Clercx, and D. Molenaar. The effects of solid boundaries on confined two-dimensional turbulence. *J. Fluid Mech.*, 554:411–431, 2006.

[117] A. Venaille and F. Bouchet. Statistical ensemble inequivalence and bicritical points for two-dimensional flows and geophysical flows. *Phys. Rev. Lett.*, 102:104501, Mar 2009.

[118] A. Venaille and F. Bouchet. Solvable phase diagrams and ensemble inequivalence for two-dimensional and geophysical turbulent flows. *J. Stat. Phys.*, 143(2):346–380, 2011.

[119] J. von Hardenberg, J. C. McWilliams, A. Provenzale, A. Shchepetkin, and J. B. Weiss. Vortex merging in quasi-geostrophic flows. *J. Fluid Mech.*, 412(1606):331–353, 2000.

[120] M. P. Wand and M. C. Jones. *Kernel Smoothing*. Chapman & Hall, London, 1995.

[121] J. B. Weiss and J. C. McWilliams. Nonergodicity of point vortices. *Phys. Fluids A*, 3(5):835–844, 1991.

[122] C. T. Wu, F. L. Yang, and D. L. Young. Application of the method of fundamental solutions and the generalized Lagally theorem to the interaction of solid body and external singularities in an inviscid fluid. *CMC-Comput. Mat. Contin.*, 23(2):135–153, 2011.

[123] Y. Yatsuyanagi, Y. Kiwamoto, H. Tomita, M. M. Sano, T. Yoshida, and T. Ebisuzaki. Dynamics of two-sign point vortices in positive and negative temperature states. *Phys. Rev. Lett.*, 94:054502, 2005.

[124] Z. Yin, D. C. Montgomery, and H. J. H. Clercx. Alternative statistical-mechanical descriptions of decaying two-dimensional turbulence in terms of "patches" and "points". *Phys. Fluids*, 15(7):1937–1953, 2003.

[125] M.-Q. Zhang and M.-Z. Qin. Explicit symplectic schemes to solve vortex systems. *Comput. Math. Appl.*, 26(5):51–56, 1993.